LARGE EDDY SIMULATION OF

OPEN CHANNEL FLOWS

FOR CONVEYANCE ESTIMATION

FAYE BEAMAN, MEng.

Thesis submitted to the University of Nottingham

for the degree of Doctor of Philosophy

MARCH 2010

ABSTRACT

Prediction of conveyance capacity in open channel flows is complex and requires adequate modelling of flow features such as secondary circulation cells and, specifically for over-bank channels, the momentum exchange that occurs at the main channel/floodplain interface. A variety of conveyance estimation methods have been developed with the objective of accurately capturing these flow characteristics through a simplified user-friendly approach. However, these methods usually require calibration of one or more empirical constants.

Within this thesis in-bank and over-bank channels have been numerically simulated using Large Eddy Simulation (LES) in order to predict accurate open channel flow behaviour. The LES results are validated against experimental data and then utilised to advise on values of calibration constants f, λ and Γ within a conveyance estimation method, the Shiono and Knight Method (SKM), which has recently been adopted by the Environment Agency (EA) for England and Wales as part of its new Conveyance Estimation System (CES). The LES results are shown to accurately predict the flow features, specifically the distribution of secondary circulations in in-bank channels of aspect ratio as large as 40 and for over-bank channels at varying depth and width ratios.

The LES derived f, λ and Γ values are then utilized in the analytical solution of the SKM in order to compute depth averaged velocity profiles for comparison to

LES results, producing very good agreement with simulated and experimental profiles.

As well as the derivation of f, λ and Γ constants, the apparent shear stress at the main channel/floodplain interface is investigated and the contributions from both Reynolds stress and secondary circulation terms compared. Also, instantaneous velocity data available from monitor points at the main channel/floodplain interface within over-bank channel simulations is utilized to investigate wave periods of interfacial vortices through spectral analysis. Comparable result to available experimental and stability analysis data are obtained.

ACKNOWLEDGEMENTS

Many thanks go first to my supervisors, Prof. Nigel Wright and Dr. Herve Morvan, for their support and encouragement. Both have been more than willing to share their knowledge and help guide me through the past 3 years. Thanks are also extended to Dr David Hargreaves for his constant technical support with CFX and Prof. Donald Knight for his kind sharing of information and numerous discussions regards the SKM.

I would like to thank those whom have become friends in L4, Michael Lees, Chris Tighe, David Stevens, Paolo Orsini, Jenny Taylor, Neil Botteril and Phrain Gu, whom have all helped along the way to make this a more pleasant journey. Special thanks go to Jonathan Paton who has been the greatest support (he got muffins out of it… it was a fair deal). More recently I would also like to thank the colleagues at Arup Brisbane for their support also.

Thanks go to the resources provided through the University of Nottingham. Also, to TU Delft for the prevision of their LES code and to Harman Talstra for his support and numerous technical advice regarding the code and help with its implementation.

I would also like to thank my family. Unbeknown to them they have been of great support. Special thanks go to Stewart Hayes for supporting me through some hard years, which will always be appreciated. Finally, I want to thank my partner, Vern, who has supported, encouraged and loved me throughout the writing of this thesis.

To mom

(1950-2004)

TABLE OF CONTENTS

LIST OF ABBREVIATIONS

ADV	Acoustic Doppler Velocimetry
ASF	Apparent Shear Force
ASM	Algebraic Stress Model
ASS	Apparent Shear Stress
CES	Conveyance Estimation System
CFD	Computational Fluid Dynamics
CM	Coherence Method
COH	Coherence
DCM	Divided Channel Method
DNS	Direct Numerical Simulation
DPIV	Digital Particle Image Velocimetry
EA	Environment Agency
FDM	Finite Difference Method
FEM	Finite Element Method
FFT	Fast Fourier Transform
FVM	Finite Volume Method
LDA	Laser Doppler Anemometry
LDM	Lateral Distribution Method
LES	Large Eddy Simulation
LETOT	Large Eddy Turn-Over Time
LRR	Launder-Reece-Rodi
N-S	Navier-Stokes

PIV   Particle Image Velocimetry

PTV   Particle Tracking Velocimetry

RANS   Reynolds Averaged Navier-Stokes

RMS   Root Mean Square

SCM   Single Channel Method

SGS   Sub-Grid Scale

SKM   Shiono and Knight Method

SSM   Scale Similarity Models

SSG   Speciale-Sarkar-Gatski

1D/2D/3D   One, Two, Three Dimensional

LIST OF FIGURES

14

17

LIST OF TABLES

LIST OF SYMBOLS

Latin Alphabet

A	cross-sectional area
A_r	aspect ratio
B	In-bank channel width/over-bank channel half width
c	log-law constant
C_r	Courant number
C_s	Smagorinsky constant
D_r	depth ratio
E	location of secondary flow cell centre
f	Darcy-Weisbach friction coefficient
f_{fp}	floodplain friction factor
f_l	local friction factor
f_{mc}	main channel friction factor
f_o	overall friction factor
f_μ	viscosity damping function
g	gravitational acceleration
G	Gaussian filter function
h	floodplain height
h_l	local depth
H	channel height

J	mean convective transport
k	kinetic energy
l	mesh grid length
L	channel length
m_0	mean of tail value
m_{+h}	mean of head value
n	Mannings 'n' roughness coefficient
Q	discharge
p	pressure
P	wetted perimeter
R	cross section hydraulic radius
R_e	Reynolds number
s	channel side slope (s =0 for vertical side walls)
S	body force term
S_0	longitudinal channel bed slope
S_{ij}	Resolved strain rate tensor
t	time
T	turbulent diffusive transport
U_{avg}	average cross-sectional velocity
U_d	depth averaged velocity
U_{max}	maximum cross-sectional velocity
U_t	velocity tangent to the wall
u	instantaneous velocity component in the x-direction
u'	turbulence intensity in the x-direction

u_*	friction velocity
u^+	near wall velocity
u_α	vector of spatial co-ordinates
v	instantaneous velocity component in the y-direction
v'	turbulence intensity in the y-direction
w	instantaneous velocity component in the z-direction
w'	turbulence intensity in the z-direction
x	streamwise direction
y	lateral direction
y^+	dimensionless distance from the wall
z	vertical direction

Greek Alphabet

α_c	critical width to depth ratio
ε	turbulent kinetic energy dissipation rate
$\bar{\varepsilon}_{yx}$	depth averaged eddy viscosity
ξ	depth function
Γ	dimensionless secondary flow term
Γ_{mc}	dimensionless secondary flow term in the main channel region
Γ_{fp}	dimensionless secondary flow term in the floodplain region
Δ	filter width
Δl	largest mesh spacing
Δt	time step

Δx	mesh spacing in the streamwise direction
Δy	mesh spacing in the lateral direction
Δz	mesh spacing in the vertical direction
δ	boundary layer width
κ	von Kármán's constant
λ	dimensionless eddy viscosity coefficient
λ_{mc}	dimensionless eddy viscosity coefficient in the main channel region
λ_{fp}	dimensionless eddy viscosity coefficient in the floodplain region
η	Kolmogorov scale
μ	dynamic viscosity
υ	kinematic viscosity
υ_R	eddy viscosity of the residual motions
υ_t	eddy viscosity
Ω	vorticity
ρ	fluid density
σ_0	standard deviation of tail value
σ_{+h}	standard deviation of head value
$\rho(h)$	correlation coefficient
τ_a	apparent shear stress
τ_{ave}	average boundary shear stress
τ_b, τ_{bed}	bed shear stress
τ_{surf}	horizontal shear stress on the free surface

τ_w	wall shear stress
$\bar{\tau}$	mean shear stress
$\overline{\overline{\tau}}_{ij}$	Reynolds stresses
τ_{ij}	SGS stress tensor
τ_{ij}^R	resolved SGS stress tensor
θ	angle between channel bed and horizontal
ω	specific dissipation

Subscripts

ave	average
b , bed	bed
d	depth-averaged
fp	floodplain
i, j, k	x, y, z directions respectively
l	local
max	maximum
mc	main channel
w	wall

CHAPTER 1:

1   INTRODUCTION

1.1   RIVERS AND FLOODING

Rivers can be things of beauty and the historic lifeblood of a settlement. People have lived near to rivers for centuries: in the past mainly for food, water, transport and protection. Even today people enjoy the peace and tranquillity flowing water can offer. Therefore, it may seem hard to believe that a small, slow-flowing stream or gentle river could cause serious damage to people and the places in which they live.

Flooding is a concern for many, as due to demographic pressure in the last centuries around 5 million people, in 2 million properties, now live in flood risk areas in England and Wales. The flooding of homes, industrial areas and amenities in recent years has brought flooding issues to the attention of the general public. Combined with the probable consequences of climate change flooding is an increasingly important issue that needs to be addressed. It is vital for society to seek protection from flooding. Historically it has been the responsibility of engineers to devise solutions by designing and constructing flood defences. However, it is now seen as vital that this engineering work, whilst essential to ensure minimum disruption from flooding, is carried out in a manner which is also sensitive to the environment and even achieves enhancement to natural habitats, whilst providing the levels of protection demanded by the public.

As flood prediction and forecasting is becoming increasingly more important so to is the focus upon the flood inundation model used to create the prediction. A flood inundation model is an engineering tool used to model water flow in rivers, lakes, canals and other water systems. These models were introduced in the late seventies, early eighties, but pioneering work can be traced back to the sixties and earlier (Price, 1974). Engineering decisions are based on flood modelling software every day. They are invaluable tools in flood prediction terms and essential when making decisions on flood risk management strategies. They allow authorities like the Environment Agency (EA) for England and Wales to foresee areas at risk of flooding, therefore ultimately saving lives and property. The hydraulic model used to make the flood prediction has to incorporate numerous flow features inherent in open channel flow to produce an accurate discharge, water level and shear stress forecast. Producing a hydraulic model capable of modelling all of these flow features adequately is a difficult task.

1.2 OPEN CHANNEL HYDRODYNAMICS

1.2.1 Experimental Results

A lot of the current knowledge regarding open channel flow and flood hydrodynamics has been gained through experimental research, with studies ranging from in-bank and over-bank channels to meandering and skewed channels. A lot of experimental data has been collected by Knight and co-workers over a 20 year period leading to the construction of a database at the University of Birmingham, containing over 400 complete sets of primary velocity and boundary shear stress data (www.flowdata.bham.ac.uk). This data ranges from small scale flume data and early

experimental work of Knight (1970-1985) to large scale flume data obtained from experiments conducted at the Flood Channel Facility (FCF). However, to understand the complex three-dimensional nature of open channel flow more detailed measurements other than velocity and boundary shear stress are required. Therefore, the likes of Nezu and Rodi (1985), Nezu and Nakagawa (1997) and Bousmar (2002) undertook experimental work using more modern measurement techniques in order to deliver a more detailed flow understanding. Research into meandering channels has also been undertaken by the likes of Knight and co-workers (1989, 1996) and Ervine et al. (1993), however, only straight channels are considered in this research.

1.2.2 Numerical Modelling

Despite its clear success an experimental approach does have some drawbacks: data is collected at a limited number of points, the model is usually not at full-scale and detailed measurements of turbulence have not usually been taken. A computational approach can, in part, overcome some of these issues and thus provide a complementary tool. In particular, a computational approach is readily repeatable, can simulate at full-scale and provide a spatially dense field of data points. However, there are significant technical challenges of which arguably the greatest is the prediction of turbulence.

In recent years numerical modelling of open channel flows has successfully reproduced experimental results. Computational Fluid Dynamics (CFD) has been used to model open channel flows ranging from in-bank channels to full-scale modelling of over-bank river reaches. Simulations have been preformed by

Krishnappan and Lau (1986), Larson (1988), Kawahara and Tamai (1988) and Cokljat, (1993). CFD has also been used to model flow features in natural rivers by Sinha et al. (1998), Hodskinson and Ferguson (1998), Lane et al. (1999) and Morvan (2001). More recently more detailed numerical modelling has been undertaken by the likes of Thomas and Williams (1995a; 1995b; 1999) and Shi et al. (2001) to examine the detailed time dependant three dimensional nature of the flow, in order, as mentioned above, to provide dense fields of data points which can be used to gain further insight into the complex nature of channel flow hydrodynamics.

1.2.3 Conveyance Estimation

As mentioned, when making a flood prediction the hydraulic model used has to incorporate numerous flow features, which is not an easy task. Within in-bank channels conveyance estimation is well defined, however, it becomes complex when modelling over-bank channels. Over-bank channels can be characterised by a deep main channel bounded on one or both sides by a relatively shallow floodplain, which is often a good deal hydraulically rougher. Consequently velocities in the main channel tend to be significantly greater than those on the floodplain and the large velocity gradients in this region produce a shear layer. The result of this shear layer is large-scale structures, which transfer momentum from the faster moving fluid (main channel) to the slower (floodplain), increasing and decreasing the main channel and floodplain conveyances respectively. This is a very complicated process to model. Therefore, a lot of experimental and numerical research has recently focussed on quantifying the momentum transfer at the main channel/floodplain interface and investigating the three-dimensional nature of the flow in this region, specifically the large-scale plan-form structures. This increase in

knowledge has given rise to recommendations by practitioners and academics that operating authorities should make better use of recent improved knowledge on conveyance and related flood level estimation. In response to this and the EA's vision for reducing uncertainty in flood level prediction a team of experts led by HR Wallingford developed a new Conveyance Estimation System (CES) which is being adopted in England, Wales, Scotland and Northern Ireland. The CES incorporates the most recent knowledge regarding open channel flow in order to make better flood level predictions. The final product is a software tool for estimating conveyance, spatial velocities and boundary shear stresses at river sections. Incorporated in the software is a roughness advisor, conveyance generator and an uncertainty estimator. The conveyance generator is based on a simplified 1D conveyance estimation method: the Shiono and Knight Method (SKM). A simplified method was chosen due to it being simple to implement, fast and efficient and easily operated with minimum input and training by practitioners on a standard desktop PC. Simplified methods have been and still are practically very popular. However, they are crude estimations of complex 3D flow features inherent in channel flow, even in straight channels and within simplified methods calibration of one or more empirical constants is usually required. Previously, industrially used conveyance estimation methods have incorporated only a roughness parameter, Mannings n and Darcy Weisbach, f, however, the SKM incorporates three calibration constants. Three calibration coefficients allow for a more detailed and clearer description of the flow, but calibrating each constant requires additional information and analysis.

1.3   AIMS AND OBJECTIVES

The aims of the following study are:

1. To numerically model flow phenomenon in straight in-bank and over-bank channel flows using Large Eddy Simulation (LES).

2. Evaluation of current knowledge regarding the Shiono and Knight Conveyance Estimation Method (SKM) and addition to knowledge of the variation of the three calibration parameters f, λ and Γ and their physical meaning and parameterisation from LES results which has previously never been undertaken;

3. To provide further study, where possible, of flow structures in both in-bank and over-bank channels and mechanisms of momentum transfer in over-bank channels. Specifically investigating periodic plan-form vortices at the main-channel/floodplain interface.

The objectives of the first aim are:

- To evaluate ANSYS-CFX and Delft LES codes and validate results against published data.

- To accurately predict velocity and boundary shear stress profiles and secondary circulations for varying in-bank channel aspect ratios. Investigating channels of aspect ratios up to 40.

The objectives of the second aim are:

- To evaluate the SKM parameters and the basis for derivation of calibration philosophies

- To be the first to derive f, λ and Γ parameters from LES results and compare to published f, λ and Γ empirical relationships.

- To examine the importance of secondary circulation cells and the Γ parameter, and its implication on the derived analytical velocity profiles.

- To generate analytical solutions of velocity profiles from LES derived f, λ and Γ parameters for validation of the LES results and SKM hypotheses.

The objectives of the third aim are:

- To numerically observe interfacial vortices.

- To utilise numerically derived instantaneous velocity data at the main channel/floodplain interface to investigate wave periods of interfacial vortices.

- To compare wave periods for both asymmetric and symmetric channels at varying depth ratios.

Experimental laboratory results are used to validate the numerical models and demonstrate the accuracy of the results where possible. Both commercial and research codes were utilised in order to perform the numerical simulations. The commercial code ANSYS-CFX (v 5.6, 10 and 11) provided a general CFD toolbox with which to perform a range of differing simulations alongside a code developed at TU Delft. Both codes are described in detail in Chapter 3.

1.4 ORGANISATION OF THE THESIS

Chapter 2 presents significant contributions to the understanding of flow in straight in-bank and over-bank channels and current knowledge on conveyance estimation methods. One dimensional conveyance estimation models proposed up to now are

reported with the SKM being discussed in detail and its derivation shown. Empirical parameters within the SKM, f, λ and Γ are also detailed and present knowledge on their estimation for a given channel geometry is discussed.

Chapter 3 details significant contributions to numerical simulation of in-bank and over-bank channels. The Navier-Stokes Equations and numerical methods and software used within this research are also discussed, with comparison of the software codes performed and compared to published experimental data for validation detailed.

Chapters 4 and 5 detail in-bank and over-bank LES and RANS channel flow results in terms of velocity, boundary shear stress, turbulence and streamwise vorticity flow features. From these results SKM parameters, f, λ and Γ are derived, their distributions analysed and values input into the SKM analytical solution. Analytically derived velocity profiles are then compared to LES simulation results and experiment.

Chapter 6 utilises monitor point data within the over-bank channel results. Signal analysis of monitor point time series of transverse velocity is undertaken to investigate wave periods of interfacial vortices.

Finally, Chapter 7 presents the conclusions reached by the current research together with recommendations for future work.

Appendix A details the derivation of the analytical solution of the SKM and Appendix B the Fortran90 code used to solve for the SKM analytical solution and compute velocity profiles for the channels presented.

Elements of this thesis have previously been published as refereed conference and journal papers:

- BEAMAN, F.L., MORVAN, H.P. & WRIGHT N.G., 2006. Large Eddy Simulation for Conveyance Estimation. NCR Days, Netherlands, pg72-73.

- BEAMAN, F.L., MORVAN, H.P. & WRIGHT N.G., 2007. Estimating Parameters for Conveyance in 1D models of open channel flow using large eddy simulation. Proceedings of XXXII IAHR Conference, Venice, Italy, July 2007.

- BEAMAN, F.L., MORVAN, H.P. & WRIGHT, N.G., 2008. Large eddy simulation of over-bank channel flow: Focusing on informing parameters for a 1D conveyance estimation model. River Flow 2008, Cesme-Ismir, Turkey, September 2008.

- OMRAN, M., KNIGHT, D.W., BEAMAN, F.L. & MORVAN, H.P., 2008. Modelling Equivalent Secondary Current Cells in Rectangular Channels. Riverflow 2008, Venice, Italy.

- STERLING, M., BEAMAN, F.L., MORVAN, H.P. & WRIGHT., N.G., 2008. Bed shear stress characteristics of a simple, prismatic, rectangular channel. Journal of Engineering Mechanics. American Society of Civil Engineers. Vol. 134, Issue 12, 1085 -1094.

2   LITERATURE REVIEW

2.1   INTRODUCTION

This review intends to present some selected significant contributions to open channel flow research. Observations concerning channel flow structures are summarised along with the development of a theoretically sound one-dimensional conveyance estimation method.   Previous works relative to the modelling of periodical structures and mass transfer in over-bank channels are also discussed.

It should be noted that a considerable amount of open channel flow research has been undertaken and a complete literature survey is out of the scope of this work. However, the interested reader may refer to the extensive literature searches by Hollinrake (1987; 1988; 1989; 1990; 1992) and for an updated state-of-the-art review the reader should refer to Knight et al. (2002).

2.2   STRAIGHT IN-BANK CHANNEL FLOW

One area of interest concerning turbulence phenomenon in open channel flow is the turbulence-driven secondary motion, usually referred to as Prandtl's second kind of secondary motion. Turbulence-driven secondary motion is only of the order of 1-3% of the streamwise bulk velocity, but despite its modest strength, its motion exerts a profound influence on the main flow as was first observed by Nikuradze (1933). Secondary circulations in the cross-section of open-channel flow differ to those in

closed channels due to the free surface and consist of two large vortices, namely a free surface vortex and a bottom vortex (Nezu and Rodi 1985). Reports on the existence of inner secondary currents at the juncture of the free-surface and sidewall in a rectangular channel have also been made (Grega et al, 1995; Longo et al, 1998; Hsu et al, 2000). Figure 1.2.3-1 shows a schematic view of secondary flows in a rectangular open-channel compared to that of closed duct flow.
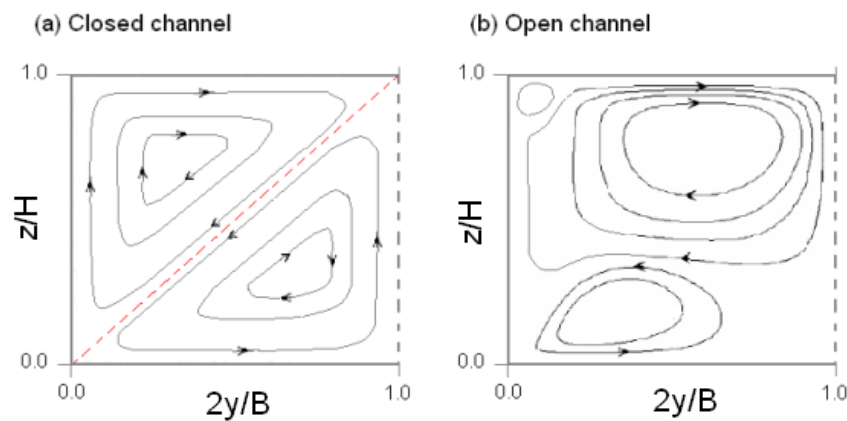
Figure 1.2.3-1: Secondary-current streamlines in (a) closed duct and (b) open channel

(Kang and Choi 2006)

An important phenomenon associated with the distortion of mean velocity contours by secondary circulations is the "velocity dip" phenomenon. The "velocity dip" phenomenon occurs due to the free surface vortex transferring high momentum fluid from the free surface towards the channel bed. This phenomenon is only observed in narrow open channels, where the width, *B,* to depth, *H,* ratio $B/H \le \alpha_c (\approx 5-6)$, where α_c is the critical width-to-depth ratio. The "velocity dip" phenomenon is avoided in wide-open channels with $B/H > \alpha_c$ because the free surface vortex, as depicted in Figure 1.2.3-1, does not extend to the channel centreline. Contours of

normalised velocity and secondary circulations can be seen in Figure 1.2.3-2 for a channel of $B/H = 3$.
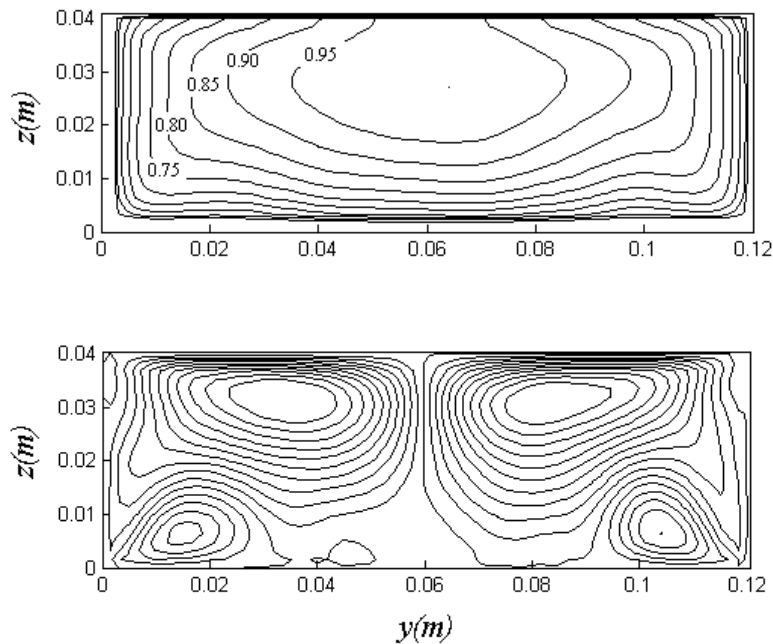
Figure 1.2.3-2: Contour plots of normalised velocity and secondary circulations for a channel of B/H=3.

The velocity is normalised by the maximum velocity and the maximum velocity can be seen to occur below the free surface. Tominaga et al. (1989) observed that the maximum velocity occurs at ~0.7-0.8H above the channel bed.

As the channel aspect ratio increases ($B/H >\sim 5$) the free surface and bottom vortex are observed in the region close to the side wall, with the free surface vortex extending to a width of ~2H from the boundary. Then further right of the free surface vortex only rather small secondary motions are present, having little influence on the longitudinal velocity (Naot and Rodi, 1982). Nezu et al. (1985) inferred that these are multicellular secondary currents occurring at a spacing of ~2H as shown in Figure 1.2.3-3.
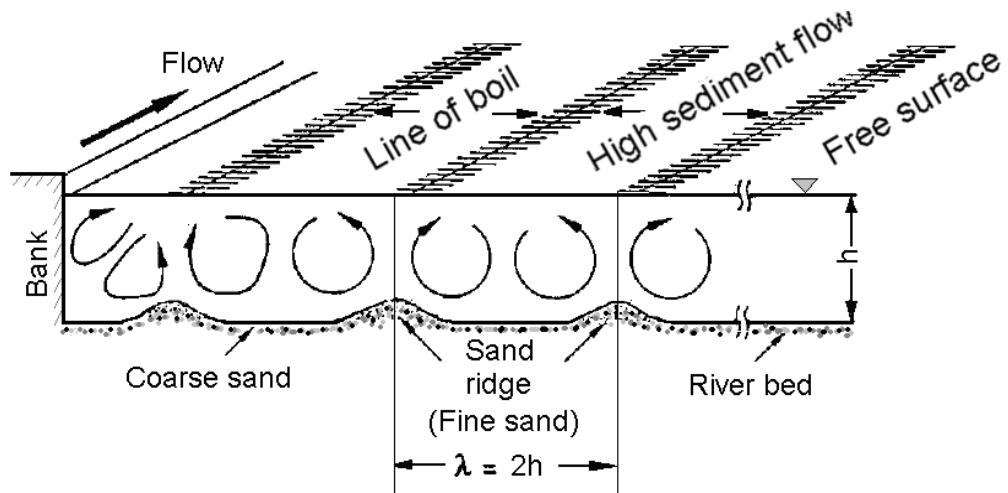
Figure 1.2.3-3: Inferred pattern of multicellular secondary currents (Nezu et al. 1985)

The distortion to the mean velocity contours by the secondary circulations also impacts the boundary shear stress distribution. Pairs of contra-rotating cells cause an increase or decrease in the boundary shear stress distribution dependant upon their sense of rotation with important consequences to the rates of heat and mass transport in that region. Knight and Patel (1985) and Knight et al. (1992) describe the effect of the number and pattern of secondary flow cells on the distribution of boundary shear stress for smooth closed ducts and trapezoidal channels respectively.

It has been briefly shown that the secondary circulation patterns differ with channel aspect ratio and more detailed investigation of specific cell distributions for specific aspect ratios is further discussed in Chapter 4.

2.3   STRAIGHT OVER-BANK CHANNEL FLOW

Open channel flow for the purposes of this research can be separated into in-bank and over-bank channels. Over-bank channels can be characterised by a deep main channel, bounded on one or both sides by a relatively shallow floodplain, which is

often a good deal hydraulically rougher. Consequently, velocities in the main channel tend to be significantly greater than those on the floodplain. This disparity can lead to large velocity gradients in the region of the interface between the main channel and floodplains. This produces a transverse shear layer influencing the flow in both the river and the floodplain. This shear manifests itself primarily in the form of large-scale structures (typically large vortices with vertical axis (Figure 1.2.3-1(a)) and results in a consequent momentum transfer from the fast moving fluid (main channel) to the slower (floodplain). The main channel conveyance decreases, while that on the floodplain significantly increases. The complicated mechanism of momentum exchange is shown in Figure 1.2.3-1(b).
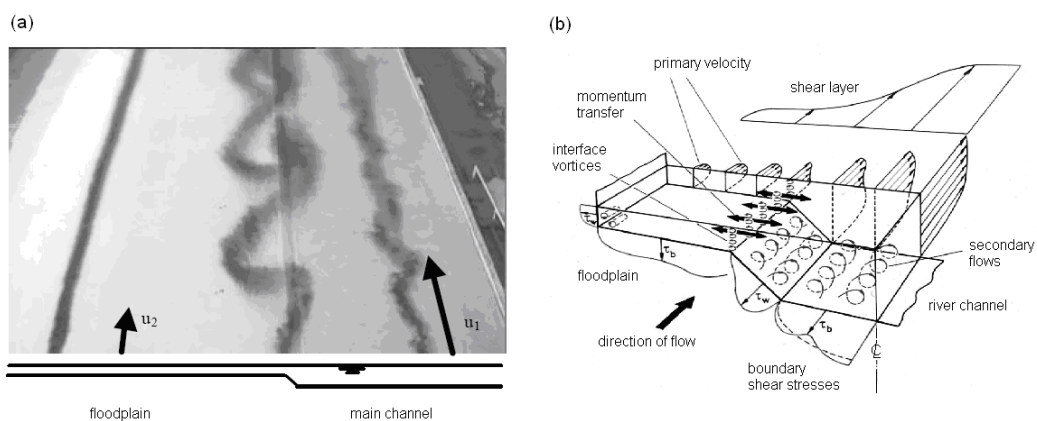
Figure 1.2.3-1: (a) Large vortices experimentally observed at the main channel/floodplain interface (van Prooijen et al., 2000) and (b) flow structures in a straight two-stage channel (Shiono and Knight, 1991)

Transverse exchange of momentum is caused by mean flow, turbulence and free surface effects. The mean flow is usually associated with secondary circulations, while the turbulence contribution is due to small-scale turbulence induced by the bottom resistance and by turbulence generated by lateral shear of the mean flow. Bottom turbulence is induced by the no-slip condition at the channel bed and as

40

mentioned above the lateral shear of the mean flow is thought to manifest itself primarily in the form of large-scale coherent structures, with their axes more or less perpendicular to the bottom (Figure 1.2.3-1(a)).

2.4   HORIZONTAL VORTICES

Sellin (1964) was the first to observe horizontal vortices at the interface between main channel and floodplain.   Since Sellin only a few experimental studies have reported periodical characteristics of such structures as a lot of work concerning over-bank channels has focused upon time averaged flow features, or a qualitative description of the flow.   Sellin (1964) recorded vortex patterns using photography of aluminium powder surface tracers.   Approximately 80 photographs were taken from which the frequency and wavelength of vortices were approximated.

Other experimental works on shallow mixing layers and the stability characteristics of the shear layer in over-bank channel flows has been undertaken by Alavian and Chu (1985), Chu and Babarutsi (1988), Chu et al. (1991), Chen and Jirka (1995), van Prooijen et al. (2000), Bousmar and Zech (2002) and Bousmar (2002).   It can be concluded that the shallowness of the channel has a marked influence on the development of the mixing layer and on the large-scale structures and in shallow flow the development of the mixing layer deviates strongly from that in deep flow. Measurements of periodic structures in natural rivers and the influence of vegetated floodplains has also been investigated by Fukuoka and Watanabe (1995, 1997) using aerial photography.

A lot of experimental studies have focussed on surface tracers and periodicity of structures at the main channel/floodplain interface. However, more recently, the three-dimensionality of these structures has been investigated by Nezu and Nakagawa (1997). Using Laser Doppler Anemometry (LDA) and Particle Image Velocimetry (PIV) experimental measurements were taken in a low depth ratio compound channel. The interactions between secondary flow cells in the main channel and the horizontal vortex development between main channel/floodplain interface were investigated along with evolutionary patterns of horizontal vortices. From all of the above Nezu and Nakagawa (1997) presented a conceptual model of coherent vortices in compound open channel flow, Figure 1.2.3-1.
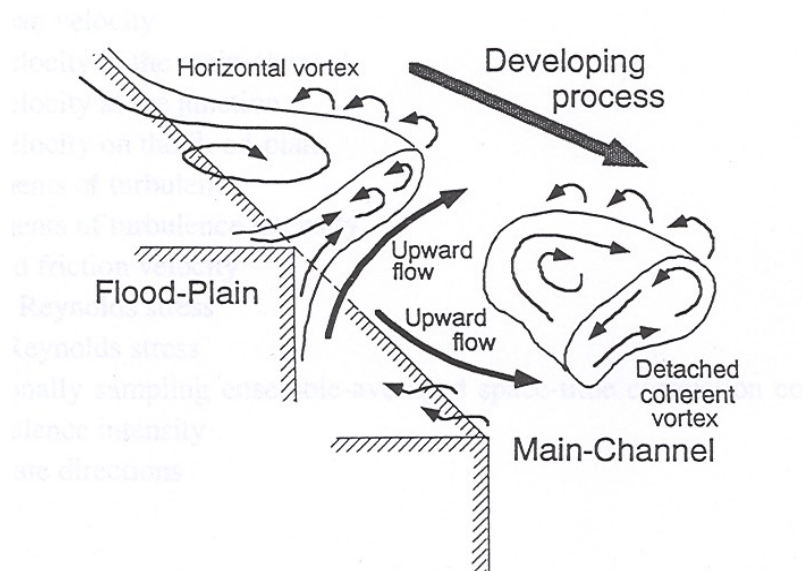
Figure 1.2.3-1: Conceptual model of 3D coherent vortices near main channel/floodplain

interface as proposed by Nezu and Nakagawa (1997)

Other than experimental observations stability analysis and numerical modelling have been undertaken in order to predict the periodicity and wavelengths of these structures.

Recently Nadaoka and Yagi (1998) developed numerical simulations of vortex evolution in a shear layer for a shallow water flow. They developed a depth-averaged model, which when applied to a partially vegetation-covered channel reproduced vortex characteristics observed experimentally. Bousmar (2002) utilised the model of Nadaoka and Yagi (1998), but also undertook hydrodynamic stability analysis in order to predict maximum growth rate and corresponding wavelength for a series of over-bank channels. Like Bousmar (2002), Ikeda et al. (1995) also studied horizontal vortices in terms of Rayleigh instability and karman's vortex street stability in a compound open channel flow. Both authors observed corresponding wavelengths from stability analysis calculations with experiment. Bousmar (2002) specifically highlighted the role of bed friction and channel geometry within the stability analysis calculation, with the role of the bed friction being two-fold in generating the small-scale turbulence and at the same time exerting a stabilizing influence on the large-scale transverse disturbance. A transverse shear flow would be stable if the bed friction influence was sufficiently strong to suppress the development of the large-scale turbulence disturbance. The study of the bed friction effect on turbulent flow with fully developed large-scale transverse motion has also been studied by the likes of Chu et al. (1991).

2.5   CONVEYANCE ESTIMATION METHODS

Discharge predictions are usually obtained from estimations of velocity and boundary shear stress, which therefore need to be accurately computed for the given channel under consideration. The prediction of boundary shear stress and velocity profiles is complicated due to the requirement to model flow phenomenon such as

the velocity dip phenomenon and the presence and location of secondary circulation cells.

1D conveyance estimation methods are practically very popular; however the terms within them effectively ignore the flow structure components arising from individual terms in 2D and 3D equations. They are essentially crude measurements of the net effect of vertical shear, lateral shear, secondary flows and roughness, even in straight prismatic channels. Within a 1D approximation all flow structure effects are simply lumped into a single bulk flow, i.e. a discharge related, resistance parameter. The Manning (1889) and Darcy-Weisbach (1857) equations are well known examples of this approach, Equations (2.5.1) and (2.5.2) respectively:

$$Q = \frac{AR^{\frac{2}{3}}}{n} S_0^{\frac{1}{2}} \tag{2.5.1}$$

$$Q = \left(\frac{8g}{f}\right)^{\frac{1}{2}} AR^{\frac{2}{3}} S_0^{\frac{1}{2}} \tag{2.5.2}$$

Where R is the cross-section hydraulic radius: S_0 is the channel bed slope: g is the acceleration due to gravity and n and f are the Manning and Darcy-Weisbach friction factors respectively. The friction parameter, either f or n in this instance, is based on the surface roughness, vegetation (in natural channels), channel geometry (Chow 1959) and other energy loss mechanisms such as turbulence. The value of roughness coefficient determines the frictional resistance of a given channel for a given flow.

Simpler conveyance estimation methods treat the channel under consideration as a single unit; termed the Single Channel Method (SCM), with some appropriate averaging of the friction factor. For over-bank channels this has been shown to be inadequate, underestimating the discharge capacity, especially at low over-bank flow depths (Myers and Brennen, 1990). Therefore, most commonly, the modelled channel is divided into sub-sections within which the velocities are more homogeneous; termed the Divided Channel Method (DCM; Lotter, 1933). The total channel discharge is estimated by summing the discharges estimated in each sub-section, still estimated by either the Manning n, Darcy Weisbach, f, or equivalent formula. Lotter (1933) used vertical division lines between panels and these remain the most common and practical choice to date. These division lines are not shear free. Due to a turbulent interaction between panels an apparent shear force must be present to produce a balance between the gravitational and boundary resistance forces (Myers 1978). However, more accurate the DCM is compared to the SCM, Sellin (1964) showed that the DCM still overestimates the discharge in a over-bank channel for a given water depth, due to the large scale structures observed at the interface. Suggestions have been made as to how to modify the DCM and simulate the main channel/floodplain interaction process in straight over-bank channels more accurately. Methods range from wetted perimeter, apparent shear stress, zero shear stress and weighted divided channel methods. The apparent shear stress and zero shear stress methods are relatively popular because when dividing any channel into sub-sections the apparent shear stress on the sub-area division lines needs estimating. Empirical equations have been developed for the apparent shear stress (ASS), or apparent shear force (ASF) on the sub-area division lines by the likes of Ervine and Baird (1982), Wormleaton et al. (1982), Knight and Demetriou (1983), Prinos and

Townsend (1984) and Wormleaton and Merret (1990). Also Leighly (1932), Keulegan (1938) and Einstein (1942) investigated sub-area division of conveyance, although not developed for flooding but for sediment transport purposes. However, it should be noted that even though most equations may fit specific sets of experimental data well they are not generally applicable.

A further advancement on the SCM and DCM is the Coherence Method (CM) reported by Ackers (1991, 1992, and 1993). Ackers (1993) stated the coherence (COH), as the ratio of basic conveyance, calculated by treating the channel as a single unit, to the conveyance calculated by summing the basic conveyances of the separate zones. The COH is a measure of the degree of interaction to be expected in an over-bank channel. As the COH approaches unity the more appropriate it is to model the channel as a single unit, using the overall geometry, involving low interaction, while a small COH indicates large floodplains and probably intensive interaction. The CM has been successively applied to natural rivers and is well established. However, the determination of the geometrical parameters involved is sometimes tedious (Wark et al. 1994).

All of the above methods are based solely on empirical relations for factors such as friction and apparent shear stress/force. More recently physically derived models have become more popular, such as the Lateral Distribution Method (LDM). The LDM is derived from a depth-averaging of the N-S Equations in the streamwise direction. Assuming a steady uniform flow, this equation reduces to a single ordinary differential equation, which is easy to solve. The basic LDM equation takes into account the effects of bed friction and lateral turbulent friction. These methods

are becoming increasingly more popular as the calibration parameters have some physical meaning and therefore logical understanding. The Shiono and Knight Method (SKM) described in Section 2.6 is an extended form of the LDM, incorporating an extra term for the secondary circulation effects.

2.5.1 Summary

It should be noted that even though a particular approach performs well in predicting the total conveyance capacity for a given stage, it does not imply a soundly based method, as most methods are derived for explicit datasets. It is also imperative to check that the division of the flow between sub-sections is also correct, as the two adjustment procedures for reducing the main channel discharge and increasing that on the floodplain for certain methods are clearly self-compensating. All of the above has briefly highlighted the diverse range of conveyance estimation methods available and that many methods are crude estimations of physical effects and empirical constants need to be treated with care. Bearing all this in mind however, an industrially viable conveyance estimation method is required and all of the flow effects cannot be explicitly incorporated in such a model due to complexity. Therefore, it is inevitable that the employed method incorporates parameters that require calibration.

2.6   THE SHIONO AND KNIGHT METHOD (SKM)

The Shiono and Knight Method (SKM) (Shiono and Knight 1988; 1990; 1991) is the conveyance estimation method incorporated in the CES. The SKM is a lateral distribution method based on the depth-averaged momentum equation for steady uniform flow in the streamwise direction.

2.6.1 Derivation of the SKM

The equation for the longitudinal streamwise component of momentum may be combined with the continuity equation to give:

$$\rho\left(\frac{\partial}{\partial y}\left(\overline{U}\overline{V}\right)+\frac{\partial}{\partial z}\left(\overline{U}\overline{W}\right)\right)=\rho g S_0 + \frac{\partial}{\partial y}\left(-\rho\overline{uv}\right)+\frac{\partial}{\partial z}\left(-\rho\overline{uw}\right) \qquad (2.6.1)$$

$$\textbf{I} \qquad \textbf{II} \qquad \textbf{III} \qquad \textbf{IV} \qquad \textbf{V}$$

where x, y, z are streamwise, lateral, and normal directions respectively, $\overline{U},\overline{V},\overline{W}$ are temporal mean velocity components corresponding to x, y, z and u, v, w are turbulent perturbations of velocity with respect to the mean. Equation 2.6.1 expresses the balance between gravitational driving force and momentum transfer resulting from both secondary currents (left-hand side) and turbulent exchanges (Reynolds stresses).

The physical meaning of the above terms in Equation 2.6.1 is:

(I,II)   secondary flow terms

(III)   weight component term

(IV)   vertical plane Reynolds stress term

(V)   horizontal plane Reynolds stress term

Taking each term one by one, for the depth integration of the left hand side of Equation 2.6.1, the Leibnitz integral rule (Equation 2.6.2) allows the differentiation of a definite integral.

$$\frac{\partial}{\partial z}\int_{a(z)}^{b(z)} f(x,z)dx = \int_{a(z)}^{b(z)}\frac{\partial f}{\partial z}dx + f(b(z),z)\frac{\partial b}{\partial z} - f(a(z),z)\frac{\partial a}{\partial z} \qquad (2.6.2)$$

48

Equation 2.6.2 applied to term I gives:

$$\int_{z_{bed}(y)}^{z_{sur}(y)} \rho \frac{\partial}{\partial y}(\overline{U}\overline{V})dz$$
$$= \frac{\partial}{\partial y}\int_{z_{bed}(y)}^{z_{sur}(y)} \rho(\overline{U}\overline{V})dz - \rho\overline{U}\overline{V}(z_{sur},y)\frac{\partial z_{sur}}{\partial y} + \rho\overline{U}\overline{V}(z_{bed},y)\frac{\partial z_{bed}}{\partial y} \qquad (2.6.3)$$

The two last terms on the right hand side of Equation 2.6.3 equal zero, as zero-velocity on the bed $((\overline{U}\overline{V})_{Z_{bed}} = 0)$ and a horizontal water surface $(\partial z_{suf}/\partial y = 0)$ are assumed in the SKM.

Term II in Equation 2.6.1 equals zero, as the vertical velocity component, w is null on both the channel bed and water surface. Term III becomes $\rho g H S_0$ and term IV, like term I is handled using Leibnitz rule, Equation 2.6.2. Again assuming zero-velocity on the bed and a horizontal water surface, the integral of term IV is expressed as:

$$\int_{z_{bed}(y)}^{z_{sur}(y)} \frac{\partial}{\partial y}(-\rho\overline{uv})dz = \frac{\partial}{\partial y}\int_{z_{bed}(y)}^{z_{sur}(y)}(-\rho\overline{uv})dz = \frac{\partial}{\partial y}(H\overline{\tau_{yx}}) \qquad (2.6.4)$$

where $\overline{\tau_{yx}}$ is the depth averaged Reynolds shear stress and equals $\frac{1}{H}\int_0^H(-\rho\overline{uv})dz$.

Finally term V is depth integrated to give Equation 2.6.5:

$$\int_{z_{bed}(y)}^{z_{sur}(y)} \frac{\partial}{\partial z}(-\rho\overline{uw})dz = \tau_{surf} - \tau_{bed} = -\tau_b\sqrt{1+s^2} \qquad (2.6.5)$$

Where τ_{bed} and τ_{surf} are the bed and surface horizontal shear stresses respectively.

The surface shear, corresponding to wind effects etc is neglected and the bed shear

stress τ_{bed}, in order to take into account a transverse bed slope as in Figure 2.6.1-1 is

replaced by τ_b times the ratio between the actual bed perimeter $\sqrt{1+s^2}\,\Delta y$ and its

horizontal projection Δy, where s = channel side slope (1: s, horizontal: vertical).
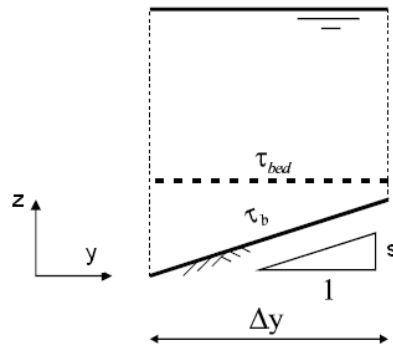
Figure 2.6.1-1: Projection of the actual bed shear stress on a horizontal plane

Thus from Equations 2.6.2 – 2.6.5, Equation 2.6.1 can now be written as:

$$\rho g H S_0 + \frac{\partial H \overline{\tau_{yx}}}{\partial y} - \tau_b \sqrt{1+s^2} = \frac{\partial}{\partial y} \int_{z_{bed}(y)}^{z_{sur}(y)} \rho \overline{UV} \partial z \qquad (2.6.6)$$

The right hand side is the so-called secondary flow term. It is generally written as:

$$\Gamma = \frac{\partial H \left(\rho \overline{UV} \right)_d}{\partial y} \qquad (2.6.7)$$

where $\left(\rho \overline{UV} \right)_d = \frac{1}{H} \int_0^H \rho \overline{UV} dz$

Combining Equations 2.6.6 and 2.6.7 gives:

$$\rho g H S_0 + \frac{\partial H \overline{\tau_{yx}}}{\partial y} - \tau_b \sqrt{1+s^2} = \Gamma \qquad (2.6.8)$$

Using models of bed friction τ_b and turbulent shear stress $\overline{\tau}_{yx}$ a solution for the lateral velocity or bed shear stress distribution can be obtained for an over-bank channel.

2.6.1.1 Bed Friction and Turbulent Shear Stress

Shiono and Knight (1988) use a Boussinesq eddy viscosity model for $\overline{\tau}_{yx}$ and assumed an eddy viscosity υ_t, proportional to the water depth H and shear velocity u_*, giving Equation 2.6.9.

$$\overline{\tau}_{yx} = \rho \upsilon_t \frac{\partial U_d}{\partial y} = \rho \overline{\varepsilon}_{yx} \frac{\partial U_d}{\partial y} \qquad (2.6.9)$$

where $\overline{\varepsilon}_{yx} = \lambda u_* H$ $\qquad (2.6.10)$

and λ is the non dimensional eddy viscosity coefficient.

Bed shear stress can be expressed through the Darcy-Weisbach friction law:

$$f = \frac{8\tau_b}{\rho U_d^2} \qquad \Rightarrow \qquad \tau_b = \left(\frac{f_b}{8}\right)\rho U_d^2 \qquad (2.6.11)$$

Substituting Equations 2.6.9, 2.6.10 and 2.6.11 into 2.6.8 gives:

$$\rho g H S_0 + \frac{\partial}{\partial y}\left(\rho \lambda H^2 \left(\frac{f}{8}\right)^{\!1/2} U_d \frac{\partial U_d}{\partial y}\right) - \frac{\rho f U_d^2}{8}\sqrt{1+s^2} = \Gamma \qquad (2.6.12)$$

Equation 2.6.12 is the basis of the SKM. It is a function of three parameters, f, λ and Γ, as prescribed above, which require careful calibration, but once prescribed Equation 2.6.12 can be solved numerically to produce velocity and (from Equation 2.6.11) bed shear stress distributions. Shiono and Knight (1988) and Knight et al. (1990) performed parameter calibration for FCF compound channel experiments and for a natural river test case, for which reasonably accurate velocity profiles and discharge calculations resulted.

2.6.2 Analytical Solution to the SKM

An analytical solution to Equation 2.6.12 has been obtained and serves as a closed form check on any numerical work. Once the three calibration coefficients are prescribed for each domain, then the analytical solution gives the lateral distributions of depth averaged velocity and boundary shear stress for each domain, and hence across the entire channel. The analytical solution may be expressed for a constant-depth, H, domain as:

$$U_d = \left\{A_1 e^{\gamma y} + A_2 e^{-\gamma y} + \frac{8 g S_0 H}{f}(1-\beta)\right\}^{1/2} \qquad (2.6.13)$$

And for a linear side-slope domain as

$$U_d = \left\{A_3 \xi^{\alpha 1} + A_4 \xi^{-\alpha 1 - 1} + \omega \xi + \eta\right\}^{1/2}, \qquad (2.6.14)$$

52

where $\quad \gamma = \left(\dfrac{2}{\lambda}\right)^{1/2}\left(\dfrac{f}{8}\right)^{1/4}\dfrac{1}{H}, \qquad \beta = \dfrac{f\Gamma}{8gS_0H},$

$$\alpha_1 = -\frac{1}{2} + \frac{1}{2}\left(1 + \frac{s\left(1+s^2\right)^{\frac{1}{2}}}{\lambda}\left(8f\right)^{\frac{1}{2}}\right)^{\frac{1}{2}},$$

$$\omega = \frac{gS_0}{\dfrac{\left(1+s^2\right)^{\frac{1}{2}}}{s}\dfrac{f}{8} - \dfrac{\lambda}{s^2}\left(\dfrac{f}{8}\right)^{\frac{1}{2}}}$$

$$\eta = \frac{\Gamma}{s\left(1+s^2\right)^{\frac{1}{2}}\dfrac{2}{\lambda}\left(\dfrac{f}{8}\right)^{\frac{1}{2}}}$$

and ξ is the depth function on the side-slope domain (e.g. $\xi = H - ((y\text{-}b)/s)$) for the main-channel side slope. Derivation of the analytical solution of the SKM is given in Appendix A.

The SKM has been shown to yield satisfactory results for the prediction of the lateral distributions of depth-averaged velocity and boundary shear stress in channels with both simple and complex cross-sectional geometries (Shiono and Knight 1989; 1991; 1996). Regarding over-bank channels Shiono and Knight (1988) drew a comparison between analytical and experimental results and showed that the analytical solution was capable of predicting most hydraulic features, such as velocity profiles and associated bed shear stress sufficiently accurately for engineering design purposes. The analytical solution is shown to perform particularly well for smaller depth ratios

$D_r = (H-h)/H<0.3$ and even at increasing flow depths where the flow becomes more obviously three-dimensional it copes surprisingly well. Other than the prediction of velocity and boundary shear stress Liao and Knight (2007) showed that through lateral integration analytical solutions for the total and zonal discharges and shear forces on particular boundary elements could be obtained. All of the aforementioned research shows that the SKM can produce accurate velocity and boundary shear stress predictions, however, with regard to small scale laboratory results only. Therefore, McGahey (2006) compared results obtained from the SKM within the CES to existing methods embedded in standard one-dimensional hydrodynamic modelling software for 24 data sets ranging from small scale laboratory experiments to measurements from large natural rivers. It was concluded that improvements in roughness representation and velocity prediction are found with the SKM as compared to other industrially used models.

2.6.3 Characterisation of *f, λ* and *Γ*

The behaviour of *f*, λ and Γ has currently been investigated using experimental data and parameter optimisation. The current knowledge on these parameters, standard model constant values and gaps in knowledge are detailed in the next section.

2.6.3.1 Friction Factor, *f*

Shiono and Knight (1991) investigated the distribution of *f* laterally across trapezoidal compound channel cross-sections. Experimentally determined values of *f* were detailed for $0.1<D_r<0.5$. The results highlighted that *f* was relatively constant in the main channel and floodplain, except for in remote regions of the floodplain. In general the friction factor on the floodplain increased, relative to that in the main

54

channel, as D_r decreased. This was expected because of the difference between the Reynolds number in each sub-area. Shiono and Knight (1991) fitted a best fit line to f_{fp} / f_{mc} versus D_r. The equation of the line was:

$$f_{fp} / f_{mc} = -0.1065 + 0.8893 D_r^{-3/7} \qquad (2.6.15)$$

According to the Blasius equation for smooth surfaces, $f \, \alpha \, R_e^{-1/4}$ and therefore the ratio f_{fp} / f_{mc} would depend on $D_r^{-3/7}$. The results also highlighted the use of overall, f_o, or local averaged, f_l, friction factors defined as:

$$f_o = \left(8gRS_0\right)/U_{avg}^2 \qquad (2.6.16)$$

$$f_l = \left(1/P\right)\!\int f dy \qquad (2.6.17)$$

Where U_{avg} is the section mean velocity. f_o and f_l were plotted for varying over-bank flows and compared with the smooth curve of Prandtl. f_o values were below the standard curve, decreasing with decreased Reynolds number and f_l values lay above, increasing with increased Reynolds number. These trends arise due to the fact that f_o is strongly influenced by the sudden decrease in hydraulic radius as the flow goes over-bank and f_l is influenced by the large values of friction on the floodplain. This all highlighted the care needed to be exercised when using standard friction factor versus R_e equations in estimating the conveyance capacity of compound channels.

2.6.3.2 Dimensionless Eddy Viscosity Coefficient, λ

The dimensionless eddy viscosity term encompasses momentum transfer effects due to turbulence. Shiono and Knight (1991) investigated the distribution of λ in over-bank channels. It was shown that within the main channel λ remains relatively constant at a value of 0.07 across the cross-section. With regard to values of λ in the floodplain, it was shown that a minimum value was reached on the channel side slope and from this minimum value λ increased across the floodplain towards the floodplain side wall. The rate of increase of λ was dependant upon the channel aspect and depth ratios, B/b and D_r respectively. As with the friction coefficient, a line of best fit was used to relate dimensionless eddy viscosity in the main channel and across the floodplain, λ_{fp} and λ_{mc} respectively, to the corresponding depth ratio, D_r:

$$\lambda_{fp} / \lambda_{mc} = \left(2D_r\right)^{-4} \qquad\qquad (2.6.18)$$

Equation (2.6.18) is only valid within the range tested, $0.1 < D_r < 0.25$. Two λ values were computed; one based on turbulent stresses alone and the other inclusive of secondary flow effects (because Γ was assumed zero). It was found that λ values in the main channel, inclusive of secondary flow effects were in the order of 10 times larger than those based solely on turbulence.

In comparison to Shiono and Knight (1991), Lau and Krishnappen (1977) and Nokes and Wood (1987, 1988) calculated λ values of around 0.134, although these reviews acknowledged that λ was a catch-all type parameter and encompassed both turbulence and secondary circulation effects. Shiono and Knight (1991) further

investigated the lateral variation of λ regards trapezoidal over-bank channels. Numerical and analytical predictions of the lateral variation of velocity and bed shear stresses where made, comparing results computed using a constant λ in the transverse shear layer, with those computed using a λ that was allowed to vary exponentially (note: in the main channel section λ was held constant). The results where λ was allowed to vary compared more favourably to experiment than those of constant λ.

As previously mentioned the focus of this research is rectangular in-bank and over-bank channels, therefore the important focus is on whether utilising a constant value in the main channel for in-bank cases and the main channel and floodplain sections in over-bank cases is physically reasonable. In in-bank channels the 'standard' value of λ used is 0.07. For example, in the works of Knight et al. (2007) and Tang and Knight (2008) the secondary circulation parameter Γ was the focus of investigation, therefore constant values of f and λ ($\lambda = 0.07$) were chosen in order to examine the influence of the variation of Γ on the analytical solution.

It is also worth pointing out at this point that in a lot of reported work on the SKM, when using the analytical solution and performing parameter investigation, parameters such as f, and λ are held constant whilst Γ is varied. This is the case for the work of Chlebek and Knight (2006) for example. However, this is not a physically reasonable assumption. Also, a further interesting comment often made is that the variation of λ has a relatively small effect on the analytical solution results. Even though this comment is regularly made (Chlebek and Knight 2006; Knight *et al.* 2007; Tang and Knight 2008) no justification is made as to why this is the case

and if the impact of varying λ is negligible then why is the choice given to the modeller to vary the parameter.

2.6.3.3 Secondary Flow Term, Γ

The dimensionless secondary flow term Γ represents the gradient of the force per unit length due to secondary flow, $\left(H\rho\overline{UV}\right)_d$. Figure 2.6.3-1 shows a schematic representation of a rectangular channel, secondary current cells and the associated sign of the force per unit length due to secondary flow.
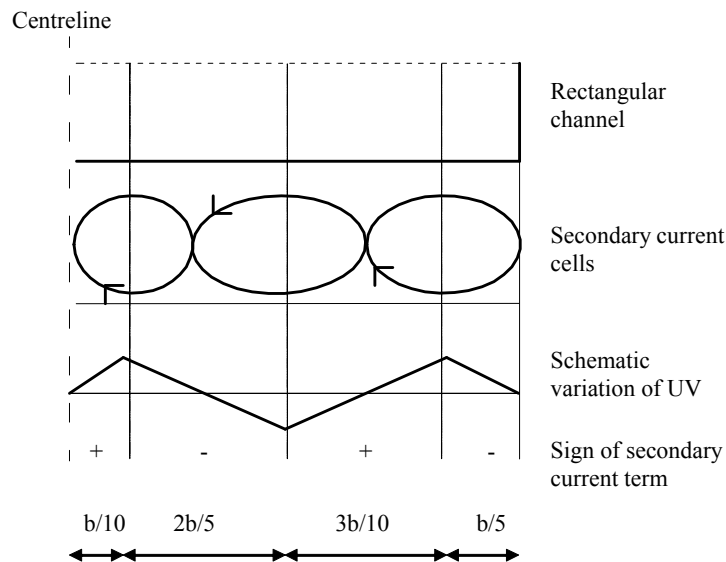
Figure 2.6.3-1: Secondary current cells, secondary flow term and panel division lines

(Omran 2005)

It can be seen from Figure 2.6.3-1 that the maxima and minima of $\left(H\rho\overline{UV}\right)_d$ occur at the cell centres, with values reaching zero at cell edges. As the dimensionless secondary flow term corresponds to the gradient of the lines in Figure 2.6.3-1, the panel locations are therefore located at the maxima and minima values so as to ensure a constant Γ value throughout the panel.

58
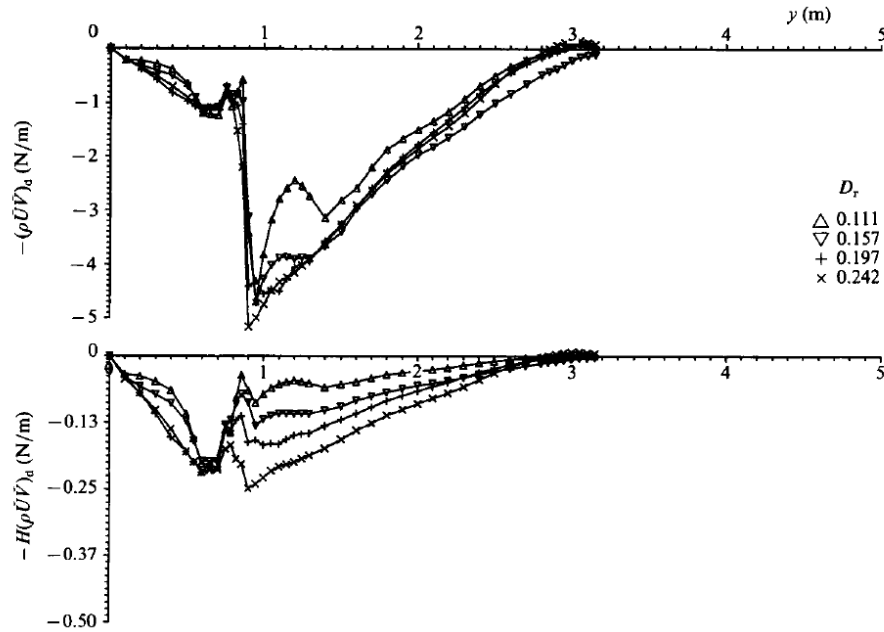
Figure 2.6.3-2: Lateral variation of apparent shear stress, $\left(\rho\overline{UV}\right)_d$ *, and force per unit length ,* $\left(H\rho\overline{UV}\right)_d$ *, due to secondary flows for different depth ratios (Shiono and Knight 1991)*

As described in Section 2.2 secondary current cells impact the boundary shear stress distribution. Some authors also think that secondary circulations play a role in lateral momentum exchange in the mixing region of over-bank channels, specifically Shiono and Knight (1991). However, Shiono and Knight (1991) did not verify this on the basis of measured secondary flow velocities. In contrast to Shiono and Knight (1991), van Prooijen (2004) concluded that secondary circulations are of minor importance. Van Prooijen (2004) concluded this on the basis that for the secondary flow to be significant it should be the same order of magnitude as the Reynolds stress and by estimating a required velocity for the secondary circulation that would satisfy this criterion, it was shown that experimentally measured velocities were 1 order of magnitude lower than the required estimated velocity.

Whatever the thought on secondary circulation cells, they still require modelling for the purposes of calibrating the SKM constants and as has already been mentioned in section 2.6.2 excluding the Γ parameter gives less accurate solutions than if it is included.

Omran (2005) studied the perturbation in the boundary shear stress across rectangular channels based on experimental data from Knight and Demetriou (1983), Tominaga et al. (1989) and Ardiclioglu (1994). Omran (2005) generated graphs of the variation of the non-dimensionalised experimentally measured boundary shear stress, $\tau/\bar{\tau}$ and average shear stress, $\bar{\tau}$. Figure 2.6.3-3 is one such graph for a channel with B/H $\geq$ 2.0 and it clearly shows the variation between $\tau/\bar{\tau}$ and $\bar{\tau}$.
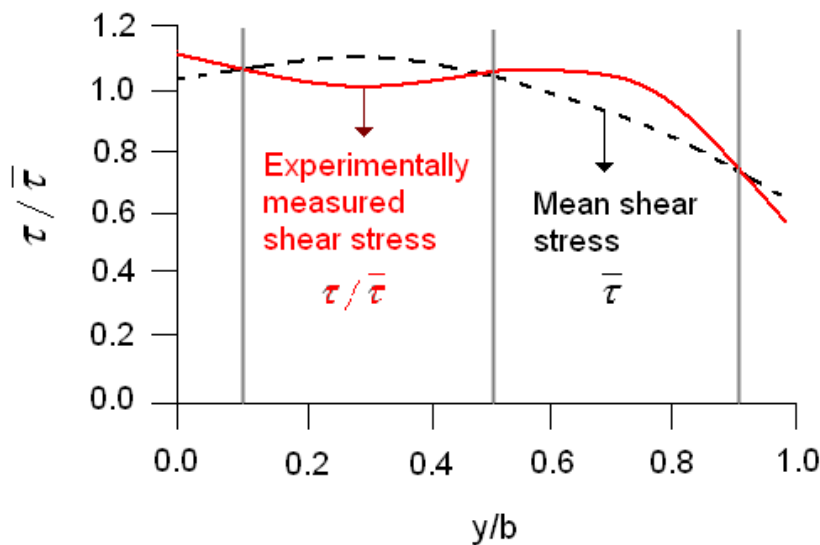
Figure 2.6.3-3: Typical boundary shear distribution for B/H ≥2 (Omran 2005)

The perturbations of $\tau/\bar{\tau}$ from $\bar{\tau}$ are due to the secondary circulation cells. Utilising figures such as Figure 2.6.3-3 Omran (2005) derived the locations of the secondary current cells for a range of rectangular channels at varying aspect ratios. From the locations of the secondary current cells panel division lines were specified

for numerous channels. For the purposes of the research reported and comparison of results, the most important finding of Omran (2005) is that division lines for panel locations were identified for rectangular in-bank channels at y/b=0.1, 0.5 and 0.9 from the channel centreline for channels of aspect ratio B/H≥2 and y/b=0.5 and 0.9 for channels of aspect ratio B/H<2.

Shiono and Knight (1991) also examined the apparent shear stresses, $\left(\rho\overline{UV}\right)_d$ and apparent shear force, $\left(H\rho\overline{UV}\right)_d$ in an over-bank trapezoidal channel. Figure 2.6.3-2 shows the lateral variation of $\left(\rho\overline{UV}\right)_d$ and $\left(H\rho\overline{UV}\right)_d$ as observed by Shiono and Knight (1991). It can be seen that a maximum value of $\left(\rho\overline{UV}\right)_d$ is found on the edge of the floodplain, which also corresponded with a maximum value of Reynolds stresses relating to turbulence exchange, from which λ is derived. The distributions of $\left(\rho\overline{UV}\right)_d$ and $\left(H\rho\overline{UV}\right)_d$ across the floodplain from their maximum value can be seen to decrease virtually linearly and this was thought to be an indication of just one secondary flow cell across the floodplain. However, in the main channel corner, floodplain corner and on the channel side slope the distributions of $\left(\rho\overline{UV}\right)_d$ and $\left(H\rho\overline{UV}\right)_d$ are more complex, indicating further possible secondary flow structures. The values of Γ were derived from a linear approximation to a plot of $\left(H\rho\overline{UV}\right)_d$ which gave $\Gamma/\rho gHS_0=0.15$ in the main channel and $\Gamma/\rho gHS_0=-0.25$ on the floodplain. These values along with approximations for f, and λ and ignoring Γ on the main channel and floodplain side slopes were used in analytical solutions for the same experimental set-up to investigate the calibration parameter values. The analytical predictions were in close agreement to those of experiment. Recently,

however, Tang and Knight (2008) have questioned the use of $\left(H\rho\overline{UV}\right)_d$ within the definition of Γ. Tang and Knight (2008) stated that observations made by Shiono and Knight (1991) showed that the lateral distributions of $\left(\rho\overline{UV}\right)_d$ within the reported trapezoidal over-bank channels was more or less linear and similar for different depth ratios, which was in contrast to $\left(H\rho\overline{UV}\right)_d$ whose gradient varied dependant on depth ratio. The variation of $\left(H\rho\overline{UV}\right)_d$ with depth can be clearly seen in Figure 2.6.3-2.

The above implies that it is more reasonable to make the assumption of a linear variation for $\left(\rho\overline{UV}\right)_d$ rather than $\left(H\rho\overline{UV}\right)_d$, which is the assumption made by Tang and Knight (2008) who report how this new assumption affects the analytical results. However, it was then concluded that even with this new assumption the same solutions are obtained for a constant depth domain as compared to the old assumption. As the focus of this work is regarding rectangular channels, all of the reported channels are of constant depth.

2.6.3.4 f, λ and Γ Optimisation

The values of f, λ and Γ obtained experimentally are generally only applicable to a specific geometrical and physical set-up. This is not extremely helpful to the practical engineer who has to provide input values for these parameters when estimating discharge for natural rivers, so further work for larger data sets has been carried out to provide a set of equations giving the general trend in f, λ and Γ based on known river aspects.

A parametric study was undertaken for a set of in-bank rectangular channels by Chlebek and Knight (2006), with 4 series of 4 flumes at various depths, giving aspect ratios varying from approximately 0.3 to 20. One half of the cross-section was modelled and one panel was used to represent half the channel section. The general approach for the optimisation was to assume values for two variables and then vary the third until the modelled discharge and percentage shear force on the boundaries were comparable to those measured. Friction factor, f, was the first calibrated value as this has been found to be the most influential. From this the 'best' value of f was used in conjunction with an initial guess for Γ and λ was varied. Finally the 'best' value of λ was then used in conjunction with that for f and Γ was varied until the optimum solution was found. For in-bank channels this approach seems sensible, however for over bank or meandering channels where Γ becomes more significant, the order of calibration may well change.

2.6.4 Summary

f, λ and Γ have been prescribed for specific channel geometries and some initial parameterisation has been undertaken for in-bank results with empirical relations derived with respect to width to depth ratio. Further work is obviously necessary to parameterise these empirical constants and associate with them some physical meaning and practical characterisation for their behaviour and also extending this work to over-bank channel cases.

$$ $$

CHAPTER 3:

3   NUMERICAL MODELLING

3.1   INTRODUCTION

This section contains a brief description of the numerical methods used within this research and applicable software descriptions.

Computational Fluid Dynamics (CFD) is a computer-based tool for simulating the behaviour of systems involving fluid flow, heat transfer, and other related physical processes. It works by numerically solving the equations of fluid flow over a region of interest, with specified boundary conditions. The solution is advanced through space and time to obtain a numerical description of the complete flow field of interest.

3.2   THE NAVIER-STOKES EQUATIONS

The Navier-Stokes (N-S) Equations describe the general motion of turbulent flow. Formulated in the 19th century, their complexity has dictated that even today they cannot be solved completely. The derivation of the N-S Equations can be found in CFD textbooks of the likes of Davidson (2004). The equations are considered to be an expression of the physical laws of conservation of mass, momentum and energy. In the absence of source terms conservation of mass can be expressed as:

$$\frac{\partial \rho}{\partial t} + \frac{\partial}{\partial x_j}\left(\rho u_j\right) = 0 \qquad\qquad (3.1)$$

where ρ is the density of the fluid, t is time and u is the velocity vector of the fluid. Considering a volumetric element through which fluid flows, term 1 in Equation 3.1 describes the rate of change in time of the density of the fluid (this term is zero for an incompressible fluid as the density is constant). The second term, the convective term, describes the net flow of mass out of the element across its boundaries. Conservation of momentum is expressed in Equation 3.2:

$$\frac{\partial(\rho u_i)}{\partial t} + \frac{\partial(\rho u_i u_j)}{\partial x_j} = -\frac{\partial p}{\partial x_j} + \mu \frac{\partial^2 u_i}{\partial x_j x_j} + S \qquad\qquad (3.2)$$

Where ρ, t and u are as defined for Equation 3.1 and μ is the dynamic viscosity of the fluid. The left hand side of Equation 3.2 is the same as that of Equation 3.1 with the addition of a velocity component. On the right hand side the first term represents the rate of change with position of the pressure in the fluid. The second term is the diffusive term and accounts for losses in the fluid due to viscosity. The third term, S, takes into account any body forces acting on the fluid body such as gravity.

3.3 DISCRETISATION

The N-S Equations are non-linear partial differential equations, which treat the whole fluid domain as a continuum. To date only simple flows have been directly solved at very low Reynolds numbers, so in order to simplify the problem the

equations are simplified. The simplification can be made using what is called discretisation.

3.3.1 Numerical Discretisation

Numerical discretisation allows the continuum to be replaced with a finite set of nodes. There are three main numerical methods of discretisation: finite volume method (FVM), finite element method (FEM) and finite difference method (FDM). The FVM is the most popular within which the domain of interest is divided into control volumes. At the centre of each volume the values of quantities, such as pressure, density and velocity that are present in the equations to be solved are stored. The flux into a region is calculated as the sum of the fluxes at the boundaries of that region. Therefore this requires some interpolation since values of quantities are stored at nodes, not boundaries.

3.3.2 Spatial Discretisation: Mesh Generation

In whichever way the domain is discretised, based on mesh based methods such as any of those mentioned above, care has to be taken in order to produce a good mesh. A mesh with too few nodes could lead to a quick solution, yet not a very accurate one: however a very dense mesh of nodes will potentially waste computational time and memory. Usually more nodes are required within areas of interest, such as near wall and wake regions, in order to capture the large variation of fluid properties expected in these regions.

3.3.3 Temporal Discretisation

For transient problems an appropriate time step needs to be specified. The time step should be sufficiently small as to capture the required features of the flow, however, not too small as to waste computational power resolving unnecessary scales. Spatial and time discretisation are linked, as evident in the Courant number.

3.3.3.1 Courant Number

A criterion often used to determine time step size is the Courant number. The Courant number stops the time step from being large enough for information to travel entirely through one cell during one iteration. For explicit time stepping schemes this number should ideally not be greater than 1. For implicit time stepping schemes this number may be higher than 1, although accuracy issues may arise. The Courant number is defined below:

$$C_r = \frac{\overline{U} \Delta t}{\Delta l} \qquad\qquad (3.3)$$

Where C_r is the Courant number, $\overline{U}$ is the average velocity, Δt is the maximum time step size and Δl is the largest grid cell size parallel to the direction of flow.

3.4   BOUNDARY CONDITIONS

Boundary conditions need to be implemented to define the behaviour of the variables at the edges of the domain. For open channel flow problems there are generally four boundary conditions to be considered: inlet, outlet, walls and free surface.

3.4.1   Inlet and Outlet Periodic Boundaries

All of the channels reported were performed with translational periodic boundaries in the streamwise direction of the flow, allowing the values on the inlet and outlet boundaries to coincide, and a pressure gradient was further specified across the domain to drive the flow.

To initialise the flow a mean velocity was specified over the whole inlet plane upon which velocity fluctuations were imposed. The inlet mean velocities were derived where possible from the experimental average values.

 In order to specify the pressure gradient the channel geometries were all created flat and the effects of gravity and channel slope implemented via a resolved gravity vector. If θ represents the angle between the channel slope and the horizontal, the gravity vector is resolved as:

$$\rho g = \left(\rho g \sin \theta, 0, -\rho g \cos \theta \right) \tag{3.4}$$

The x component causes the water to flow along the channel and the z component is responsible for creating the hydrostatic pressure.

3.4.2 Free Surface

A rigid free-slip condition was implemented at the free-surface. This specifies that the shear stress at the wall is zero and the streamwise and lateral velocities of the fluid near the wall are not retarded by wall friction effects as with a no-slip boundary condition. However, the normal velocities are damped. Many authors studying numerical modelling of open channel flow use a rigid free-slip condition (Thomas and Williams 1999a; 1995b).

3.4.3 Walls

A no-slip boundary condition is the most common boundary condition implemented at the wall and prescribes that the fluid next to the wall assumes the velocity at the wall, which is zero by default.

3.5 SOLVING FOR TURBULENCE

3.5.1 Direct Numerical Simulation (DNS)

The Navier-Stokes Equations can be directly solved without averaging or approximation and this is the most accurate approach to turbulence simulation. Referred to as direct numerical simulation (DNS) this method is conceptually the simplest approach, however, resolution of all of the scales contained within the flow means that it is also the most computationally expensive and memory demanding. In order to capture all of the significant structures of turbulence within the flow the computational domain must be at least as large as the physical domain to be considered or the largest turbulent eddy. In conjunction with modelling the largest scales there must also be resolution of the kinetic energy dissipation, which occurs on the smallest scales on which viscosity is active. Therefore the size of the grid must be no bigger than a viscously determined scale, called the Kolmogorov scale, η. (Kolmogorov 1942). The possibilities of DNS seemed endless and many fluid dynamicists were attracted to this growing field. However, there was and is a catch, to achieve a large Reynolds number a vast number of data points are necessary as the number of cells required is a function of the Reynolds number elevated to the power 9/4 per turbulent structure that decays.

In most applications to real life the Reynolds number is far beyond that capable of any DNS, however a few simple channel flow cases have been simulated using DNS techniques at low Reynolds numbers and for very simple geometries, by the likes of

Iwamoto et al. (2005), Abe et al. (2001) and Moser et al. (1999). These cases will be explored further in Section 3.6 as they are used as a validation tool for the LES.

3.5.2 Large Eddy Simulation (LES)

Large eddy simulation is an intermediate approach to DNS and RANS. In LES the large three-dimensional unsteady turbulent motions are directly represented and computed exactly, whereas the smaller-scale structures are not modelled, but their influence upon the rest of the flow is parameterised. This is advantageous because the large scales depend strongly on the boundary conditions and hence determine the basic features of the flow field for various situations, and are thought to dominate the transfer of heat, momentum and chemical transfer, which are usually the processes wished to be modelled; they account for most (80%) of the turbulence energy. The unresolved smaller sub-grid scales of motion, however, are parameterised as they are mostly isotropic and more universal in nature and therefore more amenable to modelling.

LES relies on a spatial filter, rather than a time averaging process. A filtering function (e.g. Gaussian, box cut-off, Fourier) is used to distinguish eddies that are going to be calculated from those that are going to be modelled and each filter has an associated length scale, Δ, which represents this threshold. Above Δ the DNS technique applies, whilst below Δ a space-averaged version of the Navier-Stokes Equations is produced. In most codes a cut-off approach is used and this is dependant on the mesh size.

The instantaneous velocity variable u can be written such as:

$$u = \overline{U} + u'$$

where u_i' is the unresolved part and $\overline{U}$ is the large scale part defined through volume averaging as:

$$\overline{U}(x_j,t) = \int_{vol} G(x_i - x_i')u(x_j',t)dx_i'$$

where $G(x_i - x_i')$ is the Gaussian filter. Recalling that the non-filtered Navier-Stokes Equations are:

$$\frac{\partial(\rho u_i)}{\partial t} + \frac{\partial(\rho u_i u_j)}{\partial x_j} = -\frac{\partial p}{\partial x_j} + \mu \frac{\partial^2 u_i}{\partial x_j x_j}$$

After performing the volume averaging and neglecting density functions, the filtered Navier-Stokes Equations become:

$$\frac{\partial(\rho \overline{U}_i)}{\partial t} + \frac{\partial(\rho \overline{u_i u_j})}{\partial x_j} = -\frac{\partial \overline{P}}{\partial x_j} + \mu \frac{\partial^2 \overline{U}_i}{\partial x_j x_j}$$

The non-linear transport term in Equation 3.8 can be developed as:

$$\overline{u_i u_j} = \overline{\left(\overline{U}_i + u_i'\right)\left(\overline{U}_j + u_j'\right)}$$

$$= \overline{\overline{U}_i \overline{U}_j} + \overline{\overline{U}_i u_j'} + \overline{\overline{U}_j u_i'} + \overline{u_i' u_j'}$$

$$\text{I} \qquad \text{II} \qquad \text{III} \qquad \text{IV}$$

In time averaging the terms II and III vanish, but when using volume averaging this is no longer true.

Introducing the residual stresses or sub-grid scale (SGS) stresses, τ_{ij}, as:

$$\tau_{ij} = \overline{u_i u_j} - \overline{U_i U_j}$$

(3.10)

Equation 3.8 can be written as:

$$\frac{\partial\left(\rho \overline{U_i}\right)}{\partial t} + \frac{\partial\left(\rho \overline{U_i U_j}\right)}{\partial x_j} = -\frac{\partial \overline{P}}{\partial x_j} + \mu \frac{\partial^2 \overline{U_i}}{\partial x_j x_j} - \frac{\partial\left(\rho \tau_{ij}\right)}{\partial x_j}$$

(3.11)

Equation 3.11 is the basis of the LES technique. Various LES techniques are detailed dependant upon the SGS model used.

LES has the advantage over DNS that in DNS nearly all of the computational effort goes into modelling the smaller scales whereas the energy and anisotropy are contained predominantly in the larger scales. Thus LES avoids the computational cost of explicitly modelling the smaller scale motions.

3.5.2.1 Sub-Grid Scale Models

The non-linear transport of energy generates ever-smaller scales like a cascade process until it reaches the viscous dissipation range or the size of Kolmogorov scales. An essential challenge in LES is accounting for this energy drain from

resolved large scales to the unresolved small scales properly and the interaction between the resolved and unresolved sub-grid scales. This is the role of the SGS model. Arguably the most popular class of SGS models is the eddy-viscosity type, based on (variants of) the Smagorinsky model (Smagorinsky 1963).

Smagorinsky model

The SGS stress tensor, τ_{ij}, aids in providing model closure for the LES and is modelled, most simply by an eddy-viscosity model. In these models the SGS stress tensor is related to the resolved strain-rate tensor $\overline{S_{ij}}$ through a scalar eddy viscosity coefficient. The SGS stress tensor (the traceless part of τ_{ij}) is written as:

$$\tau_{ij}{}^R = 2\rho v_R \overline{S_{ij}} + \frac{1}{3}\delta_{ij}\tau_{kk}{}^R \tag{3.12}$$

where $\overline{S_{ij}}$ is defined as:

$$\overline{S_{ij}} = \left(\frac{\partial \overline{U_i}}{\partial x_j} + \frac{\partial \overline{U_j}}{\partial x_i} \right) \tag{3.13}$$

Where the eddy viscosity of the residual motion, v_R, is defined as.

$$v_R = C_S^2 l^2 \left(2\overline{S_{ij}}\,\overline{S_{ij}} \right)^{\frac{1}{2}} \tag{3.14}$$

where C_S is the Smagorinsky constant. This is the only adjustable parameter in the subgrid model and lies in the approximate range 0.094 to 0.2, although Thomas and Williams (1995a) state that the simulation results are very insensitive to its value. Lilly (1967) determined, on theoretical grounds that for homogeneous turbulence C_S=0.17. However, in the presence of a mean shear rate Deardorff (1971) found that this value caused excessive damping of large scale motions and used C_S= 0.094. The simulations herein are performed using C_S=0.1 as later researchers found that this was the optimum value.

Further SGS models

Even though eddy viscosity models are popular they have been shown to be too dissipative near walls and cannot account for backscatter effects. Using a dynamic procedure circumvents some of the limitations. The paper of Germano et al. (1991) puts forward the idea of the dynamic Smagorinsky model, within which C_S is expressed in terms of resolved scales and then computed as a function of position and time.

Further models were created to overcome the drawbacks of eddy viscosity-type models and provide a better physical representation of the SGS stresses. They assume that most of the SGS stress can be estimated from the smallest resolved scales (scale similarity models (SSM)). However, again these models have their drawbacks, of which a fundamental one is that they are not dissipative enough and under predict the net SGS dissipation, i.e. they are not able to assure a sufficient energy drain from resolved scales of motion to unresolved ones. It has been shown

that such a drawback is due to the fact that such models do not take into account the smallest unresolved scales where the most dissipation of turbulent SGS energy takes place.

3.5.2.2 Near Wall Modelling

Near a no-slip wall, there are strong gradients in the dependent variables. In addition, viscous effects on the transport processes are large. The representation of these processes within a numerical simulation raises the problem of how to account for viscous effects at the wall and how to resolve the rapid variation of flow variables, which occurs within the boundary layer region.

Experiments and mathematical analysis have shown that the near-wall region can be subdivided into two layers. At the wall itself the flow will be stationary and therefore there will always be a narrow boundary layer of laminar flow, the so-called "viscous sublayer", where (molecular) viscosity plays a dominant role in momentum and heat transfer. Further away from the wall, in the "logarithmic layer", turbulence dominates the mixing process. Finally, there is a region between the viscous sub-layer and the logarithmic layer called the "buffer layer", where the effects of molecular viscosity and turbulence are of equal importance.

Wall functions are the most popular way to account for wall effects. The mesh node next to the wall is placed in the turbulent boundary layer and a model of flow in that region is used. This sets values for velocity, pressure and turbulent quantities, replacing the solution to the Navier-Stokes Equations at that point.

The wall-function approach in CFX is an extension of the method of Launder and Spalding (1974). In the log-law region, the near wall tangential velocity is related to the wall shear stress, τ_w, by means of a logarithmic relation.

$$u^+ = \frac{U_t}{u_*} = \frac{1}{k}\ln\left(y^+\right) + c$$ (3.15)

Where: $y^+ = \dfrac{\rho \Delta y u_*}{\mu}$ (3.16)

$$u_* = \left(\frac{\tau_\omega}{\rho}\right)^{\frac{1}{2}}$$ (3.17)

u^+ is the near wall velocity, u_* is the friction velocity, U_t is the known velocity tangent to the wall at a distance of Δy from the wall, y^+ is the dimensionless distance from the wall, τ_w is the wall shear stress, k is the von Kármán constant and c is a log-layer constant dependant on wall roughness. The implementation of a wall function eliminates the need for very fine meshes that resolve the flow down to the wall.

However, when performing LES, an extremely fine grid is required which resolves the viscous sub-layer down to a wall-normal distance $y^+ = O(1)$. Therefore LES directly computes the variables down to the wall without the implementation of a wall function. Even though LES does not replace the N-S equations with a wall-function near the wall it does use a wall-function approximation to make an estimate

of u_* at the wall. This has proven to be accurate for numerically simulated open channel flows and involves fitting a log-law to the mean velocity profile and calculating a shear velocity from it. Thomas and Williams (1995a) adopt this method and draw comparison between u^+ and y^+ for experiment, LES and Equation 3.15, for which all are comparable. Nezu and Rodi (1986) show a wall-function approximation to be satisfactory for wide channels, and Gavrilakis (1992) suggest that the logarithmic profile (based on local shear velocity) found for turbulent flow in a square duct exhibits a logarithmic region similar to Equation 3.15. The profile for the channel simulated in Thomas and Williams (1995a) was considered intermediate between square duct and open channel.

3.5.2.3 Damping Functions

Due to LES computing the variables down to the walls the turbulence viscosity needs to be damped. This can be achieved using a combination of a mixing length minimum function and a viscosity damping function, f_μ. The simplest example of a near wall modification to a turbulence model is the van Driest damping function for the mixing length. Other more detailed models incorporate either a wall damping effect or a direct effect on molecular viscosity, or in some models, both effects. By default in CFX, the damping function f_μ is 1.0. A van Driest like damping can be specified by the user, for which the damping function is:

$$f_\mu = 1 - \exp(-y/D) \qquad\qquad (3.18)$$

Where y is defined as a function of the calculated wall distance, y^+, kinematic viscosity, υ and local velocity scale. D is a constant and equal to 26 for all simulations reported, as recommended for channel flow by Thomas and Williams (1995a; 1995b; 1999), and Cater and Williams (2008).

3.5.2.4 LES of Open Channel Flow

LES has been applied with some success to a variety of turbulence problems. Reviews on the development and application of LES can be found in Rogallo and Moin (1984) and Meneveau and Katz (2000). LES has been utilised to model in-bank channel flows and investigate detailed structure of secondary circulations. Streedhar and Stern (1998) examined differences in horizontal boundary conditions using a compressible, temporally evolving LES calculation. LES has also been employed to investigate over-bank channel flow by the likes of Thomas and Williams (1995a; 1995b; 1999) and Shi et al. (1999). LES was performed at a relatively large Reynolds number, producing results of bed shear, magnitude of secondary motion and vorticity comparable to experiment.

LES to investigate free-surface turbulence has also been undertaken by the likes of Salvetti et al (1997), Pan and Banerjee (1995) and Hodges and Street (1999). Nakayama and Yokojima. (2002) recently studied LES of open channel flow with free surface fluctuations, where the free surface was filtered along with the flow field itself, which introduced extra SGS terms. Calculations were then performed with and without the free-surface SGS terms which indicated that their effects were not overwhelmingly large in sub-critical flows, but they made some differences in the mean-velocity profile near the free-surface and in the Reynolds stresses. It was

stated that further supercritical flows needed to be examined as it was thought that effects would be observed much more in spatially and temporally varying flows at higher Reynolds numbers.

Although not discussed in detail, other than LES, limited Direct Numerical Simulation (DNS) of open channel flow has been undertaken. DNS is computationally expensive due to the requirement to resolve the kinetic energy dissipation down to the smallest scales, requiring a grid no bigger than a viscously determined scale. In most applications to real life the Reynolds number is far beyond that capable of any DNS, however a few simple channel flow cases have been simulated using DNS techniques at low Reynolds numbers and for very simple geometries; Iwamoto et al. (2004), Abe et al. (2001) and Moser et al. (1999).

3.5.3 Turbulence Modelling of Open Channel Flow

The standard $k - \varepsilon$ model is by far the most widely used in industry, despite its main flaws arising from the assumption of isotropic turbulence and the reservations regarding the adequacy of the dissipation equation. Demuren (1993), Sinha et al. (1998) and Morvan (2001) made successful three-dimensional computations of semi-natural and natural channels using the standard $k - \varepsilon$ model. However, a lot of early work using the $k - \varepsilon$ model did not examine the three-dimensionality and impact of turbulence.

In light of the above, many researchers have adapted the $k - \varepsilon$ model in order to predict secondary currents. Numerical simulations using a $k - \varepsilon$ model together with an Algebraic Stress Model (ASM) have been made by Krishmappen and Lau

(1986), Larson (1988), Kawahara and Tamai (1988) and Noat, Nezu and Nakagawa (1993). Within these calculations two-dimensional model transport equations are provided for k and ε, which are solved alongside the three mean velocity components in the cross-section of the channel. The Reynolds stress components are obtained by solving a set of algebraic equations obtained from a local equilibrium approximation of the more general Reynolds stress transport equations. This treatment of the Reynolds stresses overcomes the inability of predicting flow of eddy viscosity type models. However, the model introduces a number of empirical constants that need to be determined.

Cokljat (1993) invoked two turbulence models: a Reynolds-stress-transport model and a two-equation $k - \varepsilon$ model in conjunction with a non-linear stress strain relationship to model flows in non-circular ducts and channels. It was concluded that the Reynolds-stress-model was capable of accurately predicting the strength and location of secondary-flow cells and their role in displacing the mean velocity maximum to below the free surface but in contrast the non-linear $k - \varepsilon$ model failed to reproduce this result. Both models predicted equally well the shear stress, however, the $k - \varepsilon$ when moving on to channel flow became less accurate.

Sofialidis and Prinos (1999) studied compound open channel flow using a non-linear low-Reynolds $k - \omega$ model capable of predicting the turbulence anisotrophy and the turbulence-driven secondary currents. They concluded that the model predicted secondary currents well when compared with experimental data. They observed a number of phenomena when the floodplain depth was decreased including: intensified lateral shear which extended deeper onto the floodplain, velocity

maximum depressed further from the free surface, weakening of secondary currents and enhanced turbulence levels in the interface region.

Morvan (2001) then took the work of Cokljat (1993) to meandering compound channels where it was established that the geometry dominated the flow at the aspect ratio used in the Flood Channel Facility program. A simple $k - \varepsilon$ was therefore found to provide good predictions in such circumstances.

Wright et al. (2004) investigated flow in open channels using $k - \varepsilon$, and various Reynolds stress models for a trapezoidal channel. The results showed that whilst all the models generally gave similar predictions for the bulk features of the flow, there was a marked difference in the secondary flow characteristics, with the accuracy of predictions increasing with the level of complexity of the turbulence model used. The $k - \varepsilon$ model failed to show any recirculation and the Reynolds stress models showed some recirculation in varying degrees. Wright et al. (2004) as well as drawing comparison with FCF data, compared flow features with initial LES results for the same channel set-up. The LES results were shown to predict open channel flow phenomena more successfully than the RANS based models.

Within this research LES is predominantly the turbulence model utilised to perform numerical simulations. However, comparisons are made with $k - \varepsilon$ and Reynolds Averaged Navier-Stokes (RANS) models, for comparison with certain channel bulk flow features.

3.6   COMPUTATIONAL FLUID DYNAMICS (CFD)

As stated previously CFD is a computer-based tool for simulating the behaviour of systems involving fluid flow, heat transfer and other related physical processes and CFD offers the most general treatment of the Navier-Stokes equations in which pressure and turbulence are fully accounted for.   Within this research both commercial and research codes were utilised in order to perform the numerical simulations.   The commercial CFD software being ANSYS-CFX (versions 5.7.1/10/11) and the commercial geometry and mesh generation software GAMBIT was used for meshing.   The research code is an LES code developed at TU Delft hereon-in denoted Delft code.   As with ANSYS-CFX the Delft code uses the standard Smagorinsky method (Smagorinsky 1963) as the subgrid model, but in this instance without van Driest damping, which is specified in ANSYS-CFX.   The Delft code utilised second order central differencing advection scheme in space and the predictor terms are of second order Adams-Bashfort in time.   The pressure correlation system of equations is solved by Fast Fourier Transforms (FFTs) in the x and y directions and by a double sweep (Gaussian elimination) in the z direction.   The wall functions are incorporated in the momentum balance files.   ANSYS-CFX relies on a finite element-based finite volume method operating in unstructured manner for both structured and unstructured meshes.   The advection scheme is second order central-differencing in space whilst second order backward Euler is used to discretise in time.   All geometry and mesh generation software was run on a Windows-based (XP) standard PC and most simulations were performed in parallel on multi-processor clusters at The University of Nottingham.

3.7 NUMERICAL MODELLING: VALIDATION SET-UP

This section details a channel flow case simulated using both ANSYS-CFX and Delft codes. Simulation set-up is compared and results are validated against numerous experimental data (Knight et al. 1984 and Nezu and Rodi 1985) and other previously published LES simulation results (Shi et al. 1999).

3.7.1 Geometry Set-up

Turbulent channel flow maintained by gravity, g, of an incompressible fluid of kinematic viscosity, υ, in an in-bank channel (notation shown in Figure 3.7.1-1) is considered. The channel is of depth, H, width B and the mean flow is assumed uniform in the streamwise direction so that the bed slope S_0 and energy slope are equal. The Reynolds number R_e is given by:

$$R_e = \frac{4U_{avg}R}{v} \qquad (3.19)$$

Where U_{avg} is the average velocity determined from experiment and R is the hydraulic radius defined by, A/P, where P is the channel wetted perimeter and A the cross-sectional area. The working fluid is water with density equal to 997kg/m^3 and dynamic viscosity equal to 8.89x10^{-4} kg/m/s.
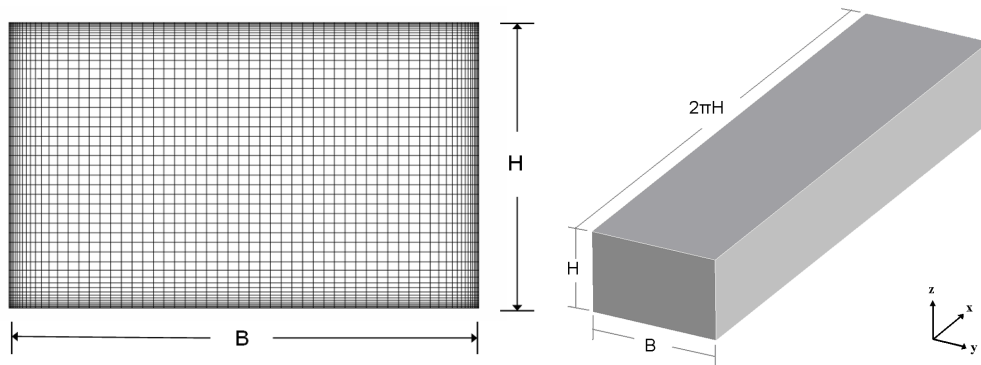
Figure 3.7.1-1: Rectangular in-bank channel geometry and coordinate system

The length of the channel is defined by $2\pi H$ in ANSYS-CFX, with the requirement for this coming from the two dominant mechanisms whereby extended spatial correlations are maintained, i.e. large scale eddy structure which is known to extend for a few times the depth and slow speed streaks which extend for a few thousand wall units, therefore a length of $\sim 6H$ was considered sufficient. The flow was also closely monitored so that structures were created and destroyed within the domain length ensuring that they did not extend through the domain body. Spatial correlations along the domain length were calculated as a quantitative check on the flow structures. A contour plot of instantaneous velocity is shown in Figure 3.7.1-2, to highlight the flow structures at the bed and Figure 3.7.1-2 also shows spatial correlations across the channel length.

It can be seen that at $x/L = 0.4$ (where L denotes the channel length) the spatial correlations tend to zero, indicating that the structures are spatially uncorrelated over half the channel length and the domain specified is adequate. As half the channel

length is found adequate the simulation performed with the Delft code was at a domain length of $3H$.
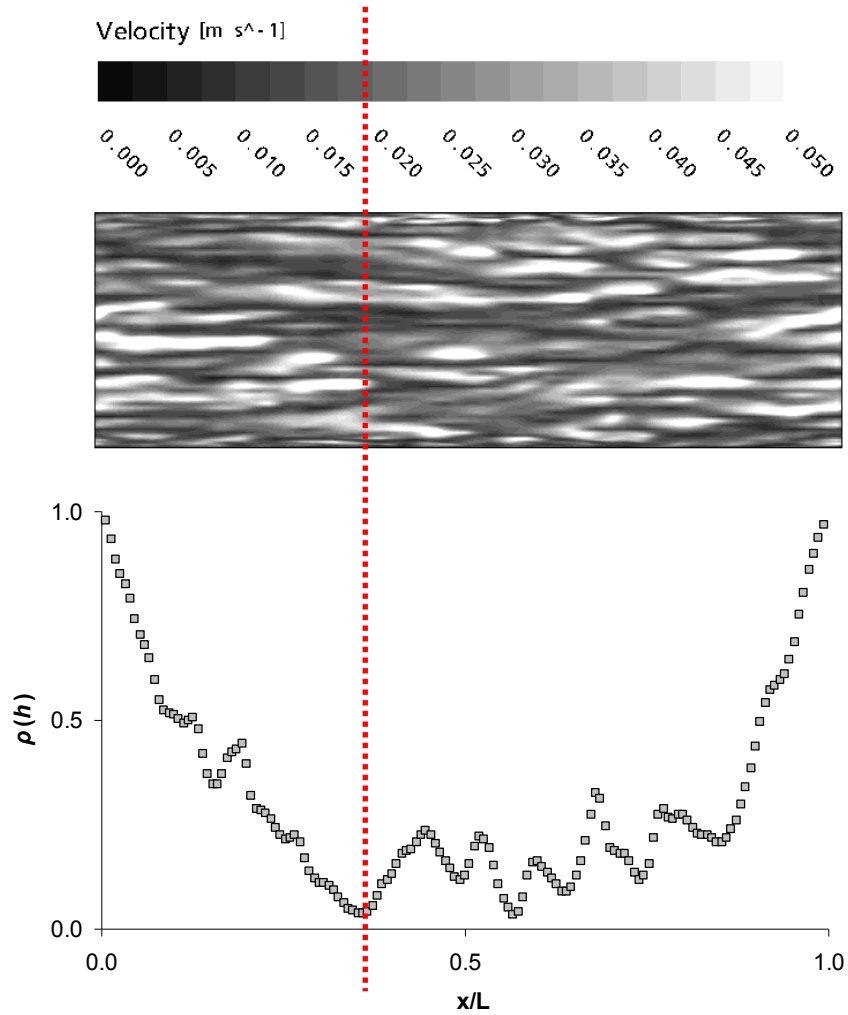
Figure 3.7.1-2: Contour plot of instantaneous velocity at the channel bed and correlation plot, comparing correlation coefficient to distance along the channel

The spatial correlations are computed as below;

$$\rho(h) = \frac{C(h)}{\sqrt{\sigma_0 + \sigma_{+h}}}$$ (3.20)

Where $C(h) = \dfrac{1}{N(h)} \displaystyle\sum_{\alpha=1}^{N(h)} z(u_\alpha) \cdot z(u_\alpha + h) - m_0 \cdot m_{+h}$

$m_0 = \dfrac{1}{N(h)} \displaystyle\sum_{\alpha=1}^{N(h)} z(u_\alpha)$

$m_{+h} = \dfrac{1}{N(h)} \displaystyle\sum_{\alpha=1}^{N(h)} z(u_\alpha + h)$

$\sigma_0 = \dfrac{1}{N(h)} \displaystyle\sum_{\alpha=1}^{N(h)} [z(u_\alpha) - m_0]^2$

$\sigma_{+h} = \dfrac{1}{N(h)} \displaystyle\sum_{\alpha=1}^{N(h)} [z(u_\alpha + h) - m_{+h}]^2$

Where $\rho(h)$ is the correlation coefficient, u_α is a vector of spatial coordinates, $z(u_\alpha)$ is the variable under consideration as a function of spatial location, h is the lag vector representing separation between two spatial locations, $z(u_\alpha + h)$ is the lagged version of the variable under consideration, $N(h)$ is the number of pairs separated by lag, h, m_0 and m_{+h} are the means of the tail and head values respectively and σ_0 and σ_{+h} are the corresponding standard deviations.

3.7.2 Channel Data

The in-bank channel is a channel of $AR = 2$ with available velocity, shear stress and secondary circulation data for comparison. Case 1a has been extensively studied previously and comparison is made here to previous LES work (Shi et al. 1999) and experimental results (Nezu and Rodi 1985). A summary of the experimental data is given in Table 3.7-1.

Table 3.7-1: Summary of experimental values data

CASE	H	B	U_{avg}	τ_{ave}	u_*	R_e	AR
-	(m)	(m)	(m/s)	(N/m^2)	(m/s)	-	-
1a	0.076	0.152	0.338	0.360	0.019	57,559	2.000

3.7.3 Mesh Construction and Simulation Time

3.7.3.1 ANSYS-CFX

The mesh was created by specifying a first cell height to all walls ensuring adequate y^+ values and a growth factor of 1.3 for 10 layers and ensuring that in the bulk flow the mesh element aspect ratio was approximately 1. Mesh details are summarised in Table 3.7-2. Element aspect ratio is important because the filter width in LES to determine between resolved and unresolved scales is determined from the lengths of the hexahedra in all 3 dimensions, i.e. $\Delta = \sqrt{l^3}$, so the cells should be as uniform as possible. Also, following published LES results for channel flow by Broglia et al. (2003) the meshes constructed for the LES included refinement to the free-slip, as well as no-slip walls.

The simulations were started from an initial profile with a mean velocity (U_{avg}) upon which fluctuations of up to 50% of the mean were imposed. The simulations were integrated over time keeping the RMS Courant number <1. A criterion for the length of the simulation is one dictated by the large-eddy turnover time (LETOT), H/u_*, which is the natural timescale of the large eddies. Thomas and Williams

(1995b) propose an initial run of 60-80 LETOTs to obtain a steady state solution and then a further 20 LETOTs to gather the data, although further LES results published by Thomas and Williams (1995a) performed simulations for just 23 LETOTs. Further authors propose 30-50 LETOT's to obtain a steady state solution and then a further 15-25 LETOTs to gather the data. The ANSYS-CFX simulation conforms to 100 LETOTs to obtain a steady state solution and a further 25 LETOTs to gather the data (Table 3.7-2). The initial simulation time was also dictated by the convergence of mass flow, body force and shear stress plots. Finally, qualitatively the appearance of secondary flow structures was ensured steady before gathering statistics.

3.7.3.2 Delft Code

The mesh construction within the Delft code is summarised in Table 3.7-3. The mesh construction within the Delft code ensured that the mesh spacing was approximately equal in all dimensions. There was no need for refinement to the solid boundaries as the first cell to the wall was the same magnitude of that used across the channel cross-section and length. This is also one of the contributing factors to the restriction of the domain length used in these simulations to only $3H$.

With regards to simulation time the Delft code was initialised in the same way as that of ANSYS-CFX with the same average velocity value. Also the initial time period was determined from the large eddy turnover time. The Delft code simulations conform to 50 LETOTs to obtain a steady state solution and a further 25 LETOTs to gather the data and the Courant numbers for all cases were kept below 0.35.

Table 3.7-2: Summary of (a) mesh and (b) simulation details for Series 01 performed using ANSYS-CFX

CASE	Length (m)			Number of elements				Mesh spacing (m)			y^+ range		AR	R_e
-	x	y	z	x	y	z	Total	Δx	Δy	Δz	min	max	-	- -
1a	0.228	0.152	0.076	150	72	45	486,000	0.0015	0.0021	0.0017	0.24	10.83	2.00	57,559

CASE	H/u_*	Estimated Simulation Time (sec) *			Time step		Actual Time (sec)			LETOT Initial	LETOT Collect	LETOT Total
-	(sec)	Initial	Collect	Total	Δt	C_r	Initial	Collect	Total			
1a	4.00	200	100	300	0.001	0.286	400	110	510	100	27	127

Table 3.7-3: Summary of (a) mesh and (b) simulation details for Series 01 performed using Delft code

CASE	Length (m)			Number of elements				Mesh spacing (m)			y^+ range		AR	R_e
-	x	y	z	x	y	z	Total	Δx	Δy	Δz	min	max	-	- -
1a	0.228	0.152	0.076	150	100	50	750,000	0.0015	0.0015	0.0015	28.80	28.80	2.00	57,559

CASE	H/u_*	Estimated Simulation Time (sec) *			Time step		Actual Time (sec)			LETOT Initial	LETOT Collect	LETOT Total
-	(sec)	Initial	Collect	Total	Δt	C_r	Initial	Collect	Total			
1a	4.00	200	100	300	0.001	0.222	200	110	300	50	25	75

[Estimated simulation time is based on an initial time of 50 LETOTs (H/u_*) and then a further 25 LETOTs to collect statistics]*

3.8 NUMERICAL MODELLING: VALIDATION RESULTS

The simulation results are investigated in terms of flow properties and structures. Firstly the prediction of velocity and shear stress is investigated as comparison can be made with experimental results, then flow structures are reported and the results from both codes are compared. All velocity and shear stress values are non-dimensionalised in order to compare with experiment, with velocities non-dimensionalised by the cross-sectional average value, U_{avg} and shear stress values by the associated bed/wall average.

3.8.1 Velocity and Boundary Shear Stress

The non-dimensionalised velocity, U_d is plotted in Figure 3.8.1-1 for Case 1a predicted using ANSYS-CFX.
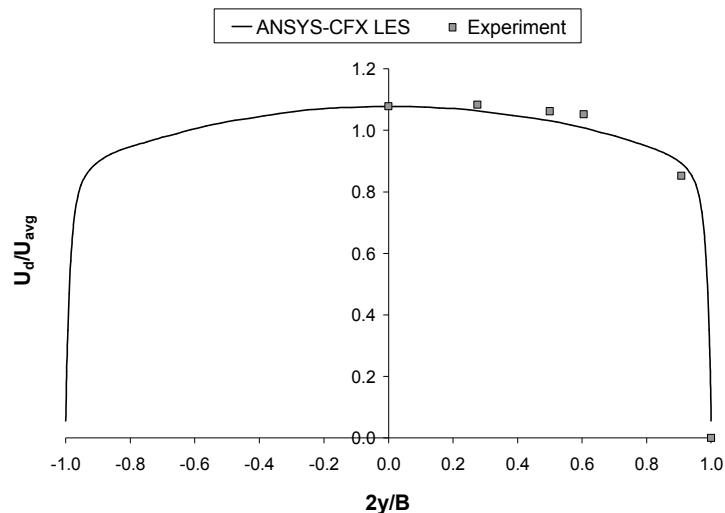
Figure 3.8.1-1: Depth averaged velocity profile for Case 1a

The LES derived profile compares well to experiment. However, when the actual velocity values are compared the ANSYS-CFX result is higher than the experimental data by 21%. The over prediction of discharge has also been highlighted in similar LES channel flow work, such as Thomas and Williams (1995) who attribute it to the use of smooth walls within the simulation where in fact the experiments are not smooth, but slightly rough. Thomas and Williams (1995) simulated velocity profile over-predicts that of experiment by around 15%. The comparable non-dimensionalised velocity plot for Case 1a produced using the Delft code can be seen in Figure 3.8.1-2. Again, it can be seen that the profile is predicted well.
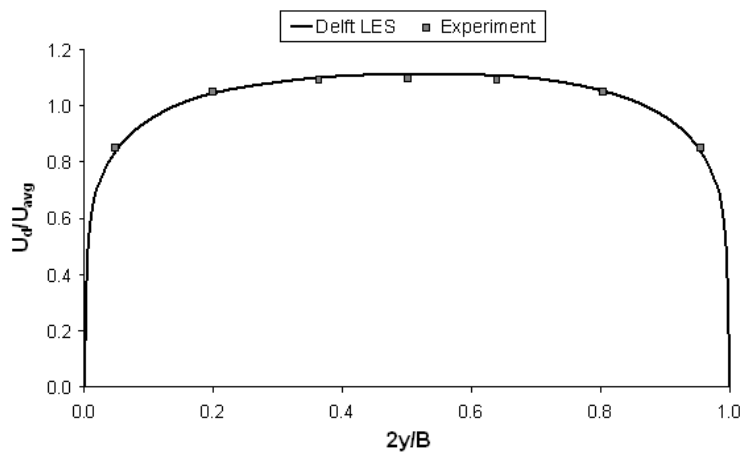
Figure 3.8.1-2: Depth averaged velocity profile for Case 1a

Also, as with the ANSYS-CFX code the Delft code also over-predicts the experimental discharge by 15%. The fact that both codes over-predict the discharge may be an indicator that the specification of smooth walls is incorrect. Figure 3.8.1-3 shows the computed and experimentally measured bed shear stress profile for Case la. The experimental data used for comparison is from Shi et al. (1999) as data were not available from Knight et al. (1984) for this specific channel.
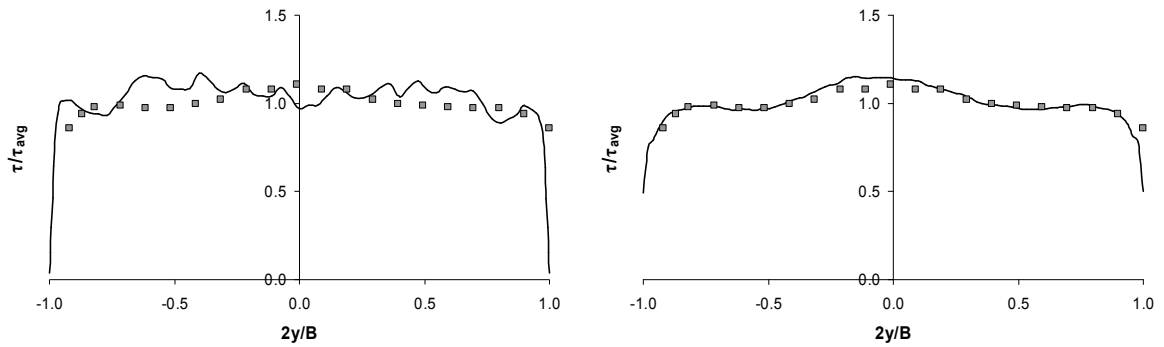
Figure 3.8.1-3: Bed shear stress profile for Case 1a (a) ANSYS-CFX and (b) Delft code

The profile produced by the Delft code can be seen to be in very good agreement with experiment. The maximum deviation from experimental data is 6% but the rest of the profile is within 5% of experiment. The averaging period may be insufficient within the ANSYS-CFX case. However, the secondary flow structures were observed to be steady (Figure 3.8.2-1). The body forces were shown to converge for both ANSYS-CFX and Delft code cases to within 6% of the analytical shear stress.

Other than depth averaged velocity and boundary shear stress data, experimental vertical velocity profiles were available for comparison with the simulated results. Figure 3.8.1-4 shows vertical velocity profiles from ANSYS-CFX and Delft. It can be seen that both codes compare well to the experimental data. However, the Delft code does replicate the 'dip' phenomenon better than ANSYS-CFX, with the maximum velocity occurring within 5% of the experimentally measured position for both cases. The velocity in the Delft code profiles can be seen to decrease as the free surface is approached whereas in the ANSYS-CFX profiles the velocity seems to be normal to the surface.
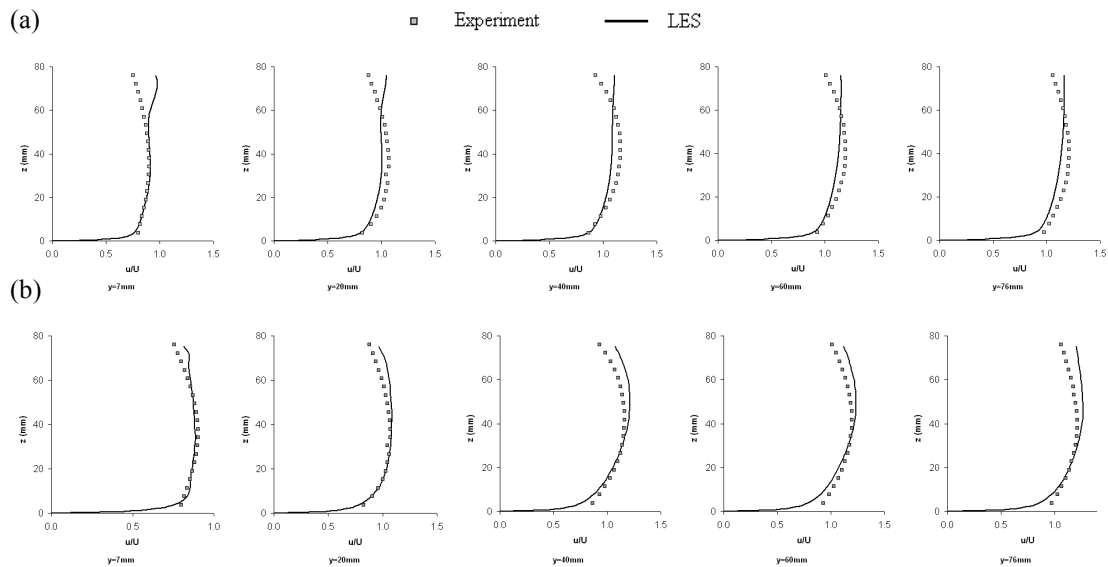
Figure 3.8.1-4: Vertical velocity profiles for Case 1a computed using (a) ANSYS-CFX and

(b) Delft code

One interesting feature to mention is the deviation of velocity at the free surface in the $y=7$mm profile for both simulations, more easily seen in the ANSYS-CFX profiles but also present in the Delft code results. The velocity can be seen to decrease from $z\sim40/50$mm to $z\sim60/100$mm, then increase from $z\sim60/100$mm. This increase is due to the existence of a small secondary current cell observed at the wall/free surface corner.

3.8.2 Flow Structures

Other than velocity and boundary shear stress measurements, plots of secondary circulation cells have been examined.

Figure 3.8.2-1 shows plots of time-averaged velocity predicted using ANSYS-CFX and Delft code. It can be seen that for coinciding cases computed with varying codes that the secondary circulations differ. Case 1a has been extensively studied

94

previously and comparison is made here to previous LES work (Shi et al. 1999) and experimental results (Nezu and Rodi 1985), to further examine the accuracy of the LES results. Case 1a shows the closest agreement with experiment when comparing both codes.

(a)   (b)
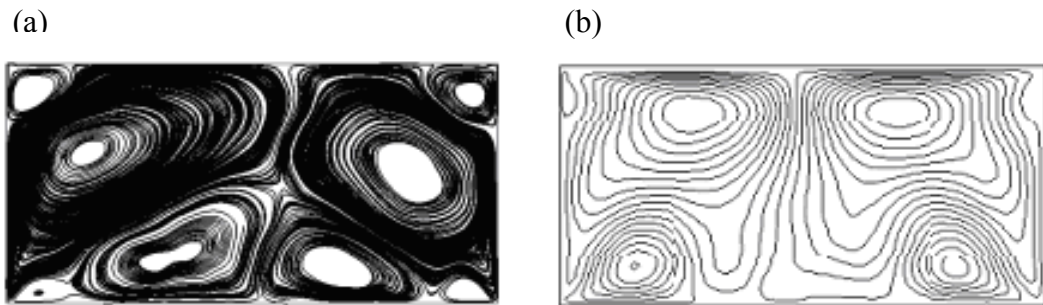
Figure 3.8.2-1: Streamline plots of time-averaged velocity computed using (a) ANSS-CFX and (b) Delft code.

Kang and Choi (2006) produced a schematic representation of secondary circulations in an open channel flow case at *AR=2*, which can be seen in Figure 3.8.2-2. It can be seen that three distinct vortices are highlighted. Comparing these to the ANSYS-CFX and Delft code results, both compare well. However, the Delft code results compare qualitatively better than those of ANSYS-CFX. Other than velocity and boundary shear stress measurements, plots of secondary circulation cells have been examined.
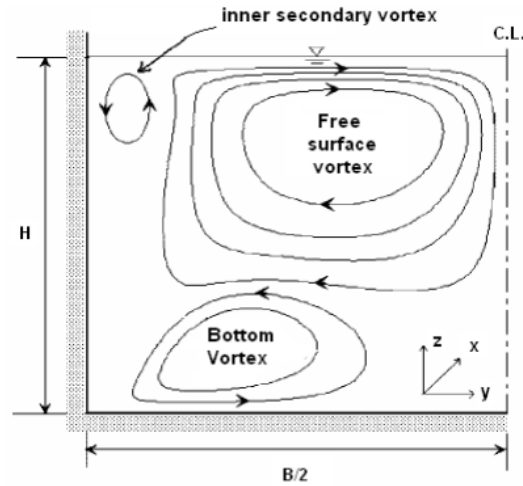
Figure 3.8.2-2: Schematic view of secondary flow in rectangular open channel (Kang and

Choi 2006)

Figure 3.8.2-3 shows the experimental results from Nezu and Rodi (1985) and LES results from Shi et al. (1999), which helped form the basis of the schematic in Figure 3.8.2-2. Again it can be seen that the Delft code results compare closer than those of ANSYS-CFX.
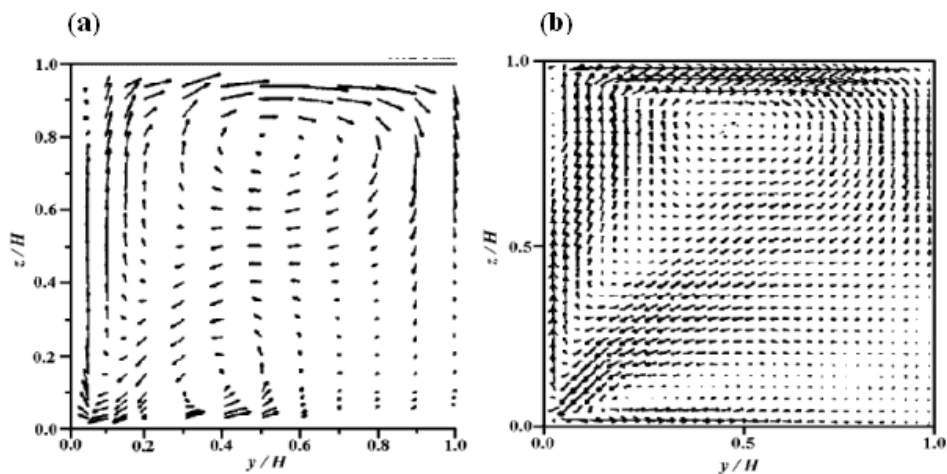
Figure 3.8.2-3: Secondary current vectors (a) experimentally measured (Nezu and Rodi

1985) and (b) computed using LES (Shi et al.1999)

It can be seen from Figure 3.8.2-1 that the location of the free surface vortex predicted by ANSYS-CFX is lower than that of the Delft code, experiment and other LES. This is due to the prediction of the inner secondary vortex, which can be seen to be larger than indicated by Kang and Choi (2006). The over-prediction of this cell has forced the free surface vortex centre down and outward in the ANSYS-CFX LES simulation as the cell cannot move down because it is restricted by the presence of the bottom vortex, which in turns is shifted inward. The bottom vortex seems to be split with the ANSYS-CFX case and two cells are present along the channel bed. The smaller bottom vortex is likely to have formed because the large one has been shifted inward. It seems that there could be a "cascade effect" due to the over prediction of the inner secondary vortex.

3.8.3 Turbulence Intensities

The distribution of turbulence intensities is very important as it contributes to the production and dissipation of vorticity and it is important that the redistribution of turbulence intensity is correctly represented at the free surface and close to solid walls. Therefore the LES results are compared quantatively with previous results (Shi et al. 1999). Figure 3.8.3-1 shows the values of normalised turbulence fluctuations u, v and w for Case 1a. Figure 3.8.3-1(a) compares the ANSYS-CFX LES results to Shi et al. (1999). It can be seen that the turbulence fluctuations v and w correspond well to Shi et al. (1999) as well as the majority of the u profile. However, it can be seen that the streamwise turbulence intensity u, is over-predicted in the ANSYS-CFX LES results. The Delft code results compare more favourably to the results of Shi et al. (1999) as can be seen from Figure 3.8.3-1(b).
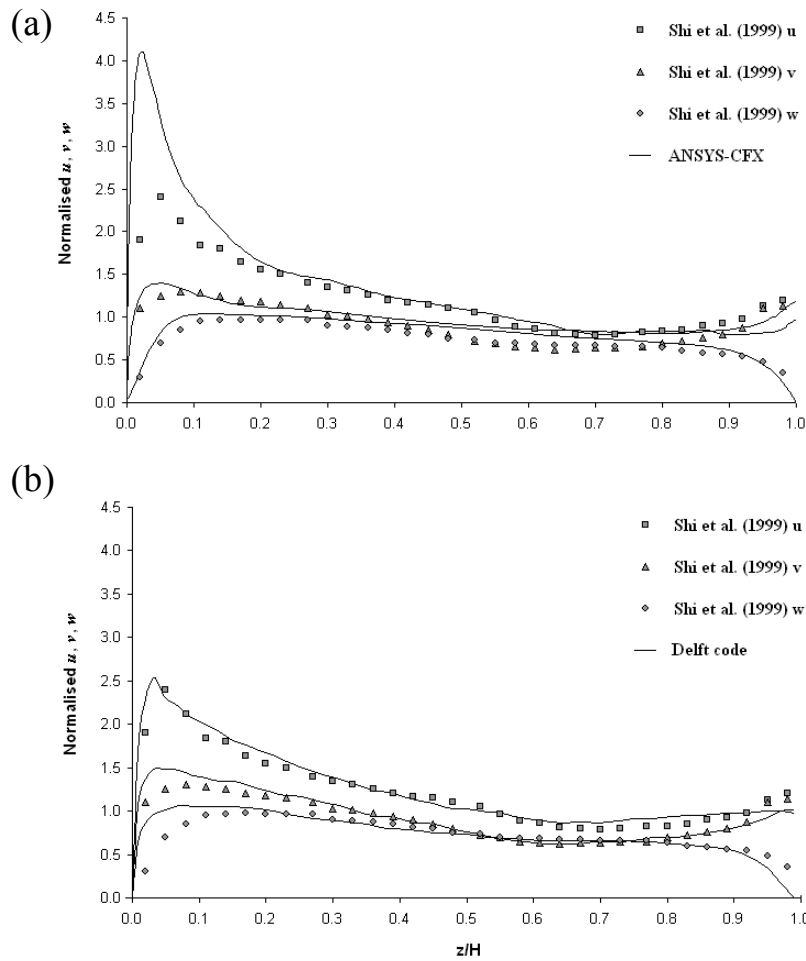
Figure 3.8.3-1: LES computed turbulence fluctuations u, v and w for Case 1a from (a) ANSYS-CFX and (b) Delft code, at the channel centre compared with Shi et al. (1999) LES values

The accuracy of the Delft code results could be due to the use of a wall function within the code, which is not utilised within ANSYS-CFX and allows the use of a coarser mesh in the near wall region. As a wall function is not utilised within ANSYS-CFX the velocity must be computed down to the wall, therefore requiring a very fine mesh in the near wall region. The mesh construction for the ANSYS-CFX results has been shown in Table 3.7-2 and it can be seen that y^+ values are small. However, the streamwise mesh spacing causes large aspect ratios for the cells in the

98

near wall region. The accuracy of the LES could be compromised by large aspect ratios in this region as the sub-grid scale filter width is therefore greatly increased.

3.9 CONCLUSIONS

The Deflt code results overall compare better to experimental and previous LES results than those of ANSYS-CFX for in-bank channels. The normalised velocity and bed shear stress profiles are well predicted by the Delft code and the distribution of secondary circulation cells conforms better to the predictions made by Shi et al. (1999) and Nezu and Rodi (1985) than those of ANSYS-CFX. Both codes predict the vertical velocity profiles away from the free surface, with the Delft code better predicting the velocity dip and velocity profile as the free surface is approached. Turbulence intensities are again predicted better with the Delft code and are over-predicted by up to 50% as the channel bed is approached within ANSYS-CFX. Therefore the next chapter utilises the Delft code to investigate numerous series of in-bank channels.

CHAPTER 4:

4 IN-BANK CHANNELS

4.1 INTRODUCTION

After the analysis of the performance of the LES, the focus of the research turns to rectangular in-bank channel flows. The Delft code was utilized to simulate these channels as it has been shown in Chapter 3 to predict in-bank channel phenomenon more accurately when compared to experiment than ANSYS-CFX.

4.2 CHANNEL GEOMETRY SERIES

Overall 3 channel series are reported in this section.

Series 01 was chosen to coincide with the first set of SKM optimized parameter data, as at this time optimization has only been performed for a limited number of channel cases. The channel cases are reported by Knight et al. (1984) and optimization of f, λ and Γ are detailed in the work of Chlebek and Knight (2006). These channels are of small aspect ratio (AR), ranging from AR =0.99-2.00

Series 02 is a higher aspect ratio series than Series 01. The reason for also performing these simulations is that experimental data available for Series 01 is only in the form of velocity and shear stress data. Therefore, to further compare results such as secondary flow cells the available experimental data of Imamoto and Ishigaki (1988) and Tominaga et al. (1989) were utilized. Two channels are

performed in comparison to Imamoto and Ishigaki (1988) at AR =3 and 5 and one

channel in comparison to Tominaga et al. (1989) at AR =8.

Series 03 is a series of 4 channels at AR =15, 25, 30 and 40. This series does not

compare to any previously reported experimental data. However, Series 01 and 02

will show that the Delft code adequately predicts velocity, shear stress and secondary

circulation patterns; therefore a series of large AR channels was set-up to investigate

the influence of aspect ratio on the aforementioned flow features. The set-up data

used for the above series is shown in Table 4.2-1.

Table 4.2-1: Summary of set-up data for Series 01-03

	CASE	H	B	U_{avg}	τ_{ave}	u_*	R_e	AR
		(m)	(m)	(m/s)	(N/m^2)	(m/s)	-	-
1	1a	0.0760	0.152	0.338	0.360	0.019	57,559	2.00
	1b	0.0970	0.152	0.380	0.404	0.020	72,567	1.57
	1c	0.1136	0.152	0.405	0.432	0.021	82,646	1.34
	1d	0.1530	0.152	0.424	0.481	0.022	96,483	0.99
2	2a	0.0400	0.120	0.250	0.214	0.015	26,888	3.00
	2b	0.0398	0.200	0.382	0.254	0.016	48,736	5.03
	2c	0.0500	0.400	0.397	0.368	0.019	71,218	8.00
3	3a	0.0333	0.500	0.340	0.289	0.017	44,778	15.00
	3b	0.0200	0.500	0.270	0.182	0.013	22,371	25.00
	3c	0.0167	0.500	0.248	0.153	0.012	17,338	30.00
	3d	0.0125	0.500	0.216	0.117	0.011	11,531	40.00

4.3   MESH CONSTRUCTION AND SIMULATION TIME

The mesh construction within the Delft code is summarized in Table 4.3-1 for Series 01-03. There was no need for refinement to the solid boundaries as the first cell to the wall was the same magnitude of that used across the channel cross-section and length.

The Delft code simulations conform to ≥50 LETOTs to obtain a steady state solution for all Series and a further ≥25 LETOTs to gather statistical data for Series 01, ≥110 LETOTs for Series 02 and ≥200 LETOTs for Series 03. The Courant number for all cases was kept below 0.35. The increased time of simulation, particularly for Series 03, is in order to capture adequately a steady state for the secondary circulation cells in the channel centre.

Table 4.3-1: Summary of (a) mesh and (b) simulation details for Series 01-03

(a)

CASE	Length (m)			Number of elements				Mesh spacing (m)			y^+ range		AR	R_e
	x	y	z	x	y	z	Total	Δx	Δy	Δz	y^+	z^+	-	-
1a	0.228	0.152	0.0760	150	100	50	750,000	0.0015	0.0015	0.0015	28.8	28.8	2.00	57,559
1b	0.291	0.152	0.0970	200	100	65	1,300,000	0.0015	0.0015	0.0015	30.5	30.0	1.57	72,567
1c	0.341	0.152	0.1140	230	100	75	1,725,000	0.0015	0.0015	0.0015	31.6	31.5	1.34	82,646
1d	0.459	0.152	0.1530	310	100	100	3,100,000	0.0015	0.0015	0.0015	33.3	33.6	0.99	96,483
2a	0.120	0.120	0.0400	75	75	25	140,625	0.0016	0.0016	0.0016	23.4	23.4	3.00	26,888
2b	0.119	0.200	0.0400	75	125	25	234,375	0.0016	0.0016	0.0016	25.5	25.4	5.03	48,736
2c	0.150	0.400	0.0500	100	300	40	1,200,000	0.0015	0.0013	0.0013	25.6	24.0	8.00	71,218
3a	0.209	0.500	0.0333	100	250	35	875,000	0.0021	0.0020	0.0010	34.0	16.2	15.00	44,778
3b	0.126	0.500	0.0200	65	250	24	390,000	0.0019	0.0020	0.0008	27.0	11.2	25.00	22,371
3c	0.105	0.500	0.0167	50	250	22	275,000	0.0021	0.0020	0.0008	24.8	9.4	30.00	17,338
3d	0.080	0.500	0.0125	40	250	20	200,000	0.0020	0.0020	0.0006	21.6	6.8	40.00	11,531

(b)

CASE	H/u_*	Estimated Simulation Time (sec)			Time step		Actual Time (sec)			LETOT Initial	LETOT Collect	LETOT Total
	(sec)	Initial	Collect	Total	Δt	C_r	Initial	Collect	Total			
1a	4.00	200	100	300	0.0010	0.222	200	100	300	50	25	75
1b	4.83	241	121	362	0.0010	0.261	250	125	375	52	26	78
1c	5.47	273	137	410	0.0010	0.273	300	150	450	55	27	82
1d	6.97	349	174	523	0.0010	0.286	350	175	525	50	25	75
2a	2.73	137	68	205	0.0010	0.156	150	300	450	55	110	165
2b	2.50	125	62	187	0.0010	0.240	150	300	450	60	120	180
2c	2.61	130	65	196	0.0010	0.265	150	300	450	58	115	173
3a	1.96	98	49	147	0.0010	0.162	400	400	800	204	204	408
3b	1.48	74	37	111	0.0015	0.209	480	480	960	323	323	646
3c	1.35	67	34	101	0.0015	0.177	525	525	1050	390	390	780
3d	1.16	58	29	87	0.0015	0.165	525	525	1050	453	453	906

4.4   RESULTS - SERIES 01

Series 01 is compared to depth averaged velocity data of Knight et al. (1984). No experimental secondary circulation data was available for comparison, but algebraic expressions detailing the distribution of secondary circulation cells were derived by Noat and Rodi (1982) for channels of AR <2 and these are used for comparison here.

4.4.1 Velocity Profiles

Figure 4.4.1-1 shows contour plots of normalised velocity for all cases. For cases 1a, 1b and 1c the maximum velocity can be seen to occur below the free surface and comparison of the vertical velocity profiles for these cases in Figure 4.4.1-2 shows that this maximum velocity is predicted to within 5% of the experimentally measured position. Case 1d is not shown in Figure 4.4.1-2 as no experimental data is available for comparison. However, from its contour plots it can be seen that like cases 1a, 1b and 1c the maximum velocity does occur below the free surface at z =0.055, but also at a second location close to the free surface, due to the secondary flow cell distribution. All contour plots are taken in the y-z plane half way along the channel length and are done so throughout the rest of this chapter. Figure 4.4.1-2 also highlights one interesting feature with regard to the vertical velocity distribution close to the channel walls as the free surface is approached. For case 1a, 1b and 1c the vertical velocity seems to increase at z ~60, 80 and 100mm respectively within the relative y =7mm profiles and then decreases at z ~70, 90 and 110mm. This increase is due to the existence of a small secondary current cell observed at the wall/free surface corner, which is further discussed in Section 4.5.6.
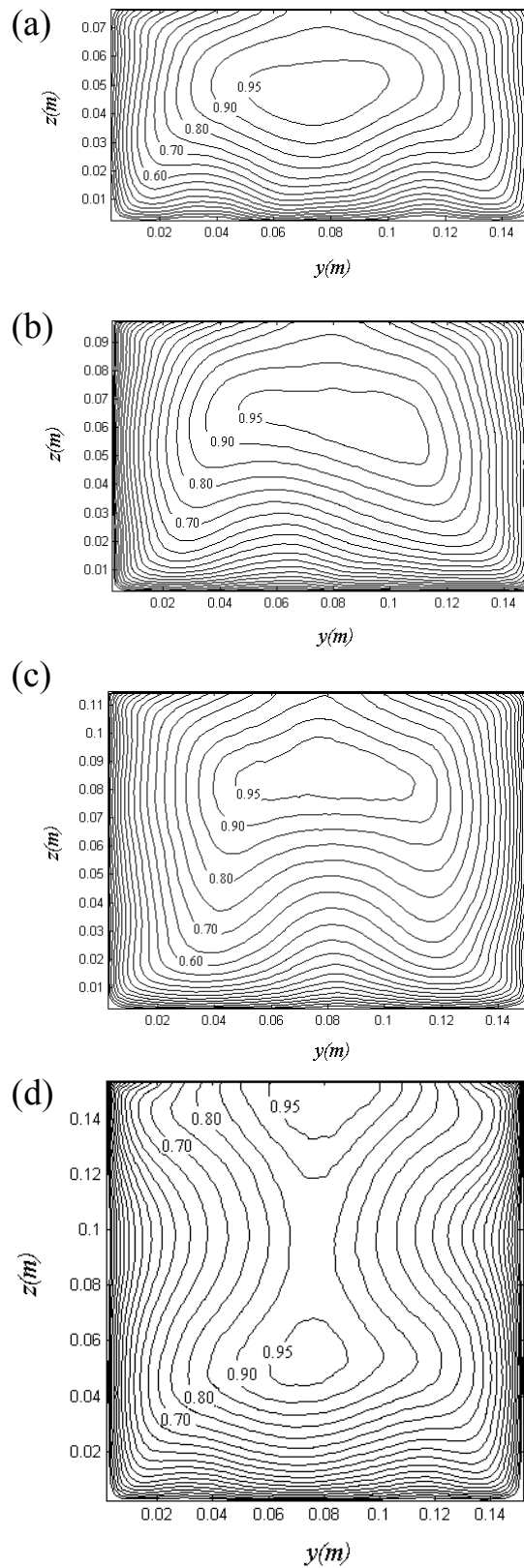
Figure 4.4.1-1: LES derived normalised velocity, $U_d / U_{\max x}$, contours for Series 01, case

(a) 1a, (b) 1b, (c) 1c and (d) 1d taken in the y-z plane half way along the channel length

(a)

Experiment — LES

(b)

(c)
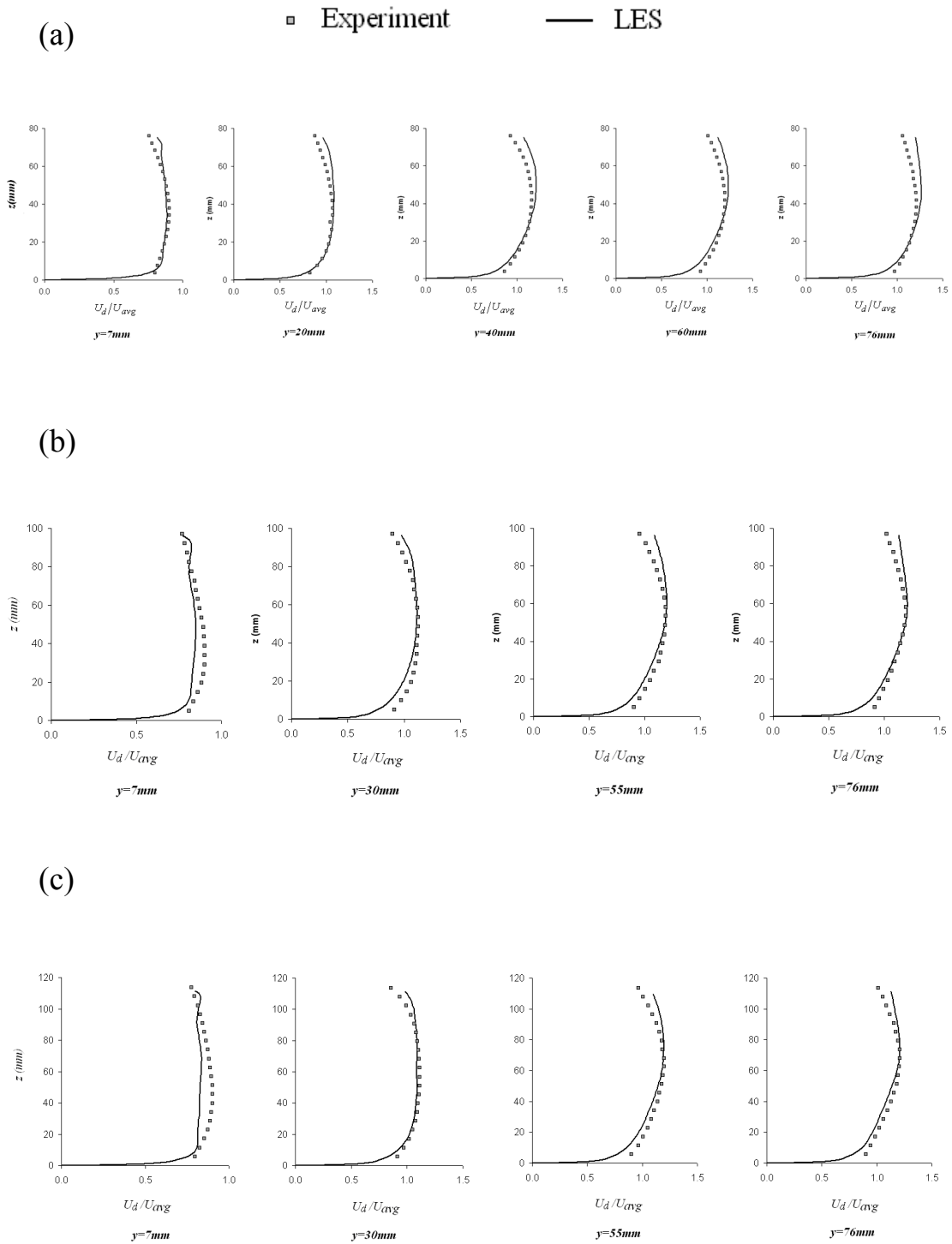
Figure 4.4.1-2: LES derived vertical velocity profiles for Series 01, case (a) 1a, (b) 1b and

(c) 1c compared to experiment (Knight et al. 1984)

4.4.2 Flow Structures

Figure 4.4.2-1 shows plots of time-averaged velocity. Limited experimental visualisation data is available to compare against for the distribution of secondary circulation cells for cases 1b-1d. However, Naot and Rodi (1982), derived algebraic expressions for the secondary motion and from their application to open channels of varying aspect ratio concluded that when AR decreases below 2, the lower, corner induced bottom vortex grows and eventually becomes the dominant one, which can be seen to happen within these results. The results from Naot and Rodi (1982) were not compared directly with any results and the accuracy of the prediction of the secondary current cells was based solely on the realistic simulation of the depression of the velocity maximum below the surface. However, the Delft code LES results compare well to this prediction.

In order to investigate the accuracy of the predicted secondary circulations further, their influence upon the boundary shear stress is examined (Figure 4.4.2-2). From Figure 4.4.2-2 it can be seen that case 1a shows an increase in bed shear stress at the channel centre and depressions in the profile at y/B=0.2 and 0.8. An increase in bed shear stress is observed due to the rotation of the free surface vortices in Figure 4.4.1-1 transferring high momentum fluid from the free surface down through the channel centre line to the channel bed. The depressions in the profile are due to the bottom vortices causing lift as they rotate along the channel bed from the channel corner to the centre line, but rising from the bed at approximately y/B=0.2 and 0.8.
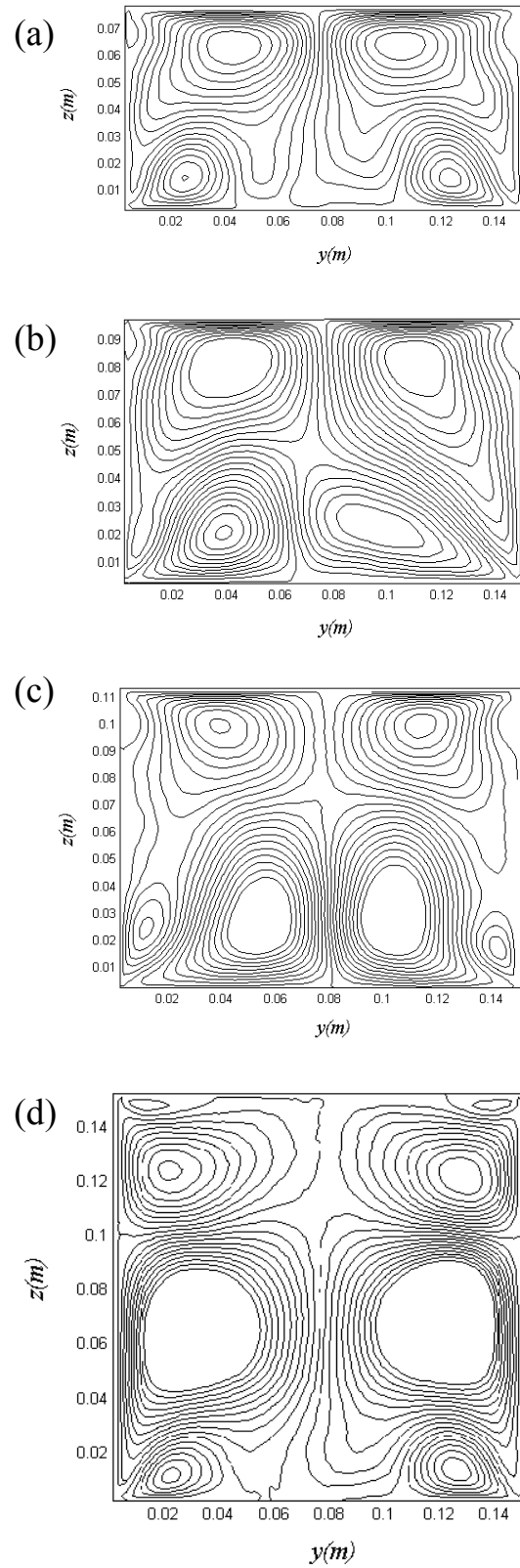
Figure 4.4.2-1: LES derived streamline plots of time-averaged velocity for Series 01, case

(a) 1a, (b) 1b, (c) 1c and (d) 1d taken in the y-z plane half way along the channel length

108
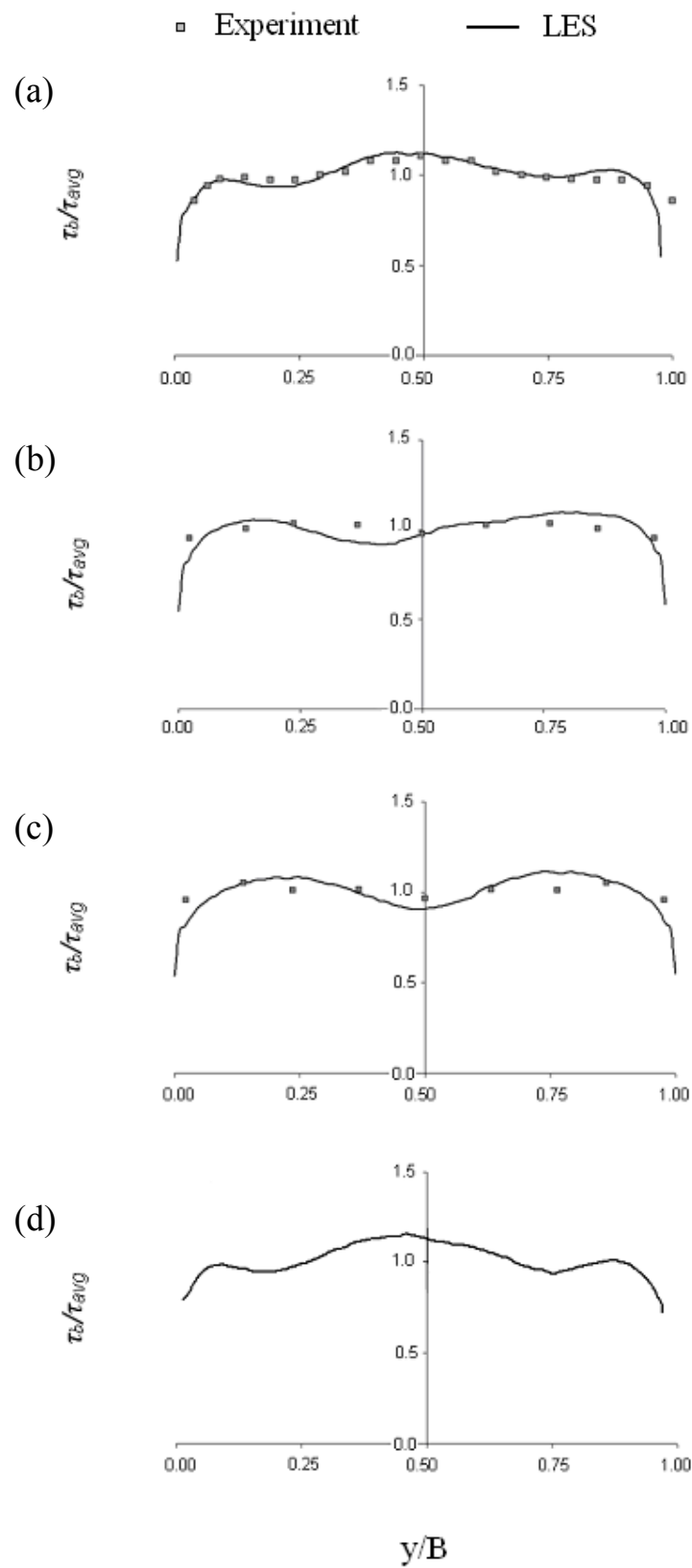
Figure 4.4.2-2: LES derived bed shear stress profiles for case (a) 1a, (b) 1b, (c) 1c and (d) 1d compared to experimental data (Shi et al. 1999; Knight et al. 1984)

For cases 1b and 1c a decrease in bed shear at the channel centreline is observed. This corresponds to the presence of bottom vortices which unlike case 1a now extend out to the channel centre. This coincides well with experimentally measured results of Shi et al. (1999) for case 1a and Knight et al. (1984) for cases 1b and 1c. As the channel *AR* decreases and case 1d is examined neither an increase nor a decrease in the shear stress profile is apparent at the channel centre from simulation results. Experimental shear stress data was unavailable for comparison with case 1d.

4.4.3 Inner Secondary Flow Cell

The secondary circulations of cases 1a-1d have been discussed in Section 4.4.2. However, other than the bottom and free surface vortices that were discussed, reports on the existence of inner secondary currents at the juncture of the free-surface and sidewall in a rectangular channel have also been made.

In recent years the turbulence associated with the horizontal flow of water along a vertical wall in the vicinity of a horizontal free surface, the mixed-boundary corner, has received much attention. Work includes experimental studies such as Grega et al. (1995), Longo et al. (1998) and Hsu et al. (2000), and LES work by Thomas and Williams (1995a; 1995b), Streedhar and Stern (1998) and Shi et al. (1999). A fundamental issue yet to be resolved however, is the exact nature of the secondary flows. There appears to be consensus regarding the existence of some sort of streamwise vortex in the near corner region. However, the size, strength and even sense of rotation has not been established, probably due to the differences between the reported studies. Grega et al. (1995) and Hsu et al. (2000) hypothesized a

working model of secondary flows formed in the mixed boundary corner, Figure 4.4.3-1.
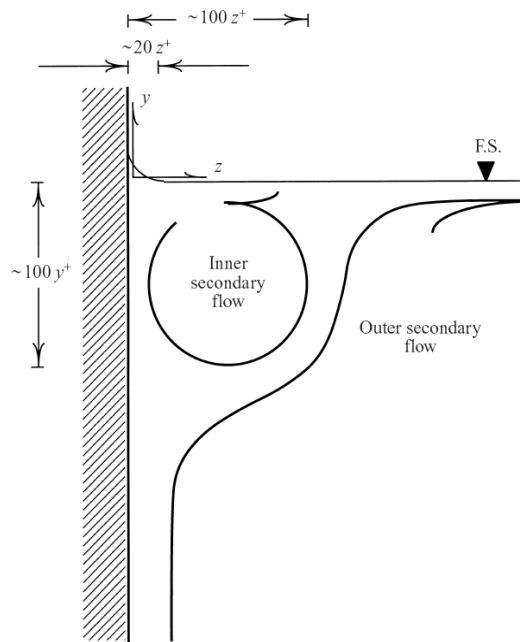
Figure 4.4.3-1: Schematic drawing of the hypothesized secondary flow patterns in a mixed-boundary corner (Grega et al. 1995)

The results from Grega et al. (1995) and Hsu et al. (2000) were, however, obtained in planes parallel to the free surface, resulting in insufficient resolution in the free surface normal direction to conclusively map the inner secondary flows. Therefore, Grega et al. (2002) performed high-resolution Digital Particle Image Velocimetry (DPIV) measurements to provide the first known direct mapping of these secondary flows.

As mentioned, Hsu et al. (2000), Grega et al. (1995, 2002) and also Longo et al. (1998) have performed experimental investigation, but limited numerical analysis in the form of LES has been performed by Thomas and Williams (1995a; 1995b) and Streedhar and Stern (1998). It should be noted that the quality of the latter results

has been questioned by Hsu et al. (2000). The interested reader is referred to Hsu et al. (2000) for a more in depth comparison and discussion of the above works.

One way to examine the inner secondary current cell is to examine the wall shear stress distribution. Researchers such as Broglia et al. (2003) and Kang and Choi (2006) computed values of wall shear stress and noted a rapid increase in shear stress values for z/H>0.9, with the shear stress at the free surface being approximately 60% higher than the mean value in the central region of the shear stress profile. They attributed this to the inner secondary currents occurring at the juncture of the free surface and sidewall. That is, the inner secondary currents transfer high momentum from the centre to the sidewall near the free surface. Grega (1995) and Broglia et al. (2003) confirmed this through laboratory experiments and LES. However, this phenomenon was not observed by researchers such as Cokljat (1993), Shi et al. (1999) and Nezu and Rodi (1985).

The wall shear stress is shown in Figure 4.4.3-2 for case 1a. The results are compared to experiment (Nezu and Rodi 1985) and other simulated data sets. The Delft code profile can be seen to sit well between all data sets and no increase in wall shear near the free surface is observed. However, if the Delft code profile is isolated (Figure 4.4.3-3) and compared only with the results of Shi et al. (1999) it can be seen further that although in good agreement with the simulated data for the majority of the profile there is a slight increase (z/H =0.9) in the wall shear compared to Shi et al. (1999) as the free surface is approached. However, this is not as high as 60% of the mean profile as observed by Broglia et al. (2003). The wall shear stress distributions for all cases in Series 01 show an increase in wall shear as the free

112

surface is approached, indicating an inner secondary circulation cell that transfers high momentum fluid from the centre to the side-wall near the free surface, agreeing with the sense of rotation predicted by Grega et al. (1995).

It should also be noted that the other published LES differ from each other, with Shi et al. (1999) agreeing more with experimental and other numerical results than Broglia et al. (2003).

The LES results show an increase in shear stress at the channel wall/free surface corner. This shear stress is only approximately 5%-10% larger than the average wall shear stress, however, unlike some previously reported data an increase is shown. The sense of rotation also corresponds to that predicted by Grega et al. (1995).
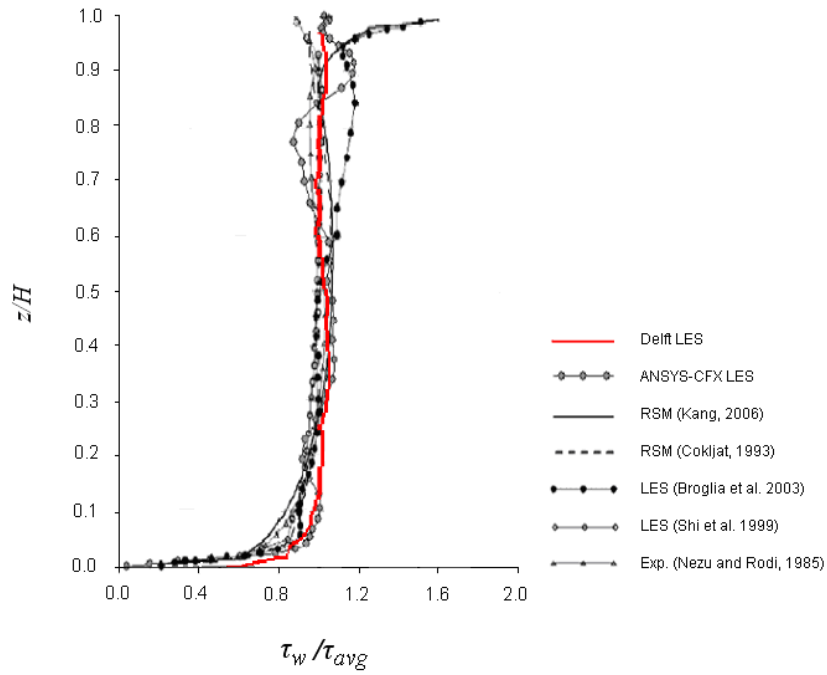
Figure 4.4.3-2: LES derived sidewall shear stress distribution for case 1a compared to

numerous experimental and simulation results.
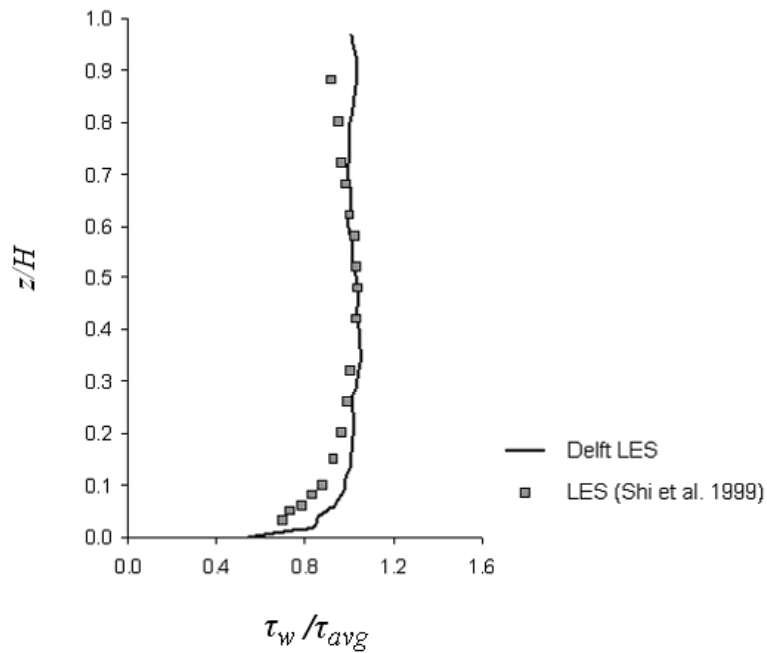
Figure 4.4.3-3:LES derived sidewall shear stress distribution for case 1a

4.5   RESULTS - SERIES 02

To further investigate rectangular open channel flows a second series of channels has been simulated for higher aspect ratios than simulated in Series 01.   Series 02 comprises 3 channels of AR =3, 5 and 8.   The results are compared to the experimental results of both Imamoto and Ishigaki (1988) and Tominaga et al. (1989).   These channels were chosen due to the experimental velocity and secondary circulation data available for comparison.   All of the 3 cases are converged to within 5% of the experimentally measured body force and discharge.

4.5.1   Velocity Profiles and Flow Structures

Figure 4.5.1-1 to Figure 4.5.1-3 show contour plots of velocity and vector potential for all three channels.   It can be seen that as the aspect ratio increases the velocity 'dip' phenomenon effect decreases.   Figure 4.5.1-3 also shows vertical velocity profiles for case 2c to highlight further the lack of velocity 'dip' throughout the channel as the velocity profiles can be seen to be almost normal to the free surface. The maximum velocities can be seen to occur at approximately z =0.03mm (z/H =0.75) for cases 2a and 2b, which corresponds to 0.2-0.3 H below the free surface for channels of AR <~5, even on the centreline of the channel (Tominaga et al. 1989).   On the other hand, for case 2c the maximum velocity occurs slightly below the free surface. This is due to the decelerated region near the free surface only extending to y/H =~2.5 (y =0.125m), not to the channel centre as in cases 2a and 2b. The decelerated region corresponds well with the free surface vortex as shown in Figure 4.5.1-3. In the region about 0.8 H (y =0.032m, 0.032m and 0.04m respectively) away from the sidewall, near the bed at AR >2 the isovels bulge

towards the free surface as is seen in cases 2a to 2c, (Figures 4.6-1 to 4.6-3). This is due to the bottom vortex, as it can be seen from the corresponding plots that all of these vortices extend to approximately $0.8H$.

The secondary circulation patterns will not be examined in detail, but the distribution of cells corresponds well to experimental results; where Imamoto and Ishigaki (1988) observed two major longitudinal vortices, one at the free surface and the other near the channel corner along the bed. Also, Naot and Rodi (1982) concluded that as the channel width increases the upper free surface vortex grows in strength and dimension thereby suppressing the growth of the lower vortex, which can be seen in all cases. It was also observed that there was little difference between cases of $AR = 4$ and 6, as in both cases the upper vortex occupied a $2H$ wide space next to the channel sidewall. This could be concluded as being the case for case 2a, as the cell can only stretch to $1.5H$ and for case 2b the upper vortex extends to the channel centre ($2.5H$). It can also be seen that the free surface and bottom vortices are separated by a horizontal plane at approximately $z/H = 0.5$ for all 3 cases, which corresponds well to the location of about $z/H = 0.6$ specified by Tominaga et al. (1989).
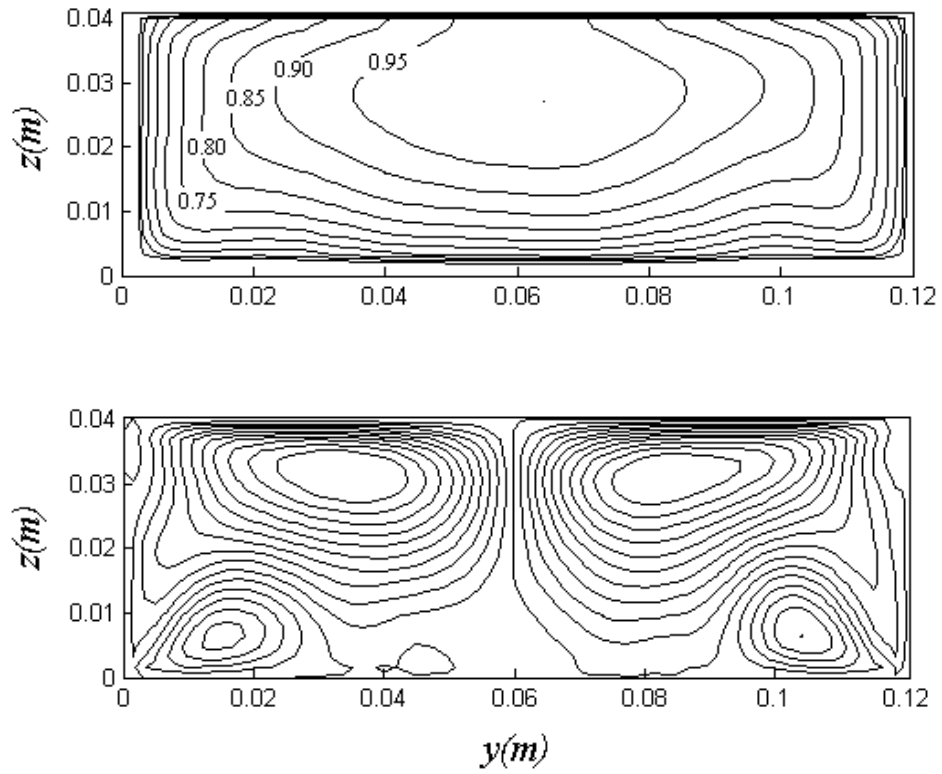
Figure 4.5.1-1: LES derived contour plots of velocity and longitudinal component of

vorticity for case 2a
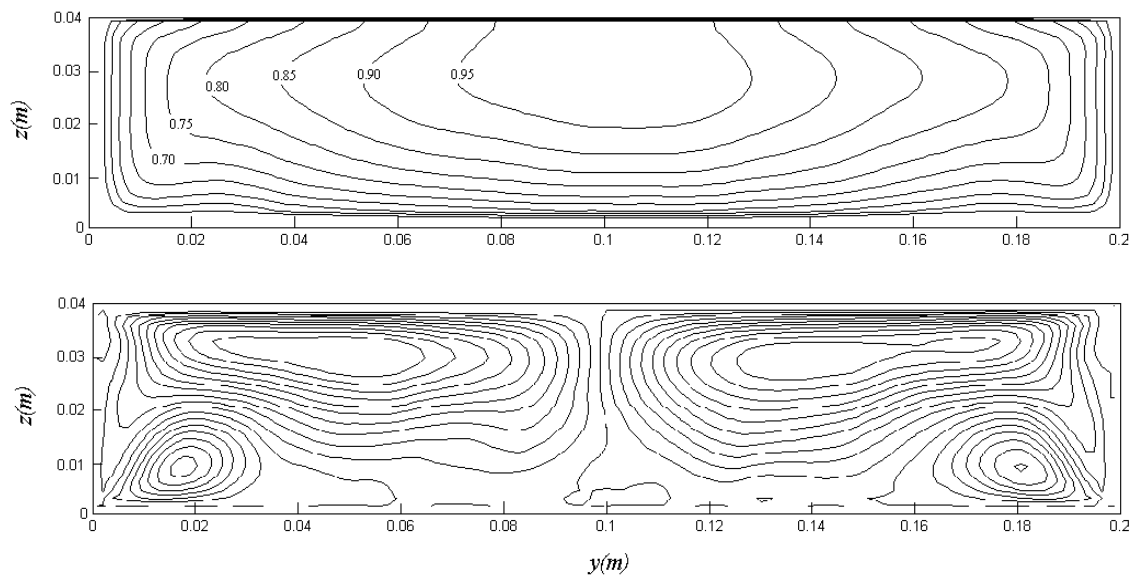
Figure 4.5.1-2: LES derived contour plots of velocity and longitudinal component of

vorticity for case 2b
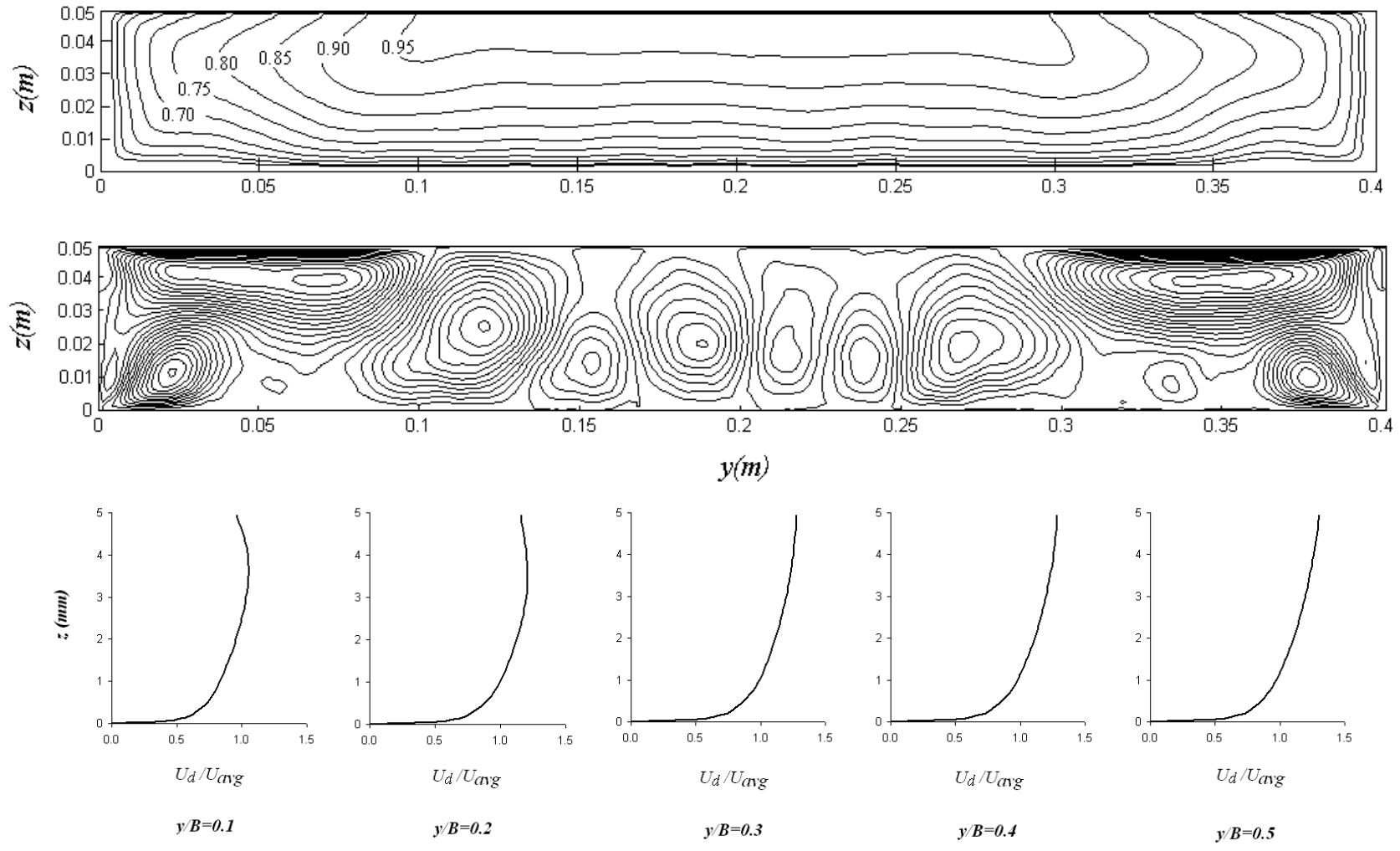
Figure 4.5.1-3: LES derived contour plots of velocity and longitudinal component of vorticity for case 2c

No experimental bed shear stress data is available for comparison for Series 02. However, channels of AR =4.8, 5.5, 7.4, 8.5, and 9.3 were performed experimentally by Omran et al. (2008). Based on the similar aspect ratio of these experimental cases to cases 2a, 2b and 2c these are used for comparison. Normalised depth averaged velocity profiles are shown below.

$\triangle$ $AR=4.8$ $\diamond$ $AR=5.5$ $\blacktriangle$ $AR=7.4$ $\blacksquare$ $AR=8.5$ $\ast$ $AR=9.3$ —— LES

(a)

(b)

y/B
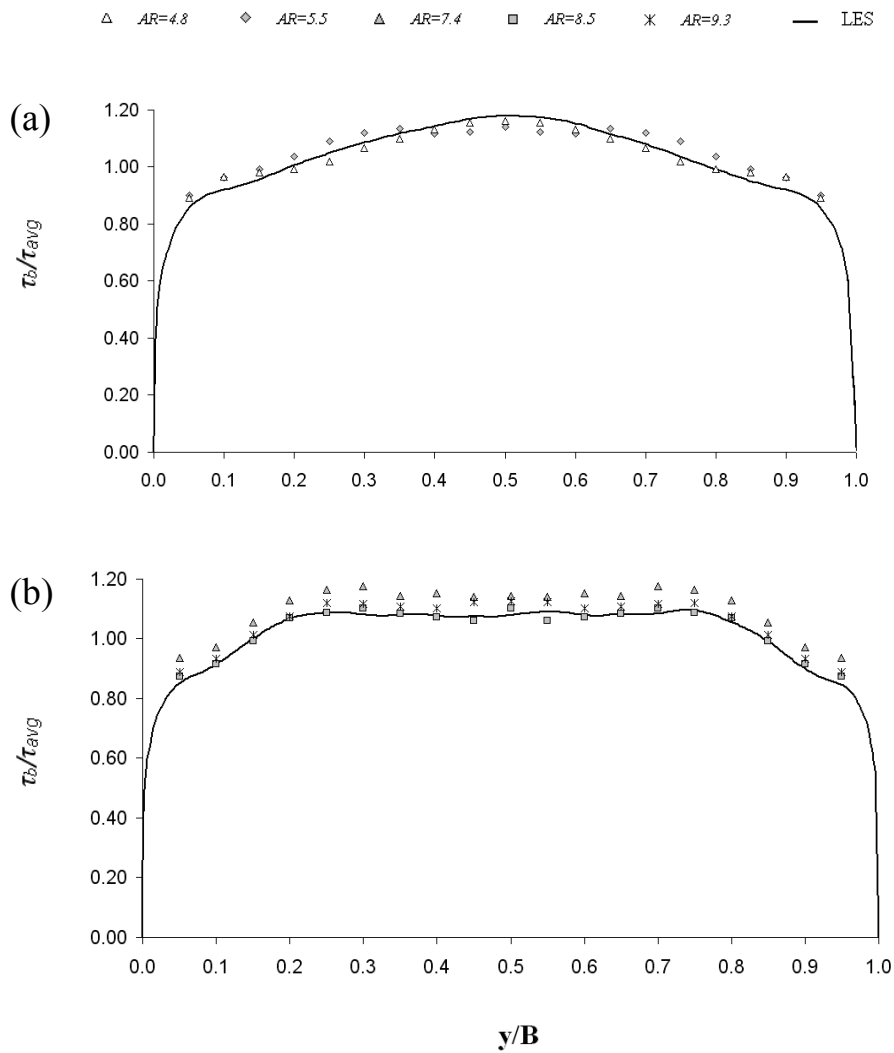
Figure 4.5.1-4: LES derived bed shear stress profiles for cases (a) 2b and (b) 2c compared to experimental data (Omran et al. 2008)

The LES profiles in both cases compare well to experiment, with peaks and troughs being well simulated by the Delft LES code, again highlighting the accurate simulation of secondary circulation cells within the LES.

4.6 RESULTS - SERIES 03

The last series of channels is of AR =15, 25, 30.and 40. As has been stated these channels have been simulated in order to investigate the affect of aspect ratio on the cellular secondary currents. Previous literature, such as Kinoshita (1967) has shown that lines of boils form periodically in the transverse direction, consisting of low speed streaks and high sediment concentration. The spanwise spacing between boil lines was found to be nearly equal to twice the flow depth. On the basis of field observations of sand ribbons and ridge patterns Nezu et al. (1985) inferred multicellular secondary currents as in Figure 4.5.1-1.
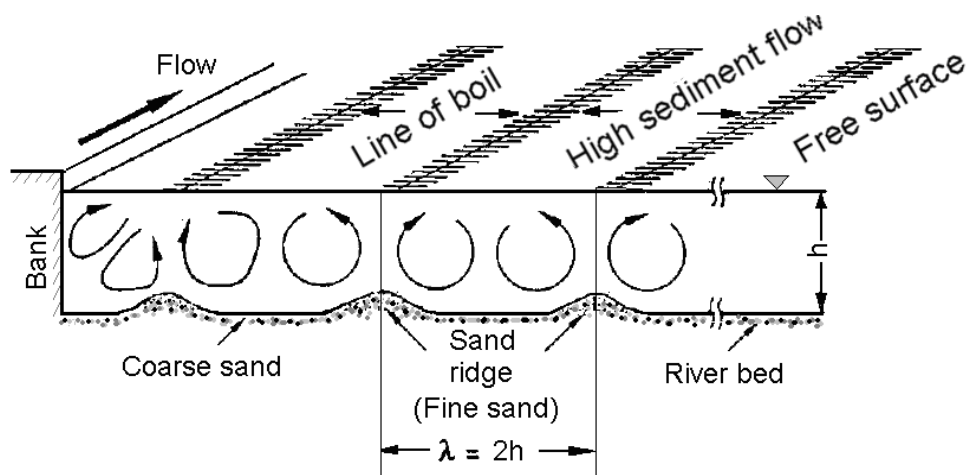
Figure 4.5.1-1: Inferred pattern of multicellular secondary currents (Nezu et al. 1985)

Time averaged secondary current patterns are not readily identified and this is highlighted in Figure 4.5.1-3, where contour plots of velocity and secondary circulations can be seen. Nezu and Rodi (1985) remarked that when $AR \geq 5$, time

averaged secondary current patterns are not readily identified, but instantaneous patterns do exist. It can be seen from the results reported in Section 4.5.1 that time averaged secondary circulation plots of channels at $AR = 5$ and 8 can clearly be seen so this section investigates even larger aspect ratio channels. Naot and Rodi (1982) also stated that for large aspect ratio channels further right of the free surface vortex, which extends to ~$2H$ from the channel side wall, there are only rather small secondary motions present, having little influence on the longitudinal velocity. From Section 4.6, classing case 2c as a large aspect ratio channel, it can be seen that the free surface vortex does extend to ~$2H$ (y =0.1m).

Figure 4.5.1-3 and Figure 4.5.1-4 show contour plots of normalised velocity and streamwise vorticity for cases 3a and 3b respectively. It can be seen that case 3a shows strong vortices in the channel corners and near the channel sidewalls compared to weaker secondary motions as the channel centre is approached. Secondary flow cells are still observed, but are weak in comparison to the corner vortices. This is also true for case 3b, with only very weak structures observed in the channel centre. This is true for cases 3c and 3d, with very weak secondary flow cells being observed in the channel centre.

As the channel aspect ratio increases it can be seen from the likes of Figure 4.5.1-3 that distinguishing between secondary circulation cells in the central region of the channel becomes difficult. However, seeing as the secondary circulation cells impact the velocity and boundary shear stress distributions, plots of both have been examined to infer information on the distribution of secondary cells. Plots of bed shear stress were found to be unsteady and no easily distinguishable features could

be observed, therefore only velocity profiles are presented. Figure 4.5.1-2 shows the velocity distribution for case 3a, with the grey dotted vertical lines representing a spacing of H from the channel sidewall. The first vertical line is placed at $y/H = 0.8$ to coincide with the bottom vortex as mentioned in Section 4.5.
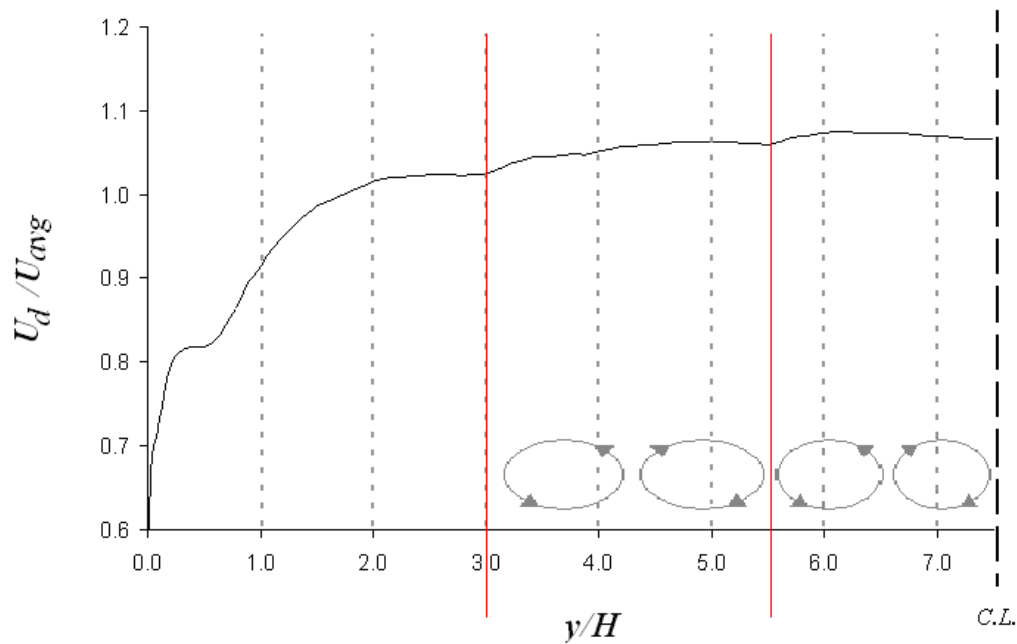
Figure 4.5.1-2: LES derived velocity profile for case 3a
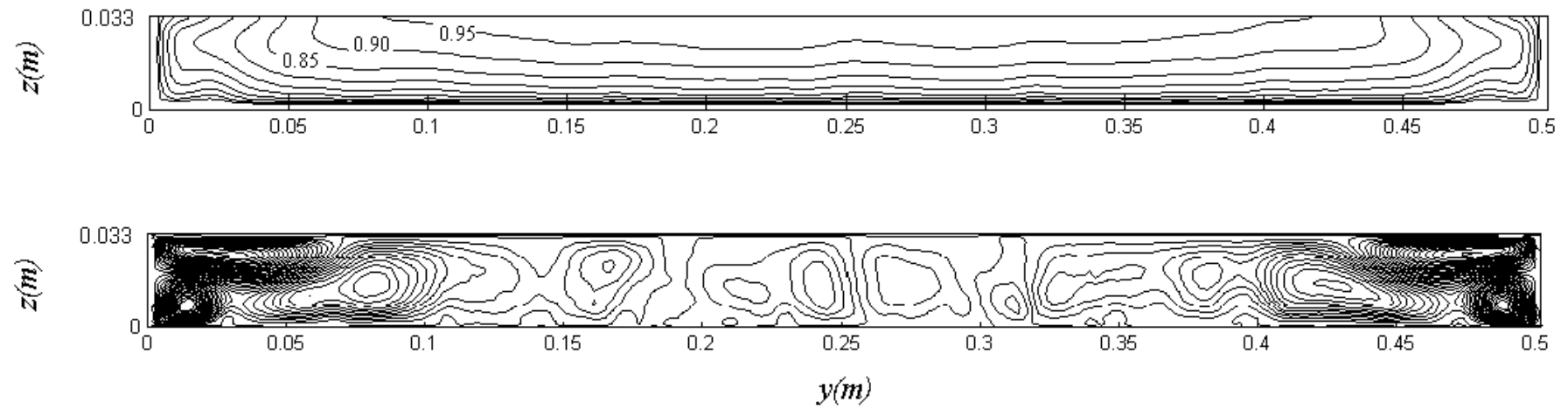
Figure 4.5.1-3: LES derived contour plots of velocity and longitudinal component of vorticity for case 3a
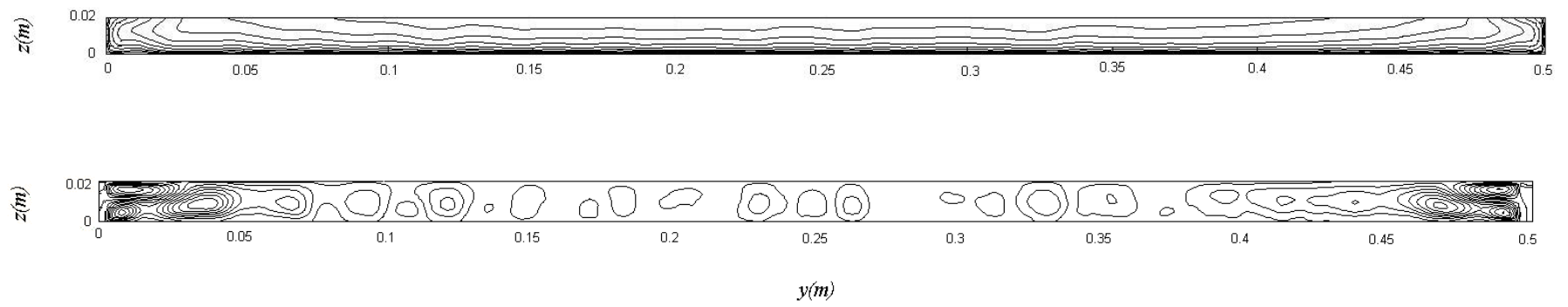
Figure 4.5.1-4: LES derived contour plots of velocity and longitudinal component of vorticity for case 3b

The effect of the secondary circulations can clearly be seen on the velocity profile and based on the peaks and troughs in the velocity profile a schematic of the cell distribution has been overlain on Figure 4.5.1-2. Inclusive of the 3 secondary cells in the near wall region and if the schematised cells are assumed correct, 7 cells are observed in total within half the channel section. The spacing between cells in the region $y/H = 3 - 7.5$ is between $2 - 2.5H$, which corresponds to the prediction of Nezu et al. (1985). As the channel is of $AR = 15$, with a cellular spacing of $2H$ either 7 or 8 cells should be expected and 7 cells have been predicted. Figure 4.5.1-5 shows the velocity distribution for case 3b. Again secondary cells are inferred from the velocity profile. This time, it is very hard to schematise any cells in the region $y/H = \sim 8$. However, even for such a large aspect ratio channel as case 3b, the estimation of $2H$ spacing by Nezu et al. (1985) is again accurate.
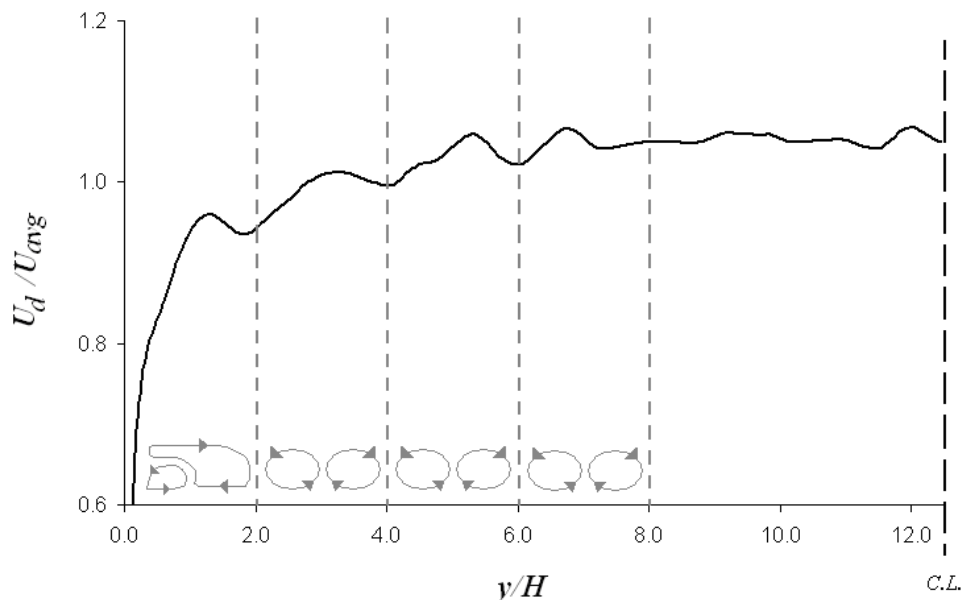
Figure 4.5.1-5: LES derived velocity profile for case 3b

The prediction of secondary circulation cells in the central region of a large aspect ratio open channel is very difficult and some attempt has been made in this section to examine their distribution, either through direct visualisation or analysis of their effect on velocity profiles. All cases reported have been shown to compare well to experimental data. Even in the central region of the channel the effects of the secondary circulations are observed to impact on the velocity profile, and from these profiles secondary circulations can be interpreted. The secondary circulation cell closest to the channel wall is show to impact on the velocity profile most, with the secondary cells becoming weaker as the channel centre is approached. Bed shear stress distributions have not been presented as extracting secondary circulation patterns from these profiles was difficult.

4.7 SKM PARAMETERS

From the simulation results the three SKM parameters, f, λ and Γ were computed. These were computed for all Series 01-03, with the results from Series 01 being compared with the work undertaken by Chlebek and Knight (2006), previously discussed in Section 2.6.3 and herein in referred to as C&K.

To compute the SKM parameters from the simulation, data was extracted along a set of vertical lines at numerous locations across the channel cross-sections. For each of these lines values of velocity, Reynolds stress and velocity correlation values were depth averaged and then used to calculate f, λ and Γ. (Equations 2.6.7, 2.6.9 and 2.6.11). Cross-sectionally averaged values were then obtained by further lateral averaging of the depth-averaged values.

4.7.1 RANS Simulations

As has been stated, Series 01 will be compared with C&K optimisation results. It is worth re-iterating at this point that the optimisation results are produced for a one-panel average, where a one-panel average value corresponds to an average value representative of half the channel cross-section. Consequently, in deriving a one-panel average value from the LES results by time and cross-sectional averaging, the transient nature of the LES is to some extent ignored. Therefore, in view of the ability of RANS to capture bulk flow features it was thought sensible to also compare RANS results to those of the LES and optimisation. Details of the RANS simulations are given within the next sections.

4.7.1.1 Boundary Conditions

The computational domains for $k - \varepsilon$, SSG and LRR models were set up in the same way as that of the LES, with translational periodic boundaries in the streamwise direction of the flow, allowing the values on the inlet and outlet boundaries to coincide.   Pressure gradients were also specified across the domains to drive the flows.   The pressure gradients were computed as in Equation 3.4.   To initialise the flow inlet velocities the same as those of the LES were imposed on the inlet plane.

The free surface implementation was in the form of a symmetry plane imposing the constraint that the flow was mirrored on either side. The normal velocity component and the scalar variable gradients at the symmetry plane boundary were set to zero. All other walls were specified as no-slip.

4.7.1.2 Mesh Construction

The domains consisted of two mesh cells in the streamwise direction with the mesh constructed of structured hexahedral cells with mesh refinement at no-slip walls. The boundary layer meshes were created by specifying a first cell height to produce an adequate y^+ range across the no-slip boundaries and a growth factor of 1.10 for 10 layers. The mesh details are tabulated in Table 4.7-1.

Table 4.7-1: Summary of RANS mesh details.

CASE	Number of elements			
	Total	x	y	z
1a	25,600	2	160	80
1b	32,000	2	160	100
1c	38,400	2	160	120
1d	51,200	2	160	160

4.7.1.3 Solver Criteria and Simulation Convergence

A steady state simulation was specified and advection fluxes were evaluated using a high resolution advection scheme that is second order accurate and bounded. Regarding time stepping, ANSYS-CFX uses a pseudo time stepping scheme even for steady state simulations. The time step in these cases was specified using the automatic time step calculation algorithm provided within the software for the initial iterations (of the order of 100 iterations). A user specified value was then used for the remainder of the simulation, speeding up the rate of convergence.

For solution convergence a root mean square residual target convergence criterion for the equation residuals was tightly set as $\leq$1e-08 for all cases. The results from the RANS simulations are summarised in Table 4.7-2 and are compared with theoretical and experimental values. It should be acknowledged that the numerical set up employed here should guarantee agreement between the numerical average shear stress and the theoretical value. However, it is encouraging seeing this agreement in Table 4.7-2 and the close agreement with the value recorded in experiment. The simulated cross-sectional average velocities and boundary shear stresses compare to within 0.5% of the experimental values.

4.7.1.4 Smooth/Rough Wall implementation

The RANS simulations were firstly performed with a smooth wall implementation, (based on the description of the experiments). However, this resulted in a discharge over-prediction of between 8% and 20%, therefore roughness was introduced on the channel boundaries to retard the flow. For rough walls, the logarithmic velocity profile near the wall still exists, but moves closer to the wall. Roughness effects are

accounted for by modifying the expression for u^+ (Equation 3.15). Only the rough wall simulation results are tabulated in Table 4.7-2 as all RANS derived SKM parameters were obtained from the rough wall simulations, not the smooth wall results.

Table 4.7-2: Summary of RANS results

CASE	Turbulence Model	Roughness Height	τ_{ave}	U_{avg}	Q	y^+ range	
	-	(mm)	(N/m^2)	(m/s)	(l/s)	min	max
1a	Experiment	smooth	0.36	0.34	3.90	-	-
	k-epsilon	0.370	0.36	0.34	3.91	8.55	18.42
	SSG	0.467	0.36	0.34	3.91	13.16	21.22
	LRR	0.148	0.36	0.34	3.91	10.05	23.34
	Theory	-	0.36	-	-	-	-
1b	Experiment	smooth	0.40	0.38	5.60	-	-
	k-epsilon	0.230	0.40	0.38	5.58	9.08	19.64
	SSG	0.285	0.40	0.38	5.62	11.98	18.97
	LRR	0.114	0.40	0.38	5.62	10.45	23.34
	Theory	-	0.40	-	-	-	-
1c	Experiment	smooth	0.43	0.41	7.00	-	-
	k-epsilon	0.169	0.43	0.41	7.02	9.36	20.38
	SSG	0.212	0.43	0.41	7.02	12.38	19.51
	LRR	0.104	0.43	0.41	7.02	10.66	23.94
	Theory	-	0.43	-	-	-	-
1d	Experiment	smooth	0.48	0.42	9.85	-	-
	k-epsilon	0.234	0.48	0.42	9.88	9.36	21.74
	SSG	0.284	0.48	0.42	9.88	12.59	20.40
	LRR	0.196	0.48	0.42	9.88	10.66	25.52
	Theory	-	0.48	-	-	-	-

4.7.2 Friction Factor, f

The LES derived lateral distribution of friction factor, f, was computed and cross-sectionally averaged values obtained. Averaged values for the varying channel heights can be seen in Table 4.7-3. The trends in the Delft code results compare with the values obtained from optimisation as the friction factor decreases as the channel height increases. However, Table 4.7-3 also shows the %error in the LES results when compared to optimisation and it can be seen that the LES results under-predict the friction factor. The friction factor is based solely on the velocity and bed shear stress prediction and as the velocity is over-predicted within the LES this impacts the derivation of f and is the reason for this under-prediction.

Table 4.7-3: Cross-sectionally averaged friction factor results for Series 01

CASE	f C&K	f LES	% Error
1a	0.022	0.0203	-7.7%
1b	0.020	0.0187	-6.5%
1c	0.019	0.0175	-7.8%
1d	0.019	0.0162	-14.7%

The RANS simulation set-up, however, ensured that the discharge and body force were within 0.5% of experiment, consequently meaning that the derived friction factor should match closely that derived from optimisation (again remembering that the lateral variation of the RANS profile does not have to correspond exactly to experiment as only a one-panel average is being computed at present). Figure 4.7.2-1 shows the computed f values from the k-ε, LRR and SSG simulations.

It can be seen that all the results are in good agreement with C&K values, with the *k-ε* model results comparing very well to C&K one-panel values. The accuracy of the values also seems to increase with increased channel depth and the maximum variation in values occurs for the shallower, $H = 76$ mm case. It can be concluded that from the good agreement between the $k - \varepsilon$ model predictions and C&K values, that the anisotropy and transient nature of the flow is not significant for the prediction of f which can therefore be predicted well using the less computationally demanding turbulence models. However, it must be noted that this stage is where the usefulness of the $k - \varepsilon$ model predictions ends, as only the f parameter can be computed.
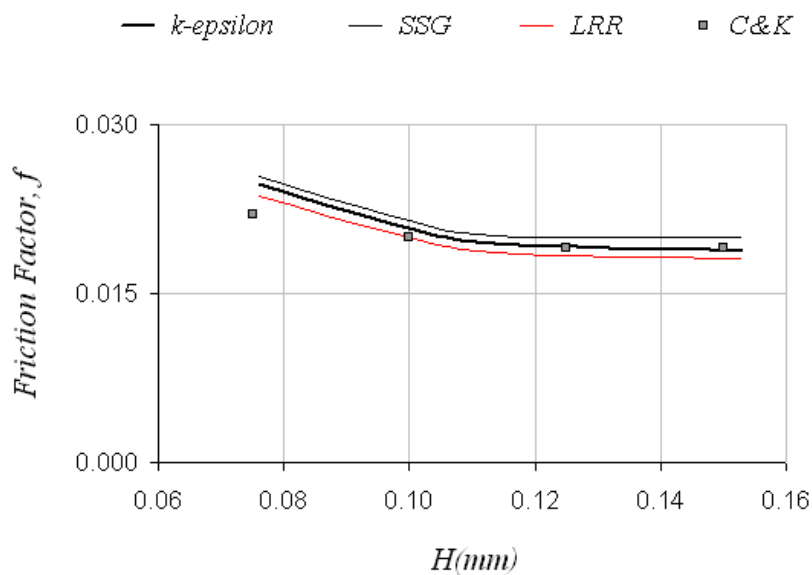
Figure 4.7.2-1: RANS derived friction factors compared to C&K values

Also, if the cross-sectional average values of velocity and shear stress in Table 4.2.1 are utilised then values of f are computed as 0.0252, 0.0224, 0.0211 and 0.0214 respectively. These can be easily computed using Equation 2.6.11. However, all of

the above negates the lateral variation of f. The lateral variation of f derived from the LES results for Series 01 can be seen in Figure 4.7.2-2.

This shows that in general the profiles decrease as the channel height increases and the average across the section is strongly influenced by the increase of f at the channel side wall. With adequate prediction of average velocity and wall shear the friction factor can be easily predicted. This is highlighted by the RANS and $k - \varepsilon$ model results, but the variation of f and its influence on the analytical solution of the SKM does change the prediction of the velocity profile and this is harder to predict.
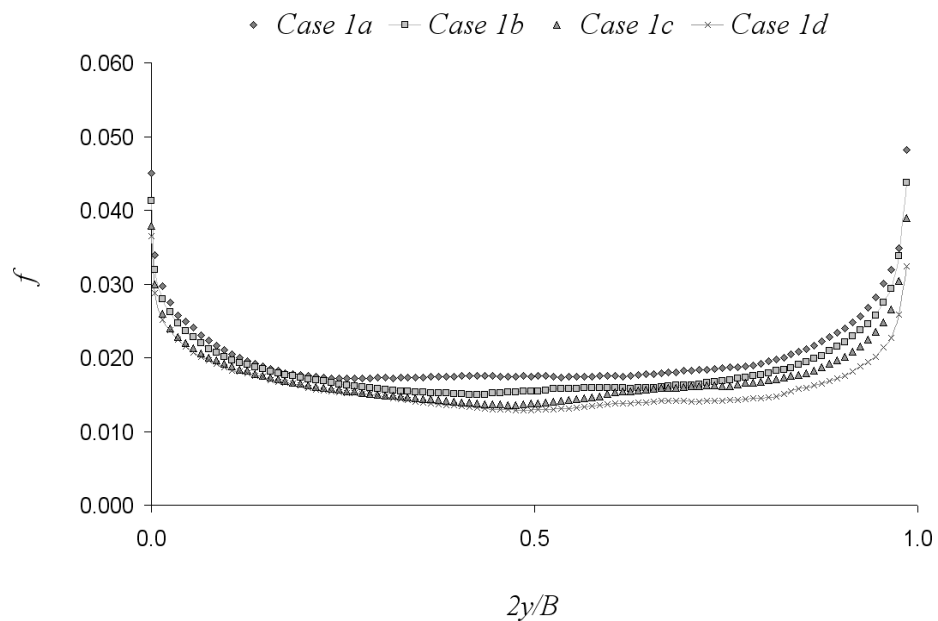
Figure 4.7.2-2: LES derived lateral distribution of f for Series 01

Figure 4.7.2-3 shows the variation of f for case 2a and Figure 4.7.2-4 shows the variation of f for case 3a. As the channel AR is increased the lateral variation of

f still remains relatively constant in the central region of the channel, again varying

only significantly as the sidewalls are approached.
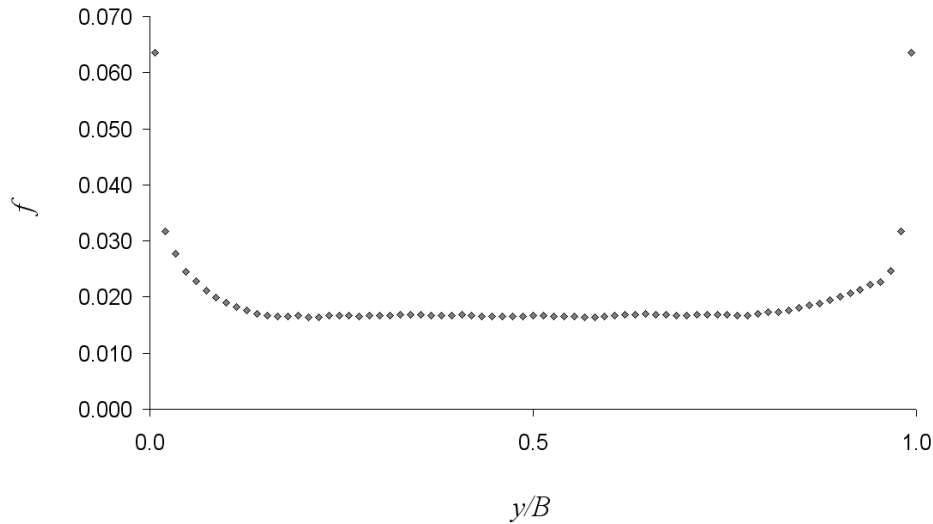
Figure 4.7.2-3: LES derived lateral distribution of friction factor, f for case 2a
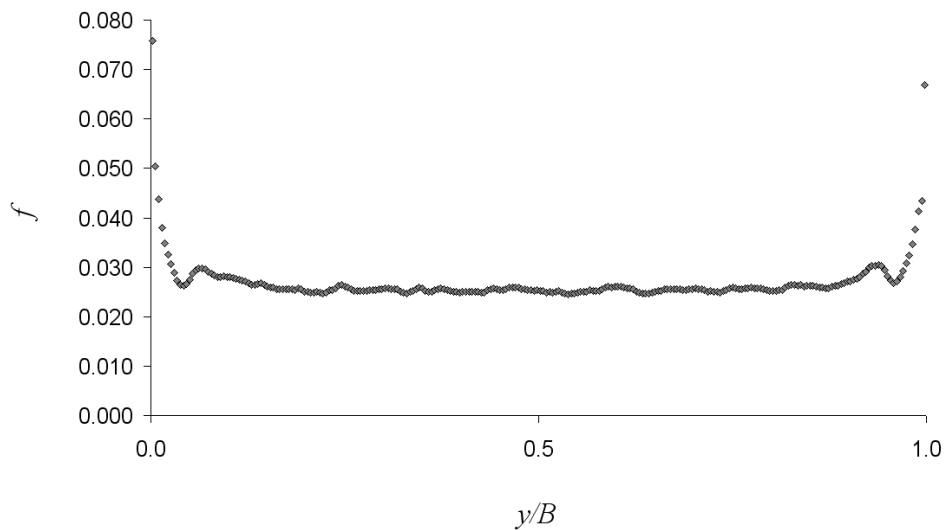
Figure 4.7.2-4: LES derived lateral distribution of friction factor, f for case 3a

One thing that can be noted in Figure 4.7.2-4 is the depressions in the profile at

$y/B = 0.046$ and 0.962, due to the impact of the magnitude of the bottom vortices on

the shear stress and velocity profiles. This is apparent in all of the lateral variations

of f for all cases in Series 03.

4.7.3 Dimensionless Eddy Viscosity Coefficient, λ

The LES derived average dimensionless eddy viscosity coefficient, λ, is derived from the Reynolds stress and gradient of velocity profile. Figure 4.7.3-1 shows the lateral distribution of λ for case 1a. It can be seen that other than the spike in the profile at the channel centre λ is relatively constant. This spike is due to the changes in gradient of the velocity profile. Omitting the central area of the profile average values of λ were determined for all cases in Series 01 and these values are reported in Table 4.7-5.

.
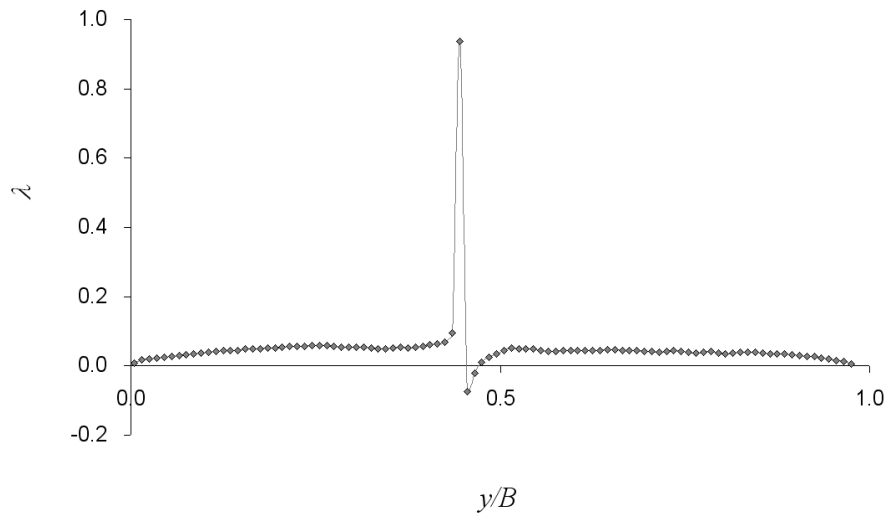
Figure 4.7.3-1: LES derived lateral distribution of, λ for case 1a

Table 4.7-4: LES derived cross-sectionally averaged λ results for Series 01

CASE	λ C&K	λ LES
1a	0.024	0.047
1b	0.020	0.043
1c	0.017	0.028
1d	0.013	0.012

The tabulated values of average LES derived λ range from 0.012 to 0.047, which are higher than those of C&K. However, the values of λ do vary throughout the channel section and producing an average across the section is somewhat difficult, especially as the *AR* of the channel increases and more spikes occur. This can be seen from Figure 4.7.3-2, which shows the lateral distribution of λ for case 3a. Prescribing an average across this section would be very difficult and also inaccurate relative to the analytical description of λ.
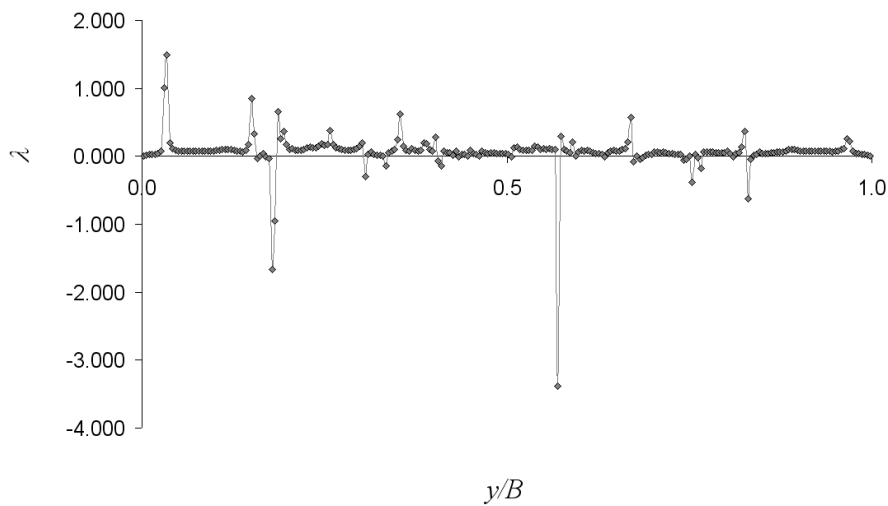
Figure 4.7.3-2: LES derived lateral distribution of λ for case 3a

The calculation of λ was also performed from the RANS results, but since the λ parameter value is essentially related to internal shear and Reynolds stresses, only results obtained from models accounting for the existence of Reynolds-stress driven secondary currents are presented for comparison. The SSG and LRR derived λ values are also shown in Figure 4.7.3-3 and it can be seen that the SSG and LRR values are higher than those of C&K and LES (Table 4.7-4). This again highlights the fact that the C&K values do not seem physically reasonable.

136
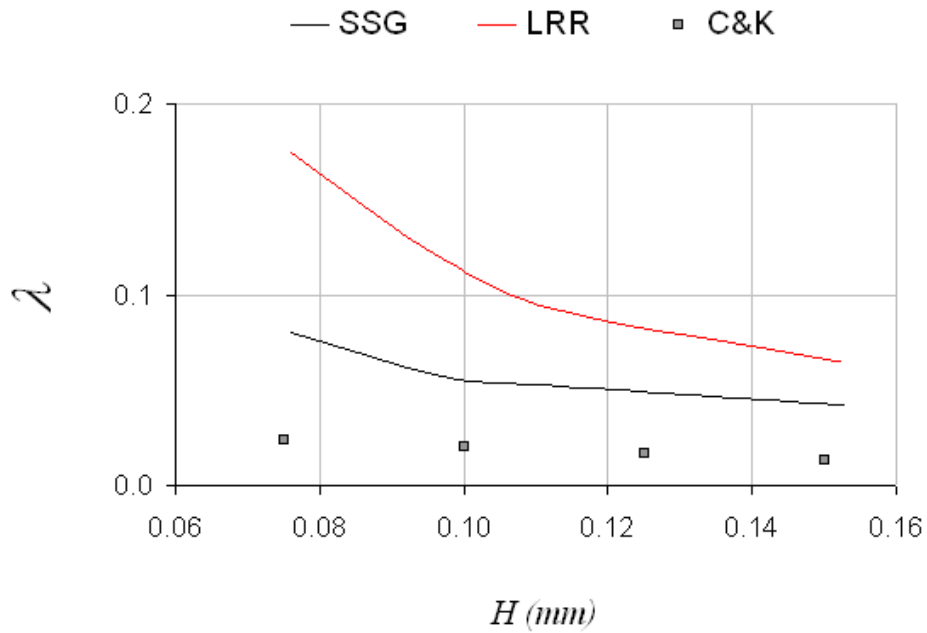
Figure 4.7.3-3: RANS derived λ values compared to C&K values

4.7.4 Secondary Flow Term, Γ

The secondary flow term, Γ, has been shown to correspond to the lateral gradient of the force due to secondary flow and as mentioned previously, is one of the main reasons for the use of LES within this research. It has been shown in Sections 4.4 - 4.6 that the distribution of secondary circulation cells can be complex and the location of cells varies significantly dependant on channel geometry.

For Series 01, Figure 4.7.4-1 is a plot of the depth averaged velocity correlation $\left(\overline{UV}\right)_d$. Firstly it can be seen that $\left(\overline{UV}\right)_d$ varies considerably across the channel cross-sections, according to the distribution of secondary flow cells.
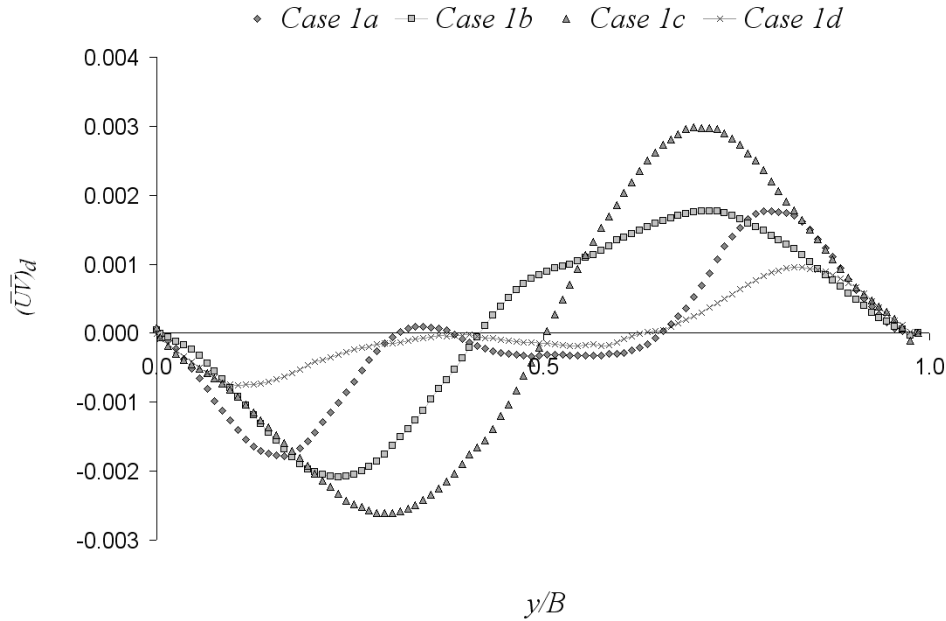
Figure 4.7.4-1: LES derived lateral distribution of $\left(\overline{UV}\right)_d$ for all cases in Series 01

From initial analysis of Γ it can be concluded that to prescribe an average over the whole cross-section as in Chlebek and Knight (2006) appears not to be an accurate description of the flow physics. As well as prescribing a cross-sectionally averaged Γ value Chlebek and Knight (2006) also publish a value of Γ that remains constant for all 4 channel heights, which from Figure 4.7.4-1 does not seem to be correct.

Most of the plots in Figure 4.7.4-1 are similar. However, those of cases 1a and 1d, differ from to those of cases 1b and 1c. This is due to the secondary circulation cells being vertically overlain as in Figure 4.4.2-1. Cases 1a and 1d, and 1b and 1c have very similar secondary flow cell structures, with for cases 1b and 1c two dominant cells per half channel, which starts to break down for cases 1a and 1d. The prediction of secondary circulation cells and therefore Γ is less complicated if the cells are not overlain.

Figure 4.7.4-2 shows profiles of $\left(\overline{\overline{UV}}\right)_d$ for the SSG simulations. It should be noted that there is no profile corresponding to the LRR-IP model as it did not show any sign of recirculation, which is consistent with other published results (Wright et al. 2004). Wright et al. (2004) note that this formulation does not contain any wall reflection terms, which may partly account for these results. It can be seen that the SSG results differ from those of the LES code results, again due to the differing predictions of size and location of secondary current cells.

As already mentioned no experimental visualisation of the secondary circulation cells is available for Series 01. However, Omran (2005) studied the perturbation in the boundary shear stress across rectangular channels based on the experimental data from Knight and Demetriou (1983) (Section 2.6.3.3) and derived the locations of the secondary current cells for a range of rectangular channels at varying AR. For channels of $AR < 2$ the panel divisions were located at $y/B = 0.25$ and 0.75 (light green) and 0.1 and 0.9 (dark green). Figure 4.7.4-3 shows Figure 4.7.4-1 overlain with the predicted panel divisions.
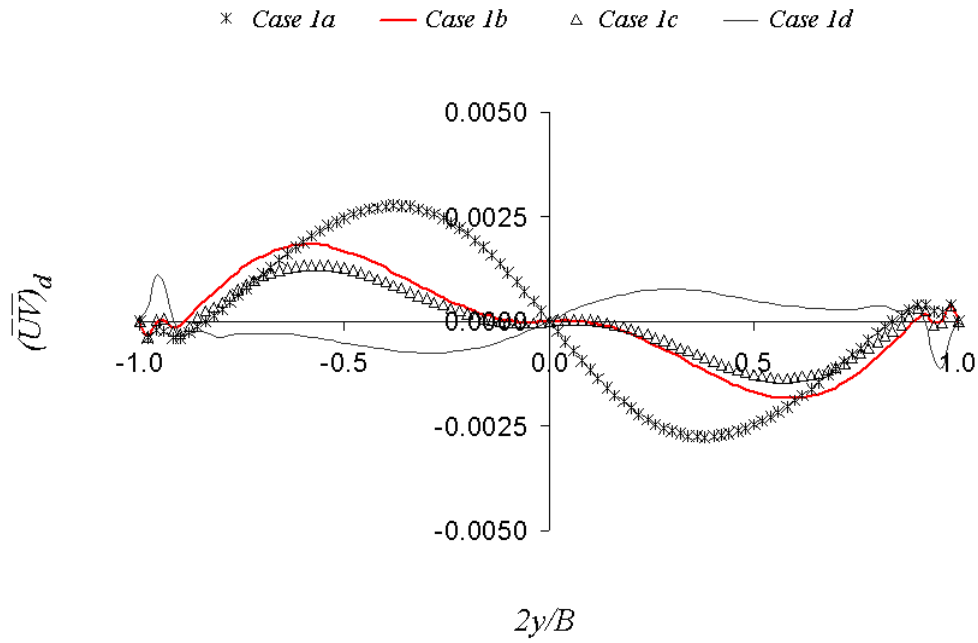
Figure 4.7.4-2: SSG derived lateral distribution of $\left(\overline{UV}\right)_d$
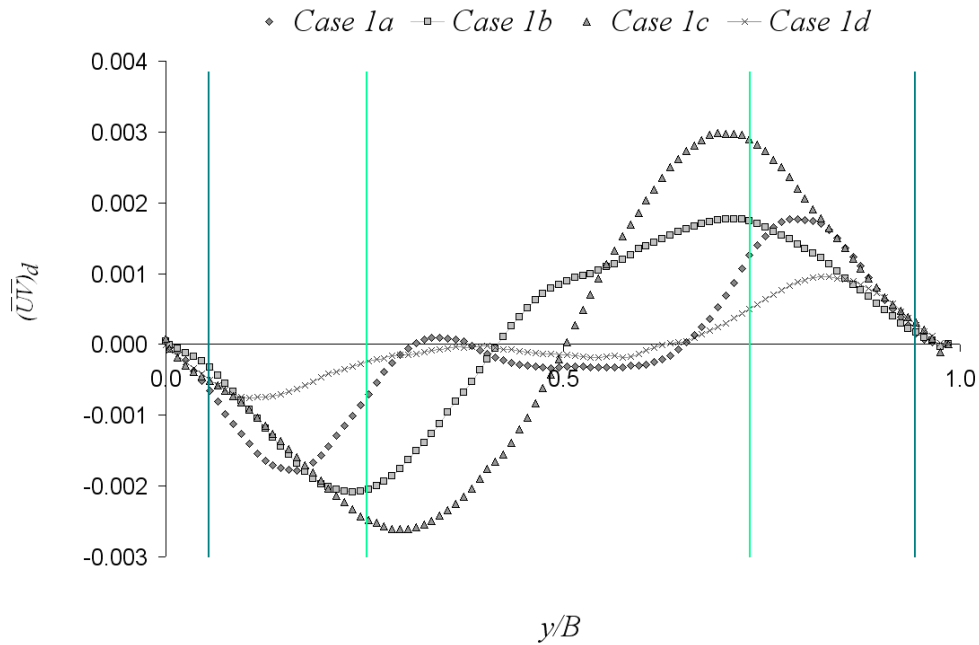
Figure 4.7.4-3: LES derived lateral distribution of $\left(\overline{UV}\right)_d$ *overlain with the secondary*

circulation divisions proposed by Omran (2005)

140

Splitting the prediction of Γ at $y/B = 0.25$ and 0.75 seems to be a reasonably accurate assumption in cases 1b and 1c, but not in cases 1a and 1d. The points of change of gradient are tabulated for all four cases in Table 4.7-5 below.

Table 4.7-5: LES derived secondary flow cell centre locations for cases 1a, 1b and 1c

CASE	LHS	RHS	AVERAGE
1a	0.17	0.80	0.185
1b	0.23	0.75	0.240
1c	0.30	0.70	0.300
1d	0.15	0.82	0.165

Further to Table 4.7-5, Figure 4.7.4-4 shows clearly the change of gradient of $\left(\overline{UV}\right)_d$
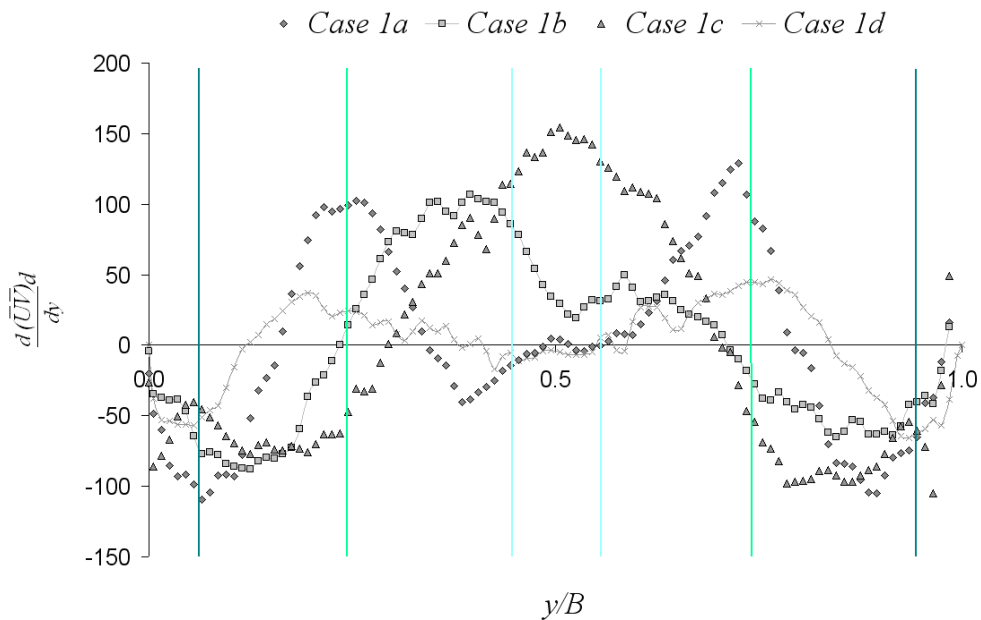
Figure 4.7.4-4: LES derived lateral distribution of $d\left(\overline{UV}\right)_d / dy$ for cases 1a, 1b and 1c

overlain with the secondary circulation divisions proposed by Omran (2005)

However, splitting the distribution at $y/B = 0.1$ and 0.9 does not seem to match the LES results. There is some change of gradient of the profiles in the near wall region, which can be seen from Figure 4.7.4-5. Figure 4.7.4-5 is a close up of case 1c and a change of gradient of the profile can be seen at $y/B = 0.97$ not 0.9. This change of gradient is present within all cases for Series 01, however, not located as far away from the wall as predicted by Omran (2005).
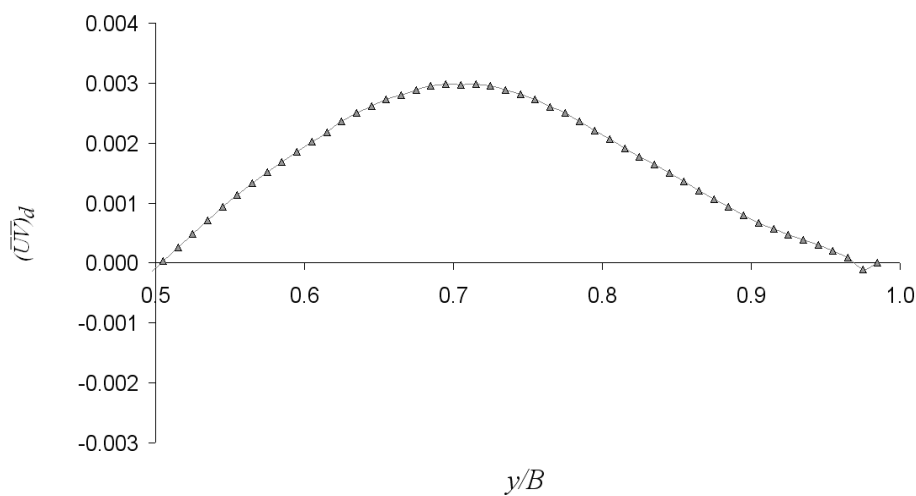
Figure 4.7.4-5: LES derived lateral distribution of $\left(\overline{UV}\right)_d$ *for case 1c*

Series 02 and 03 produce less complex distributions of secondary circulations with cells predominantly side by side across the channel section. Figure 4.7.4-6 and Figure 4.7.4-7 show plots of $\left(\overline{UV}\right)_d$ for Series 02, with the corresponding secondary flow cells accompanying each velocity correlation plot, for clarity. Cases 2a and 2b are very similar with regard $\left(\overline{UV}\right)_d$ distribution, with case 2c having more variability compared to cases 2a and 2b as the channel centre is approached.

Change of gradient of the $\left(\overline{UV}\right)_d$ has been analysed and changes of grade occur at;

Case 2a - $y/B = 0.013, \ 0.133, \ 0.413$

Case 2b - $y/B = 0.008, \ 0.088, \ 0.392$

Case 2c - $y/B = 0.003, \ 0.058, \ 0.138$

Numerous other structures are observed within case 2c, but not noted in terms of y/B location.

(a)

(b)

Figure 4.7.4-6: LES derived lateral distribution of $\left(\overline{UV}\right)_d$ for cases (a) 2a and (b) 2b

compared to LES derived contour plots of secondary circulation cells

144
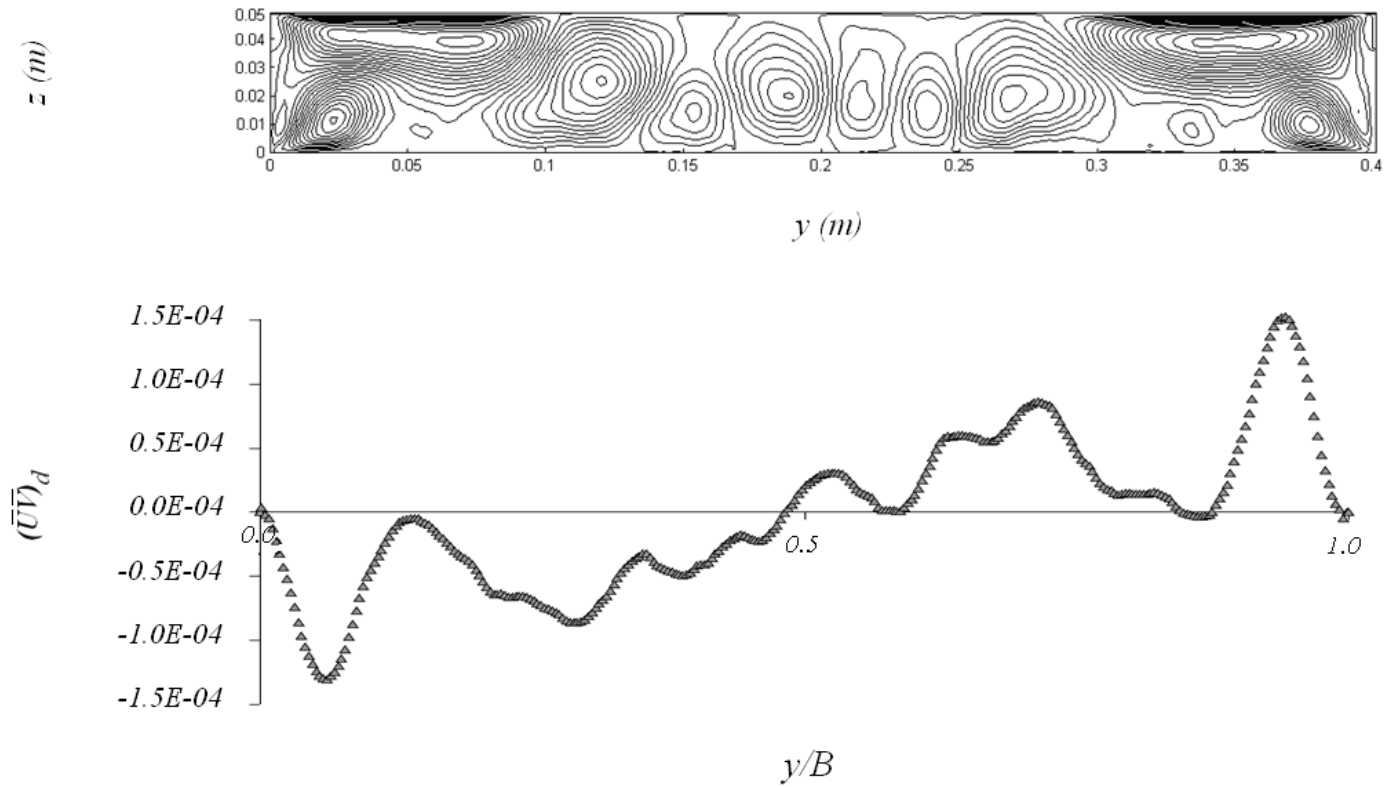
Figure 4.7.4-7: LES derived lateral distribution of $\left(\overline{UV}\right)_d$ for case 2c compared to LES derived contour plots of secondary circulation cells

Cases 3a, 3b, 3c and 3d have very complex distributions of $\left(\overline{UV}\right)_d$. Figure 4.7.4-8 shows the $\left(\overline{UV}\right)_d$ plot for case 3a. Cases 3b, 3c and 3d are not shown.
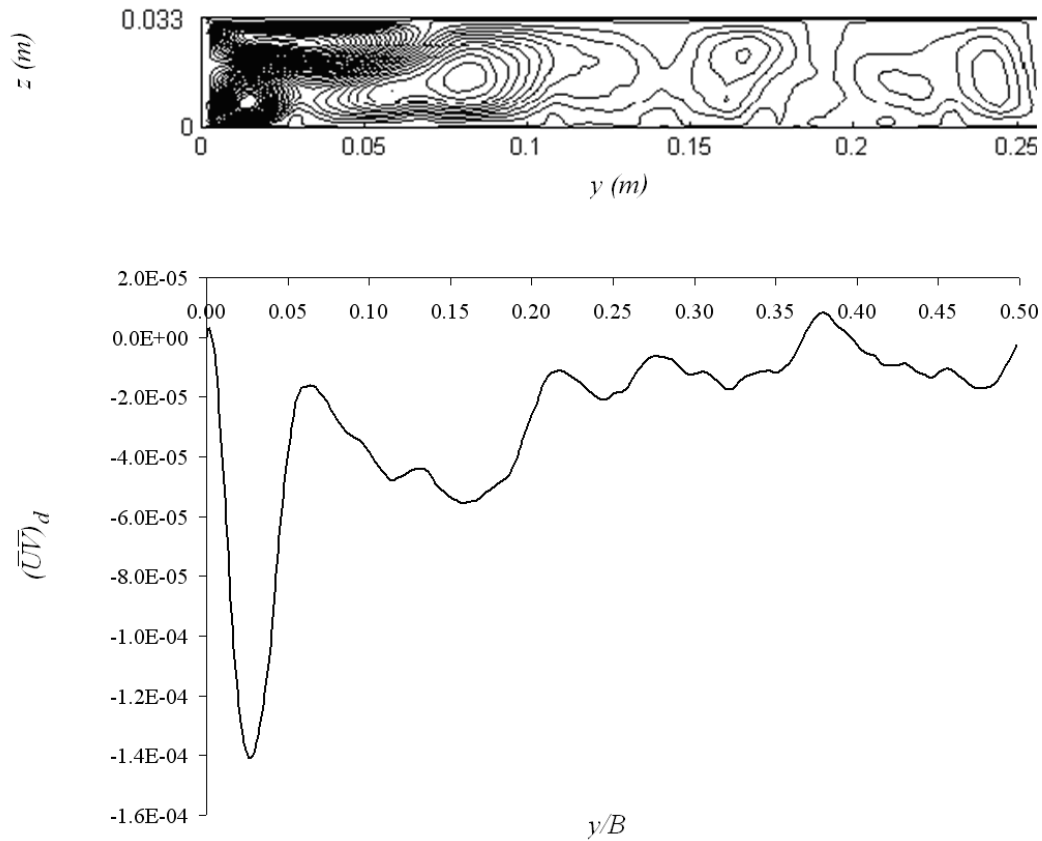
Figure 4.7.4-8: LES derived lateral distribution of $\left(\overline{UV}\right)_d$ for case 3a compared to contour

plots of simulated secondary circulation cells

Although the distributions for cases in Series 03 are complex, one thing to note is the magnitude of the first cell in each $\left(\overline{UV}\right)_d$ plot. This cell constantly shortens to accommodate increasing secondary flow cells at increased aspect ratio, but is noticeable by its magnitude near the wall boundary. Its location has been analysed for all cases in Series 02 and 03. Table 4.7-6 shows the location of the cell centre, which was computed from the minimum point on each $\left(\overline{UV}\right)_d$ profile.

146

Multiplying the location of the cell centre (y/B) by its respective AR a relatively constant value of cell location in terms of y/H is found. The relationship is:

$$E = 0.412H \tag{4.7.1}$$

Where E indicates the location of the cell centre.

Table 4.7-6: LES derived secondary flow cell centre location for all cases in Series 02 and

03

CASE	AR	Cell Centre Location y/B	Cell Centre Location y/H
2a	3	0.133	0.399
2b	5	0.088	0.440
2c	8	0.058	0.464
3a	15	0.026	0.390
3b	25	0.014	0.350
3c	30	0.012	0.360
3d	40	0.012	0.480

Numerous f, λ and Γ plots have been detailed in the last three sections, but in order to investigate how accurate the values obtained from LES are, they were substituted into the analytical solution of the SKM and depth averaged velocity profiles were obtained. The next section details these results.

4.7.5 Summary

Sections 4.7.2-4.7.4 have shown that LES can simulate in-bank open channel flow well, with the prediction of the velocity dip to within 5% of the experimentally

measured position. The secondary circulation cells compare well to results of Naot and Rodi (1982), Imamoto and Ishigaki (1988) and Tominaga et al. (1989) and the presence of an inner secondary flow cell at the free surface/channel wall has also been briefly discussed. Utilising these results f, λ and Γ values have been derived and are shown to compare to published empirical relationships. To further validate the LES and f, λ and Γ values predicted.

The next section goes on to utilise these f, λ and Γ values within the analytical solution of the SKM. Depth averaged velocity profiles are derived which can then be compared to experiment and LES simulated profiles, giving confidence in the extraction of f, λ and Γ from the LES results.

4.7.6 Analytical Solution

It has already been mentioned that Equation 2.6.12 can be solved analytically and the analytical solution for U_d for a constant depth domain can be expressed as,

$$U_d = \{A_1 e^{\gamma y} + A_2 e^{-\gamma y} + \frac{8gS_0 H}{f}(1-\beta)\}^{1/2}$$

(4.7.1)

The various different parameters in Equation (4.7.1) were defined in Chapter 2. Knight et al. (2004) specified the boundary conditions for Equation (4.7.1) in channels with vertical sidewalls, as below;

$$U_d^{(1)} = U_d^{(2)}$$

(4.7.2)

$$\left[\lambda \sqrt{\frac{f}{8}} \frac{\partial U_d}{\partial y} \right]^{(1)} = \left[\lambda \sqrt{\frac{f}{8}} \frac{\partial U_d}{\partial y} \right]^{(2)}$$

(4.7.3)

Once a channel cross-section is divided into different panels and the boundary conditions in Equations (4.7.2.) to (4.7.3) are applied, a set of linear equations is obtained in which the coefficients, A_1 and A_2, in Equation (4.7.1) are unknowns. These coefficients are then solved in order to compute the distribution of U_d across the channel from which the lateral distribution of τ_d can also be obtained (Equation 4.7.4).

$$\tau_b = \left(\frac{f_b}{8} \right) \rho U_d^2$$

(4.7.4)

The above analytical equation was solved in Fortran90 and the analytical solution of the SKM is shown in Appendix A and the Fortran90 code in Appendix B. The

reported Fortran90 code concentrates solely on rectangular channels with vertical sidewalls and varying distributions of f, λ and Γ can be input and an analytical solution produced for various panel divisions.

Omran (2005) developed a similar Visual Basic for Applications (VBA) code to solve the equivalent of Equation (4.7.1) for channels with sloping sidewalls. However, the VBA code only accommodated for up to 8 panel divisions. With being able to extract the distributions of f, λ and Γ from the LES simulation results it was thought a waste to only utilise 8 panels. Therefore the Fortran90 code allows numerous panels in a half channel section to be simulated. This allows for the distributions of f, λ and Γ from the LES simulation results to be input into the analytical solution and the resulting velocity profiles compared to simulated profiles.

4.7.6.1 1 Panel Evaluation

Section 2.6.3.4 has already described optimisation of f, λ and Γ by Chlebek and Knight (2006). Although, as was mentioned this optimisation was only undertaken for 1 panel average values, therefore, a half channel section. Further investigation of these parameters highlights that they were chosen as they produced the smallest percentage error in discharge and shear force on the wall when compared to experiment. However, from Figure 4.7.6-1 it was seen that the analytically computed profile from C&K values does not actually compare favourably to the experimental profile. Therefore 1 panel averaging is not performed.
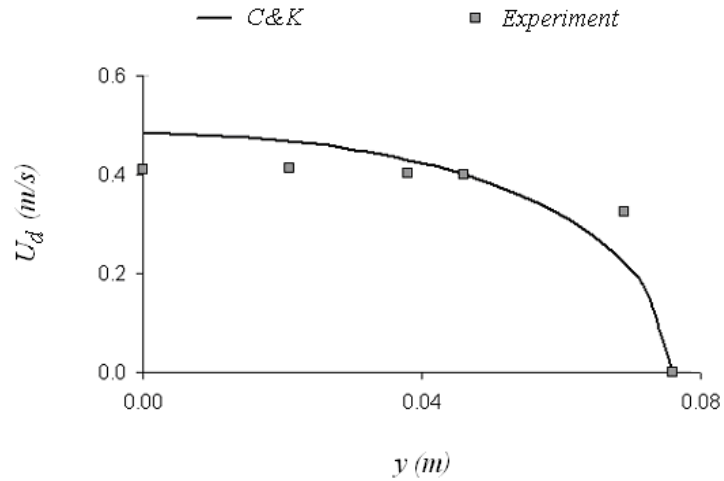
Figure 4.7.6-1: Depth averaged velocity profile produced using C&K values compared to experimental results (Knight et al. 1984) for case 1b

The next sections detail analytically derived depth average velocity profiles compared to LES simulation results.

4.7.6.2 Series 01

Utilising the continuous profiles of f, λ and Γ that can be computed from the LES results it is sensible to perform a computation with multiple panels, rather than a 1 panel average, as it is known that f, λ and Γ vary considerably in certain areas of the channel cross-section. Therefore, initially a 5 panel computation was undertaken with average values computed from the LES results and the channel split into 5 equal panels across half the channel cross-section. The averaged f, λ and Γ utilised are shown in Table 4.7-7.

Table 4.7-7: Average f, λ and Γ values utilised in the computation of the 5panel analytical

solution for Series 01

CASE 1a			CASE 1b		
f	λ	Γ	f	λ	Γ
0.0175	0.0839	-0.0472	0.0154	0.0104	0.5427
0.0175	0.0487	0.1695	0.0157	0.0175	0.5542
0.0179	0.0484	0.5211	0.0167	0.0192	-0.0471
0.0200	0.0411	-0.2514	0.0188	0.0214	-0.6291
0.0288	0.0209	-0.3957	0.0269	0.0106	-0.4268
CASE 1c			CASE 1d		
f	λ	Γ	f	λ	Γ
0.0118	0.0585	1.5859	0.0132	0.0039	-0.0861
0.0142	0.0300	0.7826	0.0141	0.0069	0.3773
0.0169	0.0221	-0.6072	0.0148	0.0183	0.7444
0.0195	0.0200	-1.0647	0.0165	0.0236	0.1055
0.0262	0.0092	-0.7103	0.0226	0.0087	-1.1536

The profiles computed using the above averaged values were compared with the LES depth averaged velocity profiles, giving both an indication of the accuracy of deriving f, λ and Γ from the LES and the accuracy of the SKM. Figure 4.7.6-2 shows the computed depth averaged velocity profiles for all cases in Series 01. The profiles can be seen to predict the depth averaged velocity distributions well, with the location of the peaks and troughs qualitatively correct, although sometimes either under or over predicted. Also, one consistent difference between the analytical and LES profiles is the under prediction of U_d by the analytical solution in the near wall regions. This is due to averaging of f in this region. If another panel is located near the side wall then this effect is eliminated.
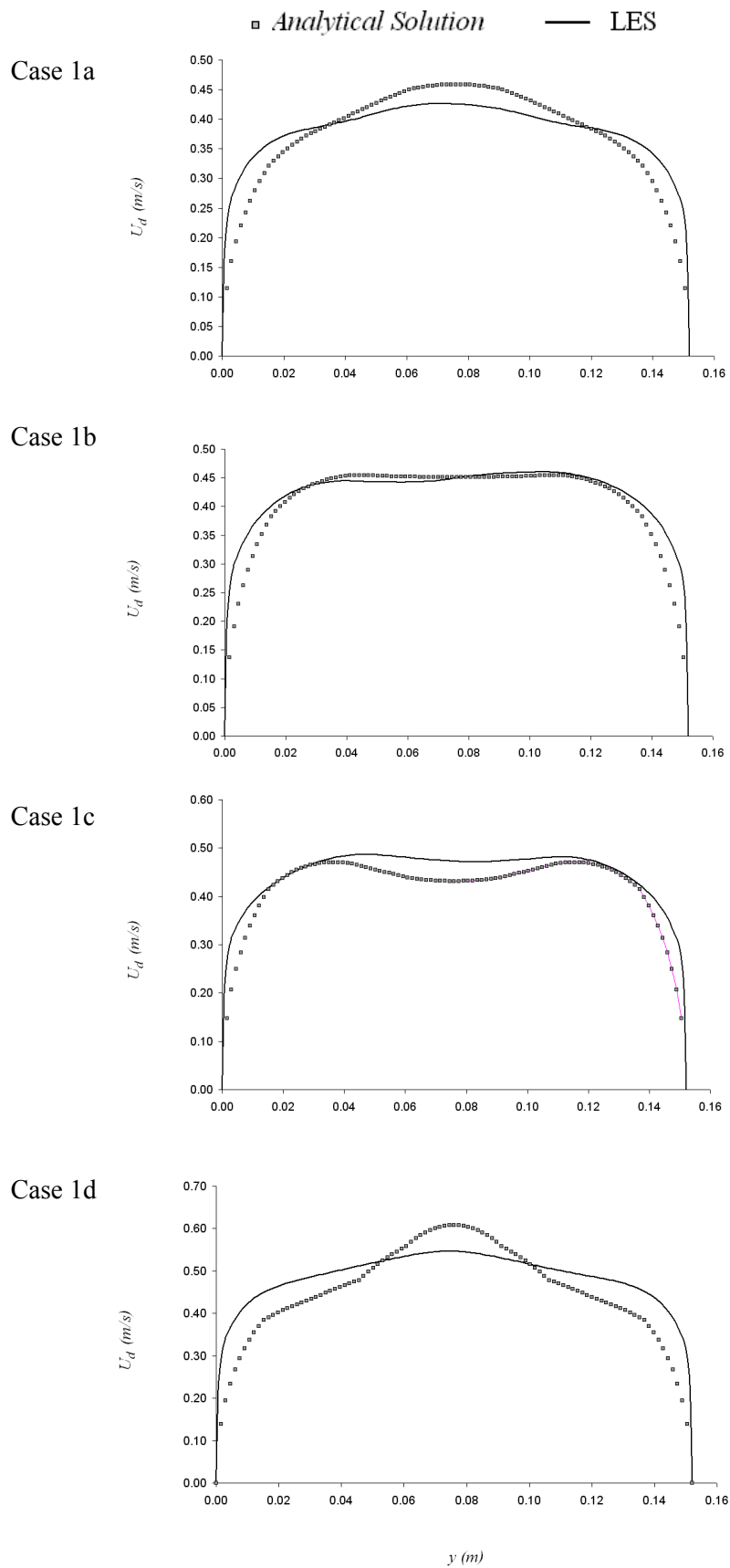
Figure 4.7.6-2: Analytically derived depth averaged velocity profiles compared to LES

results

4.7.6.3 Series 02

Figure 4.7.6-3 shows analytically derived velocity profiles for cases 2a and 2b. Case 2c is not shown as wall shear profiles were not recorded during the simulation, making the computation of f and λ not possible.
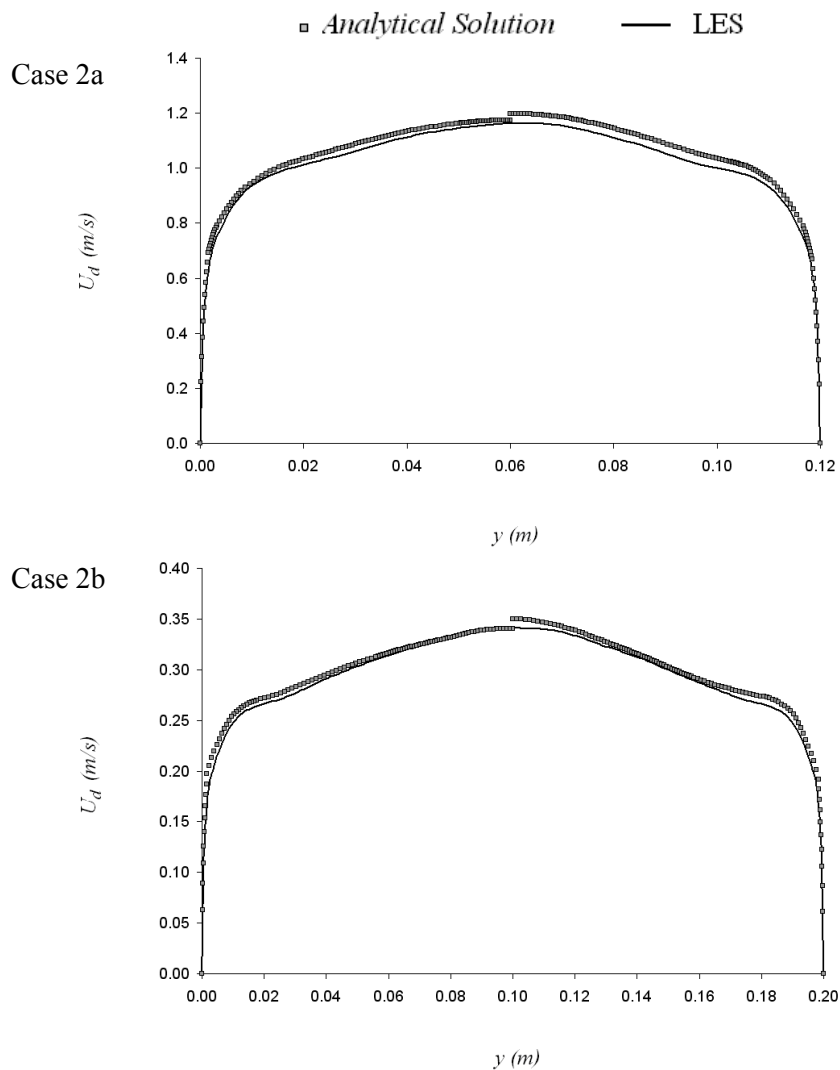
Figure 4.7.6-3: Analytically derived depth averaged velocity profiles compared to LES

results for Series 02

These analytical results were derived using 22 f, λ and Γ values in order to accurately represent the lateral variations of the constants across the channel section.

The analytical results compare more accurately to the LES simulated data than those of Series 01 with the maximum deviation from LES profile locally being 3.8% for case 2a and 2.9% for case 2b.

4.7.6.4 Series 03

So far the velocity profiles have been predicted well by the analytical solution. However, as the aspect ratio of the channel increases the velocity profiles becomes more complex in their distribution. To investigate further the adequacy of the SKM case 3b was solved analytically using a 44 panel averaging across the channel cross section. Figure 4.7.6-4 shows the analytical solution in comparison to the LES simulated profile.
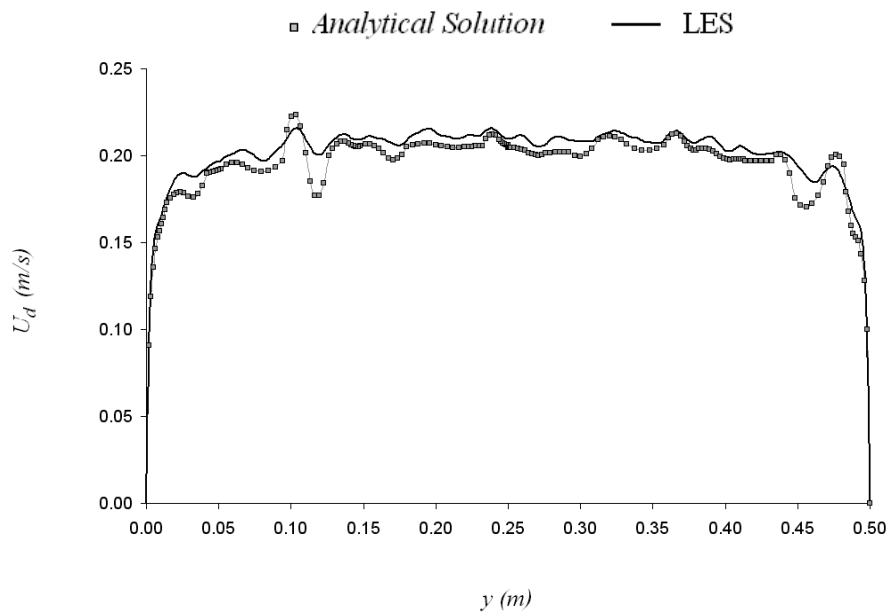
Figure 4.7.6-4: Analytically derived depth averaged velocity profiles compared to LES

results for case 3b

The analytically derived solution in Figure 4.7.6-4 compares very well to the LES simulated profile. All of the peaks and troughs within the profile are captured. The

155

magnitude of these is also similar to the LES profile with only the larger peaks and troughs being under or over predicted by up to a maximum of 11%.

4.7.6.5 Summary

Analytical solutions of U_d have been detailed in this section and compared with LES simulated results. The analytical solutions have been computed using averaged f, λ and Γ values derived from the LES simulation results. The analytical solution has been applied to various numbers of panels, dependent upon the distribution of parameters within the specific channel. All panel locations were computed by visual analysis of the f, λ and Γ distributions. Initially the channel cross-section was split according to the change in gradient of Γ and then further divided to accommodate changes in f and λ values.

The results show that the analytical solution accurately predicts the U_d profiles even for large AR channels of up to $AR = 25$. This gives both confidence in the SKM analytical solution and also in the LES simulation results.

4.8   CONCLUSIONS

- LES of in-bank open channel flows has been performed for varying AR ranging from $AR = 0.99\text{-}40$ and overall results compare well to experimental and other published data where available.

- Secondary flow cell distributions are shown to compare well to the experimental work of Naot and Rodi (1982), Nezu et al. (1985), Imamoto and Ishikagi (1988) and Tominaga et al. (1989) in relation to location, separation and magnitude of cells for cases reported. The presence of an inner

156

secondary flow cell at the free surface/wall corner comparable to that observed by Grega et al. (1995) has also been discussed.

- The location of the cell centre (change of gradient of $\left(\overline{UV}\right)_d$) for the bottom vortex in cases 2a-3d was analysed and shown to correspond well to the relationship $E = 0.412H$, where E indicates the location of the cell centre. The accuracy of all secondary current cell distributions can be validated by the accurate prediction of the depth averaged velocity, shear stress, vertical velocity and location of velocity dip. With regards prescribing an average Γ value the locations of separation of panels in some cases corresponds to that of Omran (2005), but in others the relationship is shown to be invalid due to overlain secondary circulation cells.

With regards SKM parameters,

- The distribution of f remains relatively constant in the central region of the channel, varying only significantly as the sidewalls are approached. Cross-sectionally averaged f values for Series 01 compare to average values computed by C&K. RANS derived f values are also shown to compare to those of C&K. For larger AR cases depressions in the profile of f near the channel side walls are observed due to the impact of the magnitude of the bottom vortex on the shear stress and velocity profiles.

- λ is shown to be relatively constant in the main channel section, only varying significantly as the walls are approached. If average values over the cross-section are taken for Series 01, these values compare to those of C&K. SSG and LRR derived λ values over-predict C&K results. However, the SSG results are comparable to $\lambda = 0.07$ (Shiono and Knight 1991)

- The distributions of $\left(\overline{UV}\right)_d$ are shown to vary considerably for all cases, with profiles differing due to the distribution of secondary flow cells e.g. cases 1a and 1d differ to those of 1b and 1c, due to the secondary flow cells being overlain in the former cases and not in the latter.

- LES results produce better secondary circulation predictions than RANS results, therefore it is essential to use LES rather than other turbulence models to accurately predict the distribution of secondary flow cells and therefore Γ.

The analytical solution of the SKM was utilised to investigate the derived f, λ and Γ values. It was concluded that,

- The derived f, λ and Γ values when placed back into the analytical solution produced depth-averaged velocity profiles comparable to the LES simulated results. Although not comparable exactly in magnitude the undulations in the profiles are predicted well. For cases 2a and 2b the profiles are predicted to within 3.8% and 2.9% of the simulated profile respectively and the distribution of velocity profile for case 3b is predicted extremely well. All of the above giving confidence in the LES results and accuracy of the derived SKM parameters.

<div align="right">

CHAPTER 5:

5   OVER-BANK CHANNELS

</div>

5.1   INTRODUCTION

The last chapter detailed in-bank channel flows and this chapter continues examining open channel flows, but now details over-bank channel simulation results. Results in this section are produced using ANSYS-CFX.

5.2   VALIDATION CASE

It has been shown in Chapter 3 that for an in-bank channel of $AR = 2$ the Delft code more accurately predicts in-bank channel flow features than ANSYS-CFX. Wall born instabilities are prominent in in-bank channels and therefore adequate shear stress predictions are driven by such phenomenon. However, instabilities within over-bank channels are geometry born and the effects of wall-born instabilities are minimal in comparison. Therefore, ANSYS-CFX is still investigated for use within simulating over-bank channels even though its application to in-bank channels was not favorable. ANSYS-CFX is utilized to simulate the over-bank channel case of Tominaga et al. (1989) and Tominaga and Nezu (1991) and validated against available experimental and simulation results within this section.

For over-bank channels, from hereon in the channel geometry is set-up comparable to in-bank channel geometries, where, flow is maintained by gravity, g, of an incompressible fluid of kinematic viscosity, υ. The main channel is of depth H with bottom width $2b$, top width $2B$ and sidewalls of slope s (for rectangular

compound channels s =0). The aspect ratio is $2B/H$. The mean flow is assumed

uniform in the streamwise direction so that the bed slope, S_0, and energy slope are

equal. Further to this, for a compound channel, h, is the height of the floodplain

above the channel bed and the depth ratio, $D_r = (H - h/H)$. The channel geometry

is shown in Figure 4.7.6-1
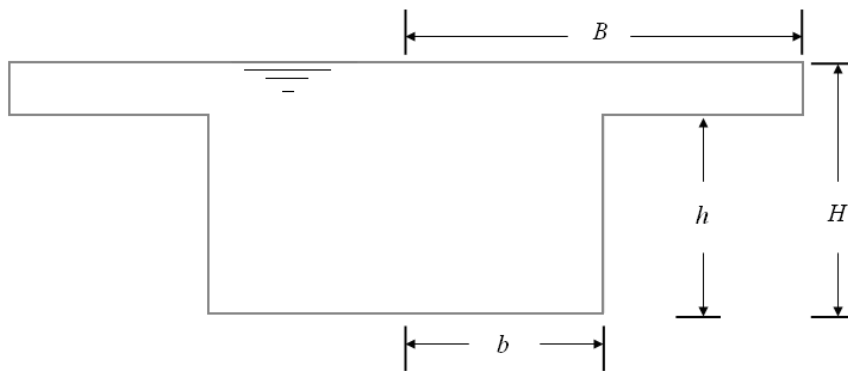
Figure 4.7.6-1: Rectangular over-bank channel geometry

Tominaga et al. (1989) reported an asymmetric over-bank channel case, with

geometry details specified in Table 5.2-1. This case has been used for validation by

numerous other authors and in the interests of comparison the results of Cater and

Williams (2008) are also utilized. Table 5.2-2 and Table 5.2-3 show the mesh and

simulation details for the ANSYS-CFX set-up.

The mesh was created by specifying a first cell height of 0.0004m and a growth

factor of 1.18 for 12 layers and ensuring that in the bulk flow the mesh element

aspect ratio was approximately 1, producing 6960 face elements and 1044000 total

elements. The simulation was started from an initial profile with a mean velocity,

U_{avg} =0.349m/s with imposed fluctuations of up to 0.175m/s. The channel bed slope,

S_0 was set to 0.00064m/m and body force to 6.257N/m^2.

The simulation was run for 150seconds, corresponding to 31 LETOTs.   The Smagorinsky model with Smagorinsky constant equal to 0.1 (Section 3.4.2.1) was implemented alongside van Driest damping.   The results of this channel were analyzed in the initial simulation period and no further time was allowed for the collection of statistics, therefore, it is acknowledged that this averaging time is minimal. However, this case is still documented to highlight comparable results to previously reported data.

The mass flow and boundary shear stress were monitored throughout the simulation and shown to converge to values within 2.2% and 0.3% of experiment respectively. The final average computed shear stress across the channel boundary being 0.274Pa comparing to 0.268Pa from experiment and the cross-sectional average velocity being 0.350m/s compared to 0.349m/s from experiment.

Table 5.2-1: Summary of experimental values for Case 4

H	h	B	b	U_{avg}	τ	u_*	R_e	D_r
(m)	(m)	(m)	(m)	(m/s)	(N/m^2)	(m/s)	-	-
0.080	0.040	0.400	0.200	0.349	0.268	0.0164	54,500	0.500

Table 5.2-2: Summary of mesh details for Case 4

Length (m)			Number of elements				y^+ range	
x	y	z	x	y	z	Total	min	max
0.480	0.400	0.080	150	160	58	1,044,000	0.3974	19.2734

Table 5.2-3: Summary of simulation details for Case 4

H/u_*	Estimated Simulation Time (sec)			Time step		Actual Time (sec)			LETOT Initial	LETOT Collect	LETOT Total
(sec)	Initial	Collect	Total	Δt	C_r	Initial	Collect	Total			
4.88	200	100	300	0.002	0.250	150	-	150	31	-	31

5.2.1 Results

Contours of U_d/U_{max} are shown in Figure 5.2.1-1(a) alongside a streamline plot of secondary circulations, Figure 5.2.1-1(b). Comparable contour plots are shown in Figure 5.2.1-1(c) and (d), from Tominaga and Nezu (1991) and Cater and Williams (2008). It can be seen that ANSYS-CFX LES results predict the velocity dip below the free surface and the contours compare qualitatively to the results of both Tominaga and Nezu (1991) and Cater and Williams (2008). All contour plots are taken in the y-z plane half way along the channel length.

In the paper of Tominaga and Nezu (1991) it is suggested that the experimental test section used is placed insufficiently far downstream from the inlet to allow for complete lateral development and the profile is not as symmetric as that of either the ANSYS-CFX results or those of Cater and Williams (2008). This may explain some of the differences between the profiles. There is also some disagreement between the velocity contours on the floodplain close to the floodplain side wall. The contours of Cater and Williams (2008) quickly become perpendicular to the floodplain bed at $y/H =4$, whereas those of ANSYS-CFX are angled at 45° to the floodplain bed until the wall is approached. This compares closer to profiles of Tominaga and Nezu (1991) than Cater and Williams (2008), however, the full profile across the floodplain for Tominaga and Nezu (1991) is not shown. It is acknowledged that the ANSYS-CFX simulation time is not significant and may also contribute to some of the differences between the reported results and other published profiles.

(a)

0.00 0.08 0.15 0.23 0.30 0.38 0.45 0.53 0.60 0.68 0.75 0.82 0.90 0.98

(b)

0.00 0.08 0.15 0.23 0.30 0.38 0.45 0.53 0.60 0.68 0.75 0.82 0.90 0.98

(c)
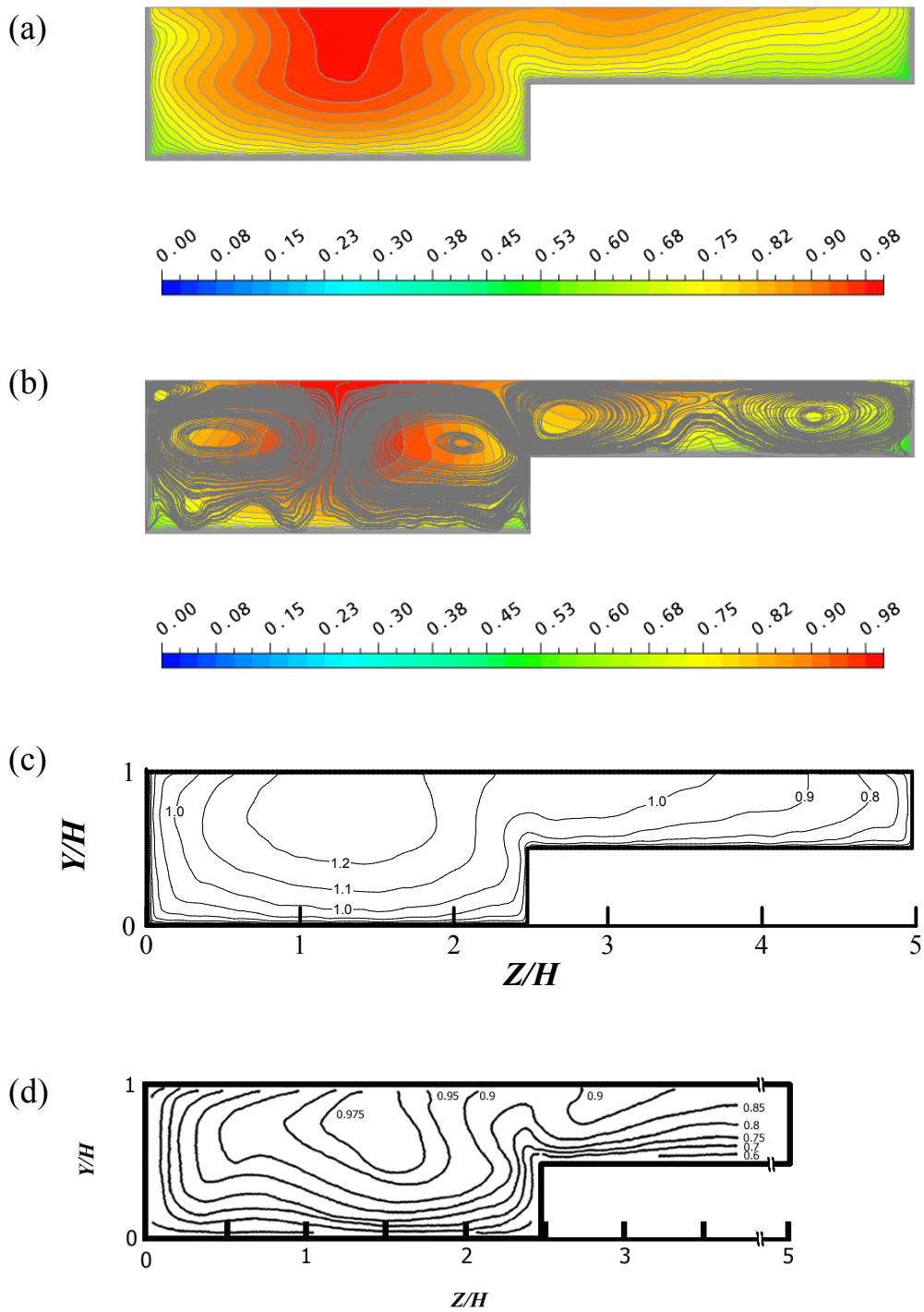
Figure 5.2.1-1: Distribution of ANSYS-CFX LES simulated (a) U_d/U_{max} and (b) streamlines of secondary circulations, and velocity distributions, U_d/U_{max} from (c) Cater and Williams (2008) and (d) Tominaga and Nezu (1991). These contours are all taken in the y-z plane at x=0.24m

Figure 5.2.1-2(a) shows a plot of U_d/U_{max} for the LES simulation. This can be compared to LES results of Cater and Williams (2008) in Figure 5.2.1-2(b) for $(U_d/U_*)^2/2g$. The distribution of the profiles compares well. A dip in the ANSYS-CFX velocity profile can be seen at approximately y/H =3.9, where it is observed at y/H =3.5 in the case of Cater and Williams (2008).
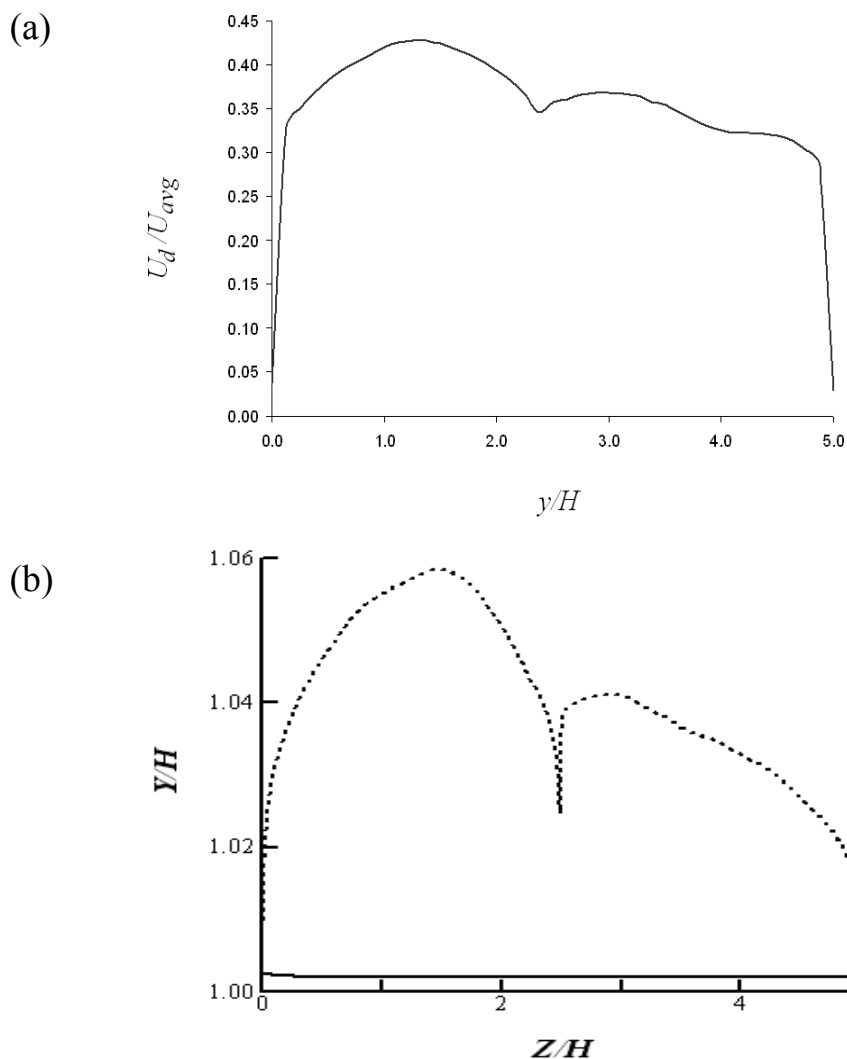
Figure 5.2.1-2: Lateral distribution of (a) ANSYS-CFX LES simulated velocity profile and (b) water surface level (-), compared with depth averaged velocity head (--) (Cater and Williams (2008)

Streamline plots of secondary circulation were shown in Figure 5.2.1-1(b). Two dominant cells can be observed in the main channel section with two further cells in the floodplain, split at approximately y/H =3.5. The separation of the two main channel secondary flow cells within the LES occurs at y/H =1.4, which corresponds to the same value from Cater and Williams (2008). The strongest secondary flow cells are generated from the junction edge to the free surface and the maximum magnitude of this inclined upwards flow is 4.3% corresponding well to the maximum of 4% predicted by Tominaga et al. (1989). Plots of vorticity, $\Omega = \dfrac{\partial W}{\partial x} - \dfrac{\partial U}{\partial z}$ are shown in Figure 5.2.1-3 to highlight the spanwise circulations in comparison to Cater and Williams (2008).

(a)

(b)
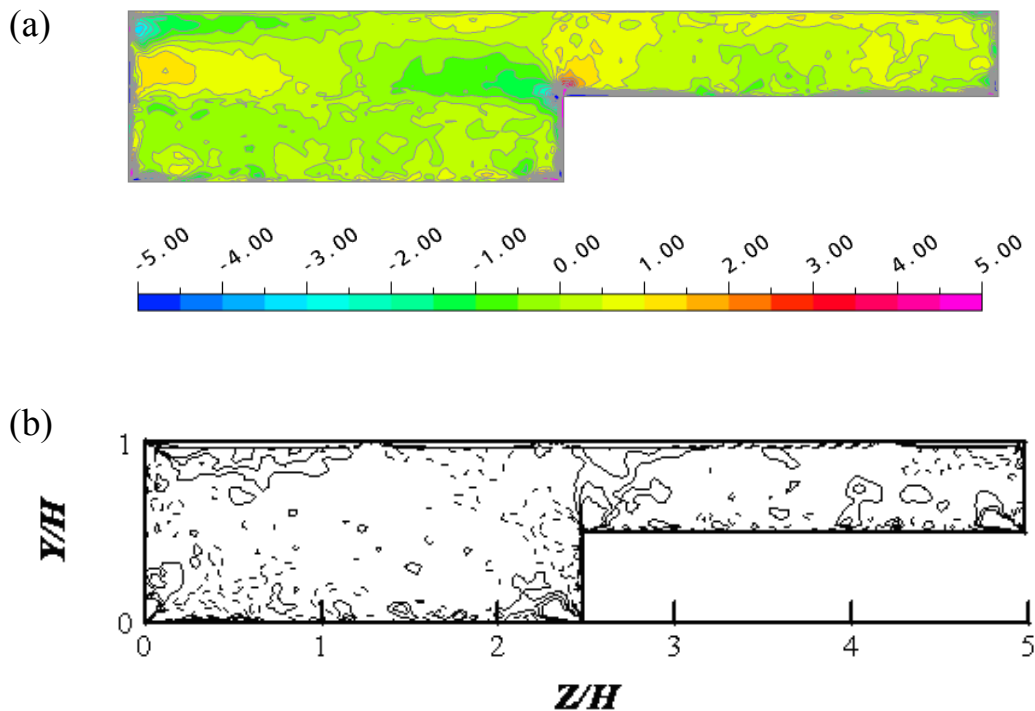
Figure 5.2.1-3: Distribution of vorticity simulated by (a) ANSYS-CFX and (b) Cater and Williams (2008)

Contour plots of u'/u_*, v'/u_* and v'/u_* are shown in Figure 5.2.1-4. The shape of distributions generally follows that of the average streamwise velocity. However, the regions of high turbulence activity are seen at the side walls, bed surface and internal corner.
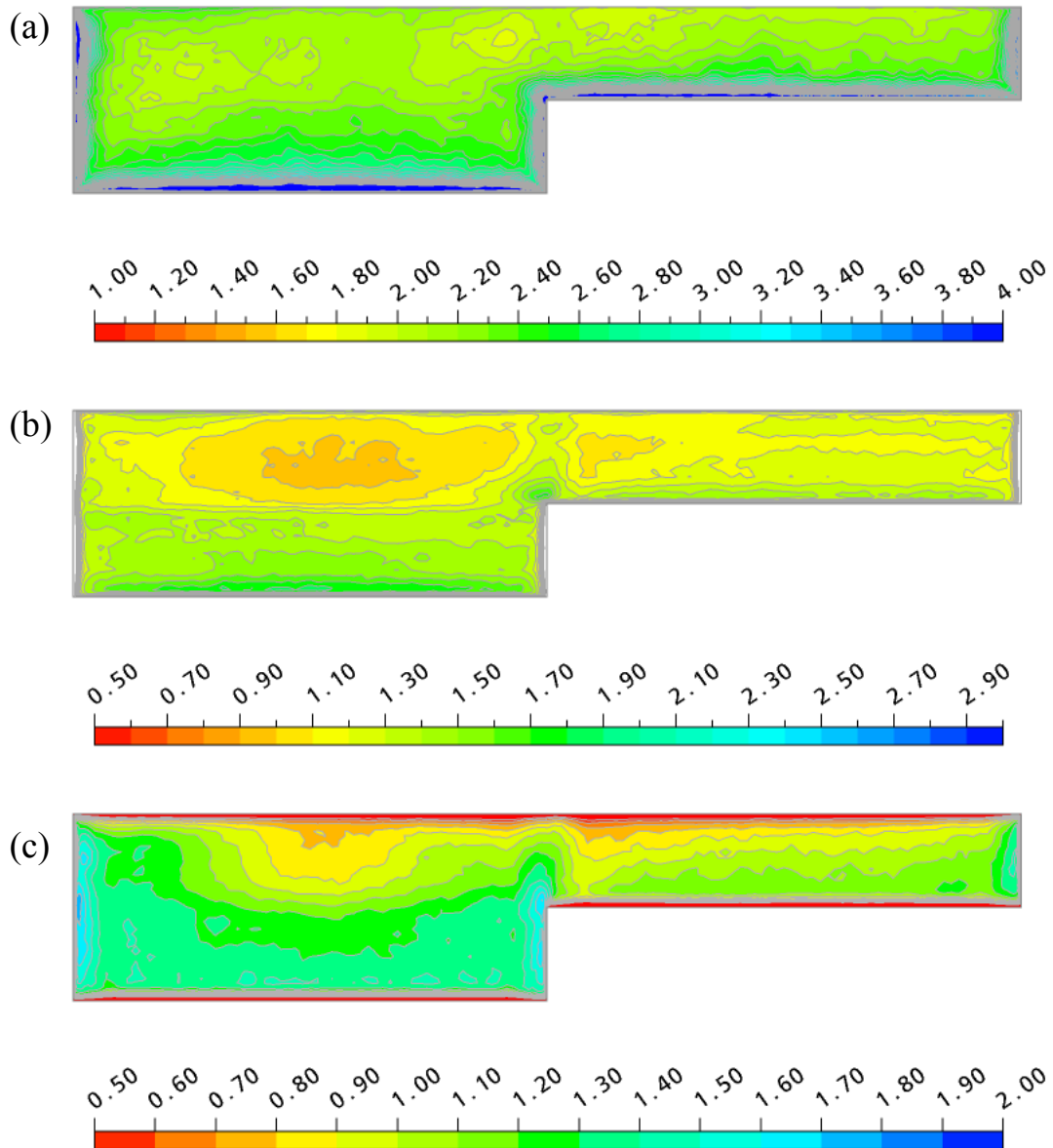
Figure 5.2.1-4: Distribution of ANSYS-CFX LES simulated turbulent stresses (a) u'/u_*, (b) v'/u_* and (c) w'/u_*

The influence of the free surface can be seen as the streamwise and spanwise values are spread parallel to the surface, whereas the vertical component reduces as the free surface is approached. Quantatively the values over predict those of Tominaga and Nezu (1991), but compare better with those of Cater and Williams (2008) shown in Figure 5.2.1-5.
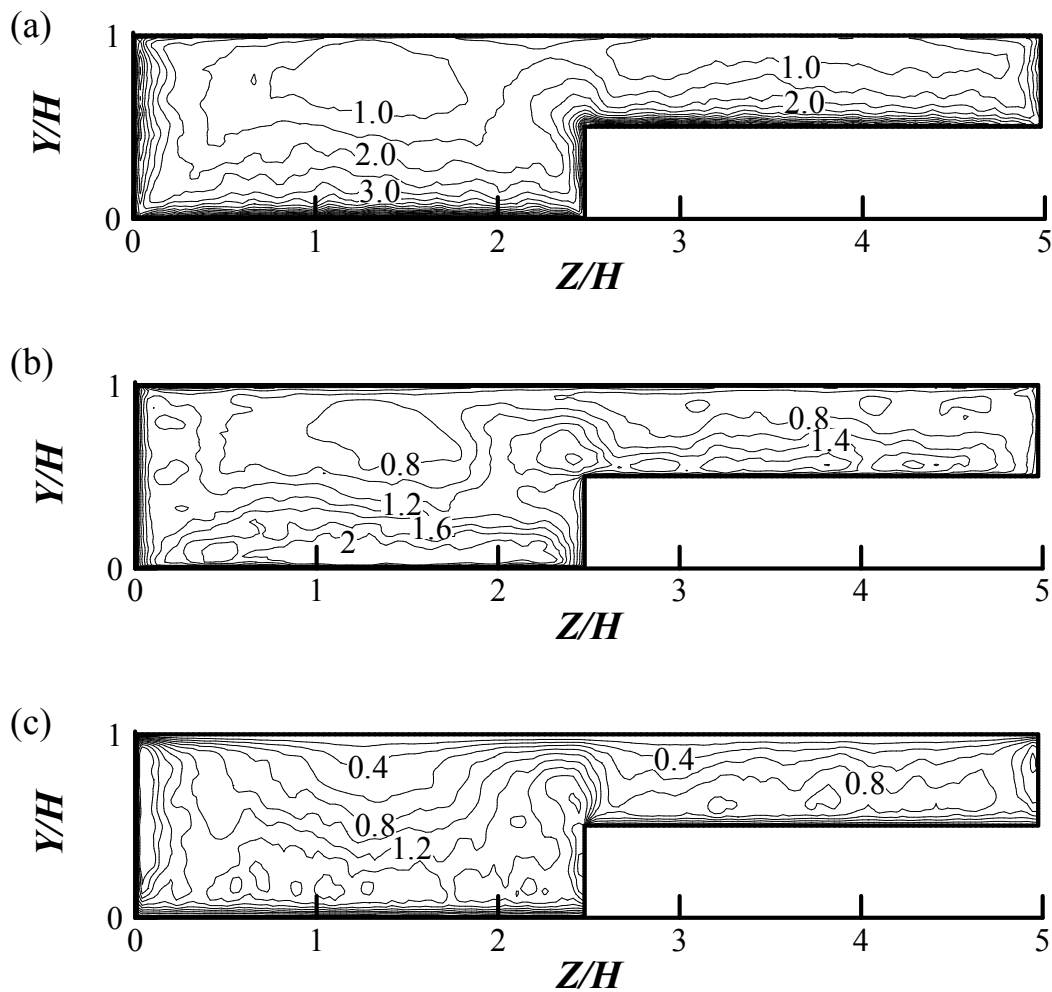
Figure 5.2.1-5: Cater and Williams (2008) simulated distributions of (a) u'/u_*, (b) v'/u_* and (c) w'/u_*

5.2.2 Summary

The ANSYS-CFX results compare qualitatively well to those of Tominga and Nezu (1991), Tominaga et al. (1989) and Cater and Williams (2008). Although sometimes over predicting turbulence intensities these were comparable to Cater and Williams (2008) results. The velocity dip was predicted well, with contour plots corresponding well to Tominaga and Nezu (1991) and streamline plots were comparable, in both location and magnitude to the results of Cater and Williams (2008).

It is acknowledged that the simulation was not run for an adequate time to collect steady state statistics, impacting on the quality of the results and their comparison to already published data. However, the analysis of the channel has shown some comparison to published work and further channel series have been simulated and as for case 4 will be validated against experimental data where available. Not shown in this section, but detailed in Section 5.3.3.3 are also the distributions of turbulent diffusive transport and secondary current transport terms, simulated by Cater and Williams (2008). The ANSYS-CFX results will be shown to compare well to the profiles of Cater and Williams (2008) and also the values of mean apparent shear stress on the partial wall and the main channel/floodplain interface.

The remainder of this chapter details Series 05, cases 5a to 5d and highlights specifically the variation of D_r on the apparent shear stress in over-bank channels and the derivation of SKM parameters from over-bank results.

5.3   OVER-BANK RECTANGULAR CHANNELS

This section describes 4 over-bank rectangular channels whose set-ups compare to Knight and Demetriou (1984) Series 02 and 04.

5.3.1   Series 02

Three of the four reported compound channels in this section are comparable to the data of Series 02 of Knight and Demetriou (1984), whose series is defined by a width ratio, B/b =2. Channels comparable to Series 02 are referred to as cases 5a, 5b and 5c respectively.

The initial case, case 5a is the highest depth ratio of the three cases. The case was run with a symmetry plane as a free surface in the initial stages of investigating the ANSYS-CFX LES software and also at a lower R_e than experiment, therefore the results are compared in non-dimensionalised form. The set-up of cases 5b and 5c are performed at the same R_e as experiment with a free-slip 'rigid lid' implementation (refer to Section 3.4.2) at the free surface. The experimental and LES set-up values are summarised in Table 5.3-1 and Table 5.3-2 and Table 5.3-3 describe the mesh and simulation time details.

Table 5.3-1: Summary of experimental values for Series 05

CASE	H (m)	h (m)	$2B$ (m)	$2b$ (m)	U_{avg} (m/s)	τ_{ave} (N/m^2)	u_* (m/s)	R_e -	D_r -
5a	0.1498	0.0749	0.304	0.152	0.059	0.0089	0.0030	15,000	0.500
5b	0.0945	0.076	0.304	0.152	0.373	0.3291	0.0182	58,237	0.196
5c	0.0852	0.076	0.304	0.152	0.362	0.2857	0.0169	49,067	0.108

Table 5.3-2: Summary of mesh details for Series 05

Length (m)			Number of elements			y^+ range	
x	y	z	x	face	Total	y^+	z^+
0.900	0.304	0.1498	120	2400	288,000	1.58	13.17
0.540	0.304	0.0945	100	7310	731,000	2.47	9.67
0.590	0.304	0.0852	100	8100	810,000	2.19	8.24

Table 5.3-3: Summary of simulation details for Series 05

CASE	H/u_* (sec)	Estimated Simulation Time (sec)			Time step		Actual Time (sec)			LETOT Initial	LETOT Collect	LETOT Total
		Initial	Collect	Total	Δt	C_r	Initial	Collect	Total			
5a	5.00	2500	1250	3750	0.1000	0.250	3012	1004	4016	60	20	80
5b	5.20	200	100	300	0.0025	0.300	200	126	326	38	24	62
5c	5.03	195	95	290	0.0020	0.200	195	91	285	39	18	57

All cases are converged to within 5% of velocity and shear stress. Table 5.3-4 shows the exact results compared to experiment.

Table 5.3-4: Summary of simulation results for Series 05

	Experiment		ANSYS-CFX LES			%Error	
CASE	U_{avg} (m/s)	τ_{ave} (N/m^2)	U_{avg} (m/s)	U_{max} (m/s)	τ_{ave} (N/m^2)	U_{avg} %	τ_{ave} %
5a	0.059	0.0089	0.056	0.065	0.0086	-5.0	-3.4
5b	0.373	0.3291	0.370	0.448	0.3238	-0.8	-1.6
5c	0.362	0.2857	0.354	0.433	0.2853	-2.2	-0.1

5.3.1.1 Case 5a

Figure 5.3.1-1 shows contour plots of U_d/U_{max} , $\sqrt{V^2 + W^2}/U_{max}$ and streamlines of secondary circulations for case 5a. Firstly, it should be noted that the velocity contours are normal to the free surface due to the implementation of a symmetry plane. However, due to the high D_r of the channel (D_r=0.5), the velocity 'dip' would not be as prominent compared to that of a channel of a lower D_r. This is also confirmed by the vertical velocity profiles shown in Figure 5.3.1-3. It can be seen that even though a symmetry plane is implemented at the free surface the vertical velocity profiles in the main channel section compare well to experimental results in the lower ¾ of the profiles with variations only occurring as the free surface is approached. The profiles are within 3% of the experimentally measured values locally.

The implementation of a symmetry plane can also be seen from the distribution of secondary flow cells and the bisector of these cells at the main channel/floodplain interface being 45° to the internal corner.

Figure 5.3.1-2 shows profiles of U_d/U_{max} and τ_b/τ_{avg} for case 5a compared to experiment. It can be seen that the depth averaged velocity profile compares well to experiment especially in the main channel section. The computed velocity profile over predicts that of experiment in the floodplain with the maximum error locally between LES and experiment of 7%. The wall shear profile also compares well to experiment, this time with the LES computed values comparing better in the floodplain region than in the main channel. Peaks and troughs within the LES profile are more exaggerated than those of experiment with the profile looking extremely smooth. The peaks and troughs in Figure 5.3.1-2(b) can be explained by the secondary circulation cells shown in Figure 5.3.1-1(c). The large troughs in the wall shear profile at y=~0.10m are due to the small secondary flow cells at the main channel bed which can be seen in Figure 5.3.1-1(c).
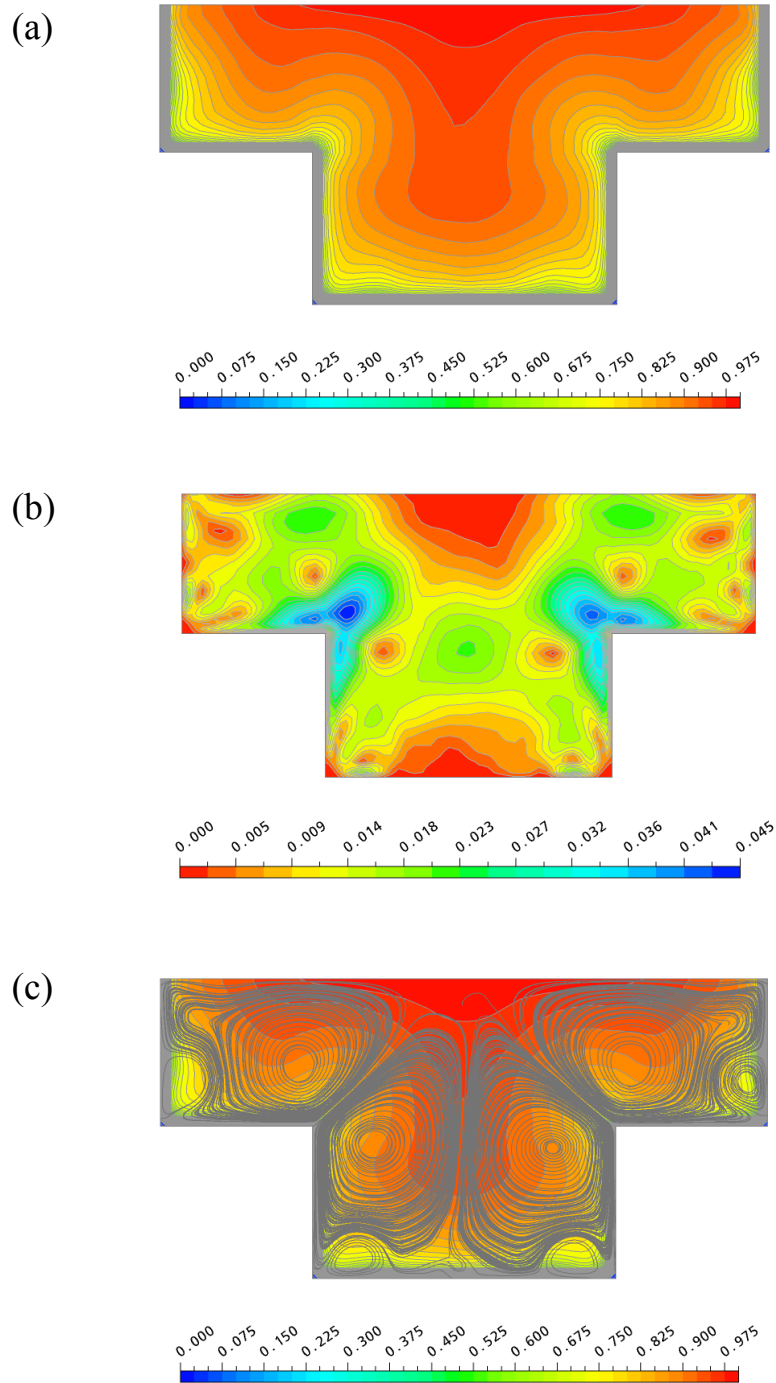
Figure 5.3.1-1: Contour plots of (a) U_d/U_{max} and (b) $\sqrt{V^2 + W^2}/U_{max}$, and (c) streamline plot of secondary circulations for case 5a
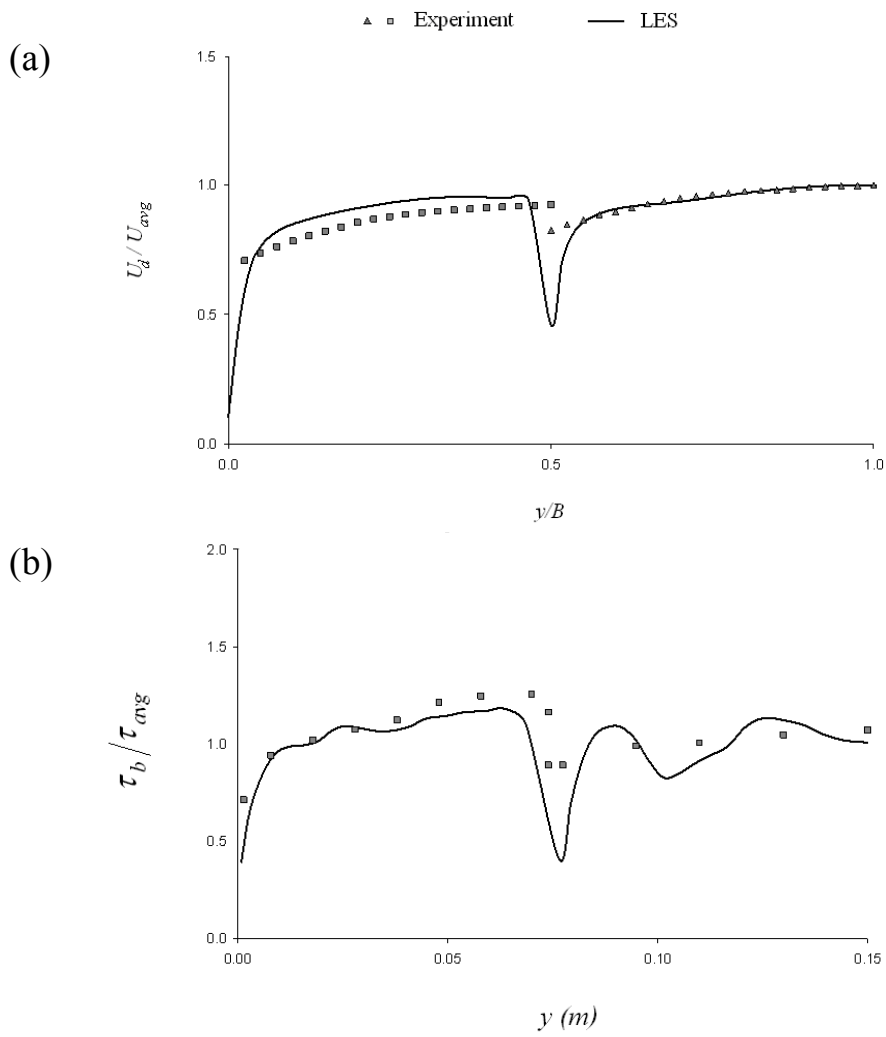
Figure 5.3.1-2: Profiles of (a) U_d/U_{max} and (b) τ_d/τ_{ave} for case 5a
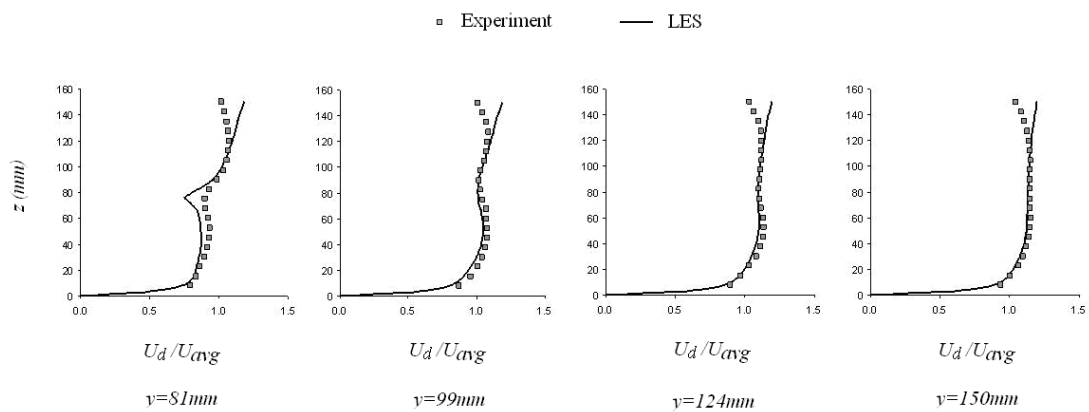
Figure 5.3.1-3: Velocity variation with depth and lateral position compared to experiment in

the main channel section; y=0, 26, 51 and 69mm for case 5a

176

5.3.1.2 Cases 5b and 5c

Figure 5.3.1-5(a) and Figure 5.3.1-6(a) show contour plots of U_d/U_{max} for cases 5b and 5c respectively. It can be seen that for both cases the maximum velocity is predicted below the free surface. With the maximum velocity occurring at $z/H = 0.783$ and 0.751 for cases 5b and 5c respectively.

Streamline plots of secondary circulation are shown in Figure 5.3.1-5(c) and Figure 5.3.1-6(c). Overall in both cases four circulation zones can be seen, two on the floodplain and two in the main channel section. Within the main channel region the vortex at the free surface is larger than that at the main channel bed/sidewall. The main channel cells are symmetric with the separation between the cells occurring at y/B=0.67 and 0.86 for cases 5b and 5c respectively. The distribution of secondary flow cells observed can be compared to the work of Cokljat (1993).

Cokljat (1993) used a non-linear $k-\varepsilon$ (NKE) model and a Reynolds stress model (RSM) following the approach of Launder, Reece and Rodi (1975), including additional terms to account for the effects of wall reflection to model open channel flow, and also implementing a specific boundary treatment for the free surface based on the modifications proposed by Naot and Rodi (1982) for adjusting ε. One geometry simulated by Cokljat (1993) corresponded to B/b=2.07 with D_r=0.243 and is used here for comparison to case 5b. The RSM and NKE results for this Cokljat (1993) case are shown in Figure 5.3.1-4 indicating four zones or circulation comparable to the LES results.

(a)   (b)
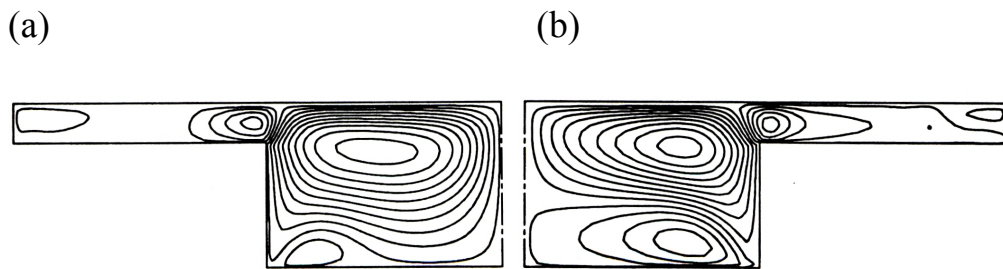
Figure 5.3.1-4: Secondary velocity streamlines (Cokljat 1993) for a relative depth of 0.243;

(a) RSM and (b) NKE.

Two dominant cells can be observed from Figure 5.3.1-4 in the main channel section with two further cells in the floodplain, similar to the results of cases 5b and 5c. The LES over-bank streamlines within the main channel are not very steady at the channel bed, however, structures similar to those of Cokljat (1993) can still be observed. Similar to case 4 the strongest secondary flow cells are generated from the junction edge to the free surface. The maximum magnitudes of these inclined upwards flows are 6.5% and 5.2% respectively, increasing as the D_r decreases (Figure 5.3.1-5(b) and Figure 5.3.1-6(b)).

(a)

(b)

(c)
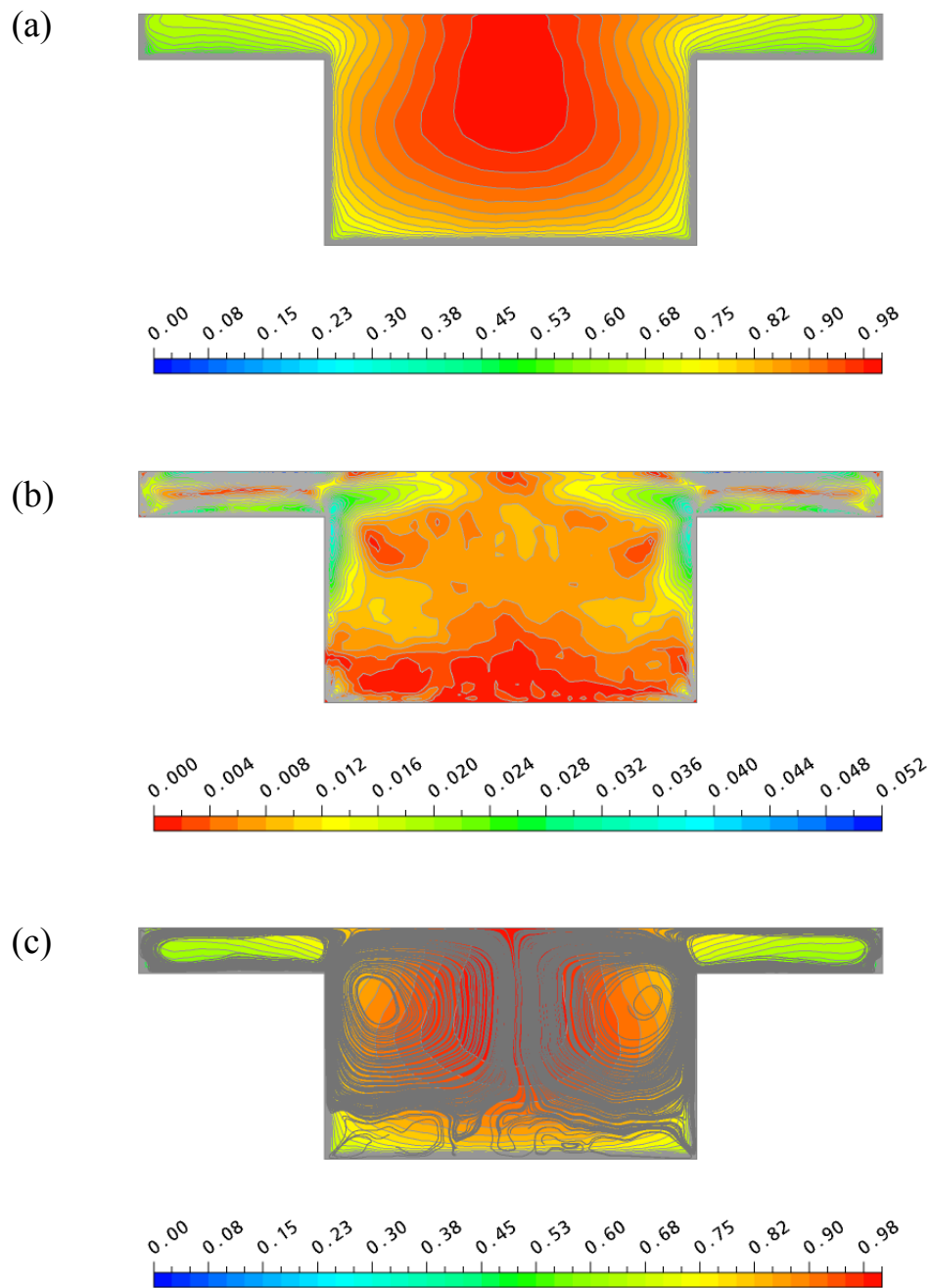
Figure 5.3.1-5: Contour plots of (a) U_d/U_{max} *and (b)* $\sqrt{V^2 + W^2}/U_{max}$, *and (c) streamline plot of secondary circulations for case 5b*

(a)

(b)

(c)
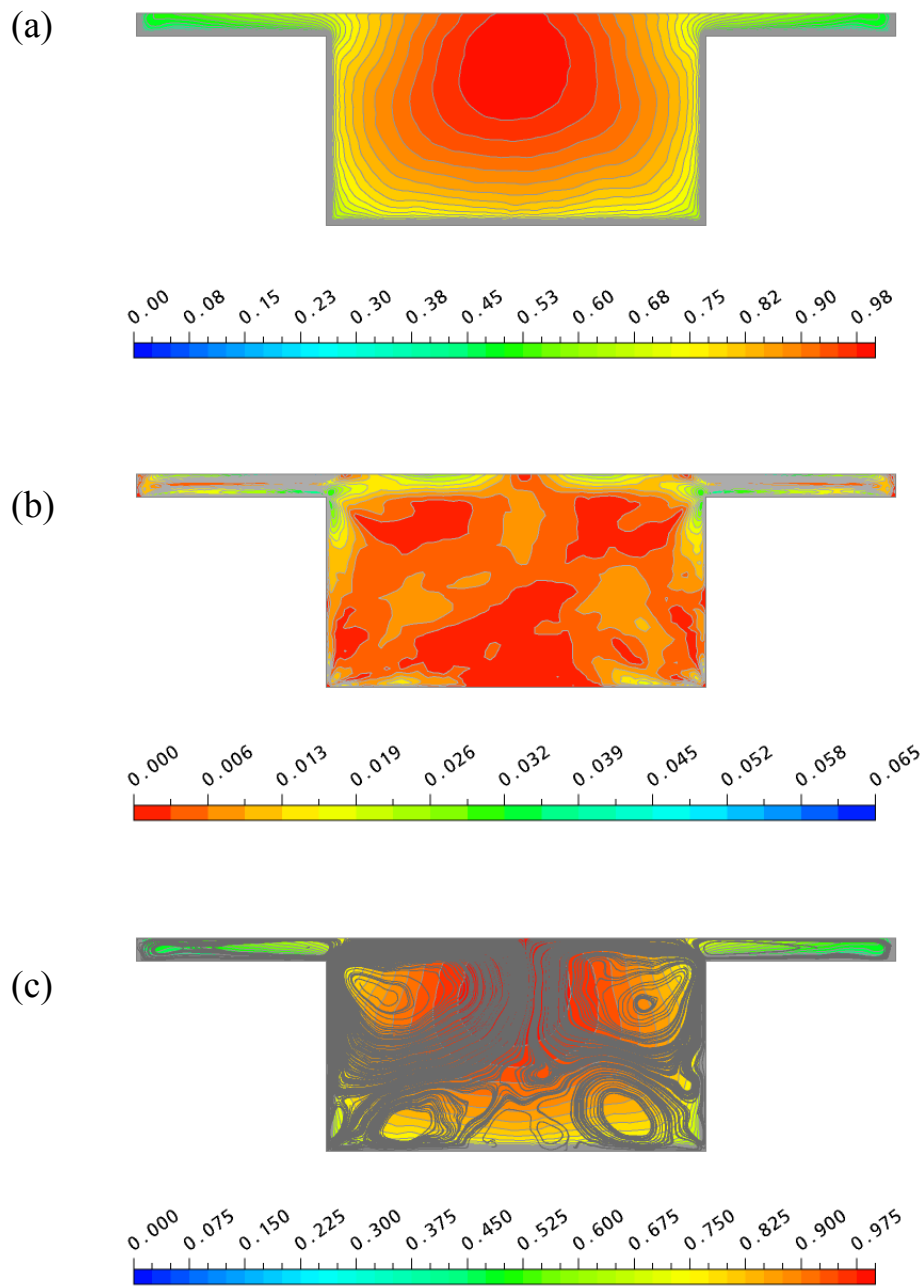
Figure 5.3.1-6: Contour plots of (a) U_d/U_{max} and (b) $\sqrt{V^2+W^2}/U_{max}$, and (c)

streamline plot of secondary circulations for case 5c

180

Turbulence statistics are shown in Figure 5.3.1-7 and Figure 5.3.1-8 for cases 5b and 5c. Contour plots of u'/u_*, v'/u_* v'/u_* and turbulence kinetic energy are shown. Again, like case 4, regions of high turbulence activity are seen at the side walls, bed surface and internal corner. Also, the influence of the free surface can be seen as the streamwise and spanwise values are spread parallel to the surface, whereas the vertical component reduces as the free surface is approached. Also, contours of u'/u_* can be seen to bulge upward near the junction edge.

Contour plots of $-uv/(u_*)^2$ and $-uw/(u_*)^2$ are shown in Figure 5.3.1-9 and Figure 5.3.1-11. The distributions are very steady and attain positive and negative peaks alternately at the junction edge. The signs of $-uv/(u_*)^2$ and $-uw/(u_*)^2$ also correlate well to that of $\partial U/\partial y$ and $\partial U/\partial z$ respectively.

Contour plots of $\omega = \dfrac{\partial W}{\partial x} - \dfrac{\partial U}{\partial z}$ are also shown in Figure 5.3.1-10 and Figure 5.3.1-12.
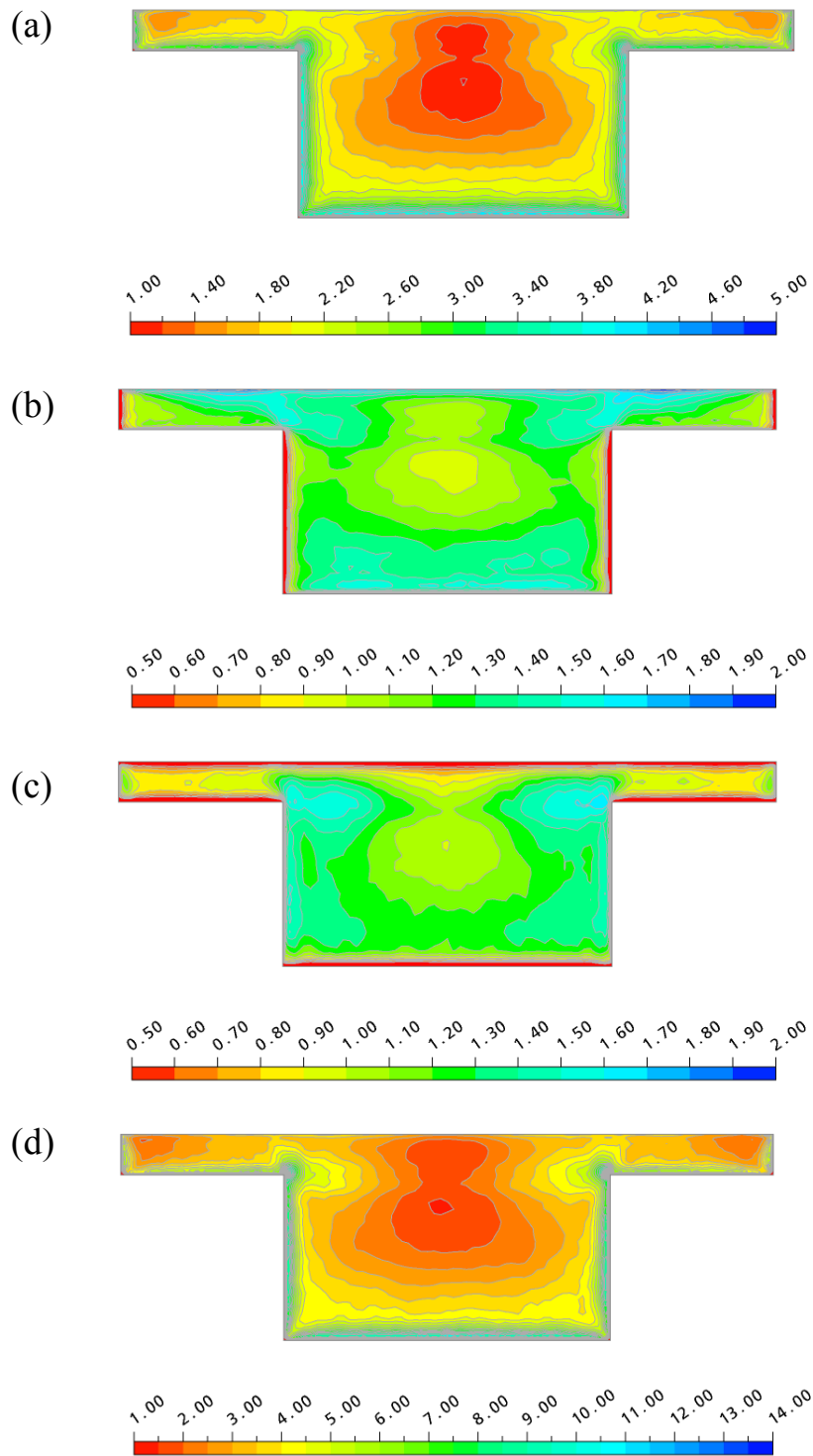
Figure 5.3.1-7: Contour plots of (a) u'/u_* , (b) v'/u_* , (c) w'/u_* and (d) turbulent kinetic energy for case 5b
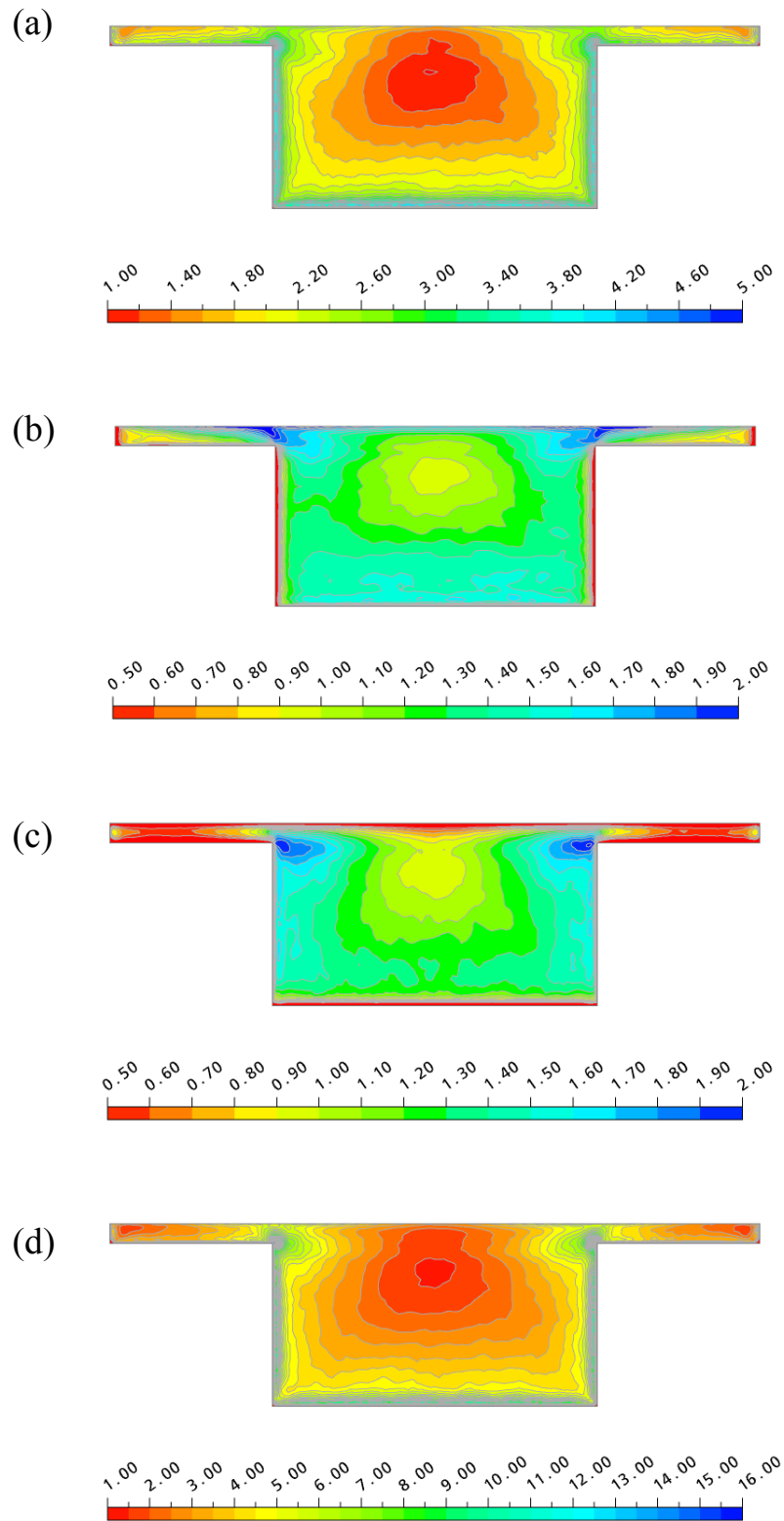
Figure 5.3.1-8: Contour plots of (a) $u^{'}/u_*$, (b) $v^{'}/u_*$, (c) $w^{'}/u_*$ and (d) turbulent kinetic energy for case 5b

(a)

(b)
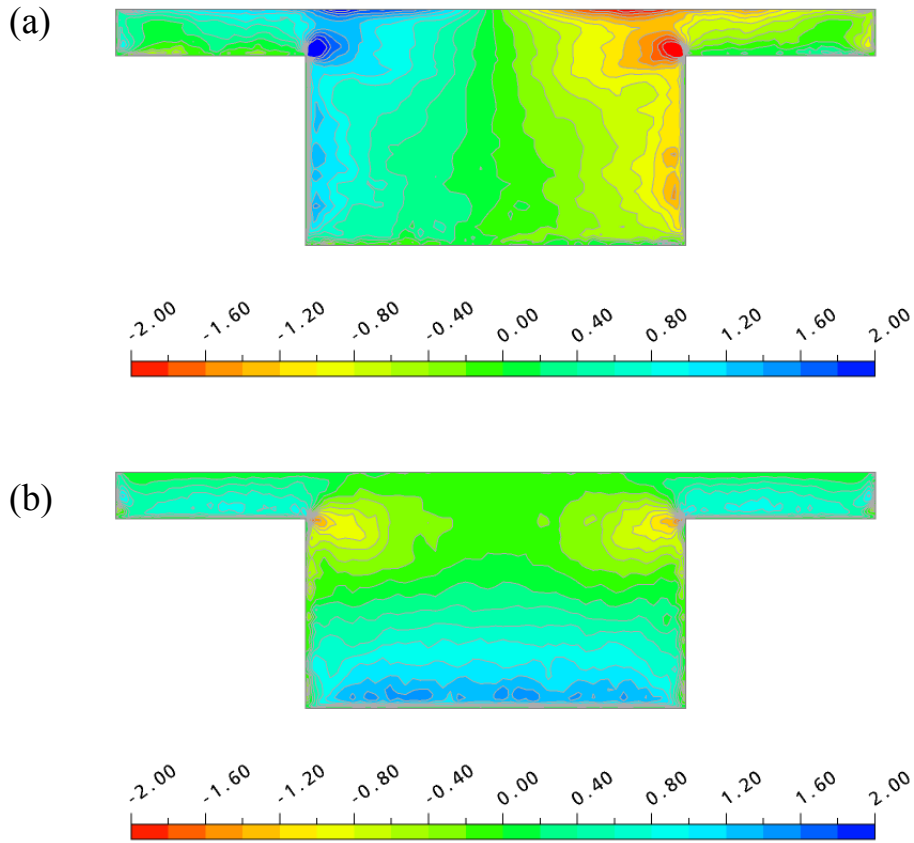
Figure 5.3.1-9: Case 5b: Contour plots of (a) $-uv/(u_*)^2$ *and (b)* $-uw/(u_*)^2$
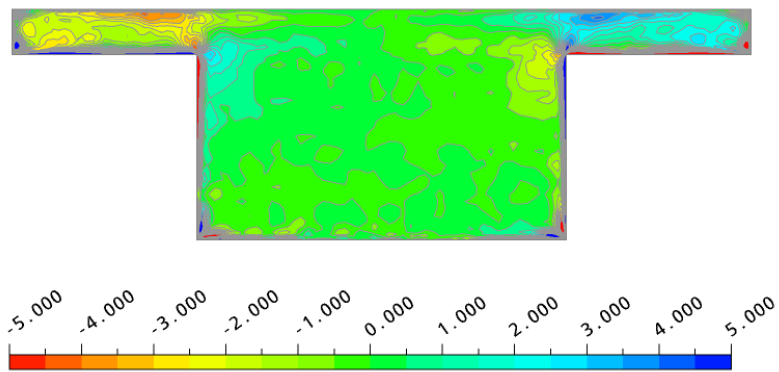
Figure 5.3.1-10: Contour plot of streamwise vorticity, $\omega = \dfrac{\partial W}{\partial x} - \dfrac{\partial U}{\partial z}$ *for case 5b*

(a)

(b)
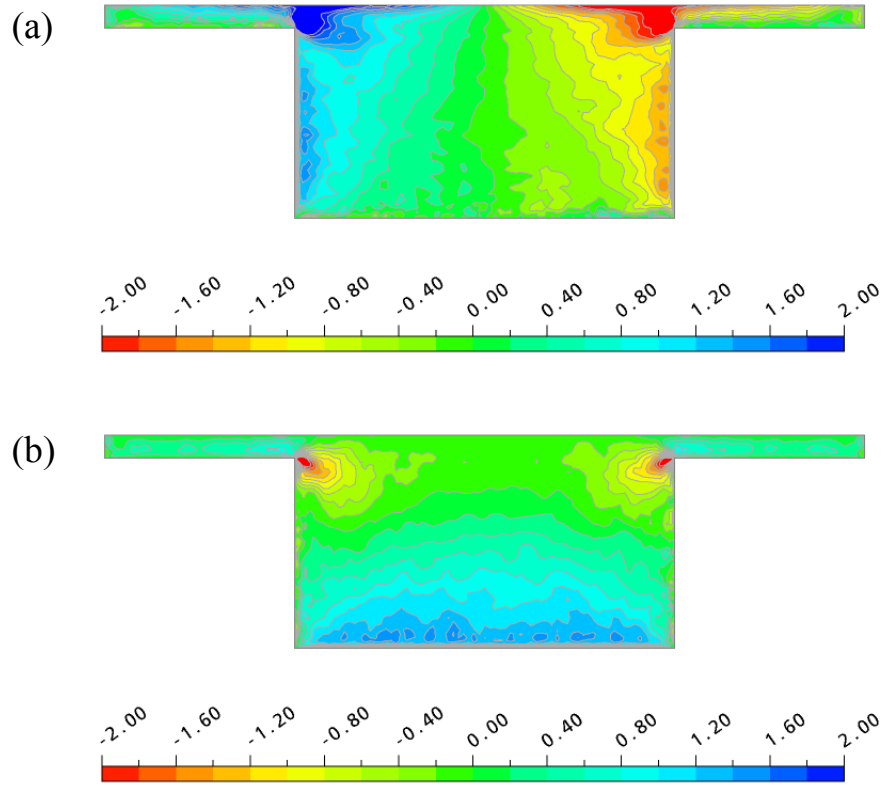
Figure 5.3.1-11: Contour plots of (a) $-uv\big/(u_*)^2$ *and (b)* $-uw\big/(u_*)^2$ *for case 5c*
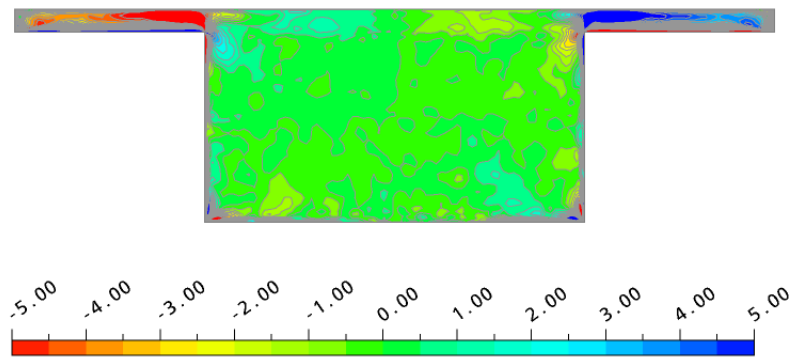
Figure 5.3.1-12: Contour plot of streamwise vorticity, $\omega = \dfrac{\partial W}{\partial x} - \dfrac{\partial U}{\partial z}$ *for case 5c*

Figure 5.3.1-13 shows velocity profiles for case 5b and 5c compared to experiment. The main channel sections compare better to experimental results than those on the floodplain. Experimental data is only available in case 5b for the floodplain region because, due the shallow floodplain depth of case 5c experimental results could not be obtained.
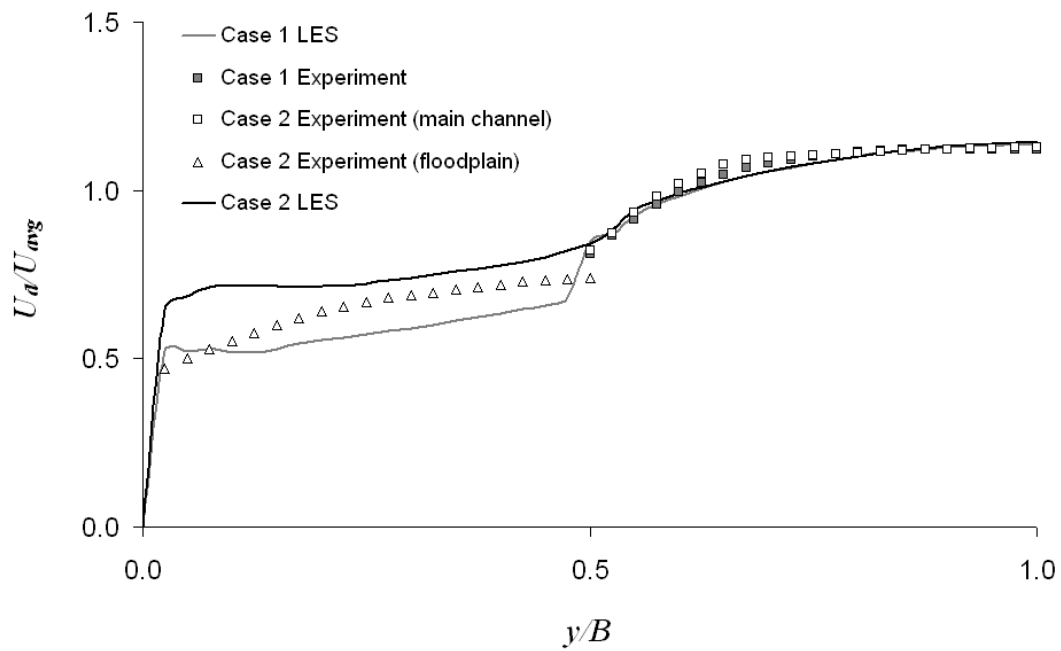
Figure 5.3.1-13: Velocity profiles for cases 5b and 5c

5.3.2 Series 04

The last compound channel in this section is comparable to the data of Series 04 of Knight and Demetriou (1984). The series is defined by a width ratio $B/b=4$ and this channel will be referred to as case 5d.

5.3.2.1 Case 5d

Case 5d is the same depth ratio as case 5a with an extended floodplain width. Also like case 5a this simulation was run with a symmetry plane implementation at the free surface, but at comparable R_e to experiment. The experimental and LES set-up values are summarised in Table 5.3-5 and the mesh and simulation time details are documented in Table 5.3-6 and Table 5.3-7.

Table 5.3-5: Summary of experimental values for case 5d

H	h	$2B$	$2b$	U_{avg}	τ_{ave}	u_*	R_e	D_r
(m)	(m)	(m)	(m)	(m/s)	(N/m^2)	(m/s)	-	-
0.1538	0.076	0.610	0.152	0.498	0.609	0.025	156,940	0.506

Table 5.3-6: Summary of mesh details for case 5d

Length (m)			Number of elements			y^+ range	
x	y	z	x	face	Total	y^+	z^+
0.900	0.304	0.1498	120	2400	288,000	1.58	13.17

Table 5.3-7: Summary of simulation details for case 5d

H/u_*	Estimated Simulation Time (sec)			Time step		Actual Time (sec)			LETOT Initial	LETOT Collect	LETOT Total
(sec)	Initial	Collect	Total	Δt	C_r	Initial	Collect	Total			
50	2500	1250	3750	0.1000	0.250	3012	1004	4016	60	20	80

As with previous cases Figure 5.3.2-1 and Figure 5.3.2-2 show normalized velocity and shear stress plots. Both plots compare well to experiment.
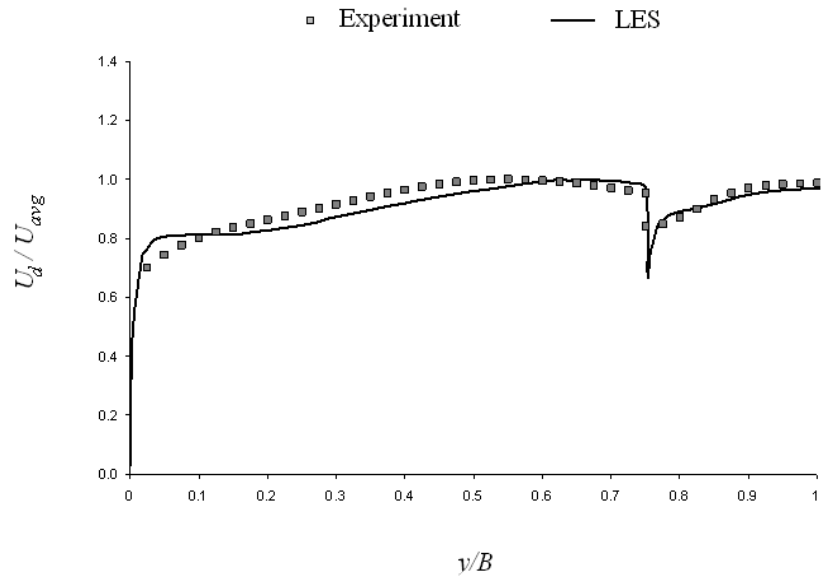
Figure 5.3.2-1: Velocity profiles for case 5d
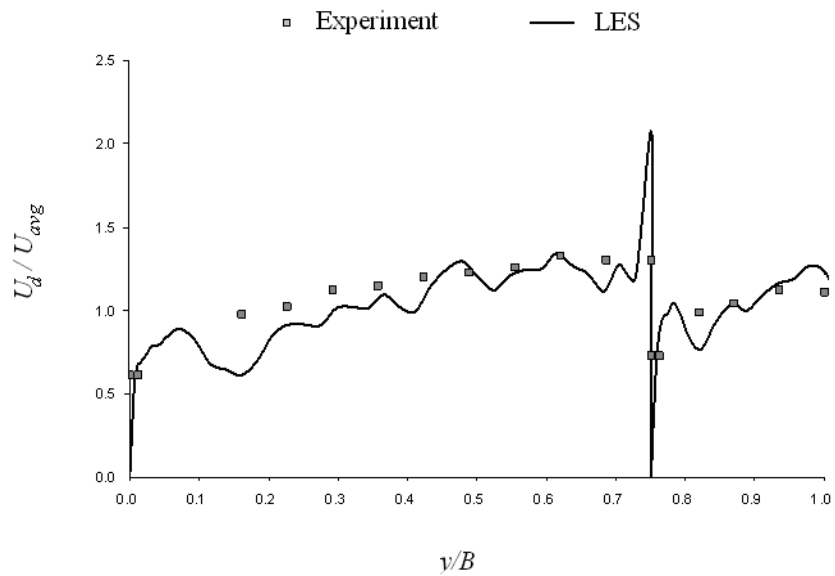
Figure 5.3.2-2: Bed shear stress profile for case 5d

Figure 5.3.2-3(a) shows contour plots of U_d/U_{max} for case 5d. Like case 5a the contours can be seen to be normal to the free surface due to the implementation of a symmetry plane at this boundary.

Figure 5.3.2-3(b) shows secondary circulation cells for case 5d. Comparing the secondary circulations to case 5a it can be seen that as the floodplain width increases three re-circulation cells can be observed on the floodplain in comparison to two for case 5a.

(a)

(b)
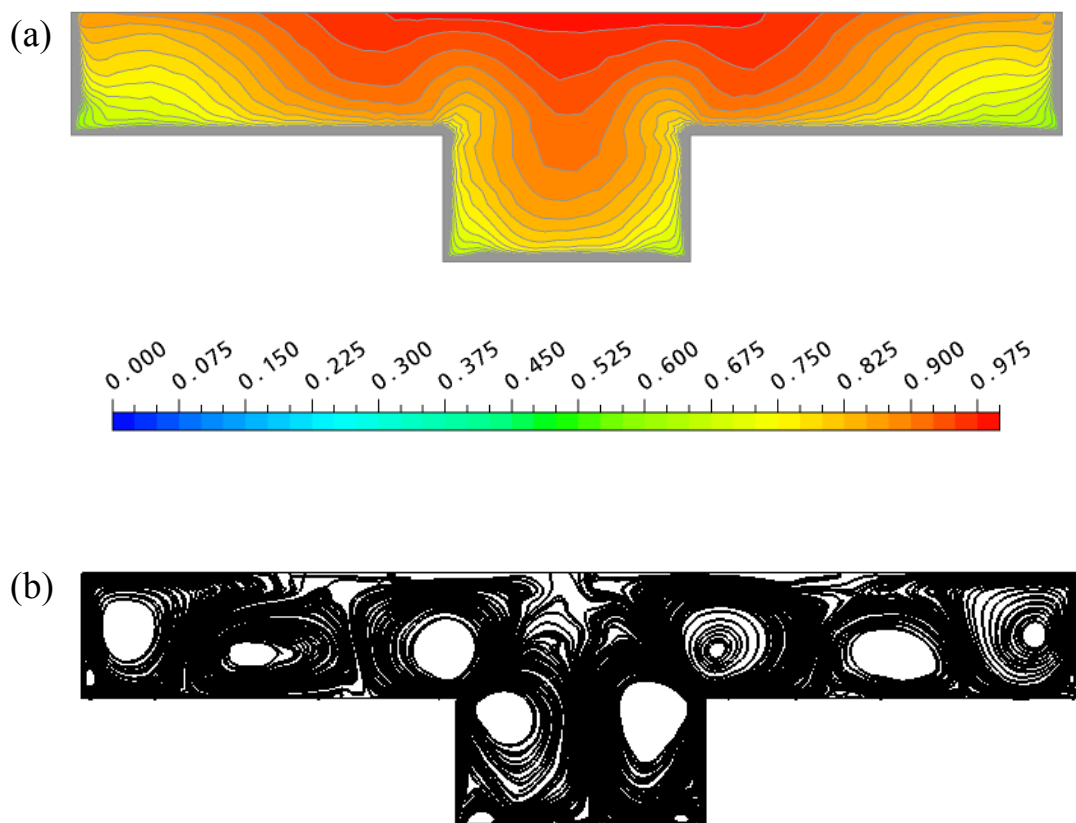
Figure 5.3.2-3: LES derived (a) contour plot of streamwise velocity and (b) streamline plot of secondary circulations for case 5d

This section has documented flow characteristic results for cases 5a to 5d and compared them, where possible, to experimental data. This is limited in some cases. The next section details SKM results derived from cases 5a to 5d and compares these with numerous empirical relationships for f, λ and Γ. Comparison to empirical values and relationships will provide further validation for the LES simulation results.

5.3.3 SKM Analysis

This section takes the results of case 4 and Series 05 and analyses them in terms of SKM parameters, f, λ and Γ. Comparison is also made to turbulent diffusive transport and mean convective transport due to secondary circulation as defined by Thomas and Williams (1995a; 1995b), with these being comparable to λ and Γ.

5.3.3.1 Friction Factor, f

The lateral distribution of friction factor, f, was computed and average values obtained for the main channel and floodplain sections. Figure 5.3.3-1 shows the lateral distribution of f for cases 5b and 5c and it can be seen that as the D_r decreases the friction factor on the floodplain increases, but the friction factor in the main channel is comparable for cases 5b and 5c. The variation across the width of the f profiles is due to the lateral variation across the channel width of the τ_b plots from which f is derived.
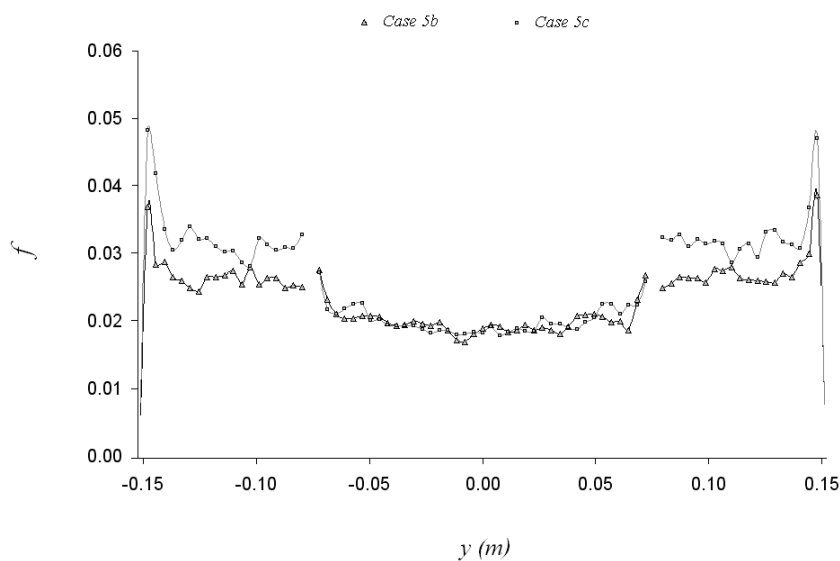
Figure 5.3.3-1: Lateral distribution of f for cases 5b and 5c

The ratio of the main channel and floodplain friction values has been investigated by Shiono and Knight (1991), resulting in Equation 5.1, which is the equation of the best fit line to experimental data of over-bank trapezoidal channels ranging from B/b=2-4.9.

$$f_{fp}/f_{mc} = -0.1065 + 0.8893 D_r^{-3/7} \qquad\qquad (5.1)$$

The average friction factors for the main channel and floodplain, f_{mc} and f_{fp} respectively are summarised in Table 5.3-8 for cases 5a to 5d. The results are compared with Equation 5.1 and it can be seen that the LES results compare more favourably to Equation 5.1 when the depth ratio increases. Also, the results compare extremely well for case 5d. However, as has been mentioned, Equation 5.1 is the equation of the best fit line fitted to experimental results ranging from B/b=2-4.9. Looking more closely at the scatter of the actual data it can be seen that the fitted equation more closely relates to values from channels at $B/b \geq 4$, such as case 5d. Therefore, for a more accurate comparison actual point values from the data of Shiono and Knight (1991) for a series of channels at B/b=2 were extracted, giving f_{fp}/f_{mc} values of ~1.72, 1.31, 1.13 for depth ratios 0.0875, 0.238 and 0.525 respectively, which more closely compare to the LES computed results than Equation 5.1.

Due to only 4 cases being investigated in comparison to the empirical relationship of Shiono and Knight (1991) here, to further investigate f_{fp}/f_{mc} values, extracting data from only one channel over various depths was investigated.

Table 5.3-8: Summary of LES derived friction factors for Series 05

CASE	D_r	f_{mc}	f_{fp}	LES f_{fp}/f_{mc}	Eq.5.1 f_{fp}/f_{mc}
5c	0.108	0.020	0.033	1.608	2.202
5b	0.196	0.020	0.027	1.347	1.681
5a	0.493	0.023	0.027	1.214	1.098
5d	0.506	0.016	0.018	1.079	1.084

Data was extracted over varying depths across the channel cross-section of case 5a. Figure 5.3.3-2 shows the ratio of the computed friction factor in the floodplain to the main channel after averaging over varying depths compared with empirical formula, Equation 5.1. The error between LES and empirical formula ranges from 2%-11% and the trend of f_{fp}/f_{mc} can be seen to be predicted well.
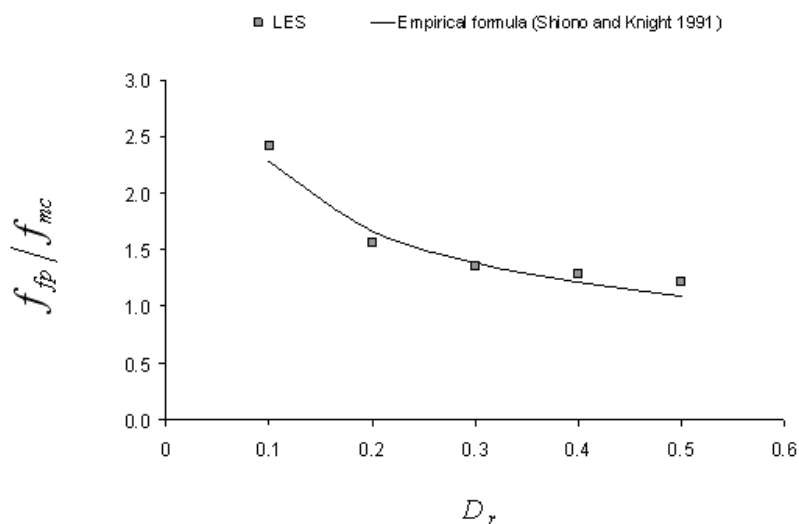
Figure 5.3.3-2: Comparison of average LES derived friction factor for case 5a and experimentally derived values (Shiono and Knight 1991)

5.3.3.2 Dimensionless Eddy Viscosity Coefficient, λ

Shiono and Knight (1991) derived values for λ from experimental data of an over-bank trapezoidal channel and concluded that the dimensionless eddy viscosity coefficient was relatively constant in the main channel and in the order of 0.07 for varying Reynolds numbers. The values of average LES derived λ for the main channel sections are 0.0902, 0.0751, 0.0638 and 0.0514 for cases 5c, 5b, 5a and 5d respectively, therefore in comparison with the stated value of 0.07. However, the above indicates a large variation within λ of $\pm$ 30% of the value stated by Shiono and Knight (1991).

Figure 5.3.3-3 shows the lateral distribution of λ from LES results and it can be seen that comparable to the main channel region values of λ within the floodplain are a lot more variable.
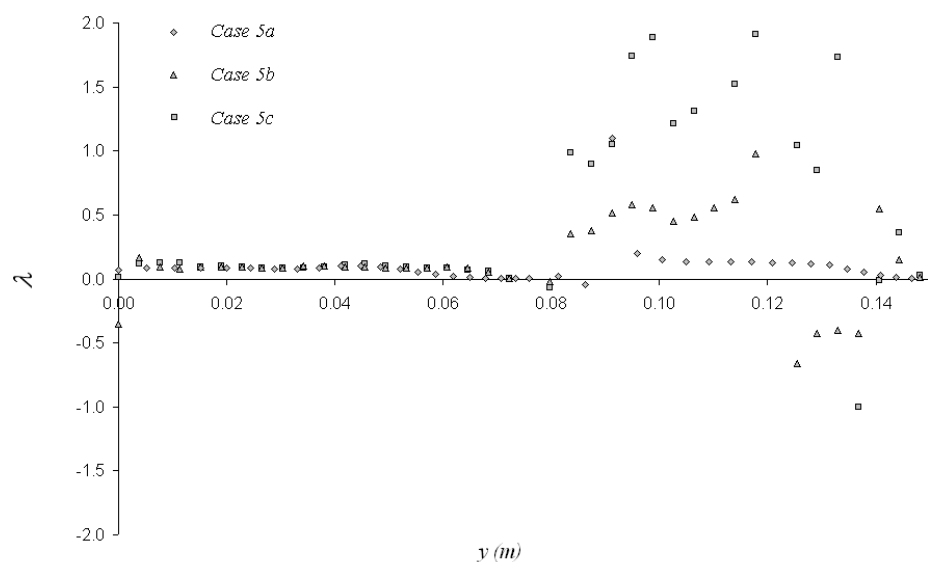
Figure 5.3.3-3: Lateral distribution of λ for cases 5a, 5b and 5c

The values of λ can be seen to decrease with increase in floodplain height, which is to be expected as the lower the depth ratio the greater the lateral shear at the main channel/floodplain interface. Average values of λ were also computed for the floodplain section and are 1.2962, 0.4513, 0.1097 and 0.2602 for cases 5c, 5b, 5a and 5d respectively. These values can also be seen to decrease with increasing floodplain depth, other than for case 5d.

Abril and Knight (2005) showed that the SKM is not very sensitive to the variation of λ across the channel and that the proposed constant value of $\lambda = 0.07$ can be used in the main channel region, together with Equation 5.2 for the description of λ in the floodplain region.

$$\lambda_{fp} = \lambda_{mc}(-0.2 + 1.2D_r^{-1.44}) \tag{5.2}$$

Where, in this case D_r is defined as $D_r = h_l/H$, where h_l is the local depth. It can be seen that Equation 5.2 will predict two distinct values, one for the main channel at $D_r = 1$, as $h_l = H$ and one for the floodplain for rectangular open channels with vertical channel and floodplain sidewalls, as $h_l = h$. Table 5.3-9 compares the results from Equation 5.2 with the average values across the floodplain region for cases 5a, 5b, 5c and 5d. It can be seen that the LES computed λ_{fp} values are lower than those computed using Equation (5.2). However, the average shear stress on the main channel/floodplain interface is computed in the next section for comparison of the contribution of mean convective transport due to secondary circulation and turbulent diffusive transport to total apparent shear stress. The values in Figure

5.3.1-11 computed for the normalised $-\overline{uv}$ term of, 0.133, 1.048 and 2.044 compare better to the λ_{fp} values from Equation 5.2.

Table 5.3-9: Comparison of LES derived and empirical relationship average λ_{fp} values for

cases 5a, 5b, 5c and 5d

D_r	λ_{mc}	λ_{fp}	
	LES	Eq. 5.2	LES
0.108	0.090	2.650	1.296
0.196	0.075	0.923	0.451
0.500	0.064	0.195	0.110
0.506	0.051	0.153	0.260

As was also mentioned in Section 2.6.3.2 Shiono and Knight (1991) derived a ratio for $\lambda_{fp}/\lambda_{mc}$ in Equation 2.6.18 of $\lambda_{fp}/\lambda_{mc} = (2D_r)^{-4}$. $\lambda_{fp}/\lambda_{mc}$ ratios are computed from the LES results and compared to Equation 2.6.18, these can be seen in Table 5.3-10

Table 5.3-10: Comparison of LES derived and empirical λ values

D_r	λ_{mc}	λ_{fp}	$\lambda_{fp}/\lambda_{mc}$ LES	$\lambda_{fp}/\lambda_{mc}$ Eq. 2.6.18
0.108	0.090	1.296	14.400	456.39
0.196	0.075	0.451	6.013	42.35
0.500	0.064	0.110	1.719	1.00
0.506	0.051	0.260	5.098	0.95

It can be seen that Equation 2.6.18 overestimates the ratio of $\lambda_{fp}/\lambda_{mc}$ especially at lower D_r compared to LES data, with the value derived from Equation 2.6.18 being extremely large.

5.3.3.3 *T* and *J* Components

Regarding over-bank channel research the turbulence characteristics of two-dimensional flow in an open channel have been well established by Nezu and Rodi (1986). However, when the flow is three dimensional, as in the case of over-bank channels the turbulent structure and boundary shear stress distribution are more complex and the boundary shear stress differs from the standard two-dimensional value, $\rho g H S_0$. The difference being due to transverse gradients in the additional shear stresses arising from lateral shear and secondary flow, termed apparent shear stress (Shiono and Knight 1991). Thomas and Williams (1995a; 1995b) investigate apparent shear stress in terms of two components T and J, where T represents turbulent diffusive transport (Reynolds stress/lateral shearing) and J corresponds to the mean convective transport due to secondary circulation. Components T and J are defined in Equations 5.3-5.4 respectively and can be related to the SKM parameters, were T can be related to λ and J to Γ.

$$T = \frac{1}{H}\int -\overline{uv}\,dz \qquad\qquad (5.3)$$

$$J = \frac{1}{H}\int -\overline{U}\,\overline{V}\,dz \qquad\qquad (5.4)$$

where *u* and *v* are the turbulent perturbations of velocity with respect to the mean. Firstly, case 4 is examined to validate further the ANSYS-CFX LES as T and J components are available for comparison from Cater and Williams (2008). Figure 5.3.3-4 shows a comparison between ANSYS-CFX LES simulated T and J components and those reported by Cater and Williams (2008).

(a)

(b)
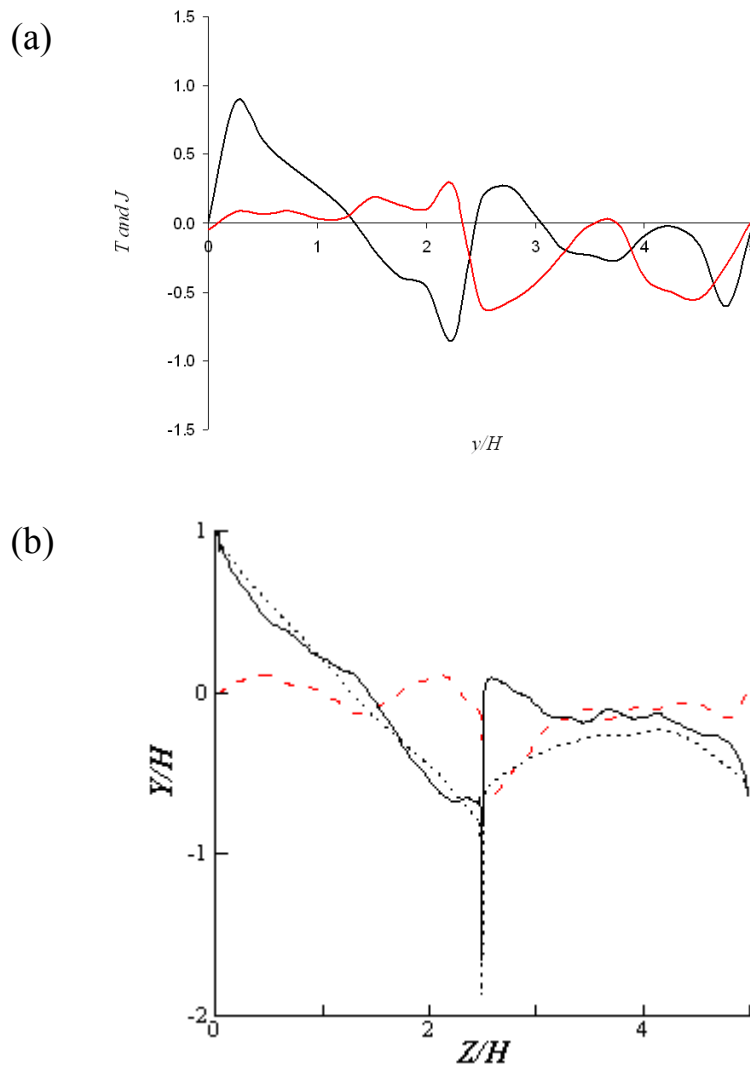
Figure 5.3.3-4: Lateral distribution of (a) ANSYS-CFX LES derived T (--) and J (--)

components , compared to (b) Cater and Williams (2008) derived apparent shear stress τ_a =

T + J; Turbulent stress component T (---), secondary circulation component J (- - -), and

total T + J (——)

Over most of the floodplain the apparent stress is dominated by the secondary current component J. The average stress on the partial wall at the interface was simulated as -1.053 u_*^2 and the mean stress over the floodplain interface is -0.700 u_*^2.

Cater and Williams (2008) simulated values of $-1.06\,u_*^2$ and $-0.655\,u_*^2$, which are comparable to the ANSYS-CFX LES results to within 0.66% and 6.8% respectively.

T and J components are shown for all cases in Series 05 in Figure 5.3.3-5. For all cases it can be seen that the apparent stress ($T+J$) in the main channel section has developed a monotonic profile with nearly constant gradient, with all cases passing through $2y/B=0$ as the channels are symmetric. The apparent stress in the main channel for all cases is carried mostly by the Reynolds stress component (cases 5b and 5c); however the main carrying mechanism within the floodplain varies from case to case. For cases 5b and 5c the secondary current component is dominant within the floodplain except near the right sidewall and very close to the main channel/floodplain interface where the Reynolds stress component dominates. However, in case 5a the main stress carrying mechanism is the secondary current component J, for half the floodplain width, until the Reynolds stress component becomes dominant. For case 5d the main stress carrying mechanism varies from J to T to J, with each spanning a third of the floodplain reach.
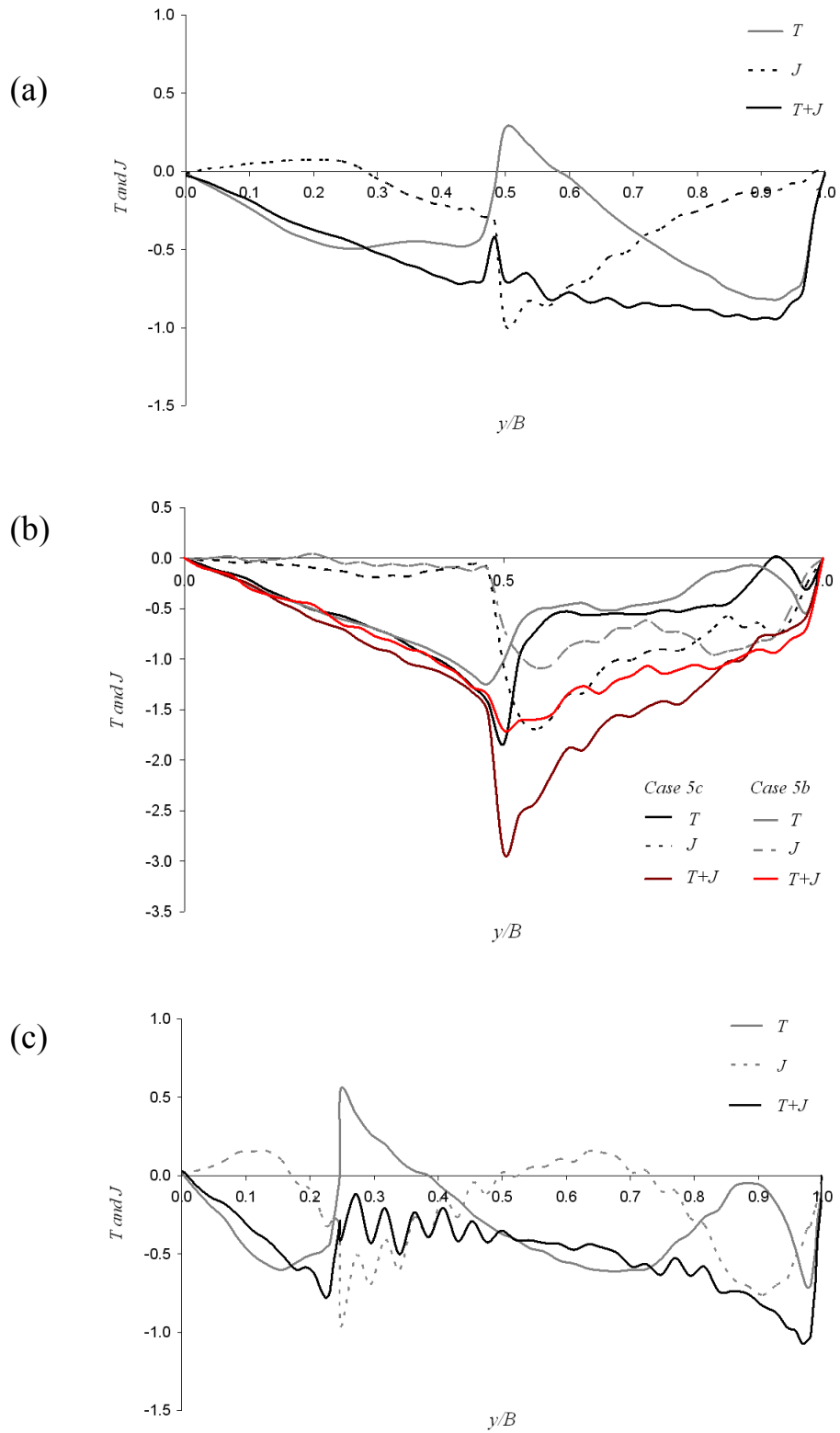
Figure 5.3.3-5: Lateral distribution of T and J components for case (a) 5a, (b) 5b and 5c and (c) 5d

From Figure 5.3.3-5 it can be seen that over the floodplain the apparent stress is dominated by the Reynolds stress component T in the first half and then in the second half of the floodplain as the floodplain wall is approached the secondary current component J is dominant. The reversal in stress carrying mechanism is characteristic of the floodplain systems: the Reynolds stress component is derived from lateral velocity gradients and diminishes quite rapidly with distance into the floodplain, the secondary circulation however is the result of streamwise vorticity distribution across the entire width of the floodplain and varies much more slowly (Thomas and Williams 1995b). The position of the cross-over point depends on the relative magnitudes of T and J near the interface. Cases 5a and 5d are at a high depth ratio, therefore have a relatively deep floodplain compared to the main channel and the velocity gradient in the interface region is not as strong as it would be for a shallower floodplain flow. Therefore the cross-over point is pushed closer to the interface than the floodplain sidewall in both cases.

Figure 5.3.3-6 shows a comparison of the T and J components for cases 5a, 5b and 5c where the values are averaged values across the channel half section. As mentioned above it can be seen that as the depth ratio decreases the velocity gradient in the interface region is greater than at a larger D_r so the Reynolds stress component is stronger in these cases. The secondary current component J also shows a significant increase at the interface region. The distributions of T are quite different from each other at $D_r=0.108$ and $D_r=0.50$. The value of T attains a large negative peak very near the junction edge for case 5c, $D_r=0.108$ and a small positive peak for case 5a, $D_r=0.50$. These results compare with those of Tominaga et al. (1989) for channels of $D_r=0.24$ and $D_r=0.50$. Tominaga et al. (1989) also showed

that the absolute value of J is greater than that of T at the main channel/floodplain interface for $D_r = 0.50$. However, for $D_r = 0.24$, T is greater than J in the main channel, but smaller than J on the floodplain.
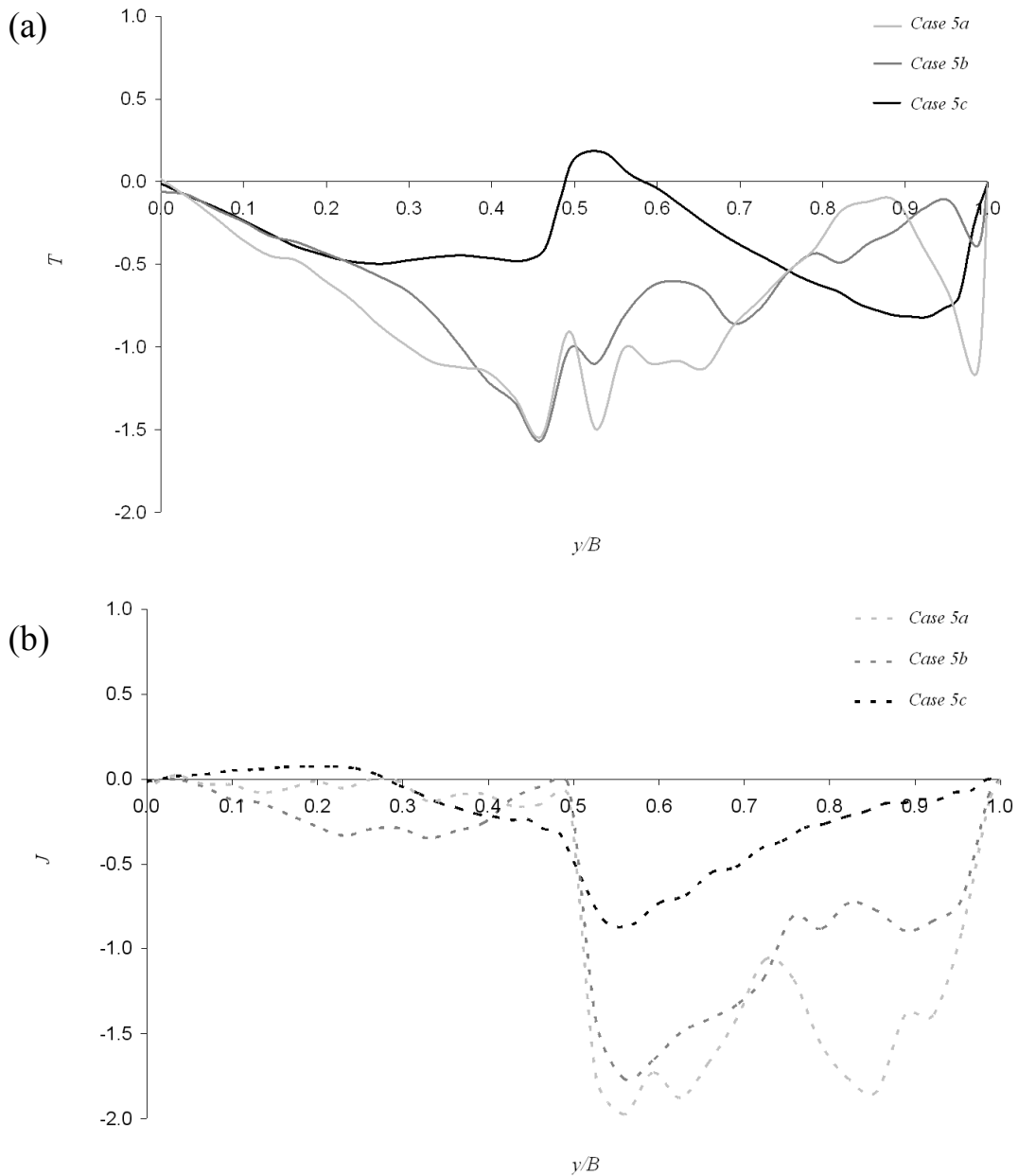
Figure 5.3.3-6: Lateral distribution of (a) turbulent stress component, T and (b) secondary circulation component, J for Cases 5a, 5b and 5c

In order to investigate the contributions of both T and J in the interface region the average shear stress at the main channel/floodplain is computed and shown alongside the average stress on the partial main channel wall(s) in Table 5.3-11 below for cases 4, 5b and 5c.

Table 5.3-11: Mean shear stress on partial wall and at the interface for cases 4, 5b and 5c

CASE	D_r	Mean shear stress	
		Partial Wall	Main channel/ floodplain interface
4	0.500	$1.053\,u_*^2$	$\pm\,0.700\,u_*^2$
5b	0.198	$1.107\,u_*^2$	$\pm\,1.746\,u_*^2$
5c	0.108	$1.233\,u_*^2$	$\pm\,3.145\,u_*^2$

It can be seen that as D_r decreases the interfacial shear at the main channel/floodplain increases and becomes greater than that of the mean shear on the partial wall. The percentage contributions to the apparent shear stress from both the Reynolds stress term and secondary circulation term are shown in Table 5.3-12.

Table 5.3-12: Apparent shear stress components for cases 4, 5b and 5c

CASE	D_r	Apparent shear stress contributions % of Mean shear stress	
		$-\overline{U}\,\overline{V}$	$-\overline{uv}$
4	0.500	81%	19%
5b	0.198	40%	60%
5c	0.108	35%	65%

The contribution of secondary current component can be seen to decrease with decreasing D_r compared to that of an increased contribution from the Reynolds

stress. This compares to the statement of van Prooijen (2004) that the momentum exchange at the interface is not dominated by secondary circulations.

The percentage contributions can also be seen to be similar for cases 5b and 5c as they are of similar D_r. Rajaratnam and Ahmadi (1981) indicated that the apparent shear stress became extremely large as D_r decreased. They stated that $T + J$ became equal to ~$10\,u_*^2$ at D_r=0.1. Table 5.3-12 shows that for case 5c reported at D_r=0.108 an absolute value of $3.145\,u_*^2$ is reached.

5.3.4 Secondary Flow Term, Γ

The secondary flow cell distributions for cases 5a, 5b, 5c and 5d are re-shown in Figure 5.3.4-1.
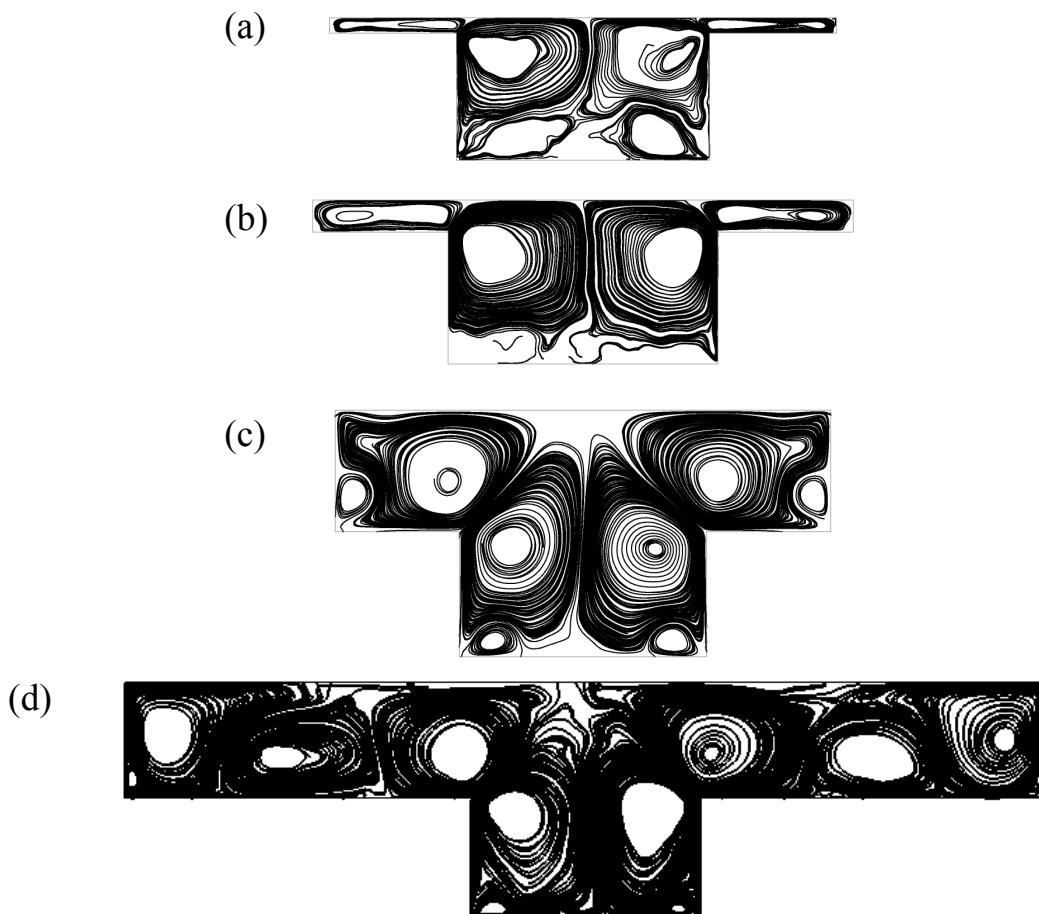
Figure 5.3.4-1: LES derived streamline plots of velocity transient average for cases (a) 5c, (b) 5b, (c) 5a and (d) 5d

The secondary flow term, Γ, corresponds to the lateral gradient of the force due to secondary flow and is comparable to J. Figure 5.3.4-2 shows the lateral distributions of $\left(\overline{UV}\right)_d$ for cases 5b and 5c.

(a)

(b)
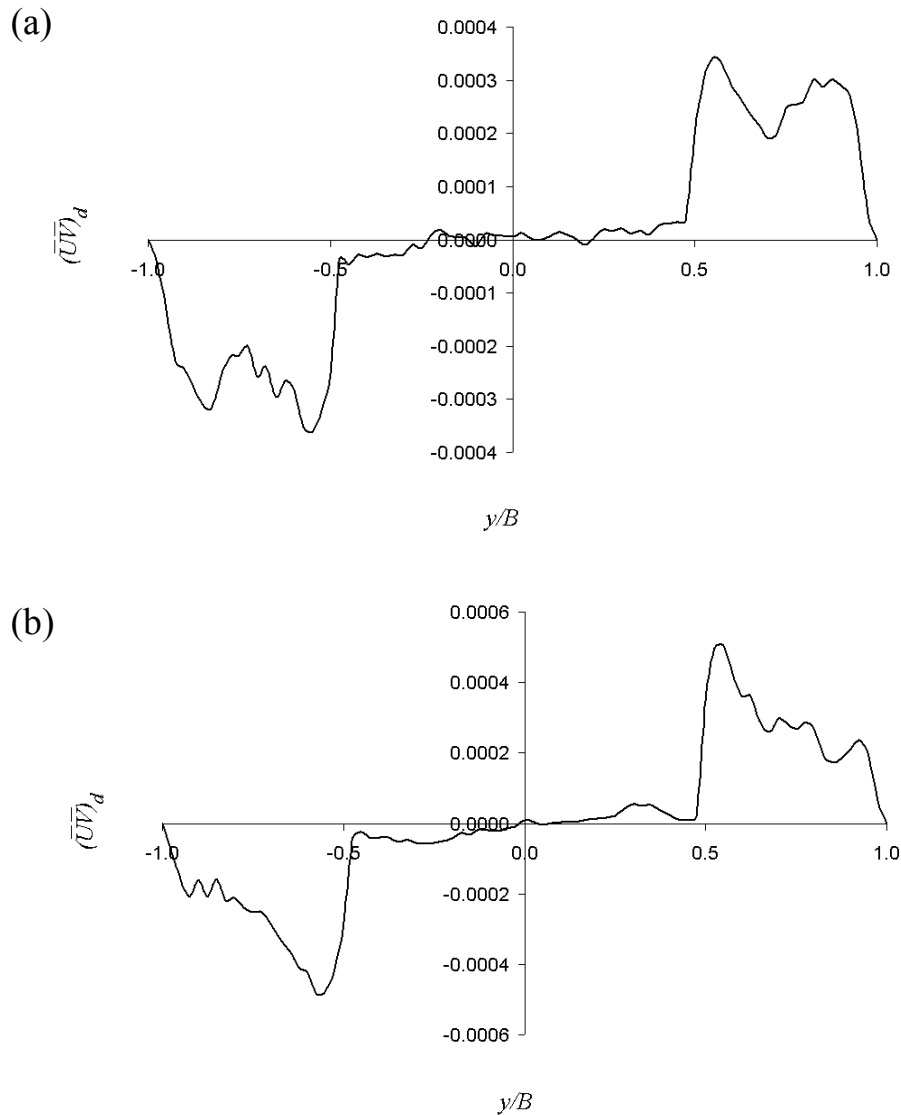
Figure 5.3.4-2: LES derived lateral distribution of $\left(\overline{UV}\right)_d$ for cases (a) 5b and (b) 5c

It can be seen that for case 5b there are large depressions in the $\left(\overline{UV}\right)_d$ profile at approximately the centre of the floodplain, corresponding to the splitting of the large secondary flow cell into two as seen in Figure 5.3.4-2(a). Case 5c can also be seen

to have depressions in the floodplain region, this time closer to the floodplain sidewall, also corresponding to the splitting of the floodplain secondary flow cell.

Analytical solutions other than those detailed in Chapter 2 have been derived by Mazen (2005) for Γ in over-bank channel flow. Analytical expressions for the variation of the secondary flow term were investigated based on the variation of a factor k which represents the ratio of average bed shear stress to two-dimensional shear stress, $\rho g H S_0$. Empirical values of k were derived and could be related back to the secondary flow term, producing a derivation of Γ, shown in Equations 5.5 and 5.6.

$$\Gamma_{mc} = \rho g H S_o \left\{ 1 - \left[\frac{\left(0.8911 - 0.0156 \frac{B}{b} \right)}{-Dr\left[-4 + 3.3812\left(\frac{B}{b}\right) - 0.8248\left(\frac{B}{b}\right)^2 + 0.0625\left(\frac{B}{b}\right)^3 \right]} \right] \right\} \tag{5.5}$$

$$\Gamma_{fp} = \rho g S_o (H-h)\left\{ 1 - \left[\frac{\left(1+0.1s_c\right) + 0.115\left(2 - num_{fp}\right)}{+ \frac{0.0189(B/b)^4 - 0.3108(B/b)^3 + 1.8172(B/b)^2 - 4.5053(B/b) + 4.0612}{Dr}} \right] \right\} \tag{5.6}$$

Equations 5.5 and 5.6 can be seen to be a function of the channel geometry, water level, density and longitudinal slope. These expressions are derived based on the assumption that the depth averaged Reynolds shear stress is only significant inside the shear layer region at the main channel/floodplain region and outside of this it is negligible (Knight and Shiono 1996). These empirical equations were developed from FCF data where $2.2 \leq B/b \geq 6.7$ and $2b/h = 10$. Cases 4, 5b and 5c reported here are at $B/b = 2$ and $2b/h = 2$, therefore fall outside of this range. Mazen (2005) examined the applicability of these equations to other data sets, including those of

cases 4, 5b and 5c, concluding that if either B/b or $2b/h$ fall outside of the limits of that of the FCF data then the values would not be predicted well. Therefore, these equations are not utilised here as they have been shown to inadequately describe the secondary circulation term for the geometries studied.

Abril and Knight (2004) also reported expressions for Γ in over-bank channels where:

$$\Gamma_{mc} = 0.15\rho g H S_0 \tag{5.7}$$

$$\Gamma_{fp} = -0.25\rho g h S_0 \tag{5.8}$$

These were also utilised by McGahey (2006) for application to natural rivers. The values are computed along with those for cases 4, 5b and 5c in Table 5.3-13.

Table 5.3-13: LES derived average Γ_{mc} and Γ_{fp} compared to Equations 5.7 and 5.8

CASE	D_r	LES derived		Equations 5.7 and 5.8	
		Γ_{mc}	Γ_{fp}	Γ_{mc}	Γ_{fp}
4	0.500	0.0091	-0.0066	0.004	-0.003
5b	0.198	0.0502	-0.0433	0.446	-0.180
5c	0.108	0.0366	-0.0313	0.121	-0.180

The Γ values derived from the LES results can be seen to be lower than those of Equations 5.7 and 5.8 for cases 5b and 5c, but higher for case 4. Some variability is expected with case 4 as it was simulated using a symmetry plane, however, cases 5b and 5c under-predict Γ_{fp} results by up to 89% compared to Equation 5.8. The derivation of Γ is based on the gradient of the $H(\overline{UV})_d$ profile and looking at

Figure 5.3.4-2 it can be seen that this value will fluctuate between positive and negative sign across the channel due to the undulations in the $(\overline{UV})_d$ profile shown. The Γ distribution for case 5b is shown in Figure 5.3.4-3. Therefore, prescribing an average over both main channel and floodplain regions is not representative of the actual distribution.
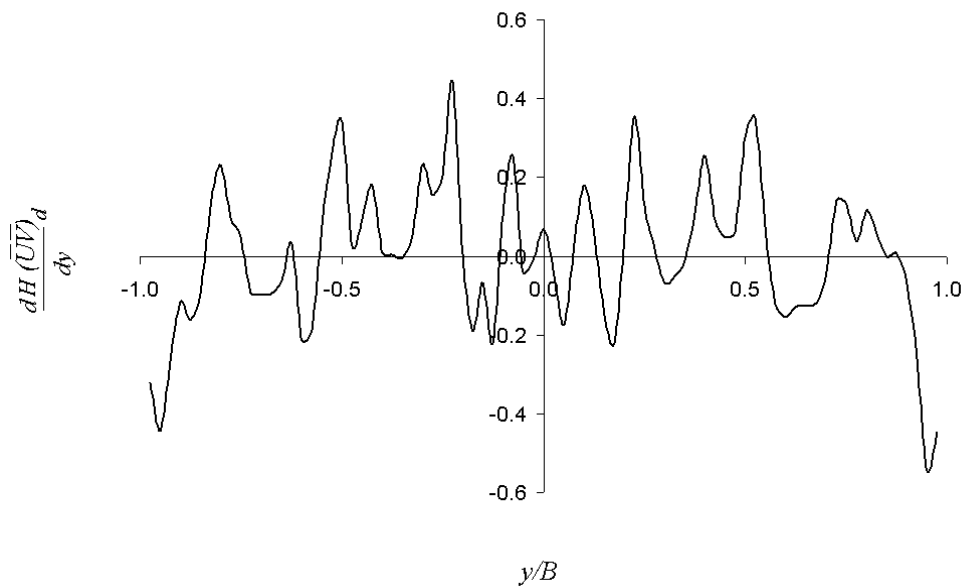
Figure 5.3.4-3: LES derived lateral distribution of Γ for case 5b

The secondary flow term, Γ is derived from the prediction of secondary circulation cells and if these cells are not steady an accurate prediction of Γ will not be obtained. From Figure 5.3.4-1 it can be seen that the secondary flow cell distributions for cases 5b and 5c are not as steady as those of 5a and 5d, impacting the derivation of Γ. The secondary flow cells in the upper main channel section can be seen to be steadier than those at the channel bed, especially for case 5b. This is also highlighted in Figure 5.3.1-6(a) in the main channel region. Therefore, a longer simulation time would be required to achieve steadier secondary circulation profiles and a more accurate prediction of Γ.

So far LES results have been reported and Section 5.4 goes on to detail comparable RANS results.

5.4 RANS RESULTS

As with the in-bank channels $k - \varepsilon$ and SSG simulations were also performed to compare to the LES over-bank channels results. Table 5.4-1 shows the experimental set-up values of velocity and shear stress and simulation derived results for comparison. All results are converged to within 0.5% for both mass flow and boundary shear stress. The $k - \varepsilon$ and SSG simulations were both run for all $B/b = 2$ cases from Knight and Demetriou (1984), with channels ranging from D_r =0.108 to D_r =0.493 and the results detailed in terms on SKM parameters below.

Table 5.4-1: RANS simulation set-up

CASE	Turbulence Model	Roughness Height (mm)	τ_{ave} (N/m²)	U_{avg} (m/s)	Q (l/s)	y^+ range min	max
D_r **0.108**	Experiment	smooth	0.287	0.362	5.200	-	-
	k epsilon	0.12	0.286	0.363	5.202	6.883	26.558
	SSG	0.16	0.286	0.361	5.176	7.892	22.735
	Theory	-	0.286	-	-	-	-
D_r **0.196**	Experiment	smooth	0.330	0.373	6.400	-	-
	k epsilon	0.14	0.329	0.373	6.400	8.306	28.140
	SSG	0.17	0.329	0.371	6.374	10.357	23.727
	Theory	-	0.329	-	-	-	-
D_r **0.242**	Experiment	smooth	0.356	0.385	7.300	-	-
	k epsilon	0.14	0.354	0.385	7.296	9.446	29.935
	SSG	0.15	0.354	0.384	7.270	12.033	24.270
	Theory	-	0.354	-	-	-	-
D_r **0.330**	Experiment	smooth	0.409	0.412	9.450	-	-
	k epsilon	0.15	0.408	0.412	9.451	10.733	31.627
	SSG	0.14	0.408	0.411	9.434	14.029	25.400
	Theory	-	0.408	-	-	-	-
D_r **0.396**	Experiment	smooth	0.455	0.438	11.700	-	-
	k epsilon	0.15	0.454	0.437	11.667	11.626	33.574
	SSG	0.15	0.454	0.435	11.618	15.351	26.535
	Theory	-	0.454	-	-	-	-
D_r **0.493**	Experiment	smooth	0.533	0.503	17.100	-	-
	k epsilon	0.08	0.532	0.507	17.017	12.948	35.537
	SSG	0.05	0.532	0.501	17.013	17.524	27.455
	Theory	-	0.532	-	-	-	-

5.4.1 Friction Factor, f

The average friction factors derived from $k - \varepsilon$ and SSG simulation results are shown in Table 5.4-2 and the ratio f_{fp}/f_{mc} is also shown in Figure 5.4.1-1 compared to Equation 5.1 results.

Table 5.4-2: Summary of $k - \varepsilon$ and SSG derived friction factors for $D_r = 0.108$ to $D_r = 0.493$

D_r	$k - \varepsilon$ f_{mc}	$k - \varepsilon$ f_{fp}	$k - \varepsilon$ f_{fp}/f_{mc}	SSG f_{mc}	SSG f_{fp}	SSG f_{fp}/f_{mc}	Eq.5.1 f_{fp}/f_{mc}
0.108	0.039	0.020	1.965	0.035	0.022	1.639	2.202
0.196	0.033	0.020	1.706	0.031	0.021	1.466	1.681
0.242	0.031	0.019	1.633	0.029	0.020	1.411	1.527
0.330	0.027	0.018	1.531	0.025	0.019	1.308	1.324
0.396	0.025	0.017	1.477	0.024	0.019	1.270	1.216
0.493	0.021	0.015	1.409	0.019	0.016	1.226	1.098

The results can be seen to not compare as well to Equation 5.1 as those of the LES in Figure 5.3.3-2, with the errors between simulation and experiment being as large as 28.4% and -25.5% for $k - \varepsilon$ and SSG results respectively. It can be seen that the $k - \varepsilon$ results perform better at lower D_r, where as the SSG performs better as D_r increases. This may be due to the implementation of a symmetry plane at the free surface, therefore inaccurate prediction of velocity and shear stress profiles, used in the derivation of f.
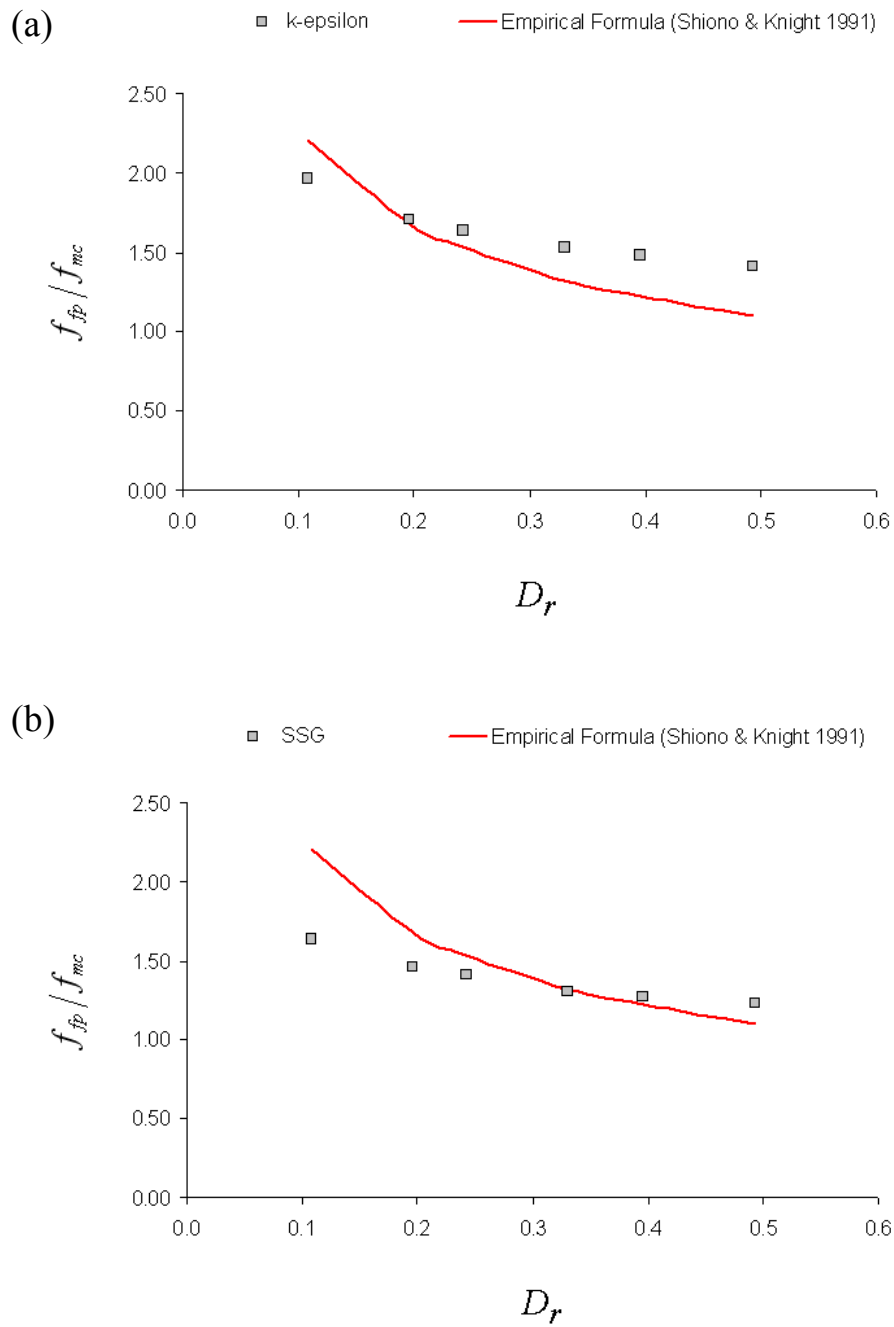
Figure 5.4.1-1: Comparison of average LES derived friction factor for case 5d from (a)

$k - \varepsilon$ *results and (b) SSG results, both compared against experimentally derived values*

(Shiono and Knight 1991)

5.4.2 Dimensionless Eddy Viscosity Coefficient, λ

Table 5.4-3 shows the average derived λ values for the main channel and floodplain regions. It can be seen that λ_{mc} compares well to the LES values of 0.090 and 0.075 for D_r=0.108 and D_r=0.196, the values differing by 3.3% and 4.0% respectively. However, λ_{fp} is significantly underestimated. As with the friction factor results, the inadequate prediction of λ could be due to the implementation of a symmetry plane, because for case 5a (D_r=0.500) where a symmetry plane is implemented the SSG results are comparable to those of the LES, where λ_{fp} average is 0.110 from LES results and -0.140 from SSG results, however, for the remaining cases λ results are not comparable to those of the LES.

Table 5.4-3: SSG derived λ values

D_r	λ_{mc}	λ_{fp}
0.108	-0.087	-0.191
0.196	-0.072	-0.171
0.242	-0.066	-0.164
0.330	-0.057	-0.151
0.396	-0.045	-0.134
0.493	-0.045	-0.140

5.4.3 Secondary Flow Term, Γ

The distribution of $H(\overline{UV})_d$ is shown in Figure 5.4.3-1(c) alongside lateral distributions of f and λ also.

(a)

(b)

(c)
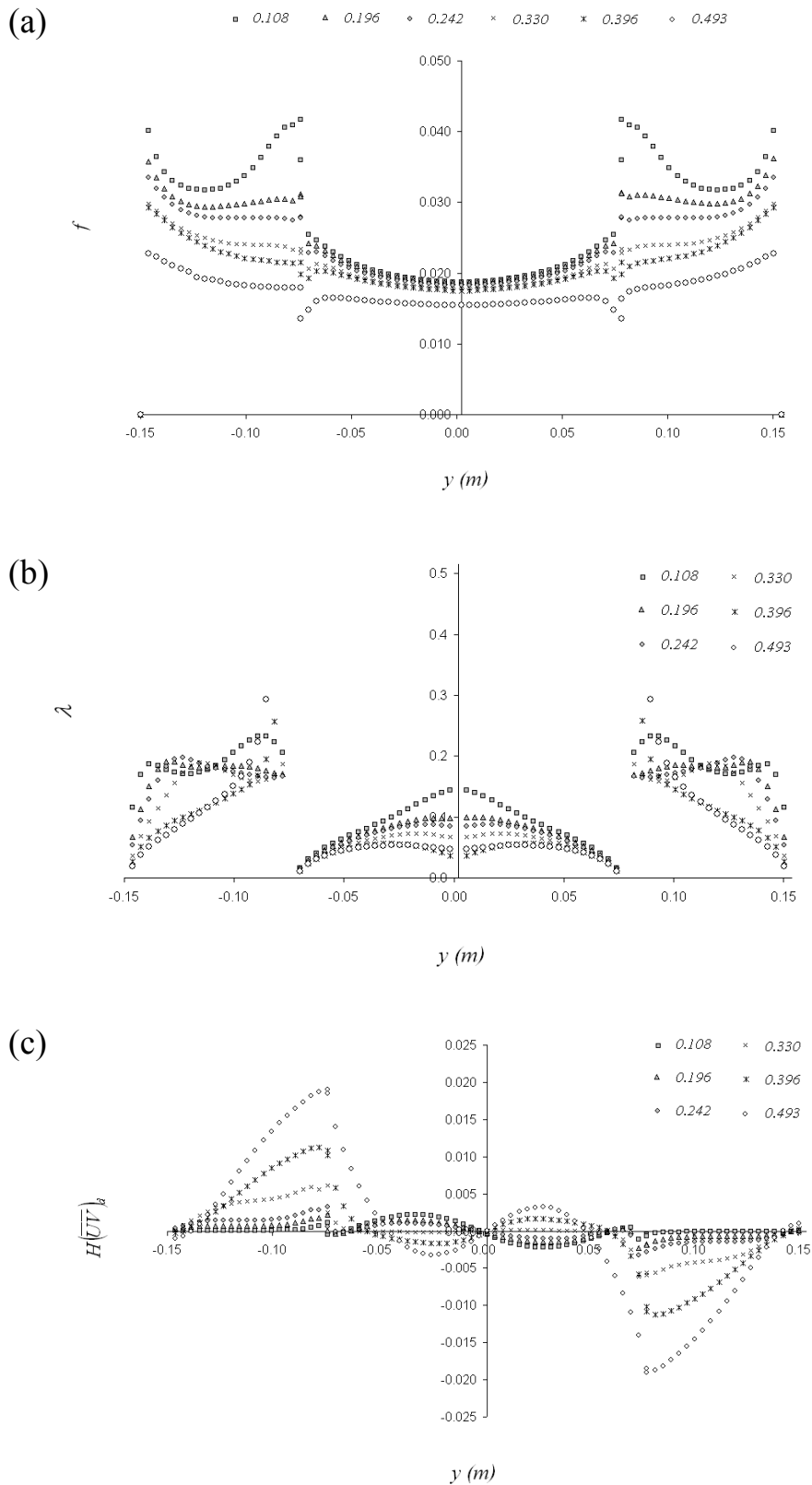
Figure 5.4.3-1: SSG derived lateral distributions of (a) f, (b) λ and (c) Γ for varying depth ratios

216

The secondary circulation cells are not investigated in depth for the $k - \varepsilon$ and SSG results as these are performed with a symmetry plane implementation at the free surface distorting the cell distributions from what would occur in open channels.

5.4.4 Discharge Distribution

As well as accurate predictions of lateral distributions of velocity and shear stress, for over-bank channels the prediction of channel discharge contributions from various sections of the channel is important and difficult to predict. This is due to the momentum exchange and presence of interfacial vortices at the main channel/floodplain region. Splitting the channel into main channel and floodplain sections the percentage discharge from the varying channel sections is shown in Figure 5.4.4-1 compared to experimental results from Knight and Demetriou (1984).
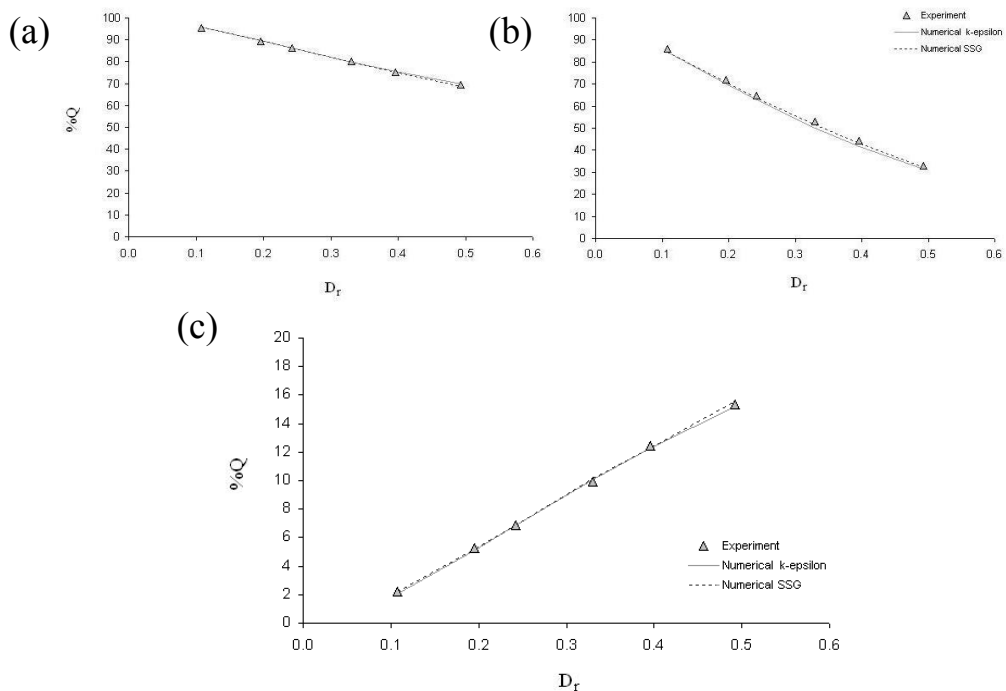
Figure 5.4.4-1: Percentage discharge in (a) the main channel, (b) lower main channel and

(c) in the floodplain versus depth ratio

It can be seen that the average discharge can be computed well by both the $k - \varepsilon$ and SSG simulations, even with the implementation of a symmetry plane. LES derived values are shown in Table 5.4-4 for comparison.

Table 5.4-4: Discharge distributions for the main channel and floodplain sections as a percentage of the total discharge for cases 5a, 5b and 5c

D_r	Main Channel	Lower Main Channel	Floodplain
Experiment (Knight and Demetriou 1984)			
0.108	95.5	85.8	2.3
0.196	89.5	72.0	5.3
0.493	69.3	33.0	15.4
LES Results			
0.108	94.5	84.0	2.8
0.196	88.0	70.0	6.0
0.493	68.5	32.0	15.8
% Error			
0.108	-1.0%	-2.1%	19.6%
0.196	-1.7%	-2.8%	13.2%
0.493	-1.2%	-3.0%	2.3%

The LES results compare better in the main channel section than on the floodplain. The LES and RANS results are also comparable, with the RANS results differing to that of experiment by up to 10%, however the trends are predicted very well.

5.5 ANALYTICAL SOLUTION

As with the in-bank LES derived f, λ and Γ values, depth averaged velocity profiles for the over-bank channel cases are computed. Case 5a is detailed below where the depth averaged velocity profile is computed using the analytical solution of the SKM and compared with the LES derived profile. For over-bank channels the cross-section was firstly divided into the main channel and floodplain regions, then 19 and 20 panels were utilised to derive average values for the main channel and floodplain regions respectively. Figure 5.4.4-1 shows the analytically derived velocity profile compared to the LES simulated profile.
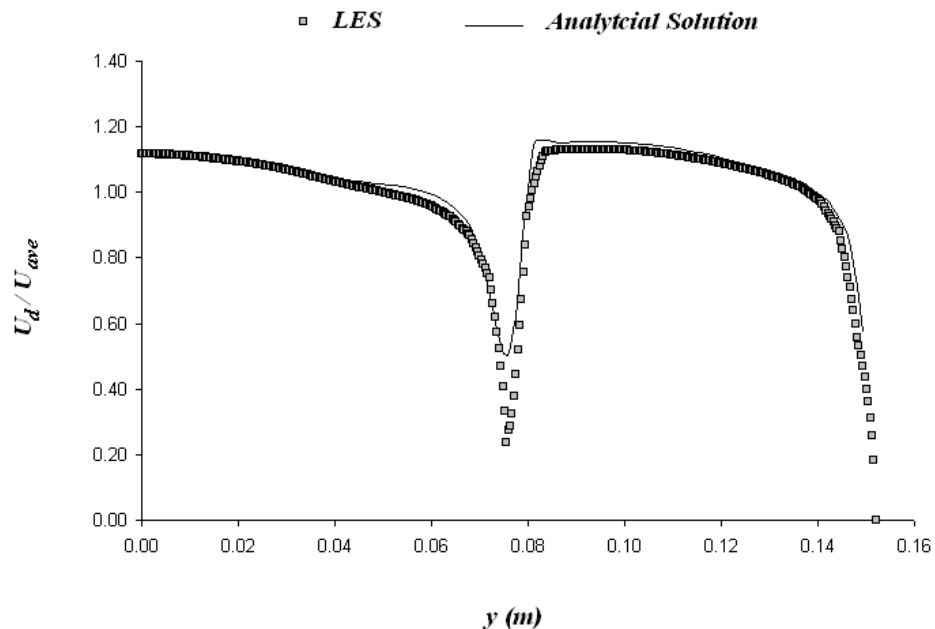
Figure 5.4.4-1: Analytically derived depth averaged velocity profiles compared to LES results

It can be seen that the profile is predicted well, with the location of the slight dip in the profile within the main channel region ($y=0.04$m) comparing well to the corresponding location within the LES profile. Cases 5b and 5c are not investigated due to the unsteadiness of the boundary shear stress profiles, which impacts the prediction of f and the analytical solution results.

5.6 CONCLUSIONS

Section 5.3 has detailed LES over-bank channel results and derived SKM parameters. The flow features were captured well within the simulations and the SKM parameters are compared to numerous empirically derived relationships. The main conclusions from this section of research are as below:

- It has been shown that the prediction of the friction factor, f, can be made using one channel and extracting results at various depths. RANS results are shown to be not as accurate as those of the LES for the derivation of f compared to Equation 5.1.

- With regards to Series 05, the main channel and floodplain friction factor values compare well with experiment when using exact values extracted from data in Shiono and Knight (1991).

- It has been shown that the prediction of the friction factor, f, can be made using one channel and extracting results at various depths, giving f values to within a maximum error of 11% when compared to Equation 5.1.

- The dimensionless eddy viscosity coefficient can be determined well from the LES results. However, even though the main channel section values cluster around the standard value of 0.07 they do range by ±30% from this

value and this is dependant on depth ratio. The standard value of 0.07 was derived by Shiono and Knight (1991) who stated that the value was only valid within the range tested, which was $0.1 < D_r > 0.25$. Only cases 5b and 5c fall within this range.

- The distributions of T and J are shown to vary across the channel sections and the stress carrying mechanisms identified for varying channels, highlighting that the momentum exchange between main channel/floodplain interface is not dominated by secondary circulations.

- The apparent shear stress is shown to be dominated by the Reynolds stress component in all 4 cases and at the interface it is shown that the apparent shear stress is larger for decreasing D_r.

- The average shear stress on the partial channel wall compared to that at the main channel/floodplain interface has been quantified for channels of varying D_r and shown to increase at the interface and decrease on the partial wall as D_r decreases.

- The discharge distribution within the main channel regions and floodplain can be predicted well from both RANS and LES results and the SKM analytical solution for case 5a compares well to the LES simulated profile.

6   INTERFACIAL VORTICES

6.1   INTRODUCTION

Chapter 2 highlighted published work on periodic vortices, such as those shown in
Figure 5.4.4-1 at the main channel floodplain interface in compound open channel
flow.
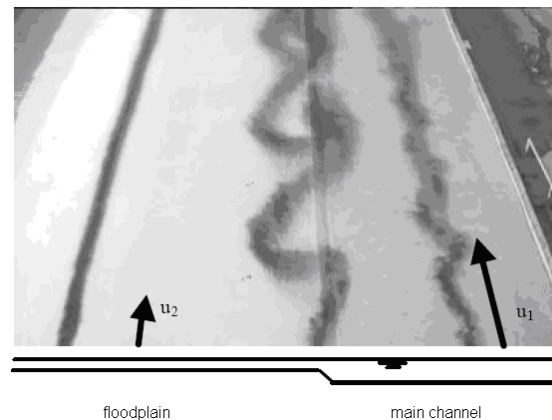
Figure 5.4.4-1: Large vortices experimentally observed at the main channel/floodplain

interface (van Prooijen et al., 2000)

Chapter 5 reported some over-bank channel results, but no exact identification of
periodic vortices was investigated. Therefore, this chapter utilises some of the
numerous data available from the 3D LES simulations in order to investigate wave
periods in relation to varying D_r in both asymmetric and symmetric compound
channels. Firstly a comparison is made to the data of Bousmar (2002) for validation
and then spectral analysis results for cases 4, 5b and 5c are discussed.

6.1.1 Case 6 - Bousmar (2002) LCA 08 Comparison

Case 6 has been simulated to match the channel set-up of Bousmar (2002). Channel geometry and set-up are shown in Figure 6.1.1-1 and Table 6.1-1.
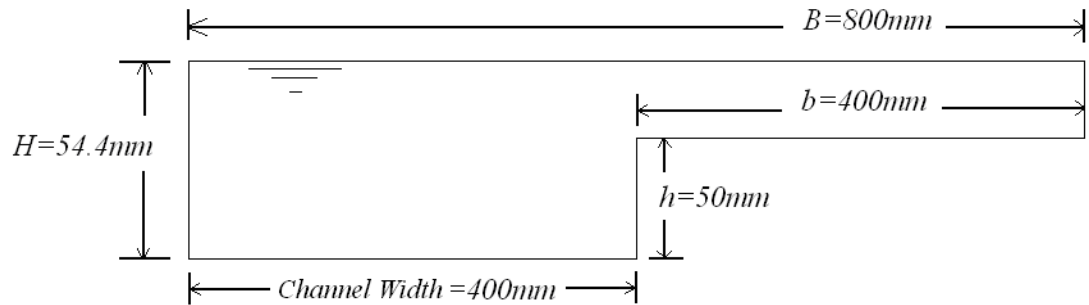
Figure 6.1.1-1: Cross section of experimental asymmetric compound channel comparable to LCA 08 of Bousmar (2002)

Table 6.1-1: Cross section of experimental asymmetric compound channel

H	h	U_{avg}	τ_{avg}	u_*	Q	D_r
(m)	(m)	(m/s)	(N/m^2)	(m/s)	(l/s)	-
0.0544	0.050	0.332	0.251	0.016	7.8	0.100

The simulation was run for 145sec at a time step of Δt =0.005sec and the domain length was specified as $L = 0.35m$, with $S_0 = 0.99 \times 10^{-3}$. This simulation was performed for initial investigation of the main channel/floodplain interfacial vortices to compare with experiment, therefore not simulated for an extensive period of time. However, once the presence of structures was observed, the channel length of $L = 0.35m$ was extended and the simulation intended to run for a sufficient 50LETOTs to obtain a steady state and a further 20LETOTs to obtain a steady state

solution. The initial channel length of $L = 0.35m$ was thought to constrict the development of interfacial vortices as Bousmar (2002) identified a vortex wavelength of 0.39m for this case. Therefore, the channel length was increased to $L = 1.2m$, to allow a sufficient number of vortices (~4) to develop along the channel length. Figure 6.1.1-2 shows velocity profiles from ANSYS-CFX and Bousmar (2002) for comparison.
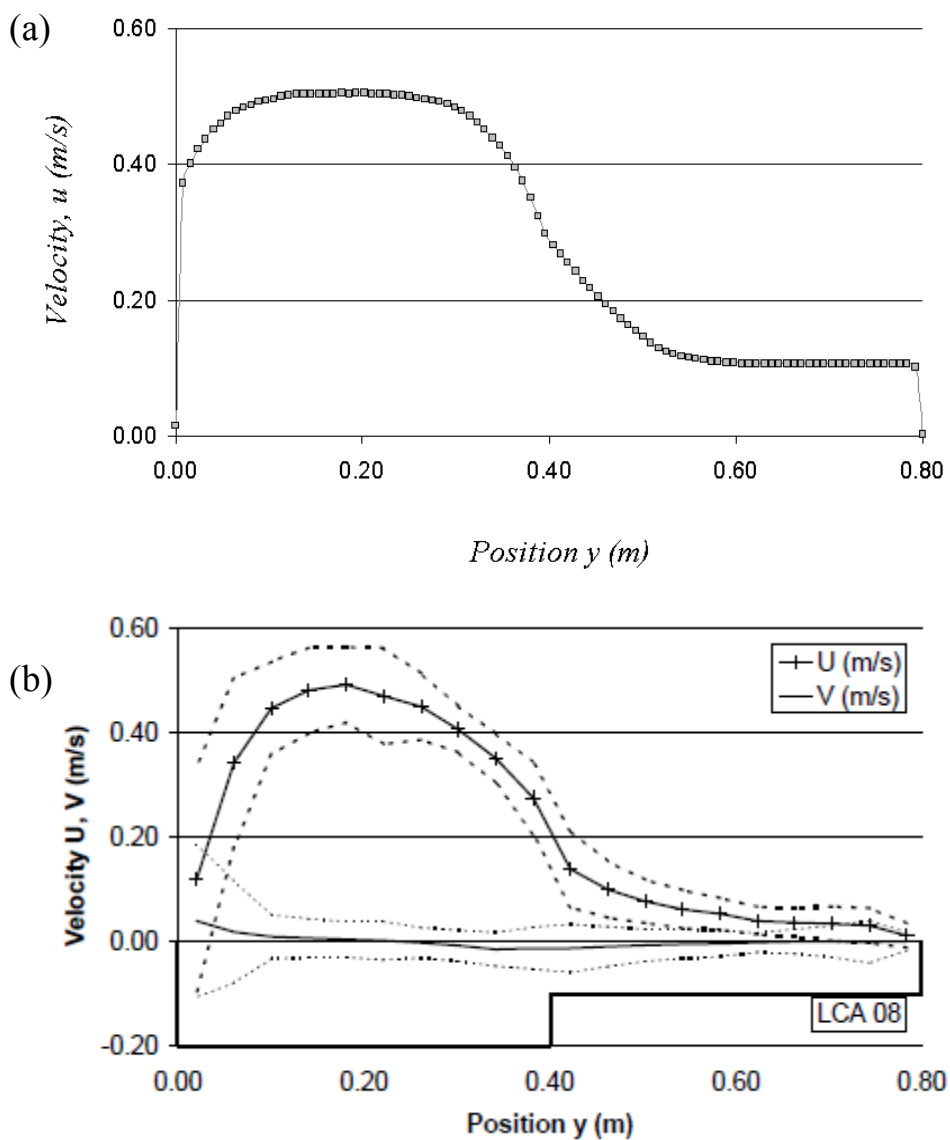
Figure 6.1.1-2: Profile of longitudinal velocity for (a) ANSYS-CFX LES and (b) experimental results (Bousmar 2002)

The profiles compare well and the simulation is shown to be relatively steady after 145sec. The velocity is constant in the main channel and floodplain regions, with average velocity, U_{avg} =0.340m/s, which is within 1.2% of the experimental value. The simulation results of case 6 are not reported in detail as the initial channel ($L = 0.35m$) was only simulated for 145sec and the extended channel ($L = 1.2m$) for only 100sec.

Interfacial vortices were initially examined in terms of instantaneous velocity and vorticity, $\Omega = \dfrac{\partial u}{\partial y} - \dfrac{\partial v}{\partial x}$, shown in Figure 6.1.1-3 and Figure 6.1.1-4 respectively. Visually, the presence of interfacial vortices is not easily distinguishable from these plots.
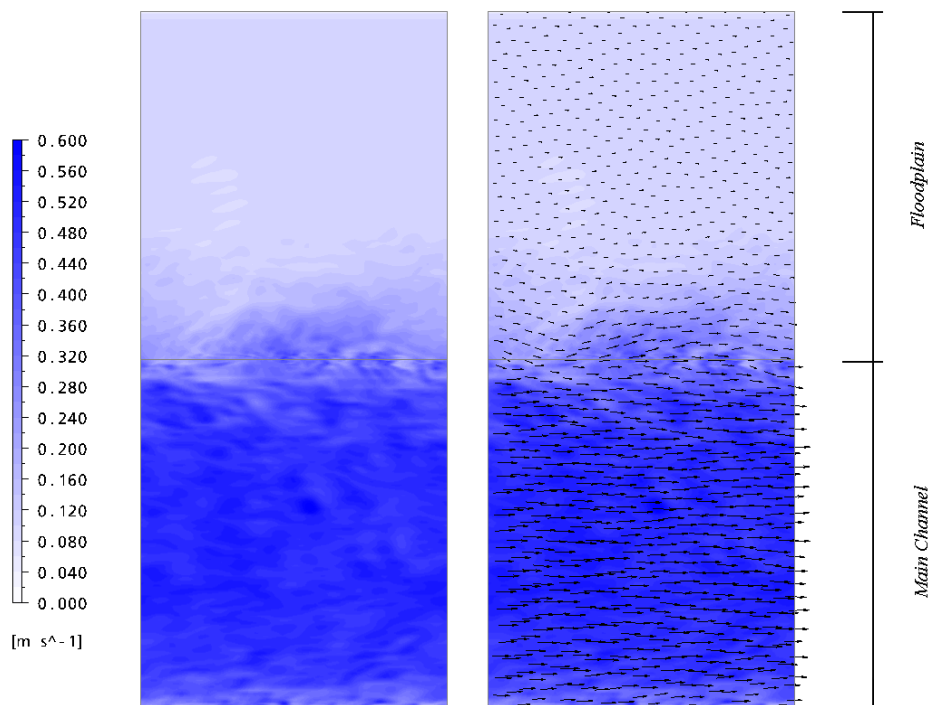
Figure 6.1.1-3: Contour plot of transverse velocity overlain with instantaneous velocity

vectors on a plane at $z = 0.0543m$ (plane in light green as shown on Figure 6.1.1-5)
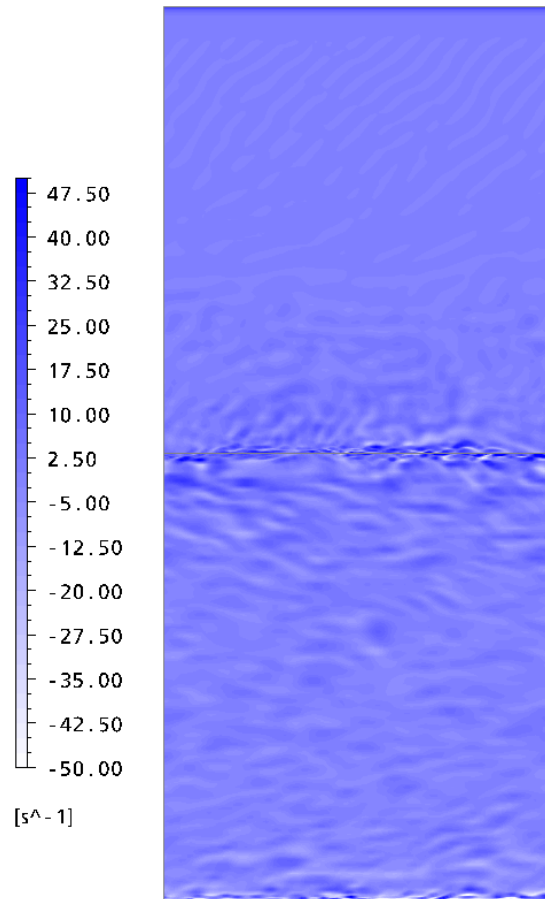
Figure 6.1.1-4: Contour plot of vorticiy, $\Omega = \dfrac{\partial u}{\partial y} - \dfrac{\partial v}{\partial x}$ *, on a plane at* $z = 0.0543m$ *(plane*

in light green as shown on Figure 6.1.1-5)

However, when periodic vortices exist at a main channel/floodplain interface the transverse velocity component should fluctuate, producing alternate positive and negative sign. If instantaneous data is stored at points along the main channel/floodplain interface the time-series plots of traverse velocity at these locations can be analysed. Using a Fourier analysis peaks within the spectrum can be identified, from which, hopefully, a clear wave period can be seen.

Bousmar (2002) recorded velocity time-series for case LCA 08 and undertook spectral analysis at a point located at $y = 0.44m$, within the floodplain region. This

point was not located at the interface itself as the transverse velocity is thought to be less clearly identifiable due to the presence of higher velocity flow in the main channel. From Fourier analysis of the recorded transverse profile Bousmar (2002) computed a clear peak in the energy spectrum.

To compare to the data of Bousmar (2002) monitor points were placed within the ANSYS-CFX LES case 6 for the extended $x = 1.2m$ set-up. The monitor points were placed every channel quarter length and at $y = 0.44m$, for both $z = 0.0522m$ and $0.05435m$. Monitor point locations are shown in Figure 6.1.1-5 for symmetric cases (cases 5b and 5c), however, case 6 is an asymmetric channel, therefore only monitor points 4 to 6 at the free surface and half the floodplain depth are required.
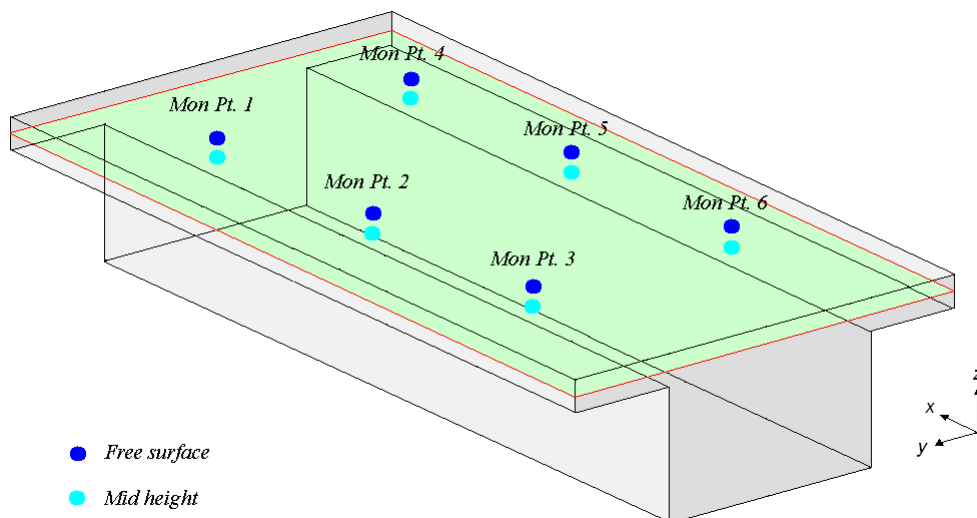
Figure 6.1.1-5: Monitor point locations

Figure 6.1.1-6 shows a time series plot of transverse velocity at location, $x = 0.6m, y = 0.44m, z = 0.05435m$. Oscillations can clearly be identified. The spectral analysis for case 6 over the simulated 100sec time period is shown in Figure 6.1.1-7, for which the dominant wave period is 3.07sec, compared to experimental

Particle-Tracking Velocimetry (PTV) and Acoustic Doppler Velocimetry (ADV) measurements of 3.63sec and 3.9-4.3sec respectively. The period is predicted well, if only slightly underestimated.
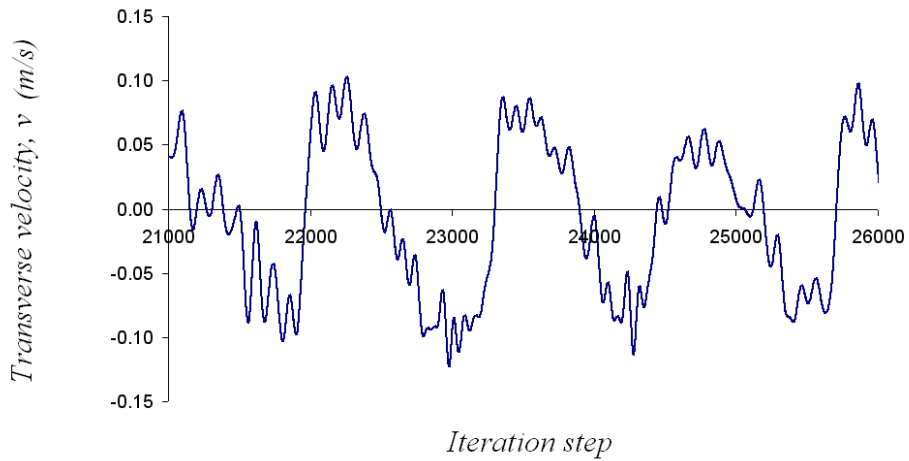
Figure 6.1.1-6: Time series of transverse velocity, v, near the main channel/floodplain

interface ($x = 0.6m, y = 0.44m, z = 0.05435m$)
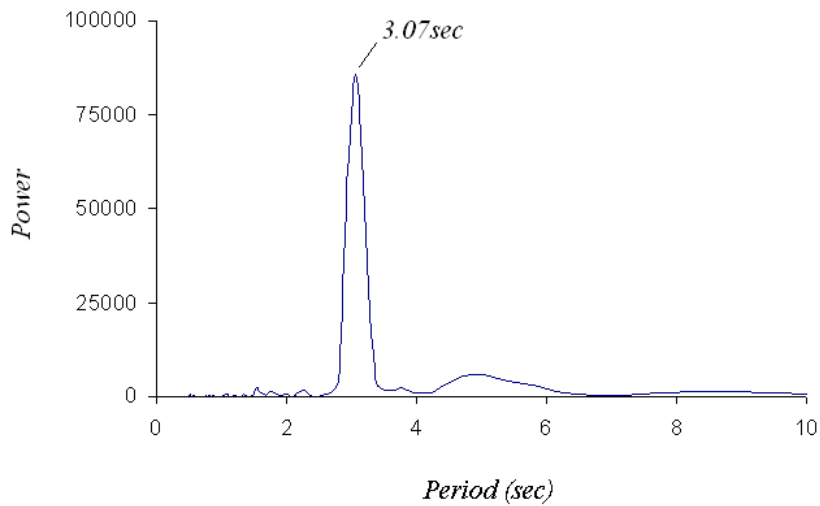
Figure 6.1.1-7: Transverse velocity, v, spectral analysis

($x = 0.6m, y = 0.44m, z = 0.05435m$)

6.1.2 Cases 4, 5b and 5c

Monitor points were also placed within cases 4, 5b and 5c documented in the previous chapter. However, unlike case 6 no experimental data is available for comparison. Therefore, it was thought appropriate to compare derived wave periods for ANSYS-CFX LES case 6 in comparison to Bousmar (2002) case LCA 08 as validation prior to reporting those of cases 4, 5b and 5c.

Figure 6.1.2-1 shows the spectral analysis of the transverse velocity time series for case 4, for all monitor points. It can be seen that a clear wave period of 1.49sec is always observed. The channel geometry is at $D_r = 0.5$, therefore, a wave period less than that of case 6 is expected. The channel geometry is comparable to the experimental cases of Bousmar (2002), with width raitio, $B/b = 0.5$, however, the floodplain depth in comparison to that of the main channel is larger than any of the channels simulated by Bousmar (2002), the largest D_r case being LCA 16 at $D_r = 0.38$. ADV measurements for LCA 16 produced a wave period of 0.6-0.9sec. Therefore, case 6 produces a larger wave period than would have been estimated by Bousmar (2002). However, the LCA 16 case was set-up with an average velocity, $U_{avg} = 0.504$m/s, whereas case 4 has $U_{avg} = 0.349$m/s. The difference in discharges will impact on the wave period.

(a)

(b)

(c)
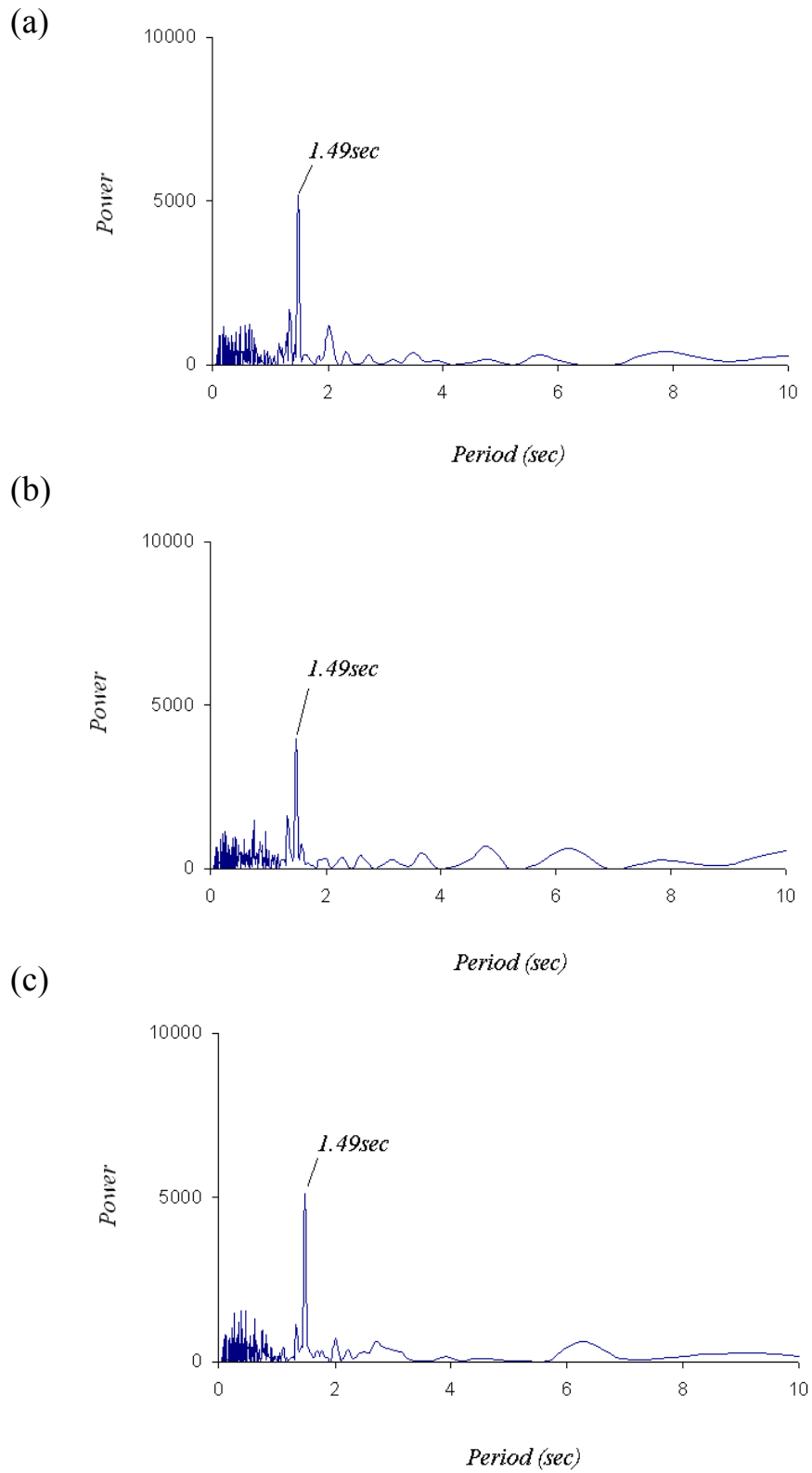
Figure 6.1.2-1: Transverse velocity, v, spectral analysis for case 4 at locations

$y = 0.2m$, $z = 0.06m$ *and (a)* $x = 0.12m$, *(b)* $x = 0.24m$ *and (c)* $x = 0.36m$

Figure 6.1.2-2 shows the spectral analysis of the transverse velocity time series for cases 5b and 5c. Initially monitor points were placed at the interface and not offset from it. However, as stated by Bousmar (2002) as the transverse velocity is less identifiable due to the higher velocity in the main channel region the monitor point should be offset from the exact interface location. It can be seen from the spectral analysis at the interface, Figure 6.1.2-2, that the signal is very noisy and a single pronounced peak is not identifiable.
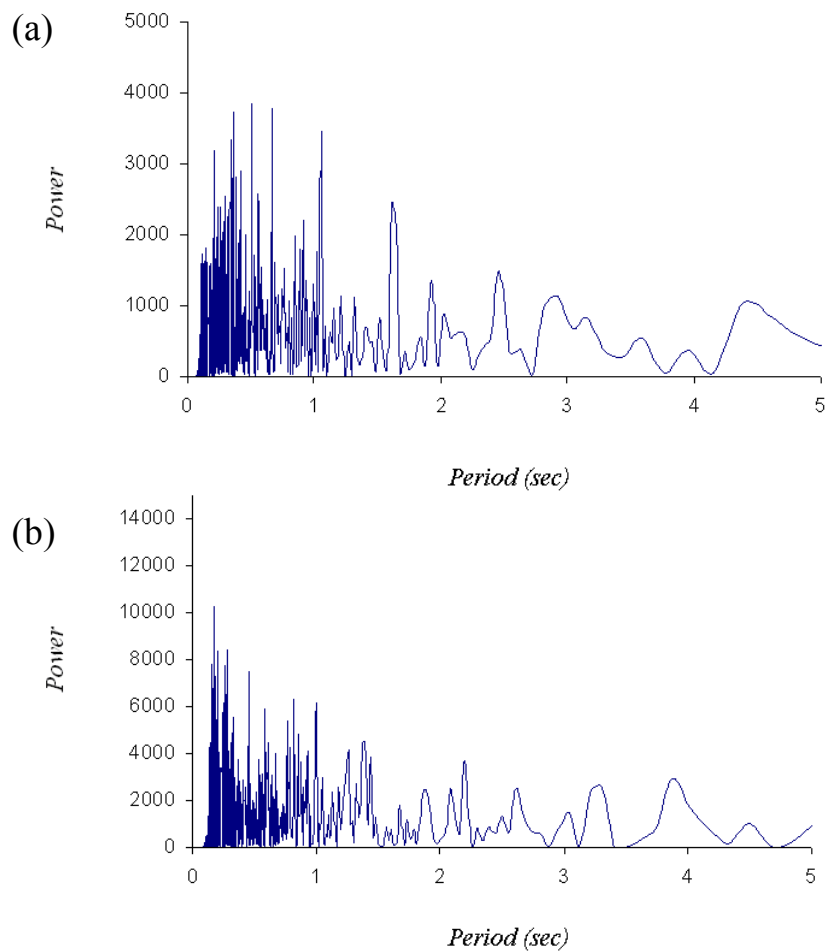
Figure 6.1.2-2: Transverse velocity, v, spectral analysis for case (a) 5b and (b) 5c at location, $x = 0.24m$, $y = 0.076m$, $z = 0.085m$

The noise within the spectral analysis may also be due to the fact that the channels are symmetric and periodic vortices that do develop, develop on both main channel/floodplain interfaces and due to the small width of main channel section these vortices may impact on each other. However, with asymmetric channels only one interface exists and no interference from other structures is observed. The derived wave periods for all monitor points is shown in Table 6.1-2.

Table 6.1-2: Wave periods (seconds) derived for all monitor points for cases 5b and 5c

Surface	$y = 0.076m$		$y = 0.084m$
	$D_r = 0.1$	$D_r = 0.2$	$D_r = 0.1$
Mon Pt. 1	1.21	0.22	1.35
Mon Pt. 2	0.18	0.51	1.35
Mon Pt. 3	0.32	0.56	1.35
Mon Pt. 4	0.25	0.26	0.88
Mon Pt. 5	0.18	0.62	1.35
Mon Pt. 6	1.07	0.28	1.35
Half Channel	$y = 0.076m$		$y = 0.084m$
	$D_r = 0.1$	$D_r = 0.2$	$D_r = 0.1$
Mon Pt. 1	1.41	0.83	1.35
Mon Pt. 2	0.33	1.76	1.35
Mon Pt. 3	0.61	0.92	1.35
Mon Pt. 4	0.57	0.34	1.35
Mon Pt. 5	0.47	0.55	0.88
Mon Pt. 6	3.04	0.39	0.88

Wave periods range from 0.18-1.21 at $D_r = 0.1$ and 0.28-0.62 at $D_r = 0.2$ at the free surface. The period interval is quite large to give some conclusion, but the trends do seem to show slightly that as D_r and Q increase, wave period decreases.

Table 6.1-2 also details offset monitor points. Due to the noise observed within the spectrums for cases 5b and 5c monitor points were re-located from $y = \pm 0.076m$ to $y = \pm 0.084m$ for case 5c to investigate the impact of monitor point location on time series data. The new spectral analysis for case 5c can be seen in Figure 6.1.2-3.
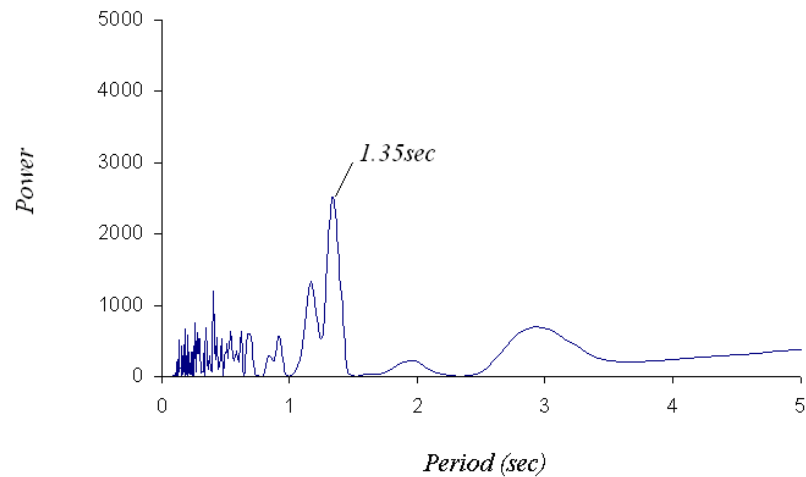
Figure 6.1.2-3: Transverse velocity, v, spectral analysis for case 5c at location, $x = 0.24m$,

$$y = 0.084m, \ z = 0.085m$$

A clearer wave period of 1.35sec can now be identified for case 5c. Monitor points were not re-located for case 5b, therefore comparison between cases cannot be made.

6.2 CONCLUSIONS

- The interfacial vortices have been investigated in terms of spectral analysis of transverse velocity time series monitored at and close to the main channel/floodplain interface for cases 4, 5b, 5c and 6.

- Validation data is only available for case 6. From the ANSYS-CFX LES results a wave period of 3.07sec was computed, which compares well to that

of 3.63sec and 3.9-4.3sec from PTV and ADV measurements (Bousmar 2002).

- Spectral analysis of case 4 shows a clear wave period of 1.49sec. This is inline with the theory that as D_r increases, T decreases.

- Spectral analyses of cases 5b and 5c produce wave periods of between 0.28-0.62sec and 0.18-1.21sec respectively. The wave periods therefore tending to increase with decreasing D_r and increasing Q.

- Spectral analysis of time series monitored at the main channel/floodplain interface for cases 5b and 5c was shown to be noisy and no clear identifiable peaks were observed within the spectrum. Therefore, wave period intervals identified were large and to draw conclusions from these may be inaccurate.

- Re-locating the monitor point for case 5c from the interface to the floodplain region allowed for a clear peak to be identified in the spectrum analysis at a wave period of 1.35sec, however no comparable data was available for case 5b.

7 CONCLUSIONS

7.1 INTRODUCTION

Flow in in-bank and over-bank channels has been simulated using Large Eddy Simulation (LES), and SKM calibration parameters have been derived from these results and compared with existing data and empirical formule for their prediction. Where appropriate, additional computations and derivations have also been carried out, based on the Reynolds Averaged Navier Stokes formulation. The most significant conclusions from this research and recommendations for future research are shown below.

7.2 CONCLUSIONS

LES can predict flow characteristics in in-bank and over-bank channels well and accurate depth averaged velocity profile results have been obtained using LES derived f, λ and Γ values in the analytical solution of the SKM. With regards to in-bank channels the analytically depth averaged velocity profiles are predicted locally to within a maximum of 11% of the simulated profiles and the undulations in the profiles are predicted well, giving confidence in the LES results and accuracy of the derived SKM parameters.

The friction factor can be predicted well for both in-bank and over-bank channels, with the influence of the secondary circulation cells close to the channel side walls

becoming prominent in comparison to those in the main channel region in large aspect ratio (AR) in-bank channels. This becomes evident in the lateral distributions of the friction factor due to the impact of the magnitude of these cells on the shear stress and velocity profiles. This secondary flow cell centre location has been shown to correspond well to Equation 4.7.1. With regard to over-bank channels the main channel and floodplain friction factor values compare well with experiment when using exact values extracted from data in Shiono and Knight (1991), which is less the case when comparing to empirical relationships derived from numerous data sets. The prediction of the friction factor, f, and ratio, f_{fp}/f_{mc} has also been derived from extracting results at various depths in just one channel, with results comparing to within 11% of Equation 5.1. RANS results are shown not to be as accurate as those of the LES for the derivation of f compared to Equation 5.1.

Distributions of λ compare well to previously published data. However, deriving averages is problematic even for some in-bank channels. When averages were derived for the analytical solution they did not adversely affect the analytically derived velocity profiles reported. Although it is shown that the main channel section λ values in over-bank channels cluster around the standard value of 0.07 it should be noted that the present work found that they do fluctuate by as much as ±30% from this value and this is dependant on. D_r. The standard value of 0.07 was derived by Shiono and Knight (1991) who stated that the value was only valid within the range tested, which was 0.1<D_r>0.25. This highlights the fact that comparable empirical relationships are limited in their application and only applicable to the

range of data and conditions tested. This is highlighted in the use of empirical relationships throughout this work where appropriate.

Secondary circulations are predicted well for both in bank and over-bank channels, with the associated distributions of $\left(\overline{UV}\right)_d$ varying considerably due to the cell locations. Overlain cells in in-bank channels still pose a challenge for the specification of Γ for channels that have not been previously investigated and are shown to differ from channels at large AR, where cells lie adjacent to each other

The interfacial region in over-bank channels has been investigated in terms of apparent shear stress and stress carrying mechanisms. The apparent shear stress is shown to be dominated by the Reynolds stress component in all over-bank cases and at the interface it is shown that the apparent shear stress is larger for decreasing D_r. Values of mean shear on the partial wall are also compared to those at the interface and that on the partial wall decreases with increasing D_r. Varying stress carrying mechanisms across the main channel and floodplain are highlighted. These observations all confirm that advanced turbulence modelling techniques are therefore necessary to modelling straight channels and in particular the interface between main channel and floodplain.

Interfacial vortices have also been investigated in terms of spectral analysis of transverse velocity time series monitored at and close to the main channel/floodplain interface. Derived wave periods compare well to published data and it is shown that the wave periods tend to increase for decreasing D_r and increasing Q. Clear, identifiable peaks from spectral analysis are reported and it is shown that placing the

monitor points slightly offset from the main channel/floodplain interface impacts on the resulting spectra.

7.3   INNOVATIVE RESREACH CONTRIBUTIONS

This research has been the first to utilise numerical modelling results to derive f, λ and Γ and also model numerous channel flows using LES which has previously not been undertaken for such a large channel dataset. Specifically, this research has shown that it is essential to use LES in favour of other turbulence models to accurately produce flow features such as secondary circulation cells and therefore accurate velocity and shear stress distributions, from which to derive f, λ and Γ.

7.4   PRACTICAL APPLICATIONS

The following points are innovative conclusions drawn from this research for use within the practical application of the SKM and conveyance modelling using f, λ and Γ:

- The assumption of a constant f across a panel close to the channel side wall has to be carefully determined as this can effect the whole lateral velocity distribution and therefore estimated water height. Due to the derivation of f its value can extend to infinity in the boundary layer region as the velocity tends to zero.

- The assumption of a constant λ across a cross section and floodplain/main channel section is not valid. The values derived within an in-bank section and main channel section of an over-bank channel have been shown to deviate from the standard value of $\lambda = 0.07$ by ±30%, causing inaccuracies in

the SKM derived velocity and shear stress profiles if inaccurate values are used. It has also been shown that the Reynolds Stress contribution deviates within the floodplain section, therefore, an assumption of a constant λ is inaccurate for varying cases.

- The analysis of T and J components, which was only made possible by the numerous data from the LES modelling, has shown the contributions from the Reynolds Stress and secondary circulation components respectively. From the J component analysis values of λ across the channel section can be determined accurately and specifically peak values at the main channel/floodplain interface can be set from the corresponding J components.

- The prediction of the secondary circulation cells and therefore a value for Γ is known to be complex. However, this research has shown for which cases the division lines shown by Omran (2005) are accurate and the locations of further panel divisions from which a more accurate description of the flow can be obtained.

7.5 RECOMMENDATIONS FOR FUTURE WORK

SKM parameter results have been shown to be comparable in most cases to published works and if not empirical relationships, the exact data they were derived from. Therefore, it is highlighted that empirical relationships are limited in their application to varying channels and deriving relationships to express all three calibration parameters, even for in-bank channels, is difficult. Within this research 10, 22, and 44 panels are used to derive the velocity profiles from the SKM analytical solution and in order to make use of the extensive LES data. However, in practise specifying 44 panel averages, therefore 44 f, λ and Γ values per panel

(22 assuming the channel is symmetric) is not practical. This research has shown that f, λ and Γ can be computed well from LES, but even further analysis of the f, λ and Γ parameters for large consistent datasets using numerical modelling could provide extensive relationships for these parameters, with this research as a starting point. CFD has the potential to bridge the gap.

However, with regards to commercial flood modelling, of interest to the flood modeller is the prediction of flood extent and inundation height, no matter whether this computation involves simplified assumptions, manning's n, or extensive f, λ and Γ computations. In this respect, further extensive CFD modelling of f, λ and Γ would be too time consuming to provide usable general formula for a real life broad range of applications, that the commercial flood modeller would be able to apply as readily and easily as with existing, well validated coefficients, that although do not compute as accurately as f, λ and Γ the flow physics, but provide an adequate estimation of inundation extent.

Also, when accessing f, λ and Γ derived parameters the success of the results from the analytically derived profiles was also investigated in terms of depth averaged velocities. However, bed shear stress profiles could be derived and compared to experiment. The bed shear stress profiles could be derived directly, through imputing LES derived f and analytically derived U_d values into Equation 2.6.11.

Other than SKM results, promising results were reported from the analysis of instantaneous transverse velocity data at the main channel/floodplain interface in over-bank channels, with this research analysing wave periods for the channels

reported. However, analysis of wave lengths of structures could also be obtained. This would by achieved by accessing celerity of vortices (Bousmar 2002) in the shear layer, from which a wave length can then be derived, requiring analysis of instantaneous velocity contours over time. Experimental results are unavailable for comparison to some wave periods derived, however, stability analysis has been shown by Bousmar (2002) and others to predict wave lengths well, and could be performed in order to examine the reliability of these results and give some validation for the data.

Also, case 6 performed for comparison with Bousmar (2002) data was initially simulated with a short channel length and then extended. The length of channel will affect the formation of periodic structures and number observed within the simulation. Analysis of various channel lengths and their impact on the number of periodic structures could be further investigated, to analyse the impact of the constraint of channel geometry.

REFERENCES

Abe, H., Kawamura, H. and Matsuo, Y. (2001). Direct numerical simulation of a fully developed turbulent channel flow with respect to the Reynolds number dependence. *Journal of Fluids Engineering*. Vol. 123(2), pp. 382-394.

Abril J.B., and Knight D.W. (2004). Stage-discharge prediction for rives in flood applying a depth-averaged model. *Journal of Hydraulic Research*, *IAHR*. Vol. 42(6), pp. 616–629.

Ackers P. (1991). Hydraulic design of straight compound channels. *SR Report 281*, HR Wallingford, UK, Vol. 1 & 2, pp 1-130 & 1-140.

Ackers P. (1992). Hydraulic design of two-stage channels. *Proceedings of ICE Journal for Water, Maritime and Energy.* Paper no. 9988, Vol. 96, Dec., pp. 247-257.

Ackers P. (1993). Flow formulae for straight two-stage channels. *Journal of Hydraulic Research*, *IAHR*. Vol. 31(4), pp. 509-531.

Alavian, V., and Chu, V.H. (1985). Turbulent exchange flow in shallow compound channel. *Proceedings of 21st Congress of IAHR, Melbourne*. Vol. 3, pp. 446-451.

Ardiclioglu, M. (1994). Investigation of turbulent velocity profile in smooth open channel flows. *PhD thesis*, University of Korova, Adana, Turkey.

Bousmar, D., and Zech, Y. (2001). Discussion of Two-dimensional solution for straight and meandering overbank flows, by D.A. Ervine, K. Babaeyan-Koopaei and R.H.J. Sellin, JHE, 2000, 126(9). *Journal of Hydraulic Engineering, ASCE.*

Bousmar, D. (2002). Flow modelling in compound channels. *PhD Thesis,* Universite catholique de Louvain.

Bousmar D. and Zech Y. (2002). Periodical turbulent structures in compound channels. *Procdings of River Flow 2002, Louvain, Belgium.* Vol. 1, pp 177-185.

Broglia, R., Pascarelli, A. and Piomelli, U. (2003). Large-eddy simulation of ducts with a free surface. *Journal of Computational Physics.* Vol. 7(120), pp. 120-133.

Cater, J.E., and Williams, J.R. (2008). Large eddy simulation of a long asymmetric compound open channel. *Journal of Hydraulic Research.* Vol. 46(4).

Chen, D., and Jirka, G.H. (1995). Experimental study of plane turbulent wake in a shallow water layer. *Fluid dynamics research.* Vol 16(11).

Chlebek, J., Knight, D.W. (2006) A new perspective on sidewall correction procedures, based on SKM modelling. *River Flow 2006. Lisbon, Portugal.*

Chow V.T. (1959). Open channel hydraulics, *McGraw-Hill Book Company*, US.

Chu, V.H., and Babarutsi, S. (1988). Confinement and bed-friction effects in shallow turbulent mixing layers. *Journal of Hydraulic Engineering, ASCE*, Vol. 114(10), pp. 1257-1274.

Chu, V.H., Wu, J.H., and Khayat, R.E. (1991). Stability of transverse shear flow in shallow open channels. *Journal of Hydraulic Engineering, ASCE.* Vol. 117(10), pp. 1370-1388.

Cokljat, D. (1993). Turbulence models for non-circular ducts and channels. *PhD Thesis*. City University, London.

Davidson, P.A. (2004). Turbulence - An introduction for scientists and engineers. *Oxford University Press*.

Darcy H. (1857). Recherches experimentales relatives au mouvement de l'eau dans les tuyaux, 2 volumes, *Mallet-Bachelier*, Paris, pp 1-268 and atlas (Experimental Research Relating to the Movement of Water in Pipes).

Deardorff, J.W. (1971). On the magnitude of the subgrid scale eddy viscosity coefficient. *Journal of Computational Physics*. Vol. 7(120).

Demuren, A.O. (1993). A numerical model for flow in meandering channels with natural bed topography. *Water Resources Research*. Vol. 29(4), pp. 1269-1277.

Einstein, H. (1942). Formulas for the transportation of bed load. *Trans. Am. Soc. Civ. Eng.* Vol. 107, pp. 561-597.

Ervine, D.A., and Baird, J.I. (1982). Rating curves for rivers with overbank flow. *Proceedings of the Institution of Civil Engineers, Part 2*. Vol. 73, pp. 465-472.

Ervine, D.A., Willets, B.B., Sellin, R.H.J. and Lorena, M. (1993). Factors affecting conveyance in meandering compound flows. *Journal of Hydraulic Engineering.* Vol. 119, pp. 1383-1398.

Fukuoka, S., and Watanabe, A. (1995). Horizontal flow structures in channels with dense vegetation clusters and the numerical analysis thereof. *Proceeding of the 26th Congress of IAHR*, *Hydra 2000*, London. Vol. 1, pp. 296-301.

Fukuoka, S., and Watanabe, A. (1997). Horizontal structure of flood flow with dense vegetation clusters along main channel banks. *Proceeding of the 27th Congress of IAHR*, San Francisco. B2, pp 1408-1413.

Gavrilakis, S. (1992). Numerical simulation of low-Reynolds-number turbulent flow through a straight square duct. *Journal of Fluid Mechanics*. Vol. 244, pp. 101.

Germano, M., Piomelli, U., Moin, P. and Cabot, W.H. (1991). A dynamic sub-grid scale eddy viscosity model. *Physics of Fluids A*. Vol. 3, pp. 1760-1765

Grega, L.M. (1995). Generation of secondary flows in turbulent flow along a solid wall-free surface corner. *PhD Dissertation*, Rutgers University.

Grega, L.M., Wei, T., Leighton, R.I. and Neves, J.C. (1995). Turbulent mixed-boundary flow in a corner formed by a solid wall and a free surface. *Journal of Fluid Mechanics.* Vol. 294, pp. 17.

Grega, L.M., Hsu, T.Y. and Wei, T. (2002). Vorticity transport in a corner formed by a solid wall and a free surface. *Journal of Fluid Mechanics.* Vol. 465, pp. 331-352.

Hodges, B.R. and Street, R.L. (1999). On simulation of turbulent nonlinear free-surface flows. *Journal of Computational Physics*. Vol. 151, pp. 425-457.

Hodskinson, A. and Ferguson, R.I. (1998). Numerical modelling of separated flow in river bends: model testing and experimental investigation of geometric controls on the extent of flow separation at the concave bank. *Hydraulic Processes.* Vol. 12, pp.1323-1338.

Hollinrake, P.G. (1987). The structure of flow in open channels, a literature survey. Vol. I. *Report SR96*, HR Wallingford, UK.

Hollinrake, P.G. (1988). The structure of flow in open channels, a literature survey. Vol. II. *Report SR153*, HR Wallingford, UK.

Hollinrake, P.G. (1989). The structure of flow in open channels, a literature survey. Vol. III. *Report SR209*, HR Wallingford, UK.

Hollinrake, P.G. (1990). The structure of flow in open channels, a literature survey. Vol. IV. *Report SR227*, HR Wallingford, UK.

Hollinrake, P.G. (1992). The structure of flow in open channels, a literature survey. Vol. V. *Report SR301*, HR Wallingford, UK.

Hsu T.Y., Grega, L.M., Leighton, R.I. and Wei, T. (2000). Turbulent kinetic energy transport in a corner formed by a solid wall and a free surface. *Journal of Fluid Mechanics*. Vol. 410, pp. 343.

Imamoto, H. and Ishigaki, T. (1988). Measurement of secondary flow in an open channel. *Proceeding of the 6th IAHR-APD Congress,* Kyoto, Japan. pp. 513-520.

Iwamoto, K., Kasagi, N. and Suzuki, Y. (2005). Direct numerical simulation of turbulent channel flow at $R_{e\tau}$=2320. *Proceeding of the 6th Symposium on Smart Control of Turbulence,* Tokyo, Japan.

Kang, H. and Choi, S. (2006). Reynolds stress modelling of rectangular open-channel flow. *International Journal for Numerical Methods in Fluids.* Vol. 51, pp. 1319-1334.

Kawahara, Y. and Tamai, N. (1988). Numerical calculation of turbulent flows in compound channels with an algebraic stress turbulence model. *Proceeding of the 3rd International Symposium on Refined Flow Modelling and Turbulence Measurements,* Tokyo, Japan, pp. 9-17.

Keulegan, C.H. (1938). Laws of turbulent flow in open channels. *Journal of Research Natl. Bur. Stand.,* Vol. 21, pp. 707-740.

Kinoshita, R. (1967). An analysis of the movement of flood waters by aerial photography, Concerning characteristics of turbulence and surface flow. *Photographic Survey.* Vol. 6, pp. 1-17.

Knight, D.W., and Demetriou, J.D. (1983). Floodplain and main channel flow interaction. *Journal of Hydraulic Engineering*, *ASCE.* Vol. 109(8), August, pp. 1073-1092.

Knight, D.W., and Demetriou, J.D. (1984). Floodplain and main channel flow interaction. *Journal of Hydraulic Engineering.* Vol. 109(8), pp. 1073-1091.

Knight, D.W., Demetriou, J.D. and Hamed, M. (1984). Boundary shear in smooth rectangular channels. *Journal of Hydraulic Engineering*. Vol. 110(4), pp. 405-422.

Knight, D.W. and Patel, H.S. (1985). Boundary shear stress distributions in smooth rectangular duct. *Journal of Hydraulic Engineering, ASCE.* Vol. 111(1), Jan. pp. 29-47.

Knight, D.W. (1989). Hydraulics of flood channels. *Floods: Hydrological Sedimentological and Geomorphological Implications.* K. Beven and P. Carling (Eds), John Wiley and Sons Ltd.

Knight, D.W. and Shiono, X. (1996). River channel and floodplain hydraulics. *Floodplain Processes.* M.G. Anderson, D.E. Walling, P.D. Bates (Eds), John Wiley and Sons Ltd., pp. 139-181.

Knight, D.W., et al. (2002). Flow in compound channels. *IAHR monograph, IAHR, Madrid, Spain.*

Knight, D.W., Omran, M. and Abril, J.B. (2004). Boundary conditions between panels in depth-averaged flow models revisited. *Proceeding of the 2nd International Symposium on River flow, IAHR, Naples, Italy*, Jun., pp. 473-483.

Knight, D.W., Omran, M. and Tang, X. (2007). Modelling depth-averaged velocity and boundary shear in trapezoidal channels with secondary flows. *Journal of Hydraulic Engineering, ASCE.* Vol. 133(1), Jan., pp. 39-47.

Kolmogorov, A. N. (1942). Equations of turbulent motion in incompressible fluid. Izv. Akad. Nauk. SSR, Seria fizicheska Vi. 1-2, pp. 56-58.

Krishnappan, B.G. and Lau, Y.L. (1986). Turbulence modelling of floodplain flows. *Journal of Hydraulic Engineering, ASCE.* Vol. 112(4), pp. 251-266.

Lane, S.N., Bradbrook, K.F., Richards, K.S., Biron, P.A. and Roy, A.G. (1999). The application of computational fluid dynamics to natural river channels: Three-dimensional versus two-dimensional approaches. *Geomorphology*. Vol. 29, pp.1-20.

Larson, R. (1988). Numerical simulation of flow in compound channels. *Proceeding of the 3rd International Symposium on Refined Flow Modelling and Turbulence Measurements, Tokyo, Japan,* pp. 527-536.

Launder, B.E. and Spalding, D.B. (1974). The numerical computation of turbulent flows. *Computer Methods in Applied Mechanics and Engineering*. Vol. 3(2), pp. 269-289.

Launder, B.E., Reece, G.L., and Rodi, W. (1975). Progress in the development of a Reynolds stress turbulence closure. *Journal of Fluid Mechanics*. Vol. 68, pp. 537-566.

Leighly, J.B. (1932). Toward a theory of morphologic significance of turbulence in flow of water in streams. *University of California, Pub. Georg.,* Vol. 6(1).

Liao, H. and Knight, D.W. (2007). Analytical stage-discharge formulae for flow in straight prismatic compound channels. *Journal of Hydraulic Engineering, ASCE*. Vol. 133(10), pp. 1111-1122.

Lilly, D.K. (1967). The representation of small-scale turbulence in numerical simulations. *In Proc. IBM scientific computing symposium on environmental sciences, IBM form no. 320-1951*. White Plains, New York, pp. 195-209.

Longo, J., Huang, H.P. and Stern, F. (1998). Solid/free surface juncture boundary layer and wake. *Exps. Fluids*. Vol. 25, pp. 283.

Lotter, G.K. (1933). Considerations on hydraulic design of channels with different roughness of walls. *Trans. All Union Scientific Research, Institute of Hydraulic Engineering*, Leningrad, pp. 238-241 (in Russian).

Manning, R. (1889). On the flow of water in open channels and pipes. *Trans. Institution of Civil Engineers of Ireland*, Vol. 20, pp. 161-207.

McGahey, C. (2006). A practical approach to estimating the flow capacity of rivers. *PhD Thesis*, The Open University.

Meneveau, C. and Katz, J. (2000). Scale-invariance and turbulence models for large-eddy simulation. *Annual Review of Fluid Mechanics*. Vol. 32, pp. 1-32.

Morvan, H.P. (2001). Three-dimensional simulation of river flood flows. *PhD Thesis*, Glasgow.

Moser, R.D., Kim, J. and Mansour, N.N. (1999). Direct numerical simulation of turbulent channel flow up to $R_{e\tau}$=590. *Physics of Fluids*. Vol 11, pp. 943.

Myers, W.R.C and Brennan, E.K. (1990). Flow resistance in compound channels. *Journal of Hydraulic Research, IAHR*, Vol. 28(2), pp. 141-155.

Myers, W.R.C. (1978). Momentum transfer in a compound channel. *Journal of Hydraulic Research, IAHR*, Vol. 16(2), pp. 139-150.

Nadaoka, K., and Yagi, H. (1998). Shallow-water turbulence modeling and horizontal large-eddy computation of river flow. *Journal of Hydraulic Engineering, ASCE*, Vol. 124(5), pp. 493-500.

Nakayama, A. and Yokojima, S. (2002). LES of open-channel flow with free-surface fluctuations. *Proc. of Hydraulic Engineering, JSCE*. Vol. 46, pp. 373-378.

Naot, D. and Rodi, W. (1982). Calculation of secondary currents in channel flow. *Journal of Hydraulic Divisions*, *ASCE*, Vol. 108, No. HY8, Aug. pp. 948-969.

Naot, D., Nezu, I. and Nakagawa, H. (1993). Hydrodynamic behaviour of compound rectangular open channels. *Journal of Hydraulic Engineering, ASCE.* Vol. 119(3), pp. 390-408.

Nezu, I. and Rodi, W. (1985). Experimental study of secondary currents in open channel flow. *Proceedings of the 21st Congress of the IAHR.* Delft, Netherlands. Vol. 2, pp. 114-119.

Nezu, I., Nakagawa, H., and Tominaga, A. (1985). Secondary currents in a straight channel flow and the relation to its aspect ratio. *Turbulent shear flows.* Vol. 4, Springer, New York, pp. 246-260.

Nezu, I. and Rodi, W. (1986). Open channel flow measurements with a laser doppler anemometer. *Journal of. Hydraulic. Engineering.* Vol. 112, pp. 335-355.

Nezu, I. and Nakagawa, T. (1997). Space-time correlation structures of horizontal coherent vortices in compound open-channel flows by using particle-tracking velocimetry. *Journal of Hydraulic Research, IAHR.* Vol. 35(2), pp. 191-208.

Nokes, J.R. and Wood, I.R. (1987). Turbulent dispersion of a steady discharge of positively or negatively buoyant particles in two dimensions. *Journal of Hydraulic research,* Vol. 25(11), pp. 103-122.

Nokes, J.R. and Wood, I.R. (1988). Vertical and Lateral Turbulent Dispersion: Some Experimental Results. *Journal of Fluid Mechanics*, Vol. 187, pp. 373-394.

Omran, M. (2005). Modelling stage-discharge curves, velocity and boundary shear stress distributions in natural and artificial channels using a depth-averaged approach. *PhD Thesis.* The University of Birmingham, UK.

Pan, Y. and Banerjee, S. (1995). A numerical study of free-surface turbulence in channel flow. *Physics of Fluids,* Vol. 7, pp. 1649.

Price, R. (1974). Comparison of four numerical methods for flood routing. *Journal of Hydraulic Engineering, ASCE.* Vol. 100.

Prinos, P., and Townsend, R.D. (1984). Comparison of methods for predicting discharge in compound open channels. *Advances in Water Resources*, Vol. 7, pp. 180-187.

Rajaratnam, N. and Ahmadi, R. (1981). Hydraulics of channels with floodplains. *Journal of Hydraulics Research*, Vol. 19(1), pp. 43-60.

Rogallo, R.S. and Moin, P. (1984). Numerical simulation of turbulent flows. *Annual Review of Fluid Mechanics*. Vol. 16, pp. 99-137.

Salvetti, M.V., Zang, Y., Street, R.L. and Banerjee, S. (1997). Large-eddy simulation of free surface decaying turbulence with dynamic subgrid-scale models. *Physics of Fluids*. Vol. 9, pp. 2405.

Sellin, R.J.H. (1964). A laboratory investigation into the interaction between flow in the channel of a river and that of its floodplains. *Le Houille Blanche*. Vol. 7, pp. 793-801.

Shi, J., Thomas, T.G. and Williams, J.J.R. (1999). Large eddy simulation of flow in a rectangular open channel. *Journal of Hydraulic Research*. Vol. 37(3), pp. 345-361.

Shi, J., Thomas, T.G. and Williams, J.J.R. (2001). Coarse resolution large-eddy simulation of turbulent channel flows. *International Journal of Numerical Methods in Fluids.* Vol. 11(1), pp. 20-35.

Shiono, K. and Knight, D.W. (1988). Two-dimensional analytical solution for a compound channel. *Proceedings of the 3rd International Symposium on Refined Flow Modelling and Turbulence Measurements,* Tokyo, Japan, July, pp. 503-510.

Shiono, K. and Knight, D.W. (1990). Mathematical models of flow in two or multistage straight channels. In: White WR, editor. *Proceedings of International conference on river flood hydraulics, Paper GI, Wallingford: J. Wiley and Sons*, pp. 229-238.

Shiono, K. and Knight, D.W. (1991). Turbulent open channel flows with variable depth across the channel, *Journal of Fluid Mechanics*, Vol. 222, pp. 617-646 (and Vol. 231, Oct., pp. 693).

Sinha, S.K., Sotiropoulos, F. and Odgaard, A.J. (1998). Three-dimensional numerical model for flow through natural rivers. *Journal of Hydraulic Engineering*. Vol. 124(1), pp. 13-24.

Smagorinsky, J. (1963). General circulation experiments with the primitive equation. *Monthly Weather Review,* Vol. 93, pp. 99-165.

Sofialidis, D. and Prinos, P. (1999). Compound open-channel flow modelling with nonlinear low-reynolds k-epsilon models. *Journal of Hydraulic Engineering*. Vol. 124(3), pp. 253-262.

Streedhar, M. and Stern, F. (1998). Large Eddy Simulation of temporally developing juncture flows. *International Journal for Numerical Methods in Fluids*. Vol. 28(1), pp. 47-72.

Tang, X. and Knight, D.W. (2008). A general model of lateral depth-averaged velocity distributions for open channel flows. *Advances in Water Resources,* Vol. 31, pp. 846-857.

Thomas, T.G. and Williams, J. (1995a). Large eddy simulation of a symmetric trapezoidal channel at Reynolds number of 430,000. *Journal of Hydraulic Research*. Vol. 33(6), pp. 825-842.

Thomas, T.G. and Williams, J. (1995b). Large eddy simulation of turbulent flow in an asymmetric compound open channel. *Journal of Hydraulic Research.* Vol. 33(1), pp. 27-41.

Thomas, T.G. and Williams, J. (1999). Large eddy simulation of flow in a rectangular open channel. *Journal of Hydraulic Research.* Vol. 37(3), pp. 345-361.

Tominaga, A., Nezu, I., Ezaki, K. and Nakagawa, H. (1989). Turbulent structure in straight open channel flows. *Journal of Hydraulic Research*, *IAHR.* Vol. 27(1), pp. 149-173

Tominaga, A., and Nezu, I. (1991). Turbulent structure in compound open channel flow. *Journal of Hydraulic Engineering, ASCE*, Vol. 117(1), pp. 21-41.

van Prooijen, B.C., Booij, R. and Uijttewaal, W.S.J. (2000). Measurement and analysis methods of large scale horizontal coherent structures in a wide shallow channel. Paper 21-3 Proceedings of the 10th International Symposium on applications of laser techniques to ….

van Prooijen, B.C., and Uijttewaal, W.S.J. (2001). Development of large turbulence structures in shallow mixing layers. *Proceedings of the 2001 International Symposium on Environmental Hydraulics*, Arizona.

van Prooijen, B.C. (2004). Shallow mixing layers. *PhD Thesis*, Delft, Netherlands.

Wark J.B., James C.S. and Ackers P. (1994). Design of straight and meandering channels. *National Roads Authority*, R&D Report No 13, pp. 1-86.

Wormleaton P.R., Allen J. and Hadjipanos P. (1982). Discharge assessment in compound channel flow. *Journal of the Hydraulics Division*, ASCE, Vol. 108(9), pp. 975-993.

Wormleaton, P.R., and Merrett, D.J. (1990). An improved method of the calculation for steady uniform flow in prismatic main channel/flood plain sections. *Journal of Hydraulic Research, IAHR*, Vol. 28(2), pp. 157-174.

Wright, N.G., Crossley, A.J., Morvan, H.P., Stoesser, T. (2004). Detailed validation of CFD for flows in straight channels. *River Flow 2004*, Naples, Italy.

APPENDIX A

SKM ANALYTICAL SOLUTION

First note, Equation A-1 is the basis of the SKM,

$$\rho g H S_0 - \frac{\rho f U_d^2}{8}\left(1+\frac{1}{s^2}\right)^{\frac{1}{2}} + \frac{\partial}{\partial y}\left(\rho\lambda H^2\left(\frac{f}{8}\right)^{\frac{1}{2}}U_d\frac{\partial U_d}{\partial y}\right) = \frac{\partial}{\partial y}\left(H\left(\rho\overline{UV}\right)_d\right)$$

(A-1)

Equation A-1 is a non-linear second order ordinary differential equation that represents the lateral distribution of depth averaged velocity in prismatic channels.

Expressing $\quad U_d\frac{\partial U_d}{\partial y} = \frac{1}{2}\frac{\partial}{\partial y}U_d^{\,2}\quad$ gives, $\quad\frac{\partial}{\partial y}\left(U_d\frac{\partial U_d}{\partial y}\right) = \frac{1}{2}\frac{\partial^2 U_d^{\,2}}{\partial y^2}\quad$ (A-2)

Also assuming $\Gamma = \frac{\partial}{\partial y}\left(H\left(\rho\overline{UV}\right)_d\right)$ (A-3)

Substituting (A-2) and (A-3) into (A-1) gives,

$$\left(\rho\lambda H^2\left(\frac{f}{8}\right)^{\frac{1}{2}}\frac{1}{2}\right)\frac{\partial^2 U_d^{\,2}}{\partial y^2} - \frac{\rho f}{8}\left(1+\frac{1}{s^2}\right)^{\frac{1}{2}}U_d^2 + \rho g H S_0 = \Gamma$$

$$\Rightarrow\left(\frac{\rho\lambda H^2}{2}\left(\frac{f}{8}\right)^{\frac{1}{2}}\right)\frac{\partial^2 U_d^{\,2}}{\partial y^2} - \frac{\rho f}{8}U_d^2 + \rho g H S_0 - \Gamma = 0\qquad$$ (A-4)

(For a constant depth domain)

Assuming a solution of the form

$$A\frac{\partial^2 U_d}{\partial y^2} - BU_d + C = 0 \qquad \text{(Auxiliary equation)} \qquad \text{(A-5)}$$

Rearranging $\Rightarrow \dfrac{\partial^2 U_d}{\partial y^2} = \dfrac{B}{A}U_d - \dfrac{C}{A}$ (A-6)

The general solution (complimentary function) of the corresponding homogeneous equation can be expressed as:

$$U_d(y) = \left[A_1 e^{\gamma y} + A_2 e^{-\gamma y} + k\right]^{1/2} \qquad \text{(A-7)}$$

where $\qquad U_d(y) = A_1 e^{(B/A)^{1/2} y} + A_2 e^{(B/A)^{1/2} y} + k$ (A-8)

and $\qquad k = \dfrac{C}{B}$ (A-9)

Calculating $\dfrac{B}{A}$ which is equivalent to γ gives:

$$\frac{\rho f}{8} \frac{2}{\rho \lambda H^2}\left(\frac{f}{8}\right)^{-1/2}$$

$$= \left(\frac{f}{8}\right)^{1/2}\left(\frac{2}{\lambda}\right)\frac{1}{H^2} \qquad \text{(A-10)}$$

Taking the square root, $\left(\dfrac{B}{A}\right)^{1/2}$ as in (A-8) gives:

$$\left(\frac{f}{8}\right)^{1/4}\left(\frac{2}{\lambda}\right)^{1/2}\frac{1}{H} \tag{A-11}$$

Calculating $k = \dfrac{C}{B}$ to give β and κ gives:

$$\frac{\rho g H S_0 - \Gamma}{\rho f / 8}$$

$$= \frac{8\rho g H S_0 - 8\Gamma}{\rho f}$$

$$= \frac{8 g H S_0}{f} - \frac{8\Gamma}{\rho f}$$

$$= \frac{8 g H S_0}{f}\left(1 - \frac{\Gamma}{\rho g H S_0}\right) = \kappa(1 - \beta) \tag{A-12}$$

Giving $\qquad \kappa = \dfrac{8 g H S_0}{f} \tag{A-13}$

and $\qquad \beta = \dfrac{\Gamma}{\rho g H S_0} \tag{A-14}$

Summary

The general solution of Equation A-1 can be expressed as:

$$U_d(y) = \left[A_1 e^{\gamma y} + A_2 e^{-\gamma y} + k\right]^{1/2} \tag{A-15}$$

257

Where
$$\gamma = \left(\frac{f}{8}\right)^{\frac{1}{4}} \left(\frac{2}{\lambda}\right)^{\frac{1}{2}} \frac{1}{H} \tag{A-16}$$

$$k = \kappa(1-\beta) \tag{A-17}$$

$$\kappa = \frac{8gHS_0}{f} \tag{A-18}$$

$$\beta = \frac{\Gamma}{\rho gHS_0} \tag{A-19}$$

APPENDIX B

FORTAN90 CODE FOR

THE ANALYTICAL SOLUTION OF THE SKM

```fortran
! ----------------------------------------------------------------

! Program to compute velocity profiles from

! the SKM analytical solution for numerous panels

! ----------------------------------------------------------------


PROGRAM SKMPanelCode


IMPLICIT NONE

REAL ChannelHeight, ChannelWidth, ChannelSlope

REAL Density, Gravity

REAL H, b, A, hydR, wetP, S0, rho, g

INTEGER NumberOfPanels, LengthOfList, P, i, j, count, S, num, ITMP, K, T, Nom,
L

REAL ypanel, C1, PI, PI1, PJ

DOUBLE PRECISION DeltaX, AVGf, AVGlamda, AVGgamma, AVGf2, Res


DOUBLE  PRECISION,  DIMENSION(:),  ALLOCATABLE    ::  sumP,  fAvg,
lamdaAvg, gammaAvg, CMatrix

DOUBLE PRECISION, DIMENSION(:), ALLOCATABLE :: beta, gam, kappa, nu
```

```fortran
DOUBLE PRECISION, DIMENSION(:,:), ALLOCATABLE  :: ParamData, ParamAvg
DOUBLE PRECISION, DIMENSION(:), ALLOCATABLE  :: interfacelocations, interfacelocations2

REAL, DIMENSION(:,:), ALLOCATABLE :: InitialMatrix, MatrixInverse, BI
REAL, DIMENSION(:), ALLOCATABLE :: gamRE, y2RE, RE, UdRE
INTEGER, DIMENSION(:), ALLOCATABLE :: INDX

DOUBLE PRECISION, DIMENSION(:), ALLOCATABLE :: C, Resultant, y, y2, Ud2

! -------------------------------------------------------------
! Specify Channel Geometry (all dimensions in metres)
! -------------------------------------------------------------

ChannelHeight = 0.076          !
ChannelWidth = 0.152           !
ChannelSlope = 0.000966        ! INPUTS
Density = 997                  !
Gravity = 9.8066502            !
NumberOfPanels = 5             !
H=ChannelHeight                !
b=ChannelWidth/2               !
A=H*(2*b)                      !
```

```
hydR=(2*b)+(2*H)                !

wetP=A/hydR                     ! Computed channel geometry parameters


S0=ChannelSlope                 !

rho = Density                   !

g = Gravity                     !

P = NumberOfPanels              !

DeltaX = b/NumberOfPanels       !


! --------------------------------------------------------------

! Read in values of f, lamda and gamma for each panel

! --------------------------------------------------------------


LengthOfList=39

L=LengthOfList


ALLOCATE(ParamData(L,4))

OPEN(10,file="VariableValues.txt")


DO i=1,L

     READ(10,*)     ParamData(i,1),     ParamData(i,2),     ParamData(i,3),

ParamData(i,4)

END DO

CLOSE(10)
```

```fortran
! --------------------------------------------------------------

! Compute panel interface locations

! --------------------------------------------------------------


ALLOCATE(interfacelocations(1:P))

OPEN(15,file="InterfaceLocations.txt")


DO i=1,P

        ypanel = 0+(DeltaX*i)

        interfacelocations(i) = ypanel

        WRITE(15,*) interfacelocations(i)

END DO


CLOSE(15)


! --------------------------------------------------------------

! Compute average f, lamda, gamma values per panel

! --------------------------------------------------------------


OPEN(20,file="SumValues.txt")

DO i=1,1

        DO j=1,L

                IF (ParamData(j,1).LE.interfacelocations(i)) THEN

                        count=count+(j/j)

                        AVGf=AVGf+ParamData(j,2)
```

```
                AVGlamda=AVGlamda+ParamData(j,3)

                AVGgamma=AVGgamma+ParamData(j,4)

        ENDIF

    END DO

    WRITE(20,FMT="(i1,2x,i2,2x,f15.12,2x,f15.12,2x,f15.12)") i, count, AVGf,

AVGlamda, AVGgamma

END DO


DO i=2,P

    DO j=1,L

        IF (ParamData(j,1).LE.interfacelocations(i)) THEN

            IF (ParamData(j,1).GE.interfacelocations(i-1)) THEN

                count=count+(j/j)

                AVGf=AVGf+ParamData(j,2)

                AVGlamda=AVGlamda+ParamData(j,3)

                AVGgamma=AVGgamma+ParamData(j,4)

            ENDIF

        ENDIF

    END DO

    WRITE(20,FMT="(i1,2x,i2,2x,f15.12,2x,f15.12,2x,f15.12)") i, count, AVGf,

AVGlamda, AVGgamma

END DO

CLOSE (20)


ALLOCATE(ParamAvg(P,5))
```

```fortran
OPEN(30,file='SumValues.txt')

DO i=1,P

        READ(30,*) ParamAvg(i,1), ParamAvg(i,2), ParamAvg(i,3), ParamAvg(i,4),
ParamAvg(i,5)

END DO

CLOSE(30)


ALLOCATE(fAvg(1:P), lamdaAvg(1:P), gammaAvg(1:P))

OPEN(40,file="AvgValues.txt")

sumP = ParamAvg(1:P,2)

fAvg = ParamAvg(1:P,3)

lamdaAvg = ParamAvg(1:P,4)

gammaAvg = ParamAvg(1:P,5)


DO i=1,1

        fAvg(i) = ParamAvg(i,3)/ParamAvg(i,2)

        lamdaAvg(i) = ParamAvg(i,4)/ParamAvg(i,2)

        gammaAvg(i) = ParamAvg(i,5)/ParamAvg(i,2)

END DO


DO i=2,P,1

        fAvg(i)  =  (ParamAvg(i,3)-ParamAvg(i-1,3))/(ParamAvg(i,2)-ParamAvg(i-
1,2))

        lamdaAvg(i)     =     (ParamAvg(i,4)-ParamAvg(i-1,4))/(ParamAvg(i,2)-
ParamAvg(i-1,2))
```

```fortran
        gammaAvg(i)      =      (ParamAvg(i,5)-ParamAvg(i-1,5))/(ParamAvg(i,2)-
ParamAvg(i-1,2))

END DO

WRITE(40,FMT="(f10.5)") fAvg(1:P)

WRITE(40,FMT="(f10.5)") lamdaAvg(1:P)

WRITE(40,FMT="(f10.5)") gammaAvg(1:P)

CLOSE(40)


! -------------------------------------------------------------

! Read in already averaged data

! -------------------------------------------------------------


!ALLOCATE(fAvg(1:P), lamdaAvg(1:P), gammaAvg(1:P))        !

!OPEN(30,file="ParamAvg.txt")                            !

!DO i=1,P                                                !

!       READ(30,*) fAvg(i), lamdaAvg(i), gammaAvg(i)     !

!END DO                                                  !

!CLOSE(30)                                               ! Use if values

!                                                        !      already
averaged

!OPEN(40,file="AvgValues.txt")                           !

!WRITE(40,FMT="(f10.5)") fAvg(1:P)                        !

!WRITE(40,FMT="(f10.5)") lamdaAvg(1:P)                    !

!WRITE(40,FMT="(f10.5)") gammaAvg(1:P)                    !

!CLOSE(40)                                                !
```

```fortran
! -------------------------------------------------------------

! Compute Beta, gamma, kappa and nu

! -------------------------------------------------------------


ALLOCATE(beta(1:P), gam(1:P), kappa(1:P), nu(1:P))

DO i=1,P

        beta(i) = gammaAvg(i)/ (g*rho*H*S0)

        gam(i) = (sqrt(2.0/lamdaAvg(i)))*((fAvg(i)/8.0)**(1.0/4.0))*(1.0/H)

        kappa(i) = ((8.0*g*h*S0)/fAvg(i))*(1-beta(i))

        nu(i) = lamdaAvg(i)*(sqrt(fAvg(i)/8.0))

END DO

OPEN(50,file='ParamSummary.txt')

DO i=1,P

        WRITE(50,FMT="(f10.5)")  fAvg(i),  lamdaAvg(i),  gammaAvg(i),  beta(i),

gam(i), kappa(i), nu(i), interfacelocations(i)

END DO

CLOSE(50)


! -------------------------------------------------------------

! Create Matrix A Solution

! -------------------------------------------------------------


S=2*P

ALLOCATE (InitialMatrix(S,S))
```

```fortran
DO i=1,S                                          !

    DO j=1,S                                       !

        InitialMatrix(i,j)=0                       ! Fill the matrix with
zeros

    END DO                                         !

END DO                                             !


! --------------------------------------------------------------


DO i=1,S

    DO j=1,S

        IF (i==1)THEN

            IF (j==1)THEN

            InitialMatrix(i,j)=1

            END IF

            IF (j==2)THEN

            InitialMatrix(i,j)=-1

            END IF

        ELSE IF (i>1.AND.mod(i,2)==0)THEN

            IF (j==i-1)THEN


    InitialMatrix(i,j)=EXP(gam(i/2)*interfacelocations(i/2))

            ELSE IF (j==i)THEN
```

267

InitialMatrix(i,j)=EXP(-

gam(i/2)*interfacelocations(i/2))

ELSE IF (j==i+1)THEN

InitialMatrix(i,j)=-

EXP(gam((i/2)+1)*interfacelocations(i/2))

ELSE IF (j==i+2)THEN

InitialMatrix(i,j)=-EXP(-

gam((i/2)+1)*interfacelocations(i/2))

ELSE

InitialMatrix(i,j)=0.0

END IF

ELSE IF (i>1.AND.mod(i,2)==1)THEN

IF (j==i-2) THEN

InitialMatrix(i,j)=(nu((i-1)/2)*gam((i-

1)/2))*(EXP(gam((i-1)/2) &

*interfacelocations((i-1)/2)))

ELSE IF (j==i-1) THEN

InitialMatrix(i,j)=-(nu((i-1)/2)*gam((i-1)/2))*(EXP(-

gam((i-1)/2) &

*interfacelocations((i-1)/2)))

ELSE IF (j==i)THEN

InitialMatrix(i,j)=-

(nu((i+1)/2)*gam((i+1)/2))*(EXP(gam((i+1)/2) &

*interfacelocations((i-1)/2)))

ELSE IF (j==i+1) THEN

```fortran
                    InitialMatrix(i,j)=(nu((i+1)/2)*gam((i+1)/2))*(EXP(-

gam((i+1)/2) &

                    *interfacelocations((i-1)/2)))

              ELSE

                    InitialMatrix(i,j)=0.0

              END IF

         END IF

    END DO

END DO


OPEN(60,file="InitialMatrix.txt")

DO j=1,S

    WRITE(60,FMT=*)  InitialMatrix(1,j), InitialMatrix(2,j), InitialMatrix(3,j),

InitialMatrix(4,j), InitialMatrix(5,j)

END DO

CLOSE(60)


! --------------------------------------------------------------

! Create Inverse Matrix A Solution

! --------------------------------------------------------------

! --------------------------------------------------------------

! Subroutine to invert matrix InitialMatrix(S,S) with the inverse

! stored in MatrixInverse(S,S) in the output

! --------------------------------------------------------------
```

```
ALLOCATE(MatrixInverse(S,S),BI(S,S),INDX(1:S),C(1:S))

DO I=1,S

  DO J=1,S

        BI(I,J)=0.0

  END DO

END DO

DO I=1,S

  BI(I,I)=1.0

END DO

! --------------------------------------------------------------

! Subroutine to perform the partial-pivoting Gaussian elimination

! InitialMatrix(S,S) is the original matrix in the input and

! transformed matrix plus the pivoting element ratios below the

! diagonal in the output INDX(S) records the pivoting order

! --------------------------------------------------------------


! Initialize the index -------------------------------------------


DO I = 1, S

  INDX(I) = I

END DO


! Find the rescaling factors, one from each row --------------------


DO I = 1, S
```

```fortran
      C1= 0.0
      DO J = 1, S
       C1 = AMAX1(C1,ABS(InitialMatrix(I,J)))
      END DO
      C(I) = C1
    END DO


! Search the pivoting (largest) element from each column -------


    DO J = 1, S-1
      PI1 = 0.0
      DO I = J, S
        PI = ABS(InitialMatrix(INDX(I),J))/C(INDX(I))
        IF (PI.GT.PI1) THEN
          PI1 = PI
          K   = I
        ENDIF
      END DO


! Interchange the rows via INDX(S) to record pivoting order ---


      ITMP    = INDX(J)
      INDX(J) = INDX(K)
      INDX(K) = ITMP
      DO I = J+1, S
```

```
PJ  = InitialMatrix(INDX(I),J)/InitialMatrix(INDX(J),J)


! Record pivoting ratios below the diagonal --------------------


   InitialMatrix(INDX(I),J) = PJ
! Modify other elements accordingly ----------------------------


   DO K = J+1, S
     InitialMatrix(INDX(I),K) = InitialMatrix(INDX(I),K)-PJ &
         *InitialMatrix(INDX(J),K)
   END DO
  END DO
END DO


! -------------------------------------------------------------------


DO I = 1, S-1
  DO J = I+1, S
    DO K = 1, S
      BI(INDX(J),K) = BI(INDX(J),K)-InitialMatrix(INDX(J),I)*BI(INDX(I),K)
    END DO
  END DO
END DO


DO I = 1, S
```

```fortran
    MatrixInverse(S,I) = BI(INDX(S),I)/InitialMatrix(INDX(S),S)

  DO J = S-1, 1, -1

    MatrixInverse(J,I) = BI(INDX(J),I)

    DO K = J+1, S

      MatrixInverse(J,I) = MatrixInverse(J,I)-InitialMatrix(INDX(J),K) &
          *MatrixInverse(K,I)

    END DO

    MatrixInverse(J,I) =  MatrixInverse(J,I)/InitialMatrix(INDX(J),J)

  END DO

END DO




OPEN(70,file="MatrixInverse.txt")

DO j=1,S

      WRITE(70,FMT=*)   MatrixInverse(1,j),              MatrixInverse(2,j),

MatrixInverse(3,j), MatrixInverse(4,j), MatrixInverse(5,j)

END DO

CLOSE(70)




! ------------------------------------------------------------

! Compute 'C' Matrix

! ------------------------------------------------------------



ALLOCATE(CMatrix(1:S))
```

```fortran
OPEN(80,file="CMatrix.txt")

DO i=1,S

        IF (mod(i,2)==1)THEN

                CMatrix(i)=0

        ELSE IF (mod(i,2)==0.AND.i<S)THEN

                CMatrix(i)=kappa((i/2)+1)-kappa(i/2)

        ELSE IF (mod(i,2)==0.AND.i==S)THEN

                CMatrix(i)=-kappa(i/2)

        END IF

        WRITE(80,FMT=*)   CMatrix(i)

END DO

CLOSE(80)


! ---------------------------------------------------------------

! Create Resultant Matrix

! ---------------------------------------------------------------


ALLOCATE(Resultant(1:S))

DO i=1,S                                        !

        Resultant(i)=0                          ! Fill the matrix with zeros

END DO                                          !


OPEN(90,file="Resultant.txt")

DO i=1,S

        DO j=1,S
```

```
                    Resultant(i)=Resultant(i)+CMatrix(j)*MatrixInverse(i,j)

        END DO

        WRITE(90,FMT=*) Resultant(i)

END DO

CLOSE(90)


! -------------------------------------------------------------

! Create list of y values

! -------------------------------------------------------------


Nom=10                                    !  10  values/panel  -can  be
changed
T=P*(Nom+1)


ALLOCATE(interfacelocations2(1:P+1),y(1:T),y2(1:T),Ud2(1:T))
OPEN(100,file="y.txt")


DO i=1,P+1

        IF(i==1) THEN

                interfacelocations2(i)=0.0

        ELSE

                interfacelocations2(i)=interfacelocations(i-1)

        END IF

END DO
```

```fortran
DO j=1,P

        DO i=1,Nom+1

                IF(i==1) THEN

                        y(((j-1)*Nom)+i)=interfacelocations2(j)

                ELSE

                        y(((j-1)*Nom)+i)=interfacelocations2(j)+(i-

1)*((interfacelocations2(j+1)-interfacelocations2(j))/Nom)

                END IF

                WRITE(100,FMT=*) y(((j-1)*Nom)+i)

        END DO

END DO



CLOSE(100)



OPEN(100,file="y.txt")

DO i=1,T

        READ(100,*) y2(i)

END DO

CLOSE(100)



! --------------------------------------------------------------

! Compute velocities

! --------------------------------------------------------------



OPEN(110,file="Ud.txt")
```

```
ALLOCATE(gamRE(1:P),y2RE(1:T))

DO i=1,P

        gamRE(i)=gam(i)

END DO


DO i=1,T

        y2RE(i)=y2(i)

END DO


ALLOCATE(RE(1:T))

DO j=1,P

        DO i=1,Nom+1

                RE(((j-1)*(Nom+1))+i)=(Resultant((2*j)-
1)*(exp(gamRE(j)*y2RE(((j-1)*(Nom+1))+i))))+(Resultant(2*j)*(exp(-
gamRE(j)*y2RE(((j-1)*(Nom+1))+i))))+kappa(j)

        END DO

END DO


ALLOCATE(UdRE(1:T))


DO i=1,T
```

```
        UdRE(i)=sqrt(RE(i))

        WRITE(110,*) y2(i), UdRE(i)

END DO


CLOSE(110)


! -------------------------------------------------------------


END PROGRAM SKMPanelCode
```